

University of Southampton Research Repository

Copyright © and Moral Rights for this thesis and, where applicable, any accompanying data are retained by the author and/or other copyright owners. A copy can be downloaded for personal non-commercial research or study, without prior permission or charge. This thesis and the accompanying data cannot be reproduced or quoted extensively from without first obtaining permission in writing from the copyright holder/s.

The content of the thesis and accompanying research data (where applicable) must not be changed in any way or sold commercially in any format or medium without the formal permission of the copyright holder/s. When referring to this thesis and any accompanying data, full bibliographic details must be given, e.g.

Thesis: Angela Andrea Bahamondes Dominguez (2019) "Meteorological controls on primary production in shelf seas", University of Southampton, School of Ocean and Earth Science, PhD Thesis, pagination.

UNIVERSITY OF SOUTHAMPTON

FACULTY OF NATURAL AND ENVIRONMENTAL SCIENCES

Ocean and Earth Science

Volume 1 of 1

Meteorological controls on primary production in shelf seas

by

Angela Andrea Bahamondes Dominguez

Thesis for the degree of Doctor of Philosophy

October 2019

UNIVERSITY OF SOUTHAMPTON

ABSTRACT

FACULTY OF NATURAL AND ENVIRONMENTAL SCIENCES

Ocean and Earth Sciences

Thesis for the degree of Doctor of Philosophy

METEOROLOGICAL CONTROLS ON PRIMARY PRODUCTION IN SHELF SEAS

by Angela Andrea Bahamondes Dominguez

Shelf seas are regions of high biological activity, contributing 15-30% of global oceanic primary production, with temperate shelf seas as an important global carbon sink. To understand how shelf seas will respond to environmental changes it is important to fully understand phytoplankton dynamics and inter-annual variability of phytoplankton production in these areas. Previous modelling works have shown that meteorology can affect phytoplankton seasonal dynamics but there is still debate in the literature about the direct mechanisms that affect long-term phytoplankton productivity. Challenges can include a lack of long-term observations and mismatch of these with numerical models due to a range of factors from the simplicity of the assumptions made in model structure to inappropriate parameterisations. This study explores the effects of wind speed, cloud coverage, air temperature, and relative humidity on primary production using a simple one-dimensional biological and physical coupled model to simulate the inter-annual variability of seasonal stratification and productivity over the last five decades (1965 - 2015) and shelf sea observations (2014 - 2015) in the Central Celtic Sea location. Results with the simplest model structure show that wind speed has the largest effect on the inter-annual variability of primary production associated to the onset of thermal stratification. However, a mismatch with observations and inconclusive results motivated further model development, introducing a nutrient-phytoplankton-zooplankton framework and modelling photo-acclimation. Extensive analysis of the new models was performed by calibration and sensitivity analyses, demonstrating that the addition of these processes produces substantial changes in the model dynamics, improving the model fit to observations. This allows reassessment of the questions analysed with the simplest model, providing new insights into the meteorological impacts on phytoplankton productivity, showing that wind speed has a direct influence on the timing of thermal stratification and, therefore, in the timing of the spring bloom, affecting annual production. In contrast to the simpler model, cloud coverage is shown to have the largest effect on the annual phytoplankton production, affecting the available light in the water column with large daily variations directly affecting daily primary production during the spring bloom and summer growth periods. Thus, in this work it is demonstrated that the structure and parameterisation of the model influences the fidelity of the simulations.

Table of Contents

Table of Contents	i
List of Tables	vii
List of Figures	xii
Academic Thesis: Declaration of Authorship	xxxiii
Acknowledgements	xxxv
Definitions and Abbreviations	xxxvii
1 Introduction	1
1.1 Shelf Seas	1
1.2 Key physical controls in temperate shelf seas	6
1.2.1 Stratification vs mixing	6
1.2.2 The onset of stratification and the spring bloom	7
1.2.3 Stratification during summer	10
1.2.4 Tidal mixing fronts	12
1.3 Biological processes	14
1.3.1 Primary production: light and nutrients supply	14
1.3.2 Photo-acclimation of algal cells	15
1.3.3 Zooplankton and grazing	16
1.4 Observing shelf sea physics and biology	19
1.4.1 SSB programme	19
1.4.2 Modelling shelf seas (1D vs 3D)	19
1.5 Structure of the following work	21
2 Methods and model development	23
2.1 S2P3 model: physics	23
2.1.1 Physical forcing	27

2.1.2	Stability criteria and resolution	29
2.2	S2P3 model: biology	32
2.2.1	S2P3 v7.0	32
2.2.2	S2P3-NPZ	39
2.2.3	S2P3-Photoacclim	43
2.2.4	S2P3 v8.0	47
2.3	Meteorological forcing	53
2.4	Model setup for the CCS location	58
2.5	Spin-up and resolution of the model	58
3	Meteorological controls on inter-annual variability in onset and duration of the spring bloom and summer growth in the Central Celtic Sea using a single 1-D model	61
3.1	Abstract	61
3.2	Introduction	62
3.2.1	Spring bloom and meteorological drivers	62
3.3	Methods	67
3.3.1	Model simulations	67
3.3.1.1	Default simulation	67
3.3.1.2	Control-based experiments	68
3.3.1.3	Knockout-wind experiment	69
3.3.2	Validation of the model	70
3.3.3	Statistical analysis	76
3.4	Results	78
3.4.1	Analysis of the default simulation	78
3.4.2	Analysis of control-based experiments	79
3.4.2.1	Insights for the spring bloom	83
3.4.3	Analysis of knockout-wind experiment	84
3.4.3.1	Spring phytoplankton bloom	88
3.4.3.2	Summer growth	92
3.5	Discussion	96
3.5.1	Default simulation and inter-annual variability of stratification	96
3.5.2	Model experiments	97

3.5.2.1	Control-based experiments: inter-annual variability of phytoplankton production and meteorological controls	97
3.5.2.2	Insights into the spring phytoplankton bloom	99
3.5.3	Knockout wind experiment: analysis of the spring phytoplankton bloom and summer growth	100
3.5.3.1	Spring phytoplankton bloom	102
3.5.3.2	Summer growth	103
3.5.4	Concluding remarks	103
4	Constraining the response of phytoplankton to zooplankton grazing and photo-acclimation in a 1-D model	106
4.1	Abstract	106
4.2	Introduction	107
4.2.1	NPZ models and S2P3 v7.0: S2P3-NPZ	107
4.2.2	Light, nutrients, and photosynthesis	109
4.2.3	Combining S2P3-NPZ and S2P3-photoacclim: S2P3 v8.0	111
4.3	Methods	112
4.3.1	Validation of the model	112
4.3.1.1	Zooplankton biomass	112
4.3.1.2	Physiological observations	115
4.3.2	Calibration of the models	119
4.3.3	Sensitivity analysis	121
4.3.3.1	S2P3-NPZ	121
4.3.3.2	S2P3-Photoacclim	122
4.3.3.3	S2P3 v8.0	122
4.4	Results	125
4.4.1	Calibration	125
4.4.1.1	S2P3-NPZ	125
4.4.1.2	S2P3-Photoacclim	127
4.4.1.3	S2P3 v8.0	128
4.4.2	Sensitivity analysis	133
4.4.2.1	S2P3-NPZ	135
4.4.2.2	S2P3-Photoacclim	149

4.4.2.3	S2P3 v8.0	164
4.5	Discussion	179
4.5.1	Calibrating models: a validation	179
4.5.2	Sensitivity analysis: dynamic responses to model parameterisations .	181
4.5.3	Concluding remarks	183
5	Inter-annual variability of primary production due to wind and cloud effects using a simple 1-D NPZ model with photo-acclimation	186
5.1	Abstract	186
5.2	Introduction	187
5.3	Methods	189
5.3.1	Model set up, meteorological forcing, and experiments	189
5.3.2	Robustness and parameterisations	189
5.3.3	Statistical analysis	190
5.4	Results	193
5.4.1	Insights into the S2P3 v8.0 model	193
5.4.2	Meteorological effects on inter-annual variability of primary production	196
5.4.3	Seasonal variability of primary production	202
5.4.4	Parameterisation: a validation for robustness	204
5.4.5	A deeper look into wind and cloud inter-annual variability and their direct mechanisms of influence on primary production	211
5.5	Discussion	224
5.5.1	Direct and indirect controls of wind speed and cloud coverage on phytoplankton production variability	224
5.5.2	Parameterisation: robustness of the meteorological effects on phytoplankton production variability	228
5.5.3	Concluding remarks	228
6	Synthesis	230
6.1	Synthesis and discussion from this work	230
6.2	Wider implications and model considerations	235
6.2.1	Modelling different regions of the ocean	235

6.2.2	Model development: can higher vertical resolution provide better insights about shelf sea dynamics?	235
6.2.3	Model physics constraining biology	236
6.2.4	Validate and support modelling results with <i>in situ</i> observations and remote sensing	237
6.2.5	Wider implications about shelf sea modelling: marine policies	239
6.3	Concluding remarks	242

List of Tables

2.1	List of variables, with their definitions and units, from the physical part of the S2P3 v7.0 model.	31
2.2	List of initialised parameters, with definitions, units, and values, for the physical part of the S2P3 v7.0 model.	32
2.3	List of variables, with their definitions and units, for the biological part of the S2P3 v7.0 model.	38
2.4	List of initialised parameters, with definitions, units, and values, for the biological part of the S2P3 v7.0 model. Parameter values obtained according to the work of Sharples (2008).	39
2.5	List of variables, with their definitions and units, for the biological part of the S2P3-NPZ model.	43
2.6	List of all the parameters, with their respective definitions, initialised values, and units, in the biological part of the S2P3-NPZ model. This includes the new variables used to simulate the new grazing rate by using zooplankton biomass, including: m , γ_1 , γ_2 , R_m , and λ . Parameter values of the newly added NPZ parameters are taken from different sources of the literature and they are specified in Chapter 4, Table 4.2.	44
2.7	List of variables, with their definitions and units, for the biological part of the S2P3-photoacclim model.	47
2.8	List of all the parameters, with their respective definitions, initialised values, and units, in the biological part of the S2P3-photoacclim model. Parameter values of the newly added photo-acclimation parameters are taken from different sources of the literature and they are specified in Chapter 4, Table 4.2.	48

2.9	List of variables, with their definitions and units, for the biological part of the S2P3 v8.0 model.	51
2.10	List of all the parameters, with their respective definitions, initialised values, and units, for the biological part of the S2P3 v8.0 model.	52
3.1	List of each experiment developed with the S2P3 v7.0 and the differences for the meteorological forcing.	70
3.2	List of relevant CTD casts for the CCS location from DY029 and DY033 cruises considering the date, location (latitude and longitude), and depth. CTD casts in red are the ones chosen in this work to validate the S2P3 v7.0 model during spring and summer.	76
4.1	Net deployments at the CCS locations including date, time during the day and night, and depth horizons. *SCM depth sampled when SCM present. Information obtained from Giering et al., 2018.	114
4.2	Ranges for parameter values for the S2P3-NPZ, S2P3-Photoacclim, and S2P3 v8.0 models. Sources from Geider et al. (1997); Langdon (1988); Falkowski et al. (1985); Coper (1982); and Yoder (1979) for phytoplankton species: <i>Skeletonema costatum</i> , <i>Thalassiosira pseudonana</i> , <i>Isochrysis galbana</i> , and <i>Pavlova lutheri</i>	120
4.3	List of experiments developed for the sensitivity studies of the S2P3-NPZ based on the Control NPZ experiment.	123
4.4	List of experiments developed for the sensitivity studies of the S2P3-Photoacclim based on the Control Photoacclim experiment.	123
4.5	List of experiments developed for the sensitivity studies of the S2P3 v8.0 model based on the Control NPZPhot experiment.	124
4.6	List of parameter values for the Control NPZ, Control Photoacclim, and Control NPZPhot experiments (for parameter units see Table 4.2).	129
4.7	Quantitative comparison of observed time-series of surface chlorophyll from buoy samples in terms of the timing and length of the spring bloom, and the total spring surface chlorophyll between the S2P3-NPZ, S2P3-Photoacclim, and S2P3 v8.0 models.	130

4.8	List of the experiments run for the S2P3-NPZ model including the year of observations, timing and magnitude of the spring phytoplankton bloom, and total annual zooplankton biomass values.	147
4.9	List of the experiments run for the S2P3-NPZ model including the year of observations, differences in the timing and magnitude of the spring phytoplankton bloom, and differences in the total annual zooplankton biomass values (differences given by the Control NPZ minus each experiment). Orange colour represents the largest difference in terms of the timing of the spring phytoplankton bloom between the Control NPZ and a given experiment; the red colour represents the largest difference in terms of the magnitude of the spring phytoplankton bloom between the Control NPZ and a given experiment; and the grey colour represents the largest difference in terms of the total annual zooplankton biomass between the Control NPZ and a given experiment.	148
4.10	List of the experiments run for the S2P3-Photoacclim model including the year of observations, and timing and magnitude of the spring phytoplankton bloom.	162
4.11	List of the experiments run for the S2P3-Photoacclim model including the year of observations, and differences in the timing and magnitude of the spring phytoplankton bloom (differences given by the Control Photoacclim minus each experiment). Orange colour represents the largest difference in terms of the timing of the spring phytoplankton bloom between the Control Photoacclim and a given experiment; the red colour represents the largest difference in terms of the magnitude of the spring phytoplankton bloom between the Control Photoacclim and a given experiment.	163
4.12	List of the experiments run for the S2P3 v8.0 model including the year of observations, timing and magnitude of the spring phytoplankton bloom, and total annual zooplankton biomass values.	177

4.13	List of the experiments run for the S2P3 v8.0 model including the year of observations, differences in the timing and magnitude of the spring phytoplankton bloom, and differences in the total annual zooplankton biomass values (differences given by the Control NPZPhot minus each experiment). Orange colour represents the largest difference in terms of the timing of the spring phytoplankton bloom between the Control NPZPhot and a given experiment; the red colour represents the largest difference in terms of the magnitude of the spring phytoplankton bloom between the Control NPZPhot and a given experiment; and the grey colour represents the largest difference in terms of the total annual zooplankton biomass between the Control NPZPhot and a given experiment.	178
5.1	List of the control-based experiments developed for the S2P3 v8.0 and corresponding meteorological forcing.	192
5.2	List of parameters previously investigated within Chapter 4 with corresponding units and values used for the Control experiment, Wind-only, Cloud-only, Temperature-only, and Humidity-only experiments.	192
5.3	List of experiment names and parameter values developed for the S2P3 v8.0 model. See meteorological forcing of each experiment in Table 5.1.	192
5.4	List of the chosen years to analyse wind speed effects on inter-annual variability of NPP, including the JD for the timing of the spring phytoplankton bloom, and total annual NPP.	212
6.1	Comparison between the S2P3 v7.0, S2P3-NPZ, S2P3-Photoacclim, and S2P3 v8.0 models in terms of the total spring NPP, total summer NPP, and total annual NPP calculated from 1965 to 2015, including the mean, maximum, minimum, and STD values.	234
A.1	Three main tidal constituents (M_2 , S_2 , and N_2) in the CCS location calculated using POLCOMS model and used to force the S2P3 model along with meteorological forcing, including a spring-neap tidal cycle using the two components (u,v) of every tidal constituent [ms^{-1}].	243

A.2 Values of correlations (r-squared) between the total annual net PP ($gCm^{-2}yr^{-1}$) and total net PP ($gCm^{-2}day^{-1}$) averaged monthly during April, April + May, April + May + June over the period of 1965-2015 using different control-based experiments for every correlation. Other periods during the year were omitted in this table because no significant correlations were found. Values of r-squared with a star (\star) represent the experiments that show significant correlation during that months ($p < 0.05$). 244

List of Figures

1.1	(a) Global ocean bathymetry (depth in kilometres), divided into shelf, slope, and abyssal ocean. Bathymetry information obtained from the General Bathymetric Chart of the Oceans (GEBCO). (b) Global annual PP, from Moderate Resolution Imaging Spectroradiometer (MODIS) satellite (Behrenfeld & Falkowski, 1997). Images taken from Simpson & Sharples, 2012.	2
1.2	Modified diagram of shelf seas processes and characteristics taken from Simpson & Sharples, 2012. The rightmost region is called the ROFI whose proximity to land leads to an input of freshwater. ROFIs are followed by a permanently mixed region, where tidal stirring (∞) is stronger at the seabed. The transition zone from a well-mixed water column to a stratified region is called the tidal mixing front. In the stratified areas of shelf seas, tidal mixing becomes less important at the seabed. Finally at the shelf edge, there is exchange with the deep ocean and internal waves can occur in the thermocline.	4
1.3	Map of the Celtic Sea and North Sea (as part of the NW European Shelf) taken from Williams et al., 2013. (A) The map shows the sea surface chlorophyll- <i>a</i> composite measured by satellite in a range between 0 to > 5 mg Chl m ⁻³ during 10 - 16 June 2010. (B) Profiles found by a CTD station marked on the map as IM1 during 6 June 2010. The plot shows profiles in the Celtic Sea of salinity (psu; blue dashed line), nitrate (mmol N m ⁻³ ; black dashed line with circles), temperature (°C; red dashed line), and chlorophyll- <i>a</i> (mg Chl m ⁻³ ; green line). The model experiments of this work were run in the CCS location shown on the map as the IM1 station.	6

1.4	Schematic illustration of a tidal mixing front and the different processes that allow high production of phytoplankton in these regions due to nutrients supply from (1) diapycnal mixing, (2) spring-neap tidal adjustment of the front, (3) eddy transfer across the front, and (4) due to lateral intrusion of mixed waters. These conditions are optimal for phytoplankton growth, because there is sufficient light and nutrients available. Figure adapted from Simpson & Sharples (2012); Loder & Platt (1985).	14
1.5	Ingestion curves for (a) Holling Type I or Mayzaud and Poulet grazing, (b) Holling Type II or Ivlev grazing, and (c) Holling Type III or sigmoidal-shaped grazing.	18
2.1	Simplified diagram of the physical part of the S2P3 model to illustrate the interdependence of the different variables used in the turbulence closure scheme (modified diagram taken from Simpson & Sharples, 2012).	30
2.2	Phytoplankton growth rate dependency on nutrient availability, based on the cellular nutrient quota. Parameters values are taken from literature (Flynn, 2008).	34
2.3	Phytoplankton growth dependency on temperature based on the Eppley curve, where the maximum growth increases with temperature. Parameter values are taken from literature (Eppley, 1972).	35
2.4	Phytoplankton growth dependency on light availability. Parameter values are taken from literature (Hickman et al., 2012).	36
2.5	Schematic illustration of the biological part of the S2P3 v7.0 model for the nitrate-phytoplankton relationship.	38
2.6	Schematic representation of the biological part of the S2P3-NPZ model illustrating the NPZ framework.	42
2.7	Schematic illustration of each version of model development.	50
2.8	Whole record of the meteorological forcing used in the S2P3 model from the start of the year 1965 to the end of the year 2015, showing (a) wind speed, (b) cloud coverage, (c) air temperature, and (d) relative humidity.	54

2.9	Seasonal variability of daily time-series for meteorological forcing (black line) and a running mean (red line) with a span of 80 days in every case. Time-series representing the year 1965 as an example for: (a) wind speed (m s^{-1}), (b) cloud coverage (%), (c) air temperature ($^{\circ}\text{C}$), and (d) relative humidity (%).	55
2.10	Annual means from daily data showing inter-annual variability throughout 1965 to 2015 for each meteorological variable (black lines) and a linear regression line (red lines) fitted in each case for (a) wind speed (m s^{-1}), (b) cloud coverage (%), (c) air temperature ($^{\circ}\text{C}$), and (d) relative humidity (%).	57
2.11	Total annual NPP ($\text{mg C m}^{-2} \text{ yr}^{-1}$) calculated from the start of the year 1960 to the end of the year 2015. First five years show the spin-up of the S2P3 v7.0 model. Dashed black line represents the mean of the time-series from 1965 to 2015 (i.e. spin-up is not included).	59
2.12	Total annual NPP ($\text{mg C m}^{-2} \text{ yr}^{-1}$) calculated from daily time-series during the years 1965 to 2015 with four different resolutions: black line for 1m, blue line for 2m, green line for 7m, and magenta line for 14m.	60
3.1	Heat fluxes across air-sea boundary showing the incoming short wave radiation (Q_{SW}) representing absorbed and scattered photons. There is long wave radiation (Q_{LW}) emitted from the sea surface, evaporation (E) is related to contributions from latent heat flux (Q_{lat}), and exchange of heating by conduction (Q_{sens}). Diagram adapted from Simpson & Sharples, 2012.	63
3.2	Idealized seasonal cycles of vertical heat fluxes at temperate latitudes over one year, showing each component of the net heat flux (units of W m^{-2}), with net cooling periods during winter months, and net heating over spring and summer months.	64
3.3	Histograms of daily meteorological data taken from the NCEP Reanalysis. Each meteorological variable is taken from the start of the year 1965 to the end of the year 2015. The black arrows represent the modal value in each histogram, the green arrows are the median, and the red arrows are the mean for (a) wind speed (m s^{-1}), (b) cloud coverage (%), (c) air temperature ($^{\circ}\text{C}$), and (d) relative humidity (%).	68

3.4	(a) DY029 cruise sampling sites, (b) Map of all CTD cast locations (black dots) from DY029 cruise and bathymetry, and (c) DY033 cruise track (blue line), CTD sampling stations (black dots), and bathymetry of the Celtic Sea.	72
3.5	Comparison to data of the S2P3 v7.0 model using the output of the default experiment for the CCS location (black lines) and time-series from buoy observations (red lines) from April 2014 to August 2015 for (a) surface temperature ($^{\circ}\text{C}$) and (c) surface chlorophyll- <i>a</i> ($\mu\text{g Chl l}^{-1}$). Scatter plots during the period of validation with significance at 95% confidence level (p-value is less than 0.05). The red line represents the regression line of correlation between (b) surface temperature of the default experiment and surface temperature from buoy observations, and (d) surface chlorophyll- <i>a</i> of the default experiment and surface chlorophyll- <i>a</i> from buoy observations.	74
3.6	CTD validation of the S2P3 v7.0 model in the CCS location (black lines) using observations taken from the UK SSB programme available data (red lines). Validation made in spring during 20/04/2015 for (a) Temperature ($^{\circ}\text{C}$), (b) Chlorophyll- <i>a</i> (mg m^{-3}), and (c) DIN ($\mu\text{mol l}^{-1}$) and during summer for day 24/07/2015 for (d) Temperature ($^{\circ}\text{C}$), (e) Chlorophyll- <i>a</i> (mg m^{-3}), and (f) DIN ($\mu\text{mol l}^{-1}$). Black dashed lines represent profiles of the model fifteen days later over spring and summer for both dates (05/05/2015 and 08/08/2015, respectively).	75
3.7	(a) Daily time-series showing the seasonal cycle for the default experiment during the year 1965 for the surface chlorophyll- <i>a</i> (black dashed line, mg Chl m^{-3}), bottom temperature (black dash-dot line, $^{\circ}\text{C}$), and surface temperature (black solid line, $^{\circ}\text{C}$), (b) Annually averaged surface chlorophyll- <i>a</i> (black dashed line, mg Chl m^{-3}), bottom temperature (black dash-dot line, $^{\circ}\text{C}$), and surface temperature (black solid line, $^{\circ}\text{C}$) from 1965 to 2015 for the default experiment.	79
3.8	Total annual NPP ($\text{mg C m}^{-2} \text{yr}^{-1}$) time-series calculated from 1965 to 2015 for the control experiment (red line) and for (a) wind-only experiment, (b) cloud-only experiment, (c) temperature-only experiment, and (d) humidity-only experiment.	81

- 3.9 (a) An RMSD for the total annual NPP ($\text{mg C m}^{-2} \text{ yr}^{-1}$) calculated between the control experiment and 1: wind-only experiment, 2: temperature-only experiment, 3: cloud-only experiment, and 4: humidity-only experiment. (b) RMSD calculated for the wind-only experiment (blue solid line), cloud-only experiment (black solid line), temperature-only experiment (red solid line), and humidity-only experiment (magenta solid line) for every year. The RMSD for (a) and (b) were calculated throughout 1965 and 2015. 82
- 3.10 Boxplot for the timing of the peak bloom NPP (days) calculated from daily NPP ($\text{mg C m}^{-2} \text{ day}^{-1}$) from 1965 to 2015 for 1: control experiment, 2: wind control-based experiment, 3: cloud control-based experiment, 4: temperature control-based experiment, and 5: humidity control-based experiment. 84
- 3.11 Time-series from the output of the default experiment (black solid line) and from the knockout wind experiment (black dashed line) using the year 1965 as an example for (a) Daily wind speed (black solid line) and daily wind speed control (black dashed line, m s^{-1}), (b) daily temperature difference (surface temperature minus bottom temperature, $^{\circ}\text{C}$) for the default experiment (black solid line) and the knockout wind experiment (black dashed line), and (c) daily NPP ($\text{mg C m}^{-2} \text{ day}^{-1}$) for the default experiment (black solid line) and the knockout wind experiment (black dashed line). . . 86
- 3.12 Contour plots of mean daily difference between the knockout-wind experiment and the default experiment during 1965 and 2015 along the whole water column with a maximum depth of 140m. (a) Temperature ($^{\circ}\text{C}$), (b) Chlorophyll-*a* (mg Chl m^{-3}), and (c) DIN (mmol N m^{-3}). The red colour represents positive values and the blue colour represents negative values. . . 88
- 3.13 Scatter plots of model output for 1965 to 2015. The red line represents the regression line of the correlations between (a) Timing of the spring phytoplankton bloom (*days*) for the default experiment and the knockout-wind experiment, (b) Total spring NPP ($\text{mg C m}^{-2} \text{ day}^{-1}$) for the default experiment and knockout-wind experiment, (c) timing of the spring phytoplankton bloom (*days*) and total spring NPP ($\text{mg C m}^{-2} \text{ day}^{-1}$) for the default experiment, and (d) timing of the spring phytoplankton bloom (*days*) and total spring NPP ($\text{mg C m}^{-2} \text{ day}^{-1}$) for the knockout-wind experiment. . . 90

3.14	Scatter plots of model output for the period 1965 and 2015. The red line represents the regression line of the correlations between (a) timing of the spring phytoplankton bloom (<i>days</i>) and surface BML (<i>m</i>) for the default experiment, (b) timing of the spring phytoplankton bloom (<i>days</i>) and surface BML (<i>m</i>) for the knockout-wind experiment, (c) total spring NPP ($\text{mg C m}^{-2} \text{ day}^{-1}$) and surface BML (<i>m</i>) for the default experiment, and (d) total spring NPP ($\text{mg C m}^{-2} \text{ day}^{-1}$) and surface BML (<i>m</i>) for the knockout-wind experiment.	92
3.15	Scatter plots calculated for the period 1965 and 2015. Red line represents the regression line of the correlations between (a) length of the stratified period (<i>days</i>) and the total summer NPP ($\text{mg C m}^{-2} \text{ day}^{-1}$) for the default experiment, (b) length of the stratified period (<i>days</i>) and the total summer NPP ($\text{mg C m}^{-2} \text{ day}^{-1}$) for the knockout-wind experiment, (c) total summer NPP ($\text{mg C m}^{-2} \text{ day}^{-1}$) and the length of the summer period (<i>days</i>) for the default experiment, and (d) total summer NPP ($\text{mg C m}^{-2} \text{ day}^{-1}$) and the length of the summer period (<i>days</i>) for the knockout-wind experiment. . . .	94
3.16	(a) Time-series of total annual NPP (black solid line; $\text{mg C m}^{-2} \text{ yr}^{-1}$) and total spring + summer NPP (blue solid line; $\text{mg C m}^{-2} \text{ yr}^{-1}$) for the default experiment throughout 1965 to 2015. (b) Time-series of total annual NPP (black solid line; $\text{mg C m}^{-2} \text{ yr}^{-1}$) and total spring + summer NPP (blue solid line; $\text{mg C m}^{-2} \text{ yr}^{-1}$) for the knockout-wind experiment from 1965 to 2015.	95
4.1	Conceptual view of NPZ models. The arrows represent the nutrient flow pathways between P (phytoplankton), Z (zooplankton), and N (DIN). . . .	108
4.2	Map of the three main stations across the Celtic Sea for the cruises DY026, DY018, DY029, and DY033. The sampling sites are represented by crosses and include the Celtic Deep, the Central Site (or CCS site), and the Shelf Edge. Grey scale shows the bathymetry (in m). Image taken from Giering et al., 2018.	113
4.3	Depth-integrated zooplankton biomass for daytime and night-time samples at the CCS location, including different species of mesozooplankton from the cruises DY026, DY018, DY029, and DY033.	115

4.4	Map for study area and stations for the JR98 (stations IS1, CS3, D2, CS1, U2, N1, CS2) and CD173 (stations B2, CS2, JB1, OB, P1, U2, ctd16) cruises, including the CCS location (in red colour). Image created with Matlab using the repository data for gridded bathymetry provided by General Bathymetric Chart of the Oceans (GEBCO). Bathymetric data only considered for the shelf sea region (0 to 300m depth) with open ocean depth neglected (deeper than 300m). Continents considered in black colour (over 0m elevation).	117
4.5	Photophysiological parameters obtained from ^{14}C -uptake photosynthesis versus irradiance experiments ($n = 55$) from the JR98 and CD173 cruises. (a) Chlorophyll- <i>a</i> specific maximum light-saturated photosynthesis rate, and (b) Light saturation parameter, spectrally corrected to the <i>in situ</i> irradiance at the sample depth (see Moore et al., 2006).	119
4.6	SSB observations (black lines) for (a) Surface chlorophyll- <i>a</i> , (b) zooplankton biomass along the S2P3-NPZ (red line), S2P3-Photoacclim (blue line), and S2P3 v8.0 (green line) calibrated models.	131
4.7	CTD observations from the SSB programme including data for: spring-time (20/04/2015) (a) temperature, (b) chlorophyll- <i>a</i> , and (c) DIN; for summertime (24/07/2015) for (d) temperature, (e) chlorophyll- <i>a</i> , and (f) DIN along the S2P3-NPZ (red line), S2P3-Photoacclim (blue line), and S2P3 v8.0 (green line) calibrated models.	132
4.8	Observations from the cruises CD173 and JR98 for:(a) chlorophyll- <i>a</i> specific maximum light-saturated photosynthesis rate ($P_{\text{max}}^{\text{Chl}}$) in different locations of the Celtic Sea and for the calibrated S2P3-Photoacclim model (blue lines) and the S2P3 v8.0 model (green lines); (b) observations of the light saturation parameter (E_k) for different stations across the Celtic Sea and E_k from the calibrated S2P3-Photoacclim model (blue lines) and the S2P3 v8.0 model (green lines). The data from both models were plotted for the same days that the observations were collected: between 15 th July to 6 th August of 2003 (JR98 cruise) and between 24 th July to 14 th August of 2005 (CD173 cruise).	133

4.9	SSB buoy observations (red line) from the start of April 2014 to end of June 2015 compared to the Control NPZ (magenta line), Run 1 ($\gamma_1 = 0.1$; black line), and Run 2 ($\gamma_1 = 0.3$; cyan line) shown from start of April 2014 to the end of August 2015 for (a) surface chlorophyll- <i>a</i> and (b) zooplankton biomass.	136
4.10	CTD observations from the SSB programme (red line) including data for: springtime (20/04/2015) (a) temperature, (b) chlorophyll- <i>a</i> , and (c) DIN; for summertime (24/07/2015) for (d) temperature, (e) chlorophyll- <i>a</i> , and (f) DIN along the S2P3-NPZ (magenta line), Run 1 ($\gamma_1 = 0.1$; black line), and Run 2 ($\gamma_1 = 0.3$; cyan line).	137
4.11	SSB buoy observations (red line) from the start of April 2014 to end of June 2015 compared to the Control NPZ (magenta line), Run 3 ($\gamma_2 = 0.25$; black line), and Run 4 ($\gamma_2 = 0.75$; cyan line) shown from start of April 2014 to the end of August 2015 for (a) surface chlorophyll- <i>a</i> and (b) zooplankton biomass.	138
4.12	CTD observations from the SSB programme (red line) including data for: springtime (20/04/2015) (a) temperature, (b) chlorophyll- <i>a</i> , and (c) DIN; for summertime (24/07/2015) for (d) temperature, (e) chlorophyll- <i>a</i> , and (f) DIN along the S2P3-NPZ (magenta line), Run 3 ($\gamma_2 = 0.25$; black line), and Run 4 ($\gamma_2 = 0.75$; cyan line).	139
4.13	SSB buoy observations (red line) from the start of April 2014 to end of June 2015 compared to the Control NPZ (magenta line), Run 5 ($\lambda = 0.375$; black line), and Run 6 ($\lambda = 1.125$; cyan line) shown from start of April 2014 to the end of August 2015 for (a) surface chlorophyll- <i>a</i> and (b) zooplankton biomass.	141
4.14	CTD observations from the SSB programme (red line) including data for: springtime (20/04/2015) (a) temperature, (b) chlorophyll- <i>a</i> , and (c) DIN; for summertime (24/07/2015) for (d) temperature, (e) chlorophyll- <i>a</i> , and (f) DIN along the S2P3-NPZ (magenta line), Run 5 ($\lambda = 0.375$; black line), and Run 6 ($\lambda = 1.125$; cyan line).	142

4.15	SSB buoy observations (red line) from the start of April 2014 to end of June 2015 compared to the Control NPZ (magenta line), Run 7 ($R_m = 1.25$; black line), and Run 8 ($R_m = 3.75$; cyan line) shown from start of April 2014 to the end of August 2015 for (a) surface chlorophyll- <i>a</i> and (b) zooplankton biomass.	143
4.16	CTD observations from the SSB programme (red line) including data for: springtime (20/04/2015) (a) temperature, (b) chlorophyll- <i>a</i> , and (c) DIN; for summertime (24/07/2015) for (d) temperature, (e) chlorophyll- <i>a</i> , and (f) DIN along the S2P3-NPZ (magenta line), Run 7 ($R_m = 1.25$; black line), and Run 8 ($R_m = 3.75$; cyan line).	144
4.17	SSB buoy observations (red line) from the start of April 2014 to end of June 2015 compared to the Control NPZ (magenta line), Run 9 ($m = 0.025$; black line), and Run 10 ($m = 0.075$; cyan line) shown from start of April 2014 to the end of August 2015 for (a) surface chlorophyll- <i>a</i> and (b) zooplankton biomass.	145
4.18	CTD observations from the SSB programme (red line) including data for: springtime (20/04/2015) (a) temperature, (b) chlorophyll- <i>a</i> , and (c) DIN; for summertime (24/07/2015) for (d) temperature, (e) chlorophyll- <i>a</i> , and (f) DIN along the S2P3-NPZ (magenta line), Run 9 ($m = 0.025$; black line), and Run 10 ($m = 0.075$; cyan line).	146
4.19	SSB buoy observations (red line) from the start of April 2014 to end of June 2015 compared to the Control Photoacclim (blue line), Phot 1 ($P_{\max}^C = 1$; black line), and Phot 2 ($P_{\max}^C = 3$; cyan line) shown from start of April 2014 to the end of August 2015 for surface chlorophyll- <i>a</i>	150
4.20	CTD observations from the SSB programme (red line) including data for: springtime (20/04/2015) (a) temperature, (b) chlorophyll- <i>a</i> , and (c) DIN; for summertime (24/07/2015) for (d) temperature, (e) chlorophyll- <i>a</i> , and (f) DIN along the S2P3-Photoacclim (blue line), Phot 1 ($P_{\max}^C = 1$; black line), and Phot 2 ($P_{\max}^C = 3$; cyan line).	151

4.21	Observations from the cruises CD173 and JR98 in different locations of the Celtic Sea, including Control Photoacclim (blue lines), Phot 1 ($P_{\max}^C = 1$; black lines), and Phot 2 ($P_{\max}^C = 3$; cyan lines) for: (a) chlorophyll- <i>a</i> specific maximum light-saturated photosynthesis rate (P_{\max}^{Chl}) and (b) light saturation parameter (E_k). The data from the model was plotted during the same days that the observations were collected.	152
4.22	SSB buoy observations (red line) from the start of April 2014 to end of June 2015 compared to the Control Photoacclim (blue line), Phot 3 ($Q_m = 0.2$; black line), and Phot 4 ($Q_m = 0.6$; cyan line) shown from start of April 2014 to the end of August 2015 for surface chlorophyll- <i>a</i>	153
4.23	CTD observations from the SSB programme (red line) including data for: springtime (20/04/2015) (a) temperature, (b) chlorophyll- <i>a</i> , and (c) DIN; for summertime (24/07/2015) for (d) temperature, (e) chlorophyll- <i>a</i> , and (f) DIN along the S2P3-Photoacclim (blue line), Phot 3 ($Q_m = 0.2$; black line), and Phot 4 ($Q_m = 0.6$; cyan line).	154
4.24	Observations from the cruises CD173 and JR98 in different locations of the Celtic Sea, including Control Photoacclim (blue lines), Phot 3 ($Q_m = 0.2$; black lines), and Phot 4 ($Q_m = 0.6$; cyan lines) for: (a) chlorophyll- <i>a</i> specific maximum light-saturated photosynthesis rate (P_{\max}^{Chl}) and (b) light saturation parameter (E_k). The data from the model was plotted for the same days that the observations were collected.	155
4.25	SSB buoy observations (red line) from the start of April 2014 to end of June 2015 compared to the Control Photoacclim (blue line), Phot 5 ($\theta_{\max}^N = 0.15$; black line), and Phot 6 ($\theta_{\max}^N = 0.45$; cyan line) shown from start of April 2014 to the end of August 2015 for surface chlorophyll- <i>a</i>	156
4.26	CTD observations from the SSB programme (red line) including data for: springtime (20/04/2015) (a) temperature, (b) chlorophyll- <i>a</i> , and (c) DIN; for summertime (24/07/2015) for (d) temperature, (e) chlorophyll- <i>a</i> , and (f) DIN along the S2P3-Photoacclim (blue line), Phot 5 ($\theta_{\max}^N = 0.15$; black line), and Phot 6 ($\theta_{\max}^N = 0.45$; cyan line).	157

4.27	Observations from the cruises CD173 and JR98 in different locations of the Celtic Sea, including Control Photoacclim (blue lines), Phot 5 ($\theta_{\max}^N = 0.15$; black lines), and Phot 6 ($\theta_{\max}^N = 0.45$; cyan lines) for: (a) chlorophyll- <i>a</i> specific maximum light-saturated photosynthesis rate (P_{\max}^{Chl}) and (b) light saturation parameter (E_k). The data from the model was plotted for the same days that the observations were collected.	158
4.28	SSB buoy observations (red line) from the start of April 2014 to end of June 2015 compared to the Control Photoacclim (blue line), Phot 7 ($R_C = R_{\text{chl}} = R_n = 0.01$; black line), and Phot8 ($R_C = R_{\text{chl}} = R_n = 0.03$; cyan line) shown from start of April 2014 to the end of August 2015 for surface chlorophyll- <i>a</i>	159
4.29	CTD observations from the SSB programme (red line) including data for: springtime (20/04/2015) (a) temperature, (b) chlorophyll- <i>a</i> , and (c) DIN; for summertime (24/07/2015) for (d) temperature, (e) chlorophyll- <i>a</i> , and (f) DIN along the S2P3-Photoacclim (blue line), Phot 7 ($R_C = R_{\text{chl}} = R_n = 0.01$; black line), and Phot8 ($R_C = R_{\text{chl}} = R_n = 0.03$; cyan line).	160
4.30	Observations from the cruises CD173 and JR98 in different locations of the Celtic Sea, including Control Photoacclim (blue lines), Phot 7 ($R_C = R_{\text{chl}} = R_n = 0.01$; black line), and Phot8 ($R_C = R_{\text{chl}} = R_n = 0.03$; cyan line) for: (a) chlorophyll- <i>a</i> specific maximum light-saturated photosynthesis rate (P_{\max}^{Chl}) and (b) light saturation parameter (E_k). The data from the model was plotted for the same days that the observations were collected.	161
4.31	SSB buoy observations (red line) from the start of April 2014 to end of June 2015 compared to the Control NPZPhot (green line), NPZPhot 1 ($P_{\max}^C = 1.75$; black line), and NPZPhot 2 ($P_{\max}^C = 5.25$; cyan line) shown from start of April 2014 to the end of August 2015 for (a) surface chlorophyll- <i>a</i> and (b) zooplankton biomass.	168
4.32	CTD observations from the SSB programme (red line) including data for: springtime (20/04/2015) (a) temperature, (b) chlorophyll- <i>a</i> , and (c) DIN; for summertime (24/07/2015) for (d) temperature, (e) chlorophyll- <i>a</i> , and (f) DIN along the Control NPZPhot (green line), NPZPhot 1 ($P_{\max}^C = 1.75$; black line), and NPZPhot 2 ($P_{\max}^C = 5.25$; cyan line).	169

4.33	Observations from the cruises CD173 and JR98 in different locations of the Celtic Sea, including Control NPZPhot (green lines), NPZPhot 1 ($P_{\max}^C = 1.75$; black lines), and NPZPhot 2 ($P_{\max}^C = 5.25$; cyan lines) for: (a) chlorophyll- <i>a</i> specific maximum light-saturated photosynthesis rate (P_{\max}^{Chl}) and (b) light saturation parameter (E_k). The data from the model was plotted for the same days that the observations were collected.	170
4.34	SSB buoy observations (red line) from the start of April 2014 to end of June 2015 compared to the Control NPZPhot (green line), NPZPhot 9 ($\gamma_1 = 0.05$; black line), and NPZPhot 10 ($\gamma_1 = 0.15$; cyan line) shown from start of April 2014 to the end of August 2015 for (a) surface chlorophyll- <i>a</i> and (b) zooplankton biomass.	171
4.35	CTD observations from the SSB programme (red line) including data for: springtime (20/04/2015) (a) temperature, (b) chlorophyll- <i>a</i> , and (c) DIN; for summertime (24/07/2015) for (d) temperature, (e) chlorophyll- <i>a</i> , and (f) DIN along the Control NPZPhot (green line), NPZPhot 9 ($\gamma_1 = 0.05$; black line), and NPZPhot 10 ($\gamma_1 = 0.15$; cyan line).	172
4.36	Observations from the cruises CD173 and JR98 in different locations of the Celtic Sea, including Control NPZPhot (green lines), NPZPhot 9 ($\gamma_1 = 0.05$; black lines), and NPZPhot 10 ($\gamma_1 = 0.15$; cyan lines) for: (a) chlorophyll- <i>a</i> specific maximum light-saturated photosynthesis rate (P_{\max}^{Chl}) and (b) light saturation parameter (E_k). The data from the model was plotted for the same days that the observations were collected.	173
4.37	SSB buoy observations (red line) from the start of April 2014 to end of June 2015 compared to the Control NPZPhot (green line), NPZPhot 11 ($\gamma_2 = 0.2$; black line), and NPZPhot 12 ($\gamma_2 = 0.6$; cyan line) shown from start of April 2014 to the end of August 2015 for (a) surface chlorophyll- <i>a</i> and (b) zooplankton biomass.	174
4.38	CTD observations from the SSB programme (red line) including data for: springtime (20/04/2015) (a) temperature, (b) chlorophyll- <i>a</i> , and (c) DIN; for summertime (24/07/2015) for (d) temperature, (e) chlorophyll- <i>a</i> , and (f) DIN along the Control NPZPhot (green line), NPZPhot 11 ($\gamma_2 = 0.2$; black line), and NPZPhot 12 ($\gamma_2 = 0.6$; cyan line).	175

4.39	Observations from the cruises CD173 and JR98 in different locations of the Celtic Sea, including Control NPZPhot (green lines), NPZPhot 11 ($\gamma_2 = 0.2$; black lines), and NPZPhot 12 ($\gamma_2 = 0.6$; cyan lines) for: (a) chlorophyll- <i>a</i> specific maximum light-saturated photosynthesis rate (P_{\max}^{Chl}) and (b) light saturation parameter (E_k). The data from the model was plotted for the same days that the observations were collected.	176
5.1	Daily time-series from 1965 to 2015 for the calibrated version of the S2P3 v8.0 model (default experiment), including: (a) surface temperature minus bottom temperature ($^{\circ}\text{C}$), (b) surface chlorophyll- <i>a</i> (mg Chl m^{-3}), (c) surface zooplankton biomass (mmol N m^{-3}), (d) surface DIN (mmol N m^{-3}), and (e) NPP ($\text{mg C m}^{-2} \text{ day}^{-1}$).	194
5.2	Contoured daily vertical profiles for the start of 2014 to the end of 2015 for the calibrated version of the S2P3 v8.0 model (default experiment) including: (a) temperature ($^{\circ}\text{C}$), (b) phytoplankton chlorophyll- <i>a</i> (mg Chl m^{-3}), (c) zooplankton biomass (mmol N m^{-3}), (d) phytoplankton chlorophyll : phytoplankton carbon ratio ($\text{mg Chl } (mgC)^{-1}$), and (e) DIN (mmol N m^{-3}).196	196
5.3	Scatter plots calculated from 1965 to 2015. Red line represents the significant regression line of the relationships between the total annual NPP ($\text{mg C m}^{-2} \text{ yr}^{-1}$) and (a) total annual average wind, (b) total annual average cloud coverage, (c) total annual average air temperature, and (d) total annual average relative humidity.	197
5.4	Differences relative to the control experiment of the wind-only experiment (represented in black), cloud-only experiment (represented in red), temperature-only experiment (represented in blue), and humidity-only experiment (represented in cyan) over the period 1965 - 2015 for (a) total annual NPP ($\text{mg C m}^{-2} \text{ yr}^{-1}$), (b) RMSD of total annual NPP ($\text{mg C m}^{-2} \text{ yr}^{-1}$), and (c) RMSD of total annual NPP ($\text{mg C m}^{-2} \text{ yr}^{-1}$), where years with a star (\star) in the x-label represent a mean value of the RMSD every five years starting from 1965.	199

5.5	Differences relative to the control experiment of the wind-only experiment (represented in black), cloud-only experiment (represented in red), temperature-only experiment (represented in blue), and humidity-only experiment (represented in cyan) over the period 1965 - 2015 for (a) the timing of the spring phytoplankton bloom, and (b) an RMSD for the timing of the spring phytoplankton bloom.	200
5.6	Daily surface PAR versus daily NPP for 1965-2015 for the (a) S2P3 v7.0 model, and (b) S2P3 v8.0 model. Colorbar represents the day of the year, from day 0 to 365.	202
5.7	Differences relative to the control experiment of the wind-only experiment (represented in black), cloud-only experiment (represented in red), temperature-only experiment (represented in blue), and humidity-only experiment (represented in cyan) over the period 1965 - 2015 for (a) total spring NPP ($\text{mg C m}^{-2} \text{ yr}^{-1}$), (b) total summer NPP ($\text{mg C m}^{-2} \text{ yr}^{-1}$), (c) total autumn + winter NPP ($\text{mg C m}^{-2} \text{ yr}^{-1}$), and (d) an RMSD for the total spring NPP (blue colour), total summer NPP (green colour), and total autumn + winter NPP (yellow colour).	204
5.8	Differences of total annual NPP ($\text{mg C m}^{-2} \text{ yr}^{-1}$) from 1965 - 2015 relative to the control 1 ($\theta_{\text{max}}^{\text{N}} \downarrow$) and control 2 ($\theta_{\text{max}}^{\text{N}} \uparrow$) experiments and the (a) wind-only 1 - 2 experiments (black and red colours, respectively) (b) cloud-only 1 - 2 experiments (black and red colours, respectively), (c) temperature-only 1 - 2 experiments (black and red colours, respectively), and (d) humidity-only 1 - 2 experiments (black and red colours, respectively).206	
5.9	Differences of total annual NPP ($\text{mg C m}^{-2} \text{ yr}^{-1}$) from 1965 - 2015 relative to the control 3 ($R_{\text{m}} \downarrow$) and control 4 ($R_{\text{m}} \uparrow$) experiments and (a) wind-only 3 - 4 experiments (black and red colours, respectively) (b) cloud-only 3 - 4 experiments (black and red colours, respectively), (c) temperature-only 3 - 4 experiments (black and red colours, respectively), and (d) humidity-only 3 - 4 experiments (black and red colours, respectively).	207

5.10	Differences of total annual NPP ($\text{mg C m}^{-2} \text{ yr}^{-1}$) from 1965 - 2015 relative to the control 5 (m \downarrow) and control 6 (m \uparrow) experiments and (a) wind-only 5 - 6 experiments (black and red colours, respectively) (b) cloud-only 5 - 6 experiments (black and red colours, respectively), (c) temperature-only 5 - 6 experiments (black and red colours, respectively), and (d) humidity-only 5 - 6 experiments (black and red colours, respectively).	208
5.11	RMSD calculations from the year 1965 to the year 2015 for the control-based experiments with $\theta_{max}^N = 0.135$ (blue bars), $\theta_{max}^N = 0.165$ (light blue bars), $R_m = 3.15$ (turquoise bars), $R_m = 3.85$ (green bars), $m = 0.018$ (orange bars), and $m = 0.022$ (yellow bars) for the wind-only 1 - 6 experiments, cloud-only 1 - 6 experiments, temperature-only 1 - 6 experiments, and humidity-only 1 - 6 experiments in terms of (a) total annual NPP ($\text{mg C m}^{-2} \text{ yr}^{-1}$), (b) total spring NPP ($\text{mg C m}^{-2} \text{ yr}^{-1}$), (c) total summer NPP ($\text{mg C m}^{-2} \text{ yr}^{-1}$), and (d) total autumn + winter NPP ($\text{mg C m}^{-2} \text{ yr}^{-1}$).	210
5.12	Comparison of daily time-series of NPP ($\text{mg C m}^{-2} \text{ day}^{-1}$) for the wind-only experiment for (a) year 1982 (black line) and year 1983 (blue line), (b) year 1984 (black line) and year 1994 (blue line), and (c) year 1997 (black line) and year 2013 (blue line).	212
5.13	Scatter plot calculated from 1965 to 2015. Red line represents the significant regression line of the relationships between the timing of the spring bloom (days) and the total annual NPP ($\text{g C m}^{-2} \text{ yr}^{-1}$) for the wind-only experiment.	213
5.14	Comparison of daily time-series of wind speed (m s^{-1}) for (a) year 1982 (black line) and year 1983 (blue line), (b) year 1984 (black line) and year 1994 (blue line), and (c) year 1997 (black line) and year 2013 (blue line). Vertical lines represent the start of the spring phytoplankton bloom for each corresponding year, horizontal blue-dashed lines represent $\pm 1 \times \text{STD}$, and horizontal red-dashed lines represent $\pm 2 \times \text{STD}$	215

5.15	Ten days averaged vertical profiles prior to the start of the spring phytoplankton bloom for temperature including: (a) year 1982 (black line) and year 1983 (red line), (c) year 1984 (black line) and year 1994 (red line), and (e) year 1997 (black line) and year 2013 (red line); and for DIN including: (b) year 1982 (black line) and year 1983 (red line), (d) year 1984 (black line) and year 1994 (red line), and (f) year 1997 (black line) and year 2013 (red line).	217
5.16	Daily wind speed time-series from 1965-2015 (black line) as a forcing of the model. Red dots represent the day when storms events occur (wind speed is higher than 15.3 m s^{-1}).	218
5.17	Comparison of daily time-series of NPP ($\text{mg C m}^{-2} \text{ day}^{-1}$) for the cloud-only experiment for (a) year 1971 (black line) and year 1980 (blue line), (b) year 1996 (black line) and year 2001 (blue line), and (c) year 2012 (black line) and year 2013 (blue line).	219
5.18	Comparison of daily time-series of cloud coverage (%) for (a) year 1971 (black line) and year 1980 (blue line), (b) year 1996 (black line) and year 2001 (blue line), and (c) year 2012 (black line) and year 2013 (blue line). Vertical lines represent the start of the spring phytoplankton bloom for each corresponding year, horizontal blue-dashed lines represent $\pm 1 \times \text{STD}$, and horizontal red-dashed lines represent $\pm 2 \times \text{STD}$	220
5.19	Daily time-series for NPP ($\text{mg C m}^{-2} \text{ day}^{-1}$; red lines) and cloud coverage (%; black lines) from the start of the spring phytoplankton bloom to the day 150 of (a) the year 1980, (b) year 2001, (c) year 2013.	221
5.20	Daily time-series for NPP ($\text{mg C m}^{-2} \text{ day}^{-1}$; red lines) and cloud coverage (%; black lines) during summer from the day 150 to the day 250 of (a) the year 1980, (b) year 2001, (c) year 2013.	222
5.21	Scatter plots calculated between cloud coverage (%) and total NPP ($\text{mg C m}^{-2} \text{ day}^{-1}$) during summer from the day 150 to the day 250 of (a) the year 1980, (b) year 2001, (c) year 2013. Red line represents the significant regression line of the relationships between the daily summer NPP and cloud coverage.	223

A1	(a) Temperature difference (surface temperature minus bottom temperature, °C). When temperature difference is more than 0.5 °C for at least ten days, it defines the start of the spring phytoplankton bloom. The vertical blue line represent the day when this criteria is met, (b) Daily NPP showing the spring phytoplankton bloom (between the days marked by the blue vertical lines), (c) Surface chlorophyll- <i>a</i> showing the end of the spring phytoplankton bloom when it is less than 1.5 mg C m ⁻³ . These plots show the year 1965 from the default experiment, as an example.	245
A2	Scatter plots calculated for the period 1965 and 2015. Correlations represented between the total annual NPP and (a) wind speed, (b) cloud coverage, (c) air temperature, and (d) relative humidity.	246
A3	Scatter plots calculated for the period 1965 and 2015. Red line represents the regression line of the correlations between the day of maximum NPP (days) and total annual NNP (mg C m ⁻² yr ⁻¹) for (a) wind-only experiment, (b) cloud-only experiment, (c) temperature-only experiment, and (d) humid-only experiment.	247
A4	Plot of vertical profiles of temperature averaged (°C) over spring period from daily profiles and gradient profiles of temperature (°C m ⁻¹) calculated during 1965 - 2015. (a) mean gradient profiles of temperature over spring for the default experiment. Red lines represent the surface BML calculated when the gradient = 0, (b) mean profiles of chlorophyll- <i>a</i> (mg m ⁻³) over spring for the default experiment, (c) mean gradient profiles of temperature over spring for the knockout-wind experiment. Red lines represent the surface BML calculated when the gradient = 0, (d) mean profiles of chlorophyll- <i>a</i> (mg m ⁻³) over spring for the knockout-wind experiment.	248
A5	SSB buoy observations (red line) from the start of April 2014 to end of June 2015 compared to the Control NPZPhot (green line), NPZPhot 3 (Q _m = 0.225; black line), and NPZPhot 4 (Q _m = 0.675; cyan line) shown from start of April 2014 to the end of August 2015 for (a) surface chlorophyll- <i>a</i> and (b) zooplankton biomass.	249

A6	CTD observations from the SSB programme (red line) including data for: springtime (20/04/2015) (a) temperature, (b) chlorophyll- <i>a</i> , and (c) DIN; for summertime (24/07/2015) for (d) temperature, (e) chlorophyll- <i>a</i> , and (f) DIN along the Control NPZPhot (green line), NPZPhot 3 ($Q_m = 0.225$; black line), and NPZPhot 4 ($Q_m = 0.675$; cyan line).	250
A7	Observations from the cruises CD173 and JR98 in different locations of the Celtic Sea, including Control NPZPhot (green lines), NPZPhot 3 ($Q_m = 0.225$; black lines), and NPZPhot 4 ($Q_m = 0.675$; cyan lines) for: (a) chlorophyll- <i>a</i> specific maximum light-saturated photosynthesis rate (P_{max}^{Chl}) and (b) light saturation parameter (E_k). The data from the model was plotted for the same days that the observations were collected.	251
A8	SSB buoy observations (red line) from the start of April 2014 to end of June 2015 compared to the Control NPZPhot (green line), NPZPhot 5 ($\theta_{max}^N = 0.075$; black line), and NPZPhot 6 ($\theta_{max}^N = 0.225$; cyan line) shown from start of April 2014 to the end of August 2015 for (a) surface chlorophyll- <i>a</i> and (b) zooplankton biomass.	252
A9	CTD observations from the SSB programme (red line) including data for: springtime (20/04/2015) (a) temperature, (b) chlorophyll- <i>a</i> , and (c) DIN; for summertime (24/07/2015) for (d) temperature, (e) chlorophyll- <i>a</i> , and (f) DIN along the Control NPZPhot (green line), NPZPhot 5 ($\theta_{max}^N = 0.075$; black line), and NPZPhot 6 ($\theta_{max}^N = 0.225$; cyan line).	253
A10	Observations from the cruises CD173 and JR98 in different locations of the Celtic Sea, including Control NPZPhot (green lines), NPZPhot 5 ($\theta_{max}^N = 0.075$; black lines), and NPZPhot 6 ($\theta_{max}^N = 0.225$; cyan lines) for: (a) chlorophyll- <i>a</i> specific maximum light-saturated photosynthesis rate (P_{max}^{Chl}) and (b) light saturation parameter (E_k). The data from the model was plotted for the same days that the observations were collected.	254
A11	SSB buoy observations (red line) from the start of April 2014 to end of June 2015 compared to the Control NPZPhot (green line), NPZPhot 7 ($R_C = R_{chl} = R_n = 0.01$; black line), and NPZPhot 8 ($R_C = R_{chl} = R_n = 0.03$; cyan line) shown from start of April 2014 to the end of August 2015 for (a) surface chlorophyll- <i>a</i> and (b) zooplankton biomass.	255

A12 CTD observations from the SSB programme (red line) including data for:
springtime (20/04/2015) (a) temperature, (b) chlorophyll-*a*, and (c) DIN;
for summertime (24/07/2015) for (d) temperature, (e) chlorophyll-*a*, and
(f) DIN along the Control NPZPhot (green line), NPZPhot 7 ($R_C = R_{chl} =$
 $R_n = 0.01$; black line), and NPZPhot 8 ($R_C = R_{chl} = R_n = 0.03$; cyan line). 256

A13 Observations from the cruises CD173 and JR98 in different locations of the
Celtic Sea, including Control NPZPhot (green lines), NPZPhot 7 ($R_C =$
 $R_{chl} = R_n = 0.01$; black lines), and NPZPhot 8 ($R_C = R_{chl} = R_n =$
 0.03 ; cyan lines) for: (a) chlorophyll-*a* specific maximum light-saturated
photosynthesis rate (P_{max}^{Chl}) and (b) light saturation parameter (E_k). The
data from the model was plotted for the same days that the observations
were collected. 257

A14 SSB buoy observations (red line) from the start of April 2014 to end of
June 2015 compared to the Control NPZPhot (green line), NPZPhot 13
($\lambda = 0.1$; black line), and NPZPhot 14 ($\lambda = 0.3$; cyan line) shown from
start of April 2014 to the end of August 2015 for (a) surface chlorophyll-*a*
and (b) zooplankton biomass. 258

A15 CTD observations from the SSB programme (red line) including data for:
springtime (20/04/2015) (a) temperature, (b) chlorophyll-*a*, and (c) DIN;
for summertime (24/07/2015) for (d) temperature, (e) chlorophyll-*a*, and (f)
DIN along the Control NPZPhot (green line), NPZPhot 13 ($\lambda = 0.1$; black
line), and NPZPhot 14 ($\lambda = 0.3$; cyan line). 259

A16 Observations from the cruises CD173 and JR98 in different locations of the
Celtic Sea, including Control NPZPhot (green lines), NPZPhot 13 ($\lambda = 0.1$;
black lines), and NPZPhot 14 ($\lambda = 0.3$; cyan lines) for: (a) chlorophyll-*a*
specific maximum light-saturated photosynthesis rate (P_{max}^{Chl}) and (b) light
saturation parameter (E_k). The data from the model was plotted for the
same days that the observations were collected. 260

A17 SSB buoy observations (red line) from the start of April 2014 to end of
June 2015 compared to the Control NPZPhot (green line), NPZPhot 15
($R_m = 1.75$; black line), and NPZPhot 16 ($R_m = 5.25$; cyan line) shown from
start of April 2014 to the end of August 2015 for (a) surface chlorophyll-*a*
and (b) zooplankton biomass. 261

A18	CTD observations from the SSB programme (red line) including data for: springtime (20/04/2015) (a) temperature, (b) chlorophyll- <i>a</i> , and (c) DIN; for summertime (24/07/2015) for (d) temperature, (e) chlorophyll- <i>a</i> , and (f) DIN along the Control NPZPhot (green line), NPZPhot 15 ($R_m = 1.75$; black line), and NPZPhot 16 ($R_m = 5.25$; cyan line).	262
A19	Observations from the cruises CD173 and JR98 in different locations of the Celtic Sea, including Control NPZPhot (green lines), NPZPhot 15 ($R_m = 1.75$; black lines), and NPZPhot 16 ($R_m = 5.25$; cyan lines) for: (a) chlorophyll- <i>a</i> specific maximum light-saturated photosynthesis rate (P_{max}^{Chl}) and (b) light saturation parameter (E_k). The data from the model was plotted for the same days that the observations were collected.	263
A20	SSB buoy observations (red line) from the start of April 2014 to end of June 2015 compared to the Control NPZPhot (green line), NPZPhot 17 ($m = 0.01$; black line), and NPZPhot 18 ($m = 0.03$; cyan line) shown from start of April 2014 to the end of August 2015 for (a) surface chlorophyll- <i>a</i> and (b) zooplankton biomass.	264
A21	CTD observations from the SSB programme (red line) including data for: springtime (20/04/2015) (a) temperature, (b) chlorophyll- <i>a</i> , and (c) DIN; for summertime (24/07/2015) for (d) temperature, (e) chlorophyll- <i>a</i> , and (f) DIN along the Control NPZPhot (green line), NPZPhot 17 ($m = 0.01$; black line), and NPZPhot 18 ($m = 0.03$; cyan line).	265
A22	Observations from the cruises CD173 and JR98 in different locations of the Celtic Sea, including Control NPZPhot (green lines), NPZPhot 17 ($m = 0.01$; black lines), and NPZPhot 18 ($m = 0.03$; cyan lines) for: (a) chlorophyll- <i>a</i> specific maximum light-saturated photosynthesis rate (P_{max}^{Chl}) and (b) light saturation parameter (E_k). The data from the model was plotted for the same days that the observations were collected.	266
A23	RMSD calculations from the year 1965 to the year 2015 for the control-based experiments with $\theta_{max}^N = 0.1425$ (blue bars) and $\theta_{max}^N = 0.1425$ (yellow bars) of (a) total annual NPP ($\text{mg C m}^{-2} \text{ yr}^{-1}$), (b) total spring NPP ($\text{mg C m}^{-2} \text{ yr}^{-1}$), (c) total summer NPP ($\text{mg C m}^{-2} \text{ yr}^{-1}$), and (d) total autumn + winter NPP ($\text{mg C m}^{-2} \text{ yr}^{-1}$).	267

A24	RMSD calculations from the year 1965 to the year 2015 for the control-based experiments with $R_m = 2.8$ (blue bars), $R_m = 4.2$ (turquoise bars), $m = 0.016$ (green bars), and $m = 0.024$ (yellow bars) of (a) total annual NPP ($\text{mg C m}^{-2} \text{ yr}^{-1}$), (b) total spring NPP ($\text{mg C m}^{-2} \text{ yr}^{-1}$), (c) total summer NPP ($\text{mg C m}^{-2} \text{ yr}^{-1}$), and (d) total autumn + winter NPP ($\text{mg C m}^{-2} \text{ yr}^{-1}$).	268
A25	RMSD calculations from the year 1965 to the year 2015 for the control-based experiments with $R_m = 2.45$ (blue bars), $R_m = 4.55$ (turquoise bars), $m = 0.014$ (green bars), and $m = 0.026$ (yellow bars) of (a) total annual NPP ($\text{mg C m}^{-2} \text{ yr}^{-1}$), (b) total spring NPP ($\text{mg C m}^{-2} \text{ yr}^{-1}$), (c) total summer NPP ($\text{mg C m}^{-2} \text{ yr}^{-1}$), and (d) total autumn + winter NPP ($\text{mg C m}^{-2} \text{ yr}^{-1}$).	269

Academic Thesis: Declaration of Authorship

I,
declare that this thesis and the work presented in it are my own and has been generated
by me as the results of my own original research.
.....
.....

I confirm that:

1. This work was done wholly or mainly in candidature for a research degree at this University;
2. Where any part of this thesis has previously been submitted for a degree or any other qualification at this University or any other institution, this has been clearly stated;
3. Where I have consulted the published work of others, this is always clearly attributed;
4. Where I have quoted from the work of others, the source is always given. With the exception of such quotations, this thesis is entirely my own work;
5. I have acknowledged all main sources of help;
6. Where the thesis is based on work done by myself jointly with others, I have made clear exactly what was done by others and what I have contributed myself;
7. None of this work has been published before submission:

Signed:

Date:

Acknowledgements

I would like to thank my supervisors: Anna, Bob, and Mark. They helped me whenever I needed it over these past four years. To them, I will always be grateful for the advice, the feedback, and the opportunities; despite the language barrier and our different ways of looking at things, they always coped with me. Thanks to Steph Henson because, as my panel chair, she always posed interesting questions and supported me through my progress. Thanks to the work of Jonathan Sharples, whose knowledge was a guide for me to develop my interest in the unknowns that remain in shelf seas.

I would also like to thank the people that always supported and believed in me, maybe even more than I did. To my family, I am grateful for all you have done for me, without which I would not be where I stand today. Special thanks to my dear friend Che Carlitos for always being there; you are my brother. I really would like to thank and pay honours to my physics teacher from high school, Alejandro Guajardo, who in his own way, led me into the wonderful world of physics. He inspired many generations of students to learn to love science and I hope that wherever he is now, he is at peace, knowing that his words, lessons, and support shall remain in my memory. Finally, I would like to thank Matt, for inspiring me, believing in me, accepting me, and for being my partner of adventures.

This work was funded by the CONICYT PFCHA/DOCTORADO BECAS CHILE/2015 - 72160249.

Definitions and Abbreviations

BML - Bottom Mixed Layer

BODC - British Oceanographic Data Centre

C - Carbon

CaNDyFloSS - Carbon and Nutrient Dynamics and Fluxes over Shelf Systems

CCS - Central Celtic Sea

CFL - Courant-Friedrichs-Lewy

Chl - Chlorophyll

CO₂ - Carbon Dioxide

CS - Celtic Sea

CTD - Conductivity-Temperature-Depth

DCM - Deep Chlorophyll Maximum

DIN - Dissolved Inorganic Nitrogen

DW - Dry Weight

ERSEM - European Regional Seas Ecosystem Model

ESA - European Space Agency

FVCOM - Finite Volume Community Ocean Model

GCM - General Circulation Model

GEBCO - General Bathymetric Chart of the Oceans

GPP - Gross Primary Production

ICES - International Council for the Exploration of the Sea

IPCC - Inter-governmental Panel on Climate Change

JD - Julian Day

MAPPS - Marine Primary Production: Model Parameters from Space

MLD - Mixed Layer Depth

MODIS - Moderate Resolution Imaging Spectroradiometer

N - Nitrate

NCEP - National Centers for Environmental Predictions

NEMO - Nucleus for European Modelling of the Ocean

NP - Nitrogen-Phytoplankton

NPP - Net Primary Production

NPZ - Nitrogen-Phytoplankton-Zooplankton

NPZD - Nitrogen-Phytoplankton-Zooplankton-Detritus
NW - North-Western
PAR - Photosynthetically Available Radiation
PE - Photosynthesis vs Irradiance
PEA - Potential Energy Anomaly
POLCOMS - Proudman Oceanographic Laboratory Coastal Ocean Modelling Systems
PP - Primary Production
RMSD - Root Mean Squared Deviation
ROFI - Region of Freshwater Exchange
ROMS - Regional Oceanic Modelling System
SeaWiFS - Sea-Viewing Wide Field-of-View
S2P3 - Shelf Sea Physics and Primary Production
SCM - Subsurface Chlorophyll Maximum
SML - Surface Mixed Layer
SSB - Shelf Sea Biogeochemistry
SST - Sea Surface Temperature
STD - Standard Deviation
TKE - Turbulent Kinetic Energy
UK - United Kingdom

Chapter 1

Introduction

This introduction provides a background of general knowledge about the physical and biological dynamics of shelf seas and the purpose of the work presented. This chapter is divided into five sections. The first section includes a general background on shelf seas, their main characteristics, and a description of the study area. The second section shows the physical controls in temperate shelf seas, including seasonal stratification, spring bloom development, and tidal mixing fronts. The third section explains about the biological processes driving shelf sea ecosystems, including a general review on photo-acclimation and grazing. The fourth section shows the different methods to study shelf seas and justifies the use of a 1-D model to study phytoplankton production. The final section of this chapter provides an outline of this work.

1.1 Shelf Seas

Shelf seas are ocean regions where water depth is less than a few hundred metres (~ 200 m). They are separated from the deep ocean by a shelf break, where the seabed inclination generally increases rapidly from the top of the continental slope to the abyssal ocean. In these regions, the effects of friction and boundaries play a crucial role in determining ocean dynamics, experiencing a physical regime which is distinct from that of the abyssal ocean where depths are measured in kilometres (Simpson & Sharples, 2012).

Shelf seas represent less than 10% by area of the global ocean as shown in Figure 1.1a (white regions). Despite this small area in comparison to the slope and abyssal ocean, shelf seas have a disproportionate importance because of their exceptionally high biological productivity (Figure 1.1b; Holt & Proctor., 2008), being responsible for 15 to 30% of

the total oceanic primary production (PP) in the ocean (Davis et al., 2014; Muller-Karger et al., 2005; Wollast, 1998).

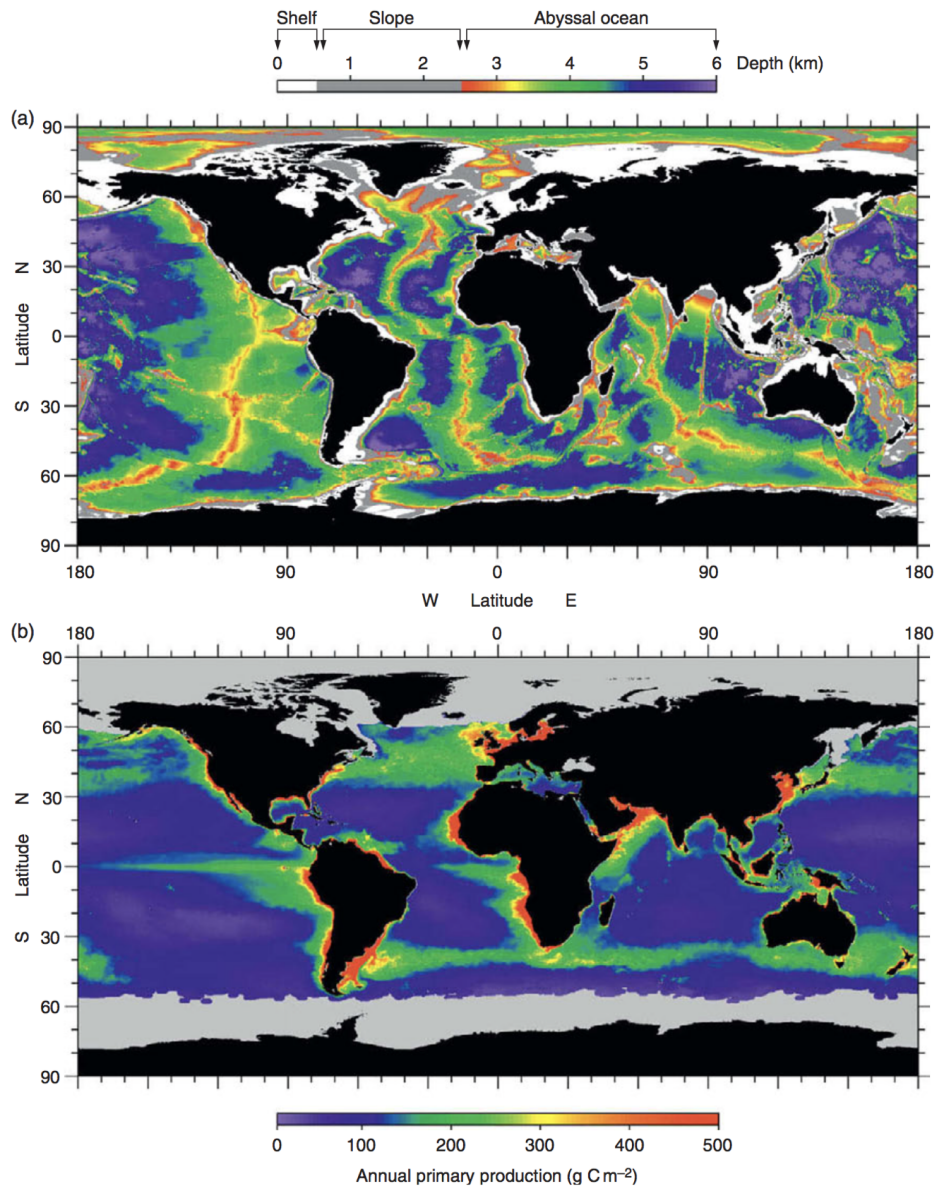


Figure 1.1: (a) Global ocean bathymetry (depth in kilometres), divided into shelf, slope, and abyssal ocean. Bathymetry information obtained from the General Bathymetric Chart of the Oceans (GEBCO). (b) Global annual PP, from Moderate Resolution Imaging Spectroradiometer (MODIS) satellite (Behrenfeld & Falkowski, 1997). Images taken from Simpson & Sharples, 2012.

Many aspects of the marine environment and human activities (e.g. food, renewable energy,

transport) rely on shelf seas (Holt et al., 2017). Approximately 40% of the human population lives in regions close to the sea, and these coastal zones host high industrial activity and provide more than 90% of the fish consumed by humanity (Simpson & Sharples, 2012).

The focus of this work is on temperate shelf seas, which are characterised by key features as illustrated in Figure 1.2. Closest to land are the regions of freshwater exchange (ROFIs), where freshwater river discharge is a source of buoyancy, which is balanced by tidal and wind stirring (Simpson, 1997). ROFIs exhibit changes in stratification and mixing cycles varying from semi-diurnal to spring-neap tidal cycles. The next closest zone to the shore is a permanently mixed region where phytoplankton are transported through the whole water column. Nutrients are abundant in this zone, but the light is limited and high levels of re-suspended sediments maintained by vertical mixing can reduce growth rates of phytoplankton (Rippeth, 2005). The boundaries between the permanently mixed region and those that are thermally stratified during spring and summer are called tidal mixing fronts (Simpson et al., 1981). In the regions of temperate shelf seas that are seasonally stratified, the effect of tides (Kobayashi et al., 2006) and wind (Williams et al., 2013) is small in comparison to the very large seasonal exchange of heat energy through the sea surface (Sharples, 2008; Simpson & Bowers, 1984), which will modify buoyancy of the water column leading to stratification during spring in some parts of the temperate shelf sea, when the increased solar irradiance and reduced mixing can trigger phytoplankton blooms (Riley, 1942). Finally, shelf edge regions act as a control on the productivity of the shelf seas due to important biochemical exchanges with the open ocean, supplying large fluxes of nitrate and phosphate from the deep sea for phytoplankton growth (Liu et al., 2010). Due to the variety and strength of forcing, shelf seas are the most dynamic regions of the ocean and play an important role in biogeochemical processes (Simpson & Sharples, 2012).

Other characteristics can be observed in temperate shelf seas during summer months when the surface and stratified waters, are relatively warm, nutrient-depleted and with low concentrations of chlorophyll-*a* allowing light penetration to the thermocline and, consequently, developing an sub-surface chlorophyll maximum (SCM; Hickman et al., 2012; Hickman et al. 2009; Moore et al. 2006; Holligan et al. 1984a,b). During the autumn and winter months, the net heat flux becomes negative (net cooling/loss of heat to the atmosphere) and, with an increase in wind speed, the water column is mixed. The deeper mixing

and shortened day length reduces light availability, inhibiting phytoplankton growth.

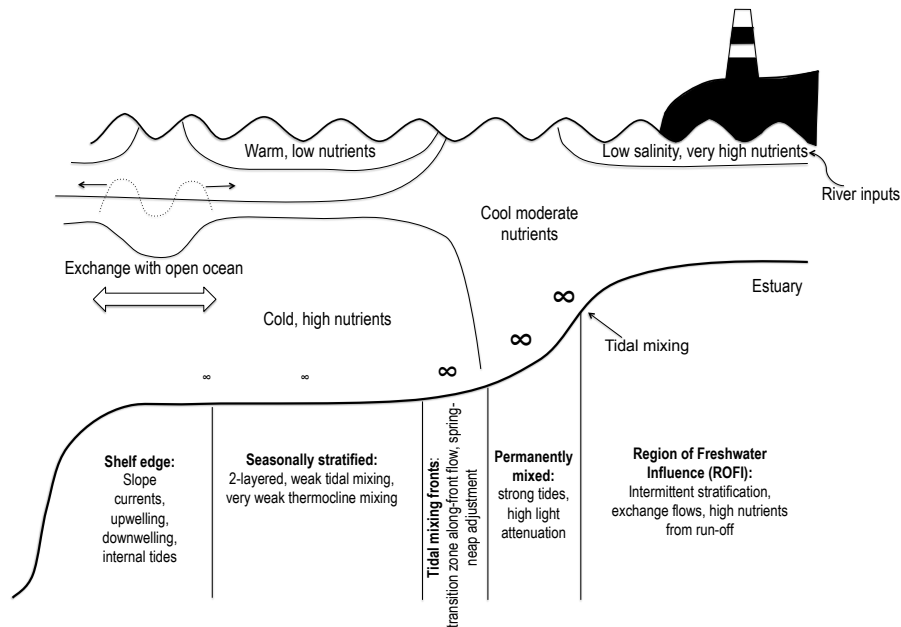


Figure 1.2: Modified diagram of shelf seas processes and characteristics taken from Simpson & Sharples, 2012. The rightmost region is called the ROFI whose proximity to land leads to an input of freshwater. ROFIs are followed by a permanently mixed region, where tidal stirring (∞) is stronger at the seabed. The transition zone from a well-mixed water column to a stratified region is called the tidal mixing front. In the stratified areas of shelf seas, tidal mixing becomes less important at the seabed. Finally at the shelf edge, there is exchange with the deep ocean and internal waves can occur in the thermocline.

Shelf seas experience a supply of nutrients from the continents which results in these regions maintaining of high PP (Joint & Pomroy, 1993), representing 48% of the global total production (Carr et al., 2006; Field et al., 1998). This high PP mediates carbon dioxide (CO_2) drawdown from the atmosphere and exports it to the sub-surface layers via the biological pump. The CO_2 is then transported to the open ocean in a process called the Continental Shelf Pump (Thomas et al., 2004). Shelf seas strongly affect the global carbon cycle and have been suggested to act as a source of atmospheric CO_2 (Bozec et al., 2005).

Because of the characteristics of temperate shelf seas described in this section, there is a need to understand the biological and physical processes governing these ecosystems. This is why it is necessary to have *in situ* observations to understand the dynamics of these regions and to validate models, through research programmes such as the Shelf Sea Biogeochemistry (SSB) programme, which was developed and run from 2011 to 2017 to reduce the uncertainty in the understanding of nutrient and carbon cycling within the shelf seas, and their role in global biogeochemical cycles.

This study is focused on the Central Celtic Sea (CCS), a region located in the North-Western (NW) European Shelf (Figure 1.3), which is characterised by its tidally dynamic environment and summer stratification (Hickman et al., 2012; Sharples & Holligan, 2006; Pingree et al., 1978). Figure 1.3 shows that the seasonally stratified regions of the NW European Shelf are the area with high sea surface temperature (SST) values during summer. In the CCS region (marked as IM1 point in the map), conductivity-temperature-depth (CTD) profiles clearly show the development of an SCM with chlorophyll-*a* reaching values of $\sim 1.2 \text{ mg Chl m}^{-3}$ at $\sim 40 \text{ m}$ depth and inorganic nutrients depleted in the surface waters with high values below the SCM ($\sim 10 \text{ mmol N m}^{-3}$).

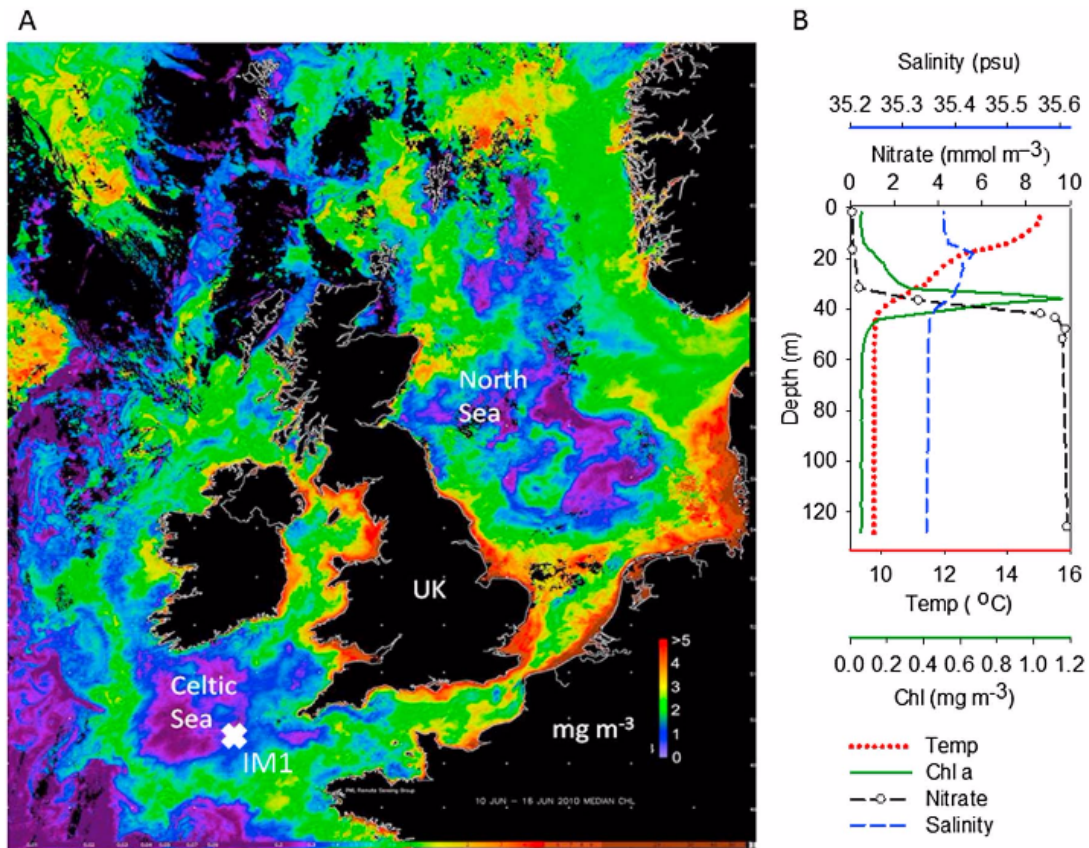


Figure 1.3: Map of the Celtic Sea and North Sea (as part of the NW European Shelf) taken from Williams et al., 2013. (A) The map shows the sea surface chlorophyll-*a* composite measured by satellite in a range between 0 to > 5 mg Chl m⁻³ during 10 - 16 June 2010. (B) Profiles found by a CTD station marked on the map as IM1 during 6 June 2010. The plot shows profiles in the Celtic Sea of salinity (psu; blue dashed line), nitrate (mmol N m⁻³; black dashed line with circles), temperature (°C; red dashed line), and chlorophyll-*a* (mg Chl m⁻³; green line). The model experiments of this work were run in the CCS location shown on the map as the IM1 station.

1.2 Key physical controls in temperate shelf seas

1.2.1 Stratification vs mixing

As described in section 1.1, the development of stratification in temperate shelf seas results from the competition between the buoyancy inputs due to surface heating or freshwater input (Sharples, 2008), stirring by the tides (Kobayashi et al., 2006), and wind stress

(Williams et al., 2013). Towards late winter and the start of spring, the sun gains more elevation and the water column receives more heat until this eventually exceeds the losses of heat back into the atmosphere. Initially, wind and tidal mixing prevent stratification until the heat flux switches to net warming and a weak thermocline is developed, inhibiting the vertical turbulent transfer of water between the surface and bottom layers of the water column. The process that allows the development of stratification can be defined by the potential energy anomaly (PEA, Φ ; Simpson et al., 1981). This parameter is a quantitative measure of stratification and represents the work required per unit volume to completely mix the water column [Jm^{-3}] (Simpson & Sharples, 2012).

$$\Phi = \frac{1}{h} \int_{-h}^0 (\bar{\rho} - \rho(z))gzdz$$

where z is the water column depth (m), h is the mixed layer thickness (m), $g=9.81$ ($m\ s^{-2}$) is the gravitational acceleration, $\bar{\rho}$ is the water column mean density determined from temperature and salinity profiles, $\rho(z)$ is the density profile determined from temperature and salinity profiles. PEA defines a criteria for stratification:

- $\Phi > 0$: water column is stratified,
- $\Phi = 0$: water column is vertically mixed,
- $\Phi < 0$: water column is convectively unstable (high density above low density).

1.2.2 The onset of stratification and the spring bloom

In temperate shelf seas, towards springtime changes occur in the vertical profile of turbulent mixing in the water column in response to the development of stratification driven by the seasonal cycle of the Sun, which increases its elevation during late winter and spring. These changes in the physical environment control the availability of resources (light and nutrients) to the phytoplankton (Simpson & Sharples, 2012). During this period, it is possible to observe the spring bloom, a process that can be defined as the fast growth and accumulation of phytoplankton, generated by high concentrations of inorganic nutrients that have been trapped above the thermocline and high irradiance, sufficient for photo-

synthesis to exceed respiration (Goffart et al., 2015). This process can represent one-third of the annual phytoplankton production in some regions (Townsend et al., 1994), while Joint et al. (2001) demonstrated with observations and satellite measurements over 1993 - 1995 that in the Celtic Sea about 39 - 42% of the total annual PP corresponds to the spring bloom production (April and May). The spring bloom will depend on environmental factors including incident sunlight and its subsurface attenuation, surface layer mixing, nutrients, and temperature (Behrenfeld & Boss, 2018), which are physical properties linked to climate and therefore, the timing, magnitude, and duration of the spring bloom will be regulated by climate and local meteorology.

The start timing of the spring bloom can vary every year due to variability in weather conditions including changes in the air-sea exchange of heat and wind stirring (Simpson & Sharples, 2012). Inter-annual shifts of the spring-neap tidal cycle can also be a source of variability in the timing of the spring phytoplankton bloom as shown by Sharples et al. (2006). The timing of the spring phytoplankton bloom is an important feature because many organisms depend on it: directly, organisms that feed on phytoplankton such as zooplankton, whose spring bloom will also depend on the start timing of the spring phytoplankton bloom (Sarmiento & Gruber, 2006); and indirectly, organisms at higher trophic levels (Platt et al., 2003; Rey et al., 1987).

There is general agreement that the spring phytoplankton bloom is closely dependent on the development of thermal stratification (Simpson & Sharples, 2012; Riley, 1942). In the late winter and spring, the increase in irradiance creates a warm surface layer (Sharples et al., 2006; Gill, 1982) that cannot be dissipated by tidal (Simpson & Hunter, 1974) and wind mixing. This process leads to the formation of a thermocline, separating the warming layer from the colder layer (deeper waters). As stratification develops from the balance between buoyancy and mixing (Turner, 1973), the phytoplankton are split into two separate communities: the cells that are in the warm surface layer, and the cells that are trapped in the cold bottom layer (Simpson & Bowers, 1990; Simpson & Bowers, 1984). The phytoplankton cells in the surface layer will have enough light and nutrients to grow until they have used all the available nutrients in that layer.

The onset of the spring phytoplankton bloom is determined by a balance between the

amount of solar radiation received by a phytoplankton population, availability of nutrients, and phytoplankton biomass losses associated with respiration, grazing, and sedimentation. However, finding a quantitative definition of the timing of the spring bloom has been a matter of discussion in the literature, with many different approaches used. Sverdrup (1953) developed the critical depth model theory to establish a relationship between the depth of water column mixing and the available light as main controllers of the start timing of the spring bloom, being valid in temperate and sub-polar latitudes where the seasonal phytoplankton cycle is a distinct feature. Yet there are observations in the North Atlantic of earlier blooms prior to stratification (Townsend et al., 1994; Garside & Garside, 1993; Townsend et al., 1992; Colebrook, 1979), which can be the result of favourable weather conditions (i.e. calm and clear days), producing intermittent changes in the mixed layer depth (MLD; Henson et al., 2006; Durbin et al., 2003; Townsend et al., 1992). Therefore, some studies report the timing of the spring bloom as once a specific threshold in phytoplankton biomass has been exceeded (Henson et al., 2009; Fleming & Kaitala, 2005; Greve et al., 2005; Siegel et al., 2002), while Beherenfeld & Boss (2018) report the start of the spring bloom as the rate of change of phytoplankton biomass, resulting from the difference between carbon production and loss rates.

Sharples et al. (2006) showed that the inter-annual variability of the onset of thermal stratification and the spring phytoplankton bloom are correlated to meteorological forcing of mean spring values of wind stress, solar irradiance, and air temperature. Wind stress variability and spring air temperature controlled the timing of spring stratification and bloom by balancing the water column mixing due to wind stress at the surface, and the increase of heating during spring to stabilise the water column and develop stratification, showing significant correlations between meteorological variables and the timing of the spring phytoplankton bloom. Despite these results, no significant correlation has been found between phytoplankton long-term variability and local atmospheric forcing (Barton et al., 2014), suggesting that a non-linear response from plankton communities to inter-annual variability of ocean surface wind speed, heat fluxes, turbulence, MLD, stratification, or SST might be the cause; Barton et al., (2014) also suggests that the year-to-year variability in phytoplankton assemblages is greater than in the physical drivers. This lack of sensitivity of phytoplankton biomass inter-annual variability may be because there are other ecological (e.g. zooplankton grazing) and physical mechanisms (e.g. ocean circulation) that play a

role in driving ecological dynamics.

The magnitude and duration of the spring phytoplankton bloom in a temperate shelf sea can affect the amount of energy transferred to higher trophic levels (Shi et al., 2017; Sigler et al., 2014). Inter-annual variability has been observed in the magnitude and duration of spring phytoplankton bloom, affected by changes in the vertical mixing induced by atmospheric forcing variability (Follows & Dutkiewicz, 2001). Variations in mean wind speed, cloudiness (which affects surface irradiance as well as night convection), and air temperature can condition phytoplankton growth. Knowing these processes in shelf seas is relevant for understanding the ecology and biogeochemistry of these systems.

1.2.3 Stratification during summer

A two-mixed layer model can be considered for a stratified region in temperate shelf seas: a surface mixed layer, heated and stirred by the atmosphere with high levels of light and low in nutrients; and a bottom mixed layer, stirred by tides, rich in nutrients but with low light. These two layers are separated by a thermocline, a high gradient region of water temperature that inhibits the vertical turbulent transfer of water, nutrients, and phytoplankton between the surface and bottom layer (Simpson & Sharples, 2012; Pingree et al., 1976).

Seasonal stratification develops in early spring as surface heating rate increases and the turbulent kinetic energy (TKE) of the water decreases (due to decreasing wind speeds) and then strengthens throughout the summer months (Elliott & Clarke, 1991). During summer, warm waters at the surface are nutrient depleted because phytoplankton fed on them during the spring bloom, consequently, concentrations of chlorophyll-*a* are also low in the surface layer after the peak of the bloom has decreased (Pingree et al., 1978). The low concentrations of chlorophyll-*a* in the surface mixed layer allows light penetration to the thermocline (Hickman et al., 2012), which is rich in inorganic nutrients due to mixing at the bottom of the thermocline (Sharples & Tett, 1994). Wind pulses can supply nutrients to the thermocline and increase growth, deepening the thermocline to a depth where light received by the phytoplankton cells is typically low. The spring-neap tidal cycle also plays a role in the strength of mixing (Sharples, 2008), increasing the turbulent mixing of

the water column during spring tides and eroding the base of the thermocline, allowing phytoplankton carbon to be mixed downward into the bottom layer (Sharples et al., 2001). During neap tides, tidal currents decrease while wind stirring weakens stratification and mixes up nutrients to be incorporated into the base of the thermocline from the bottom mixed layer. In this bottom mixed layer, light is limited, although sometimes irradiance is still high enough for PP to be possible (Van Leeuwen et al., 2013).

During anomalous heating periods, model experiments have suggested that sensible heat flux driven by air-sea temperature difference can restore the heat content and temperature structure to normal. In shelf seas wind speed is reduced during a hot summer, limiting the depth of the mixed-layer. In this shallower mixed-layer, temperatures are increased due to the absorption of incoming radiation, stabilising the thermocline and thus restricting the penetration of the wind mixing and driving a sensible heat flux from the sea to the atmosphere.

In a temperate shelf sea, a maximum concentration of chlorophyll-*a* within the thermocline is often referred to as SCM (Simpson & Sharples, 2012). The SCM is near-ubiquitous in stratified surface waters, formed by interacting processes, including enhanced growth of phytoplankton under an optimal combination of light and nutrients, physiologically controlled swimming behavior or buoyancy regulation, and photoacclimation of the algal cells (Cullen et al., 2015). Cells may sink to form a layer at a location within a pycnocline or nitracline where they are neutrally buoyant (Steele & Yentsch, 1960). Phytoplankton in the thermocline have high concentrations because the characteristic mixing time of the water is longer than the algal generation time, allowing growth and accumulation (Cullen, 1982), and because beneath the thermocline, tidal turbulence maintains these cold waters with supplies of inorganic nutrients from sediments.

Studies in the Western English Channel have found that the enhanced PP in the SCM is $0.5 - 0.8 \text{ g C m}^{-2} \text{ d}^{-1}$ (Moore et al., 2003), with similar results found in the Celtic Sea of 0.1 to $0.6 \text{ g C m}^{-2} \text{ d}^{-1}$ (Joint & Groom, 2000) and the estimated rates of PP for the same location by Hickman et al. (2012) of 0.174 to $0.386 \text{ g C m}^{-2} \text{ d}^{-1}$ (compared to cruise observations done by Marañón et al., 2005). These reported observations are less than the value reported by Pingree et al (1976) for the spring phytoplankton bloom in

the same region of $6 \text{ g C m}^{-2} \text{ d}^{-1}$. These differences are due to the low light availability at the thermocline but compared to the spring phytoplankton bloom, these production rates are maintained for many weeks. On the other hand, in the North Sea, values for PP rate during summer of $0.91 \text{ g C m}^{-2} \text{ d}^{-1}$ (Fernand et al., 2013) have been found. In a typical year, the total annual new PP (creation of new organic material from the input of inorganic nutrients) corresponds to $40 \text{ g C m}^{-2} \text{ yr}^{-1}$, where 40% of this production would be associated with the spring phytoplankton bloom in the stratified surface waters (Richardson & Pedersen, 1998).

1.2.4 Tidal mixing fronts

Tidal mixing fronts can be identified as the transition zone between vertically mixed areas and those that are seasonally stratified. Their position depends on the balance between buoyancy input by heating, tidal mixing at the seabed and, to a lesser extent, mixing by the wind at the surface.

PEA (Φ) theory formulates the basic competition between the stratifying and stirring agencies in terms of stratification. Φ is zero for a fully mixed water column and becomes increasingly positive as stratification increases. In the development of an equation for the position of tidal fronts, considering the mechanical stirring by the tides and the influence of stirring by wind stress, the full equation to observe frontal positions postulated by Simpson & Hunter (1974) can be written as:

$$\frac{\partial \Phi}{\partial t} = \frac{\alpha g Q_i}{2c_p} - \frac{ek_b \rho_o |u|^3}{h} - \frac{e_s k_s \rho_a W^3}{h}. \quad (1.1)$$

The first term on the right side of eq. 1.1 represents the net change of Φ by heating, where α is the volume expansion coefficient of seawater, g is the gravitational force, Q_i is the heat supplied in a short interval of time, and c_p is the specific heat capacity of seawater. The second and third terms on the right side of the equation represent the net change of Φ due to tidal stirring and wind mixing, respectively. e is an efficiency term of tidal stirring, ρ_o is the density of seawater, u is the depth-mean tidal current, ρ_a is the density of the air, W is the wind speed, e_s is an efficiency of wind mixing, h is the full depth, k_b and k_s are drag coefficients.

The condition for frontal transition, balancing heating and stirring is:

$$\frac{\partial \Phi}{\partial t} = 0.$$

For a region where Q_i and W can be assumed uniform and considering the other parameters as constants, except u and h , then from eq. 1.1, the position of a tidal mixing front can be represented by a critical value of h/u^3 , which is derived by a balance between potential energy induced by surface heating and tide-induced turbulent kinetic energy (heating - stirring theory) to identify front locations (Simpson & Hunter, 1974). As the depth of water increases, the strength of the tidal currents required to maintain vertical mixing also increases. For example, when $h < 30$ m stratification can only exist for low values of u (Bowers & Simpson, 1987). Tidal mixing fronts represent important physical and chemical boundaries and, therefore, become important biological boundaries (Pingree & Griffiths, 1978; Pingree et al., 1975), enhancing chlorophyll-*a* concentrations in the surface waters.

The enhanced phytoplankton populations found at tidal fronts occurs due to nitrate supply to surface frontal waters, with different possible ways of transferring nutrients across, and into, a front as shown in Figure 1.4, including: (1) increased vertical mixing allowed by the weakening of stratification at the front, (2) effect of spring-neap tidal cycle leading to fortnightly re-stratification (when neap tides are not strong enough to balance the solar heating input that leads to stratification), and mixing (due to spring tides that can breakdown stratification as they increase turbulent mixing) which can increase the annual productivity in tidal mixing fronts by 70% compared to a front only driven by the M_2 tide (Sharples, 2008), (3) eddy transfers across the front, and (4) fluxes associated with the friction within fronts (Simpson & Sharples, 2012; Loder & Platt, 1985).

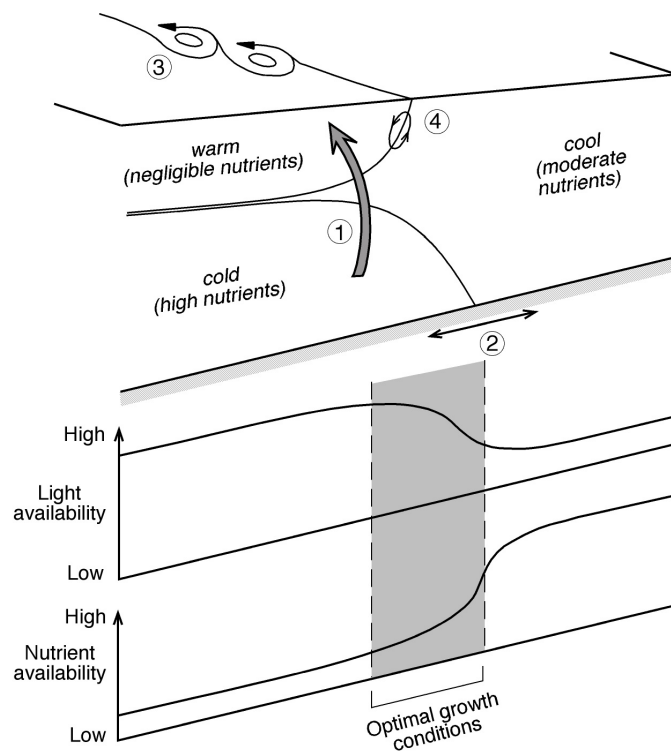


Figure 1.4: Schematic illustration of a tidal mixing front and the different processes that allow high production of phytoplankton in these regions due to nutrients supply from (1) diapycnal mixing, (2) spring-neap tidal adjustment of the front, (3) eddy transfer across the front, and (4) due to lateral intrusion of mixed waters. These conditions are optimal for phytoplankton growth, because there is sufficient light and nutrients available. Figure adapted from Simpson & Sharples (2012); Loder & Platt (1985).

1.3 Biological processes

1.3.1 Primary production: light and nutrients supply

Phytoplankton are the foundation of the aquatic food web because they are primary producers (Vargas et al., 2006), using photosynthetic carotenoids, chlorophyll-*a* and other pigments to absorb solar energy and convert CO_2 into organic compounds (Barlow et al., 2008; Kirk, 1994). This process can be referred to as photosynthetic fixation of carbon and

can be described as gross PP (GPP) or net PP (NPP). GPP is the total amount of carbon fixed by phytoplankton, while NPP is the gross production minus the amount of carbon consumed in cell respiration (Simpson & Sharples, 2012), with phytoplanktonic respiration defined as the release of CO₂ by photosynthetic organisms. Thus, PP can be defined as the amount of organic material produced per unit area per unit time (units usually namely mg C m⁻² d⁻¹; Cloern et al., 2014).

The phytoplankton carbon fixation is also influenced by the concentration of inorganic nutrients during the year in the photic zone, and it requires corresponding uptakes of these inorganic nutrient elements (nitrogen, phosphorus, silicon, etc) in stoichiometric proportions (Heath & Beare, 2008; Redfield et al., 1963). Therefore, phytoplankton production will depend on the rate of supply of nutrients or fluxes to the photic zone through advection, convection, mixing, diffusion or atmospheric input; it can also depend on the uptake of nutrients from synthesized organic matter by excretion and microbial activity.

In seasonally stratified temperate seas, vertical mixing during winter can supply nitrate concentrations to the photic zone from deeper waters, whilst vertical diffusion across the seasonal thermocline is the main process that delivers nitrate from depth to the photic zone during the summer (Rippeth, 2005).

1.3.2 Photo-acclimation of algal cells

In algal cells, photosynthesis is carried out by organelles called chloroplasts, which contain specialised membranes called thylakoids (Kirk, 1994). In the thylakoid, some pigments capture the necessary light to enable photosynthesis. However, variations in light intensity can produce phenotypic adjustments in the cells by changing the disposition of chloroplasts and, therefore, the cellular cross-section occupied by chloroplasts (MacIntyre et al., 2002). This phenotypic change in response to variations in the photon flux density is called photo-acclimation (Moore et al., 2006; Falkowski & LaRoche, 1991).

The main property of photo-acclimation is the reduction of photosynthetic pigment content in response to increased irradiance, but it can also have morphological implications by changing the cell volume, number and density of thylakoid membranes, etc; and physiologi-

cal implications by changing the minimum quantum requirement for growth rate (Falkowski & La Roche, 1991). Photo-acclimation can be assessed by analysing the differences in the photosynthetic physiology or biochemistry of a given taxa in response to a range of light intensities and phytoplankton growth (Moore et al., 2006).

Despite widespread measurements of chlorophyll-*a* concentrations to understand marine PP, it is a poor measure for phytoplankton biomass (Cullen, 1982; Strickland, 1960) because it only contributes about 0.1 to 5% to phytoplankton biomass (Geider et al., 1997; Geider, 1993). Consequently, studying the phytoplankton chlorophyll-*a* : phytoplankton carbon ratio can give better estimates about phytoplankton growth rates from CO₂ assimilation measurements. According to phytoplankton culture studies performed by Geider (1993) and Geider (1987), this ratio can vary from 0.1 to 1 g g⁻¹ responding to changes in irradiance, nutrient availability, and temperature, reaching a maximum under high temperatures, low irradiance, and nutrient replete conditions. Down regulation of the phytoplankton chlorophyll-*a* : phytoplankton carbon ratio at high irradiance occurs because the rate of light absorption exceeds the maximum capacity to assimilate photosynthate, however, temperature or restricted nutrient availability can constrain phytoplankton growth rates reducing the demand for energy.

Attempts to describe and quantify phytoplankton growth rates were performed and introduced by cell quota models as in Droop (1983). The cell quota or nutrient quota (Q) could be defined as the quantity of substrate required to produce a given biomass, introducing a concept of internal nutrient pool upon which phytoplankton growth depends on, therefore, it assumes that phytoplankton growth rate is a function of the dissolved nutrient concentration availability. Geider et al. (1998) describes the light-, nutrient-, and temperature-dependencies of phytoplankton growth rate in one model based on the cell quota theory with varying ratios of N : C : Chl.

1.3.3 Zooplankton and grazing

Plankton in the ocean can be divided into two main groups: phytoplankton (photosynthetic algal cells) and zooplankton (heterotrophs). Phytoplankton are at the base of the oceanic trophic chain, being able to take carbon using the uptake of nutrients from the

environment through photosynthesis. Zooplankton are at a second trophic level, grazing on the available phytoplankton based on a predator-prey relationship (Irigoien et al., 2005; Cushing, 1990). In shelf seas, zooplankton play a central role in the biogeochemical cycles of the ocean, because they transfer energy to higher trophic levels (Giering et al., 2018). Thus, understanding the dynamics of planktonic ecosystems becomes important.

Zooplankton grazing has important effects on biomass in the upper ocean (Kiørboe et al., 1998) because it has a direct influence on the amount of phytoplankton (Lee et al., 2012; Calbet, 2008) and, also, because some proportion of the food ingested by zooplankton is excreted as particulate matter. The sinking of that detrital matter is one of the important mechanisms that removes organic matter from the surface waters (Legendre & Rivkin, 2002). Thus, the relevance of understanding the role of zooplankton in shelf seas through models that can capture their dynamics with accuracy is crucial (Giering et al., 2018). In many biogeochemical models, zooplankton are represented by 1-3 groups (Everett et al., 2017), from microzooplankton (> 0.002 mm) to krill or jellyfish (> 5000 mm).

Microzooplankton includes single-celled heterotrophic flagellates, dinoflagellates, tintinnids, and ciliates, along with the early stages of some of the mesozooplankton (e.g. copepod larvae, called nauplii). These grazers feed on bacteria and autotrophic phytoplankton. The response of microzooplankton growth rates is similar to that of phytoplankton (Irigoien et al., 2004), providing a top-down control on the concentration of small phytoplankton (Simpson & Sharples, 2012). Mesozooplankton communities include multicellular animals, that feed on the microzooplankton and phytoplankton. Mesozooplankton can be divided into two groups: holoplankton, which means that they spend their entire life as plankton including copepods, krill, ostracods, chaetognaths, tunicates, and amphipods; and meroplankton communities, which means that they spend only the early stage of their life as plankton, including larvae of larger marine organisms and young gelatinous plankton (e.g. jellyfish; Simpson & Sharples, 2012). Mesozooplankton response to changes in the growth rate of phytoplankton takes time (Peterson & Keister, 2003), which can allow phytoplankton to briefly bloom in response to nutrient availability before they come under grazer control.

Simple models have been used to study the effect of zooplankton grazing on phytoplank-

ton (Riley, 1946). As described by Franks (2002), the response of zooplankton grazing on phytoplankton depends on the functions that are used (Holling, 1959). The first function described in this paper is a Holling Type I or Mayzaud and Poulet grazing, where the functional response assumes a linear increase of the grazing rate with phytoplankton biomass (Figure 1.5a). The second functional response corresponds to a Holling Type 2 or Ivlev grazing, which shows a saturating response to increasing food (Figure 1.5b). Finally, a third function is called Holling Type III or sigmoidal-shaped response, which shows saturation at high levels of phytoplankton biomass, and a linear response when the value of prey density is low and zero gradient when it is near zero (Figure 1.5c).

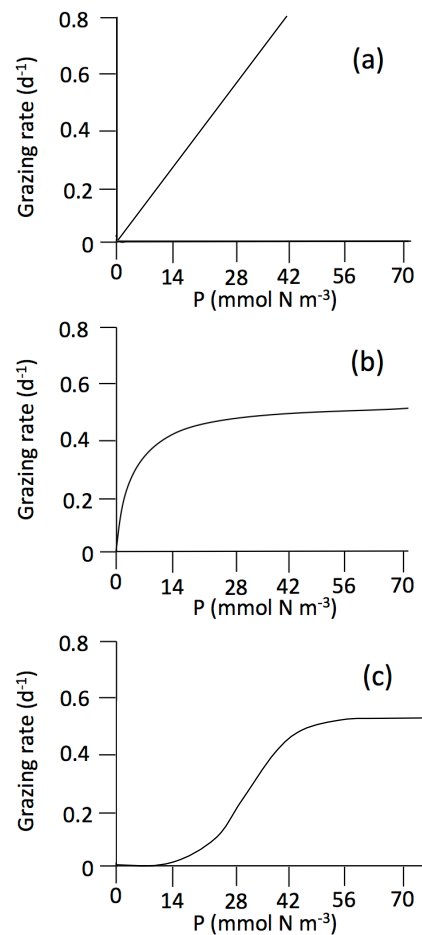


Figure 1.5: Ingestion curves for (a) Holling Type I or Mayzaud and Poulet grazing, (b) Holling Type II or Ivlev grazing, and (c) Holling Type III or sigmoidal-shaped grazing.

1.4 Observing shelf sea physics and biology

1.4.1 SSB programme

As described in section 1.1, shelf seas are highly valuable ecosystems in many aspects (e.g. fisheries, food production, carbon and nutrient cycling, etc). However, these ecosystems are under considerable stress, as a result of anthropogenic nutrient loading, overfishing, habitat disturbance, climate change, amongst other impacts. However, even within the relatively well-studied European shelf sea, fundamental biogeochemical processes are poorly understood (e.g. the role of shelf sea in carbon storage, in the global cycles of key nutrients, and in determining primary and secondary production). This is the main reason for the creation of the UK SSB research programme, whose aim was to increase the understanding of how physical, chemical and biological processes interact on UK and European shelf seas (for more information, <https://www.uk-ssb.org/>).

Large fieldwork campaigns were done throughout 2014 and 2015, along with laboratory experiments and biogeochemistry modelling. Data were obtained for oxygen, phytoplankton and zooplankton using CTD casts in different regions of the UK shelf sea, water samples, etc.

Multiple observations obtained from the SSB programme have been used in this work to validate the results obtained from modelling the CCS location.

1.4.2 Modelling shelf seas (1D vs 3D)

There are different ways to study shelf seas including using research vessels and remote, autonomous vehicles. Water samples are needed to understand the ecology and biogeochemistry of the system. However, data from research vessels is limited as it is not synoptic, i.e. it is not sampled at different locations simultaneously and, because of this, remote sensing plays an important role in the study of shelf seas (Joint & Groom, 2000). With satellite data it is possible to obtain information about the distribution of net phytoplankton production in the ocean (Behrenfeld and Falkowski, 1997), but other phenomena such as the SCM are difficult to observe. Besides, suspended sediments and dissolved organic material can influence this data (Hyde et al., 2007; Melin et al., 2007; Longhurst et al., 1995).

To complement the available data from research vessels and remote sensing, ocean models are used to study and understand marine biogeochemistry. A variety of high spatial resolution models have been developed to represent the biogeochemistry of shelf seas with high complexity and horizontal spatial resolution.

One of these models is the physical model Nucleus for European Modelling of the Ocean (NEMO), which can be coupled with the European Regional Seas Ecosystem Model (ERSEM) and is called NEMO-ERSEM (Edwards et al., 2012). This Nitrogen - Phytoplankton - Zooplankton - Detritus (NPZD) model has been developed to gain a better understanding of shelf sea biogeochemistry, nutrient fluxes, effects of eutrophication, harmful algal blooms, etc. Other physical models can be coupled with ERSEM, such as Regional Oceanic Modelling System (ROMS) and Finite Volume Community Ocean Model (FVCOM). ROMS is a 3D model that uses a free-surface and terrain-following coordinates (Shchepetkin & McWilliams, 2005). It includes physical algorithms and several coupled models for biogeochemical, bio-optical, sediment, and sea ice applications. FVCOM is a 3D model that uses an unstructured mesh to study the physical properties of the ocean (e.g. currents, stratification, salinity, temperature) (Chen et al., 2003).

Simulations of models like NEMO-ERSEM, ROMS, and FVCOM rely on high-performance computing resources as well as a high level of complexity which can make the results difficult to understand in terms of the behaviour of processes. Moreover, running multiple sensitivity analyses and experiments is difficult. In contrast, the Shelf Sea Physics and Primary Production (S2P3) model (Simpson and Sharples, 2012; Sharples, 1999) can study the dynamics of shelf seas and simulate seasonal stratification with greater computational efficiency by using a 1-D Nutrient-Phytoplankton (NP) model to represent physical and biogeochemical processes in the water column.

At the CCS location, which is situated in the central continental shelf and in the middle of the seasonally-stratifying region about 100 km from the shelf edge and approximately 200 km from the British Isles (Sharples et al., 2013), the seasonal changes in the vertical water column structure and the seasonal cycle of PP is dependent on the changes of the vertical water column structure (Sharples et al., 2013; Hu et al., 2011; Thomas et al., 2003;

Tett et al., 1993), and vertical ocean-atmosphere heat fluxes to control the development and breakdown of the seasonal stratification (Simpson & Bowers, 1981). Furthermore, different studies have calculated and analysed the flushing times of different sites of the NW European shelf, showing that for the complete renewal of the water, is about one to three years (Simpson, 1998) for the North Sea over the period 1987 - 1993, the overall flushing time for the Irish Sea as a whole is about one year (Knight & Howarth, 1999), while Hydes et al. (2004) identifies the transit time for Atlantic water crossing the Celtic Sea into the Irish Sea to be 6 yr with this flushing time being generally longer than the seasonal cycle of heating and cooling. Consequently, the S2P3 model will be able to accurately simulate the vertical dynamics of different temperate shelf sea locations that might present a flushing time longer than 1 yr, but awareness about changes in the winter nitrate concentration should be considered for long-time series for inter-annual studies where advective fluxes could play a bigger role than in year-to-year simulations due to advective fluxes. In conclusion, away from advective sources such as the shelf break or plumes from rivers, and for the purposes of this work that aims to understand the influence of meteorological forcing in the water column, then horizontal processes can be neglected in comparison to vertical processes for the CCS location. S2P3 does not consider advective fluxes but can make a good representation of the dynamics in the water column for temperate shelf seas and the CCS location. There is evidence in former studies done across the NW European shelf sea, where S2P3 successfully simulated vertical processes, with results showing a good approach in comparison with observational data (Marsh et al., 2015; Sharples, 2008; Sharples et al., 2006).

1.5 Structure of the following work

The structure of this thesis is as follows: in Chapter 2 the methodology and model development of this work is presented as well as the meteorological forcing used, and general set up for all the models in the CCS location; Chapter 3 provides an analysis and discussion about the effect of meteorology on the timing of the spring phytoplankton bloom and PP in the CCS location using the original simplest model of S2P3 v7.0 alongside the description of the *in situ* data used to validate this model; Chapter 4 includes the sensitivity analyses, validation, and calibration of three new versions of the original model used in Chapter 3 and developed into a Nutrient-Phytoplankton-Zooplankton (NPZ) framework

(S2P3-NPZ), a version of S2P3 v7.0 that incorporates the photo-acclimation process of phytoplankton (S2P3-Photoacclim), and a version of the model that combines the NPZ framework and the photo-acclimation of phytoplankton (S2P3 v8.0); Chapter 5 shows a long-term analysis of the S2P3 v8.0 model, to give a well-informed perspective of the effect of meteorology on PP in the CCS location, revisiting the open questions and hypotheses from Chapter 3; finally, Chapter 6 summarises the main findings, and provides conclusions and implications for future work.

The appendix and all references are listed at the end of this work.

Chapter 2

Methods and model development

Chapter 1 explained the importance of shelf seas for the global ocean production and the populations that rely on them, it also described the advantages of using a simple 1-D model in order to study these ecosystems. A 1-D model can be useful for addressing some questions by trying, for example, different forcing, changing parameters, and running different experiments simultaneously at a low computational cost.

This chapter presents the S2P3 v7.0 model (Sharples et al., 2006) followed by the development of that model into an NPZ-framework (S2P3-NPZ), a model that includes the photo-acclimation process of algal cells (S2P3-Photoacclim), and finally a model that combines the NPZ framework and photo-acclimation into one (S2P3 v8.0). The description of the model will be divided into the physical details of S2P3 and the methods of the biological part for each subsequent model version. Finally it is presented the general set-up for the meteorological forcing in the CCS location, and the spin-up considerations.

2.1 S2P3 model: physics

S2P3 v7.0 is a 1-D model developed for regional modelling of physical and biological processes in shelf seas that allows simulation of the seasonal cycle, stratification, and PP at a selected location defined by water depth and tidal current amplitude.

The model can be divided into two different components: a physical part and a biological part. For this research, the model is an improved version of the original described in Sharples et al. (2006) to be compiled and executed in a Unix environment (Marsh et al.,

2015).

All of the variables and parameters required by the physical part of the model explained in this methodology are listed in Tables 2.1 and 2.2.

The equations of motion in this model for the x and y horizontal directions, with u (m s^{-1}) the x -component of velocity and v (m s^{-1}) the y -component of velocity are as follow:

$$\frac{\partial u}{\partial t} = -g \sum_{i=1}^m A_{ix} \cos(\omega_i t - \phi_{ix}) + fv + \frac{\partial}{\partial z} \left(N_z \frac{\partial u}{\partial z} \right), \quad (2.1)$$

$$\frac{\partial v}{\partial t} = -g \sum_{i=1}^m A_{iy} \cos(\omega_i t - \phi_{iy}) + fu + \frac{\partial}{\partial z} \left(N_z \frac{\partial v}{\partial z} \right), \quad (2.2)$$

where z (m) is the vertical co-ordinate set as zero at the seabed and positive upwards, t is time, $g = 9.81$ (m s^{-2}) is the gravitational acceleration, A_{ix} and A_{iy} (dimensionless) are the amplitudes of the oscillating sea surface slopes in the x and y directions, ϕ_{ix} and ϕ_{iy} are the phases of the slope oscillations, N_z ($\text{m}^2 \text{s}^{-1}$) is the coefficient of vertical eddy viscosity, m represent the number of tidal constituents (e.g if $m = 2$, the tidal constituents are M_2 and S_2), ω_i is the frequency of every tidal constituents, f (s^{-1}) is the Coriolis parameter calculated as:

$$f = 2w_d \sin \phi,$$

where ϕ is the latitude set by the user and w_d is the rotational velocity of the earth.

Sharples (1999) produced the original work that developed the S2P3 model, using the turbulence closure scheme of Mellor-Yamada (Mellor & Yamada, 1982), contrary to the model used in this work based on Sharples et al. (2006). Improvements were subsequently made to the physical assumptions used in the models to deal with turbulence, and in the S2P3 v7.0 a new turbulence model was used based on Canuto et al. (2001).

This new methodology aimed to represent the wide spectrum of eddies in the ocean, choosing a variable to represent large scale processes (the TKE, represented as E in the following

equations) and another variable to represent the small scale processes that contain little energy but have a large vorticity (the dissipation ϵ). From these physical foundations, this model was called the $k - \epsilon$ model (Canuto et al., 2001).

S2P3 v7.0 calculates vertical profiles of eddy viscosity and eddy diffusivity at each time step using the $k - \epsilon$ turbulence scheme. The local changes of E are calculated as:

$$\frac{\partial E}{\partial t} = \frac{\partial}{\partial z} \left(N_z \frac{\partial E}{\partial z} \right) + N_z \left[\left(\frac{\partial u}{\partial z} \right)^2 + \left(\frac{\partial v}{\partial z} \right)^2 \right] + K_z \left(\frac{g}{\rho} \frac{\partial \rho}{\partial z} \right) - \epsilon, \quad (2.3)$$

where z is the vertical coordinate (positive upwards), u and v are respectively the x- and y-components of velocity, t is time, N_z is a depth-, time-dependent coefficient of vertical eddy viscosity, K_z is a depth-, time-dependent coefficient of vertical eddy diffusivity, g is the gravitational acceleration, ρ is the water density, and ϵ is the dissipation rate of E . The first term on the right side of eq. 2.3 is the vertical diffusion of E , the next three terms represent the shear production of turbulence, work done against buoyancy, and dissipation of TKE due to viscous forces, respectively.

The dissipation rate of TKE also needs a closure and is calculated as follows:

$$\frac{\partial \epsilon}{\partial t} = \frac{\partial}{\partial z} \left(N_\epsilon \frac{\partial \epsilon}{\partial z} \right) + \frac{\epsilon}{E} (c_1 N_z \left[\left(\frac{\partial u}{\partial z} \right)^2 + \left(\frac{\partial v}{\partial z} \right)^2 \right] + c_3 K_z \left(\frac{g}{\rho} \frac{\partial \rho}{\partial z} \right) - c_2 \epsilon), \quad (2.4)$$

where c_1 , c_2 , and c_3 are dimensionless model constants that were determined based on prediction methods tested on different types of turbulent flows (Sharples et al., 2006; Canuto et al., 2001; Canuto & Dubovikov, 1996):

$$c_1 = 1.44 \quad , \quad c_2 = 1.92 \quad , \quad c_3 = \begin{cases} -0.629, -K_z \left(\frac{g}{\rho} \frac{\partial \rho}{\partial z} \right) \geq 0 \\ 1, -K_z \left(\frac{g}{\rho} \frac{\partial \rho}{\partial z} \right) < 0. \end{cases}$$

$$N_\epsilon = \frac{N_z}{1.08}.$$

The TKE and turbulent dissipation are related via a turbulent length scale:

$$\epsilon = (c_\mu)^3 \frac{E^{\frac{3}{2}}}{L},$$

where L (m) is a length scale used to measure the size of turbulent eddies with $L = \kappa z_0$, $\kappa = 0.41$ is the von Karman's constant, z_0 is the roughness length of the boundary, and $c_\mu = 0.5562$ is a parameter for the stability function.

N_z and K_z depend on the amount of turbulence in the flow and are obtained from the turbulence closure model. They can be obtained from the product between the intensity of turbulence E ($\text{m}^2 \text{s}^{-2}$), the depth-dependant length scale L , and two stability functions (S_M , S_H) that represent the inhibition effect of stratification on mixing and depend on the gradient Richardson number, derived from the velocity and density fields. Therefore, the following equations represent the vertical eddy viscosity and vertical eddy diffusivity, respectively:

$$N_z = S_M \sqrt{E} L; \quad (2.5)$$

$$K_z = S_H \sqrt{E} L. \quad (2.6)$$

The stability functions S_M and S_H depend on the flux Richardson number (R_f) which is the ratio of power demand to power supply and must be less than 1 if turbulence is to be sustained; and the Richardson number (R_i):

$$R_f = \frac{K_z}{N_z} R_i,$$

where the Richardson number is calculated as:

$$R_i = \frac{\frac{-g}{\rho} \frac{\partial \rho}{\partial z}}{\left(\frac{\partial u}{\partial z}\right)^2 + \left(\frac{\partial v}{\partial z}\right)^2}. \quad (2.7)$$

Boundary conditions for the E profile are determined by surface (wind) and seabed (tides) stresses, respectively:

$$E = \begin{pmatrix} \tau_s \\ c_\mu \end{pmatrix} \quad \text{at } z = h,$$

$$E = \begin{pmatrix} \tau_b \\ c_\mu \end{pmatrix} \quad \text{at } z = 0.$$

where $c_\mu = 0.5562$ is a parameter for the stability function, τ_s is the surface stress due to wind and τ_b is the near-bottom stress due to tidal currents (see Sharples et al., 2006, for calculations of τ_s and τ_b).

2.1.1 Physical forcing

For temperate latitudes, it can be assumed that of the total incident solar radiation, 45% corresponds to the photosynthetically available radiation (PAR) in the visible range of the spectral energy distribution of solar radiation (between 400 - 700 nm) and the remaining 55% corresponds to the infra-red range (> 700 nm) and to the radiation < 400 nm (Kirk, 1994). Therefore, the S2P3 model calculates that from the total incident radiation, 55% is absorbed within the top depth grid cell (eq. 2.8) to simulate the rapid attenuation of the infra-red portion of the incident radiation spectrum, while the remaining 45% is distributed exponentially through the water column (eq. 2.8) according to:

$$\frac{\partial Q_h(z)}{\partial z} = -Q_h(z)(\lambda_o + \epsilon_x X_T(z)), \quad (2.8)$$

where ϵ_x is the pigment absorption cross-section, λ_o is the local heat attenuation coefficient, and $X_T(z)$ is the concentration of chlorophyll-*a* biomass.

Once the water column has been heated and cooled, the thermal structure in the water column will be defined as:

$$\frac{\partial T}{\partial t} = \frac{\partial}{\partial z} \left(K_z \frac{\partial T}{\partial z} \right) + Q_h(z). \quad (2.9)$$

The available irradiance for photosynthesis (I_{PAR}) is then distributed through the water column as:

$$\frac{\partial I_{PAR}(z)}{\partial z} = -I_{PAR}(z)(\lambda_{PAR} + \epsilon_x X_T(z)), \quad (2.10)$$

where λ_{PAR} (m^{-1}) is the vertical absorption coefficient of PAR. A surface PAR irradiance boundary condition is set, being a fraction of the incident daily mean solar irradiance defined by the user, in this case that fraction corresponds to 45% of the daily mean solar irradiance.

A surface net heat flux (Q_{net}) is defined as the sum of incoming shortwave radiation (Q_{SW}), long-wave back radiation (Q_{LW}), and latent and sensible heat exchange with the atmosphere (Q_{lat} and Q_{sens}). The latent heat flux is defined as heat loss due to evaporation (related to air temperature, relative humidity, and wind speed), while the sensible heat flux is a direct conduction of heat across the air-sea interface due to differences in temperature and wind speed.

$$Q_{\text{net}} = Q_{\text{SW}} - (Q_{\text{LW}} + Q_{\text{sens}} + Q_{\text{lat}}). \quad (2.11)$$

The surface net heat flux (Q_{net}) is partitioned down the water column: the red end of the spectrum, 55% of shortwave radiation is assumed to be absorbed at the top depth level: $Q_{\text{h},0} = 0.55Q_{\text{SW}} - (Q_{\text{LW}} + Q_{\text{lat}} + Q_{\text{sens}})$. The remaining 45% of insolation is available for heating at lower levels, distributed exponentially throughout the water column as shown in eq. 2.8.

Incoming shortwave radiation is a function of cloud cover (C), calculated as:

$$Q_{\text{SW}} = (1.0 - 0.004C - 0.000038C^2)Q_o, \quad (2.12)$$

where Q_o is the clear sky daily mean irradiance at the surface, calculated as a function of the atmospheric albedo, and the seasonal variation in day length at a given latitude.

Long-wave heat flux is the energy radiated from the sea surface back into the atmosphere, calculated as a function of the cloud fraction and the relative humidity (R):

$$Q_{\text{LW}} = \varepsilon_{\text{LW}}(1.0 - 0.6 \times 10^{-4}C^2)(0.39 - 0.05q_V^{0.5})\sigma T^4, \quad (2.13)$$

where ε_{LW} is long-wave emissivity, q_V is vapour pressure ($q_V = Rq_s$, given saturated vapour pressure and relative humidity), and σ is the Stefan-Boltzmann constant.

The sensible and evaporative heat fluxes are calculated as:

$$Q_{sens} = \rho_a c_p C_h W_s (T_s - T_a), \quad (2.14)$$

$$Q_{lat} = \rho_a L_v C_e W_s (q_s - q). \quad (2.15)$$

where ρ_a is the density of air, c_p is the specific heat capacity of air, C_h is the Dalton number, W_s is surface wind speed, T_s is the sea surface temperature, T_a is the surface air temperature, L_v is the specific heat capacity of air as a function of T_s ($L_v = 2.5 \times 10^{-6} - 2.3 \times 10^{-3} T_s$), and C_e is the Stanton number. See Sharples et al. (2006) for calculations of q_s and q .

2.1.2 Stability criteria and resolution

The integration scheme of the model is explicit using a 4th order Runge-Kutta method. Time-step intervals (Δt) are constrained by the diffusive stability criterion or Courant-Friedrichs-Lewy (CFL) condition, controlling the speed at which the model runs.

$$\Delta t = \frac{\Delta z^2}{2N_z}. \quad (2.16)$$

By changing the vertical resolution in the model, it changes the number of vertical levels and Δz .

The user needs to specify some initialisation parameters such as the location, depth, and amplitude of tidal constituents. For this work, the M_2 , S_2 , and N_2 tidal constituents were used, so that the model can simulate the spring-neap tidal cycle (Sharples, 2008).

A simplified diagram of the physical part of S2P3 v7.0 is illustrated in Figure 2.1, showing the different dependencies between variables, processes, and respective equations.

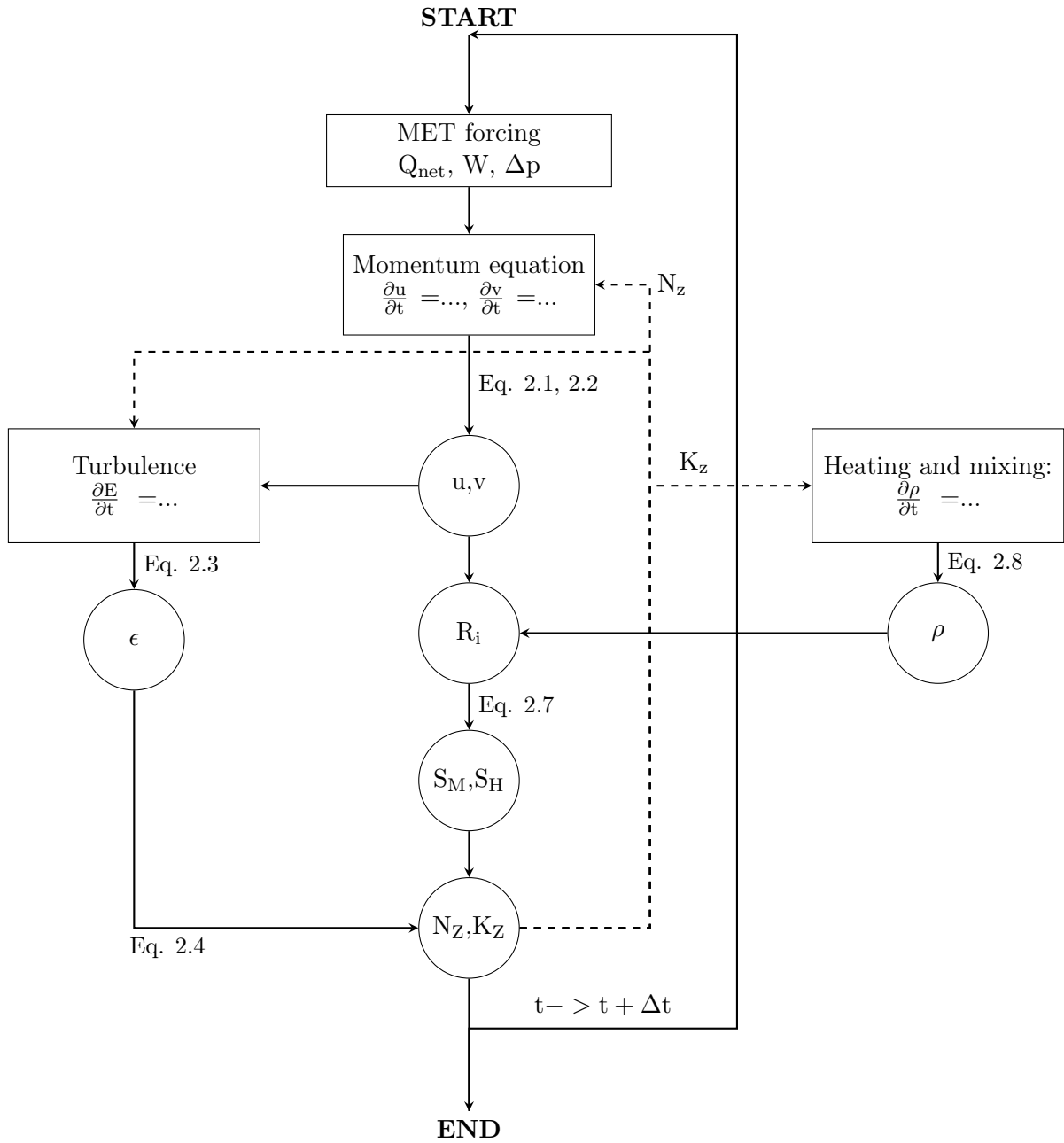


Figure 2.1: Simplified diagram of the physical part of the S2P3 model to illustrate the interdependence of the different variables used in the turbulence closure scheme (modified diagram taken from Simpson & Sharples, 2012).

Variables	Definition	Units
A_{ix}, A_{iy}	Amplitudes of the oscillating sea surface in the x and y-directions, respectively	dimensionless
C	Cloud fraction	%
E	TKE	$\text{m}^2 \text{s}^{-2}$
f	Coriolis parameter	s^{-1}
I_{PAR}	Photosynthetically available radiation	Wm^{-2}
K_z	Depth-dependant vertical eddy diffusivity	$\text{m}^2 \text{s}^{-1}$
L	Length scale for turbulent eddies size	m
L_v	Specific heat capacity of air depending on T_S	$\text{Jkg}^{-1} \text{K}^{-1}$
N_ϵ	Coefficient of vertical eddy viscosity	$\text{m}^2 \text{s}^{-1}$
N_z	Coefficient of vertical eddy viscosity	$\text{m}^2 \text{s}^{-1}$
q	Specific humidity of air at sea temperature	kg kg^{-1}
Q_h	Local heating irradiance	Wm^{-2}
Q_{lat}	Latent heat exchange with the atmosphere	Wm^{-2}
Q_{LW}	Long-wave back radiation	Wm^{-2}
Q_{net}	Surface net heat flux	Wm^{-2}
Q_o	Clear sky daily mean irradiance at the surface	W m^{-2}
q_s	Specific humidity of air at air temperature	kg kg^{-1}
Q_{sens}	Sensible heat exchange with the atmosphere	Wm^{-2}
Q_{SW}	Incoming shortwave radiation	Wm^{-2}
q_v	Vapour pressure	kg kg^{-1}
R	Relative humidity	%
R_f	Flux Richardson number	dimensionless
R_i	Richardson number	dimensionless
S_H	Stability function related to the flux Richardson number	dimensionless
S_M	Stability function related to the flux Richardson number	dimensionless
T_a	Surface air temperature	$^\circ\text{C}$
u	x-component of velocity	ms^{-1}
v	y-component of velocity	ms^{-1}
w_i	Angular frequency of the i th tidal constituent	s^{-1}
W_s	Surface wind speed	m s^{-1}
X_T	Local total concentration of chlorophyll biomass	mgChlm^{-3}
z	Vertical coordinate (positive upwards)	m
z_0	Roughness length of the boundary	m
ρ	Water density depending on water temperature with a fixed salinity value	kg m^{-3}
ϵ	Dissipation rate of TKE	$\text{m}^2 \text{s}^{-3}$
τ_b	Bottom stress of the water column due to tidal currents	N m^{-2}
τ_s	Surface stress of the water column due to wind	N m^{-2}
ϕ_{ix}, ϕ_{iy}	Phase of the slope oscillation in the x and y directions, respectively	s^{-1}

Table 2.1: List of variables, with their definitions and units, from the physical part of the S2P3 v7.0 model.

Parameters	Definition	Units	Value
c_1	Turbulence model constant	dimensionless	1.44
c_2	Turbulence model constant	dimensionless	1.92
c_3	Turbulence model constant	dimensionless	-0.629, 1
C_e	Dalton number	dimensionless	1.45×10^{-3}
C_h	Stanton number	dimensionless	1.5×10^{-3}
c_p	Specific heat capacity of air	$\text{Jkg}^{-1}\text{K}^{-1}$	1004
c_μ	Stability function	dimensionless	0.5562
g	Gravitational acceleration	m s^{-2}	9.8
h	Total water column depth	m	140.0
T	Initial water temperature	$^\circ\text{C}$	10.10
T_s	Sea surface temperature	$^\circ\text{C}$	10.1
Δt	Time step	s	2.50
w_d	Angular velocity of the earth	rad s^{-1}	0.000072
Δz	Depth resolution	m	1.0
λ_o	Vertical attenuation of PAR	m^{-1}	0.1
λ_{PAR}	Vertical absorption coefficient of PAR	m^{-1}	0.1
ϵ_x	Pigment absorption cross-section	$\text{m}^2(\text{mgChl})^{-1}$	0.012
ϵ_{LW}	Long-wave emissivity	Wm^{-2}	0.985
κ	von Karman's constant	dimensionless	0.41
ρ_a	Air density	kgm^{-3}	1.3
σ	Stefan-Boltzmann constant	$\text{Wm}^{-2}\text{K}^{-4}$	5.67×10^{-8}
ϕ	Latitude	degrees	$49.4^\circ N$

Table 2.2: List of initialised parameters, with definitions, units, and values, for the physical part of the S2P3 v7.0 model.

2.2 S2P3 model: biology

This section describes the biological part of each model version developed from the original S2P3 v7.0 model. The physical part of each model version is exactly the same, therefore only differences in the biological methodology are presented.

2.2.1 S2P3 v7.0

The biological part of the S2P3 v7.0 model calculates the development of one or more groups of phytoplankton in response to light and DIN (Sharples, 2008). In this study, only one species was used.

Phytoplankton biomass is modelled in terms of chlorophyll ($Phyto_{chl}$, mg Chl m^{-3})

$$\frac{\partial Phyto_{chl}}{\partial t} = \frac{\partial}{\partial z} \left(K_z \frac{\partial Phyto_{chl}}{\partial z} \right) + \mu Phyto_{chl} - G Phyto_{chl}. \quad (2.17)$$

The change of $Phyto_{chl}$ over time is due to the net effect of vertical turbulent transport of biomass, growth of phytoplankton, and losses of phytoplankton biomass through grazing.

The model does not explicitly calculate densities of zooplankton, but it does include a grazing rate for phytoplankton (G ; d^{-1}), which is calculated as a fraction of phytoplankton biomass removed each time step to be recycled back into the available pool of water column DIN (e ; eq. 2.22), which in this study corresponds to 50% of the grazed phytoplankton. The grazing rate is then calculated as a seasonally-varying sinusoidal function.

Growth of phytoplankton biomass (μ) can be either nutrient-limited or temperature-limited. To account for nutrient and temperature effects, the maximum growth rate is calculated as:

$$\mu_m = \left(\frac{Q - Q_{sub}}{Q_m - Q_{sub}} \right) 0.59 e^{-0.0633T}. \quad (2.18)$$

The maximum growth rate (μ_m) is related to temperature (T ; $^{\circ}C$) and modified by the nutrient quota Q ($mmol\ N\ (mg\ Chl)^{-1}$), which corresponds to the ratio between phytoplankton internal nitrogen and phytoplankton biomass (Figure 2.2). So:

$$Q = \frac{Phyto_N}{Phyto_{chl}}.$$

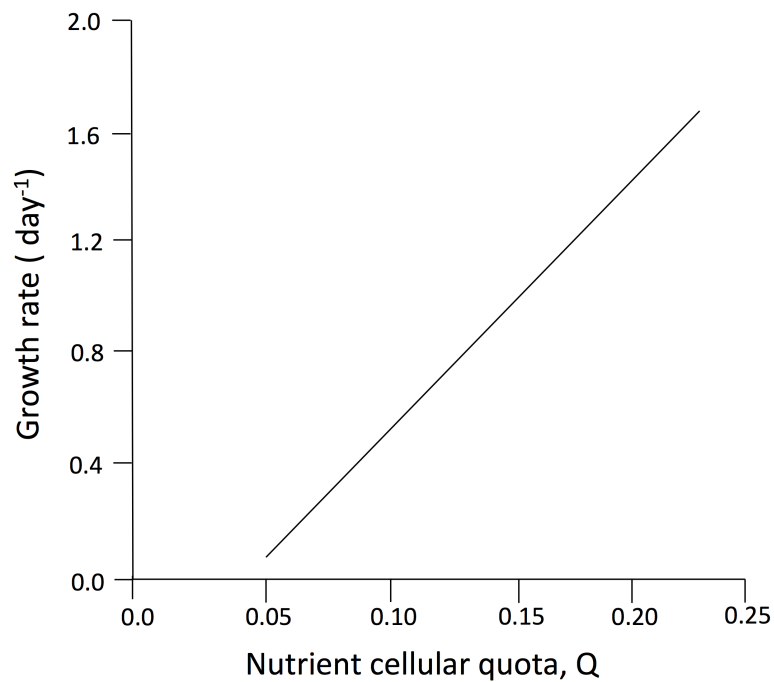


Figure 2.2: Phytoplankton growth rate dependency on nutrient availability, based on the cellular nutrient quota. Parameters values are taken from literature (Flynn, 2008).

The S2P3 v7.0 model considers two growth models for the temperature dependence of phytoplankton: (1) relating the maximum phytoplankton growth rate and temperature by using the Eppley function (Eppley, 1972), and (2) relating biological rates to temperature by using the Q10 model (Valiela, 2010). According to the study of Bissinger et al. (2008), there is no significant difference between the Eppley curve and Q10 values, suggesting that the Eppley curve is an appropriate estimate of the thermal sensitivity of phytoplankton growth rates in temperate regions. Therefore, in this study, the Eppley function was used (Figure 2.3; eq. 2.18).

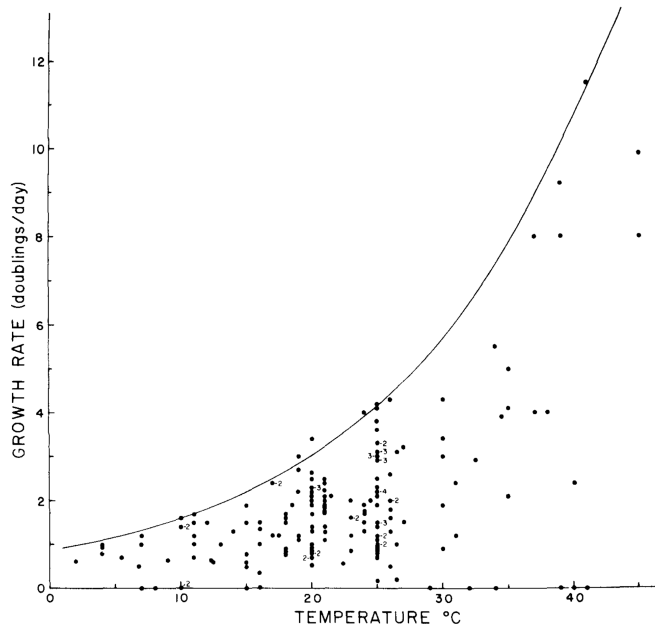


Figure 2.3: Phytoplankton growth dependency on temperature based on the Eppley curve, where the maximum growth increases with temperature. Parameter values are taken from literature (Eppley, 1972).

The maximum cell nutrient quota (Q_m ; $\text{mmol N (mg Chl)}^{-1}$) is the maximum amount of nitrogen that phytoplankton can contain per unit chlorophyll-*a* and the subsistence cell nutrient quota (Q_{sub} ; $\text{mmol N (mg Chl)}^{-1}$) corresponds to the internal nitrate concentration required before there can be phytoplankton growth.

Phytoplankton growth rate can also be light-determined by PAR (I_{PAR} , W m^{-2}), where surface PAR is taken to be a fixed 45% of the solar irradiance:

$$\mu = \mu_m(1 - e^{-(\alpha I_{PAR}\theta/\mu_m)}) - r^B. \quad (2.19)$$

Eq. 2.19 shows the relationship between phytoplankton growth and irradiance (Figure 2.4), but physiological acclimation (i.e. photoacclimation of cells) to changes in light intensity are not considered in this version of the model.

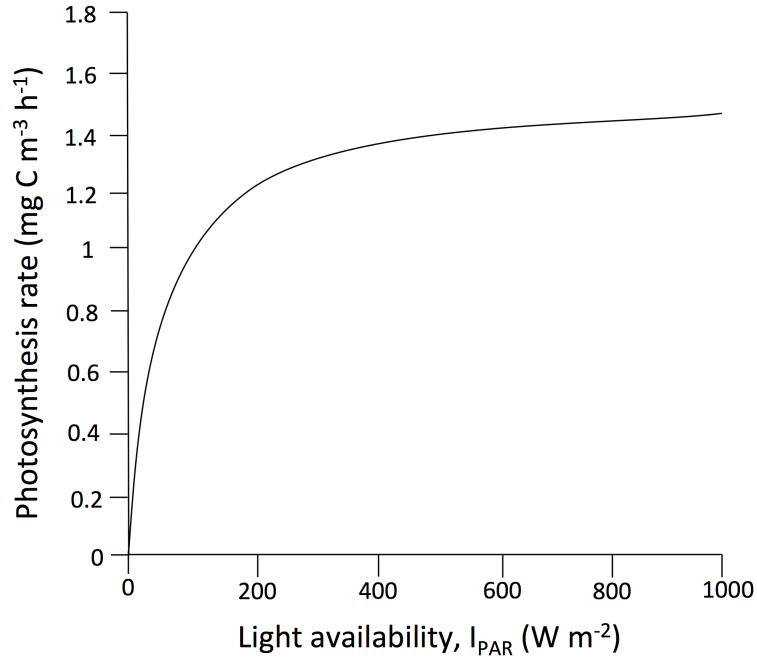


Figure 2.4: Phytoplankton growth dependency on light availability. Parameter values are taken from literature (Hickman et al., 2012).

Phytoplankton biomass is also modelled in terms of internal cellular nitrogen:

$$\frac{\partial Phyto_N}{\partial t} = \frac{\partial}{\partial z} \left(K_z \frac{\partial Phyto_N}{\partial z} \right) + u Phyto_{chl} - GQ Phyto_{chl}, \quad (2.20)$$

where u is the uptake rate obtained as a Michaelis-Menton function of the external DIN concentration (mmol N m^{-3}):

$$u = \left[u_m \left(1 - \frac{Q}{Q_m} \right) \frac{N}{k_u + N} \right] + \begin{cases} \mu Q, \mu < 0 \\ 0, \mu \geq 0 \end{cases} \quad (2.21)$$

The last term on the right side of eq. 2.21 represents the regeneration of cellular nitrogen following dark respiration.

The change in time for external DIN is calculated as:

$$\frac{\partial N}{\partial t} = \frac{\partial}{\partial z} \left(K_z \frac{\partial N}{\partial z} \right) - u Phyto_{chl} + eGQ Phyto_{chl}, \quad (2.22)$$

where the second term on the right side of eq. 2.22 represents the loss of nitrogen from the DIN pool due to phytoplankton uptake of nutrients; the third term on the right side of the equation represents the source of nitrogen into the DIN pool due to grazed phytoplankton, where e is a fraction of the recycled grazed phytoplankton that goes back into the DIN pool; and the rest of the grazed phytoplankton $(1-e)$ is transferred to sediments or higher trophic levels.

Water column nitrogen is constantly restored towards an initial winter concentration, N_0 (mmol N m^{-3}), by a flux of inorganic nitrogen from the seabed (Marsh et al., 2015):

$$\frac{\partial N_1}{\partial t} = \frac{f_N}{\Delta z} \left(1 - \frac{N_1}{N_0} \right) \quad (2.23)$$

where N_1 is the dissolved nitrogen in the bottom depth cell of the model grid.

Note that the user needs to set initial values for the internal cell nitrate, biomass of phytoplankton, and DIN using the available information from the literature and based on observations from the CCS location.

A simplified diagram of the biological part of the S2P3 v7.0 model is illustrated in Figure 2.5. Information about the biological variables is listed in Table 2.3 and the information about biological parameters is listed in Table 2.4, with parameter values obtained from similar model setups for temperate shelf sea environments (Marsh et al., 2015; Sharples, 2008, according to observations from the Proudman Laboratory Liverpool).

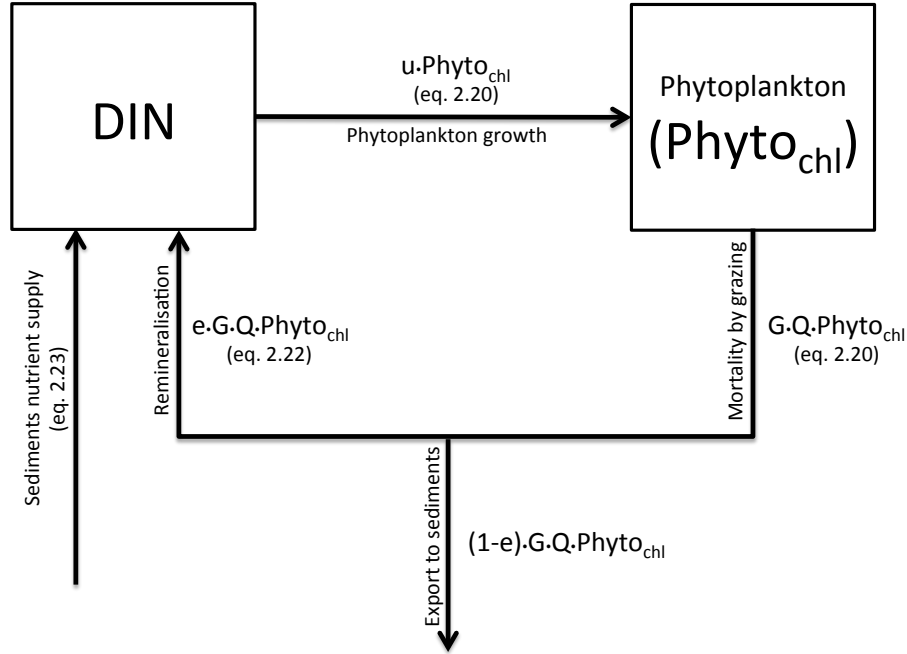


Figure 2.5: Schematic illustration of the biological part of the S2P3 v7.0 model for the nitrate-phytoplankton relationship.

Variables	Definition	Units
N	External DIN concentration	mmol N m^{-3}
N_1	Dissolved nitrogen in the bottom grid cell of the water column	mmol N m^{-3}
$Phyto_{chl}$	Phytoplankton biomass in chlorophyll currency	mg Chl m^{-3}
$Phyto_N$	Phytoplankton biomass in nitrogen currency	mmol N m^{-3}
Q	Cellular nutrient quota	$\text{mmol N (mg Chl)}^{-1}$
u	Uptake rate of external DIN	$\text{mmol N (mg Chl)}^{-1} \text{d}^{-1}$
μ	Phytoplankton growth rate	d^{-1}
μ_m	Maximum growth rate of phytoplankton	d^{-1}

Table 2.3: List of variables, with their definitions and units, for the biological part of the S2P3 v7.0 model.

Parameters	Definition	Units	Value
e	Recycled grazed phytoplankton nitrogen	dimensionless	0.5
f_N	Seabed nitrogen flux	$\text{mmol m}^2 \text{d}^{-1}$	10.0
G	Maximum grazing rate of phytoplankton	d^{-1}	0.12
k_u	Half-saturation quota	mmol N m^{-3}	0.3
N_0	Seabed nitrogen concentration	mmol N m^{-3}	7.0
Q_m	Maximum cellular quota of N:Chl	$\text{mmol N (mg Chl)}^{-1}$	1.0
Q_{sub}	Subsistence cell quota	$\text{mmol N (mg Chl)}^{-1}$	0.2
r^B	Respiration rate	$\text{mg C (mg Chl)}^{-1} \text{d}^{-1}$	3.5
u_m	Maximum nitrogen uptake rate	$\text{mmol N (mg Chl)}^{-1} \text{d}^{-1}$	2.0
α	Maximum light utilisation coefficient	$\text{mg C (mg Chl)}^{-1} (\text{W m}^{-2})^{-1} \text{d}^{-1}$	4.0
θ	Cellular Chl:carbon ratio	$\text{mg Chl (mg C)}^{-1}$	0.03
μ_m	Maximum growth rate	d^{-1}	See eq. 2.18

Table 2.4: List of initialised parameters, with definitions, units, and values, for the biological part of the S2P3 v7.0 model. Parameter values obtained according to the work of Sharples (2008).

2.2.2 S2P3-NPZ

In order to explicitly account for the influence of zooplankton grazing and, hence, predator-prey relationship dynamics, the simplest version of the S2P3 model (S2P3 v7.0) was developed into an NPZ framework. This new version of the model (S2P3-NPZ) includes zooplankton as a state variable, contrary to the S2P3 v7.0 model where grazing was considered as a constant rate every year. The development of the S2P3-NPZ model includes new parameters to be described in this section but with the advantage that this new version will allow comparison to data on zooplankton biomass.

The biological part of the S2P3-NPZ model calculates phytoplankton biomass in chlorophyll currency ($Phyto_{chl}$; mg Chl m^{-3}). Additionally, phytoplankton modelled in terms of internal nitrogen (mmol N m^{-3}) is represented by $Phyto_N$. Zooplankton biomass and external DIN are modelled in terms of nitrogen (mmol N m^{-3}).

Changes of phytoplankton biomass ($Phyto_{chl}$) over time can then be described by:

$$\frac{\partial Phyto_{chl}}{\partial t} = \frac{\partial}{\partial z} \left(K_Z \frac{\partial Phyto_{chl}}{\partial z} \right) + \mu Phyto_{chl} - \frac{IZ}{Q}. \quad (2.24)$$

The change of $Phyto_{chl}$ over time is due to the net effect of vertical turbulent transport of biomass, growth of phytoplankton, and losses due to an ingestion rate of phytoplankton by zooplankton.

Phytoplankton biomass is also modelled in terms of internal nitrogen, $Phyto_N$. The S2P3-NPZ model calculates $Phyto_N$ as:

$$\frac{\partial Phyto_N}{\partial t} = \frac{\partial}{\partial z} \left(K_Z \frac{\partial Phyto_N}{\partial z} \right) + u Phyto_{chl} - IZ, \quad (2.25)$$

where the changes over time of $Phyto_N$ are due to vertical mixing in the water column, growth of phytoplankton due to the uptake of nitrogen from the DIN pool, and losses due to zooplankton grazing.

Because most formulations show a saturating response to increasing food, the use of an Ivlev response to describe phytoplankton concentrations was chosen (see Chapter 1, section 1.3.3; Franks et al., 1986; Vidal, 1980; Steele & Mullin, 1977; Mullin et al., 1975). Therefore, the ingestion rate of zooplankton (I) in this model can be described as a Holling Type II or Ivlev grazing:

$$I = R_m(1 - e^{(-\lambda Phyto_N)}),$$

where R_m is the maximum ingestion rate (d^{-1}) and λ is the rate at which saturation is achieved with increasing food levels ($mmol\ N\ m^{-3}$) $^{-1}$.

Zooplankton biomass is modelled as:

$$\frac{\partial Z}{\partial t} = \frac{\partial}{\partial z} \left(K_Z \frac{\partial Z}{\partial z} \right) + (1 - \gamma_1)IZ - mZ, \quad (2.26)$$

where the change zooplankton biomass (Z) over time is due to the net effect of vertical turbulent transport of biomass, growth of zooplankton due to the ingested phytoplankton, and losses due to mortality of zooplankton.

The change in time of external DIN is calculated as:

$$\frac{\partial N}{\partial t} = \frac{\partial}{\partial z} \left(K_Z \frac{\partial N}{\partial z} \right) + \gamma_1 IZ + \gamma_2 mZ - uPhyto_{chl}. \quad (2.27)$$

Eq. 2.27 describes the cycle of inorganic nitrogen, where a fraction of the grazed phytoplankton is added into the DIN pool due to inefficient grazing or messy eating of zooplankton. Another addition to external nutrients corresponds to a fraction coming from zooplankton mortality, which is lost to sediments or higher trophic levels.

Equations (2.24) - (2.27) describe how each state variable is linked in the S2P3-NPZ model via the uptake of nutrients by phytoplankton (μP), phytoplankton grazed by zooplankton (IZ), and a loss term for zooplankton due to a death rate (mZ), where a fraction of the zooplankton ($\gamma_2 mZ$) is recycled back into the nitrogen pool and the rest is assumed to go into sediments ($(1 - \gamma_2)mZ$), which is conceptually added in the model (as shown in Figure 2.6) but not explicitly calculated. A non-assimilated fraction of the consumed food by zooplankton ($\gamma_1 IZ$) is also recycled back into the nitrogen pool due to "sloppy feeding" and/or excretion and the rest ($(1 - \gamma_1)IZ$) is grazed by zooplankton.

Balance in the model is reached when nutrients are supplied by resuspension from the seabed through a flux of DIN that restores water column nitrogen back to an initial winter concentration (N_0 ; eq. 2.28):

$$\frac{\partial N_1}{\partial t} = \frac{f_N}{\Delta z} \left(1 - \frac{N_1}{N_0} \right), \quad (2.28)$$

where N_1 is the DIN in the bottom depth cell of the model grid, and f_N corresponds to a constant nitrogen flux from the seabed.

Similar to the S2P3 v7.0 model described in section 2.2.1, phytoplankton net growth rate is represented by μ (d^{-1} ; eq. 2.29), determined by the photosynthetically available radiation (I_{PAR}) and by losses due to a cellular respiration rate (r^B) dependent on temperature via a Q_{10} relationship (Sharples, 1999; Valiela, 1995).

$$\mu = \mu_m \left(1 - e^{-\left(\frac{\alpha I_{PAR}^\theta}{\mu_m} \right)} \right) - \theta r^B \left(r Q_{10}^{\left(\frac{T-rT_0}{10} \right)} \right) \quad (2.29)$$

The maximum growth rate of phytoplankton (μ_m ; d^{-1}) is modified by temperature following an Eppley curve and also by a cellular nutrient quota (Q) that varies over time (for more information see Tables 2.5 and 2.6).

$$\mu_m = \left(\frac{Q - Q_{sub}}{Q_m - Q_{sub}} \right) 0.59e^{-(0.0633T)} \quad (2.30)$$

The uptake rate of external nutrients (u ; $\text{mmol N (mg Chl)}^{-1} \text{d}^{-1}$) is again obtained using a Michaelis-Menton function:

$$u = u_m \left(1 - \frac{Q}{Q_m} \right) \left(\frac{N}{k_u + N} \right), \quad (2.31)$$

where Q corresponds to the nutrient cellular quota (N:Chl), Q_m is the maximum cellular quota, and k_u is the nitrate uptake concentration.

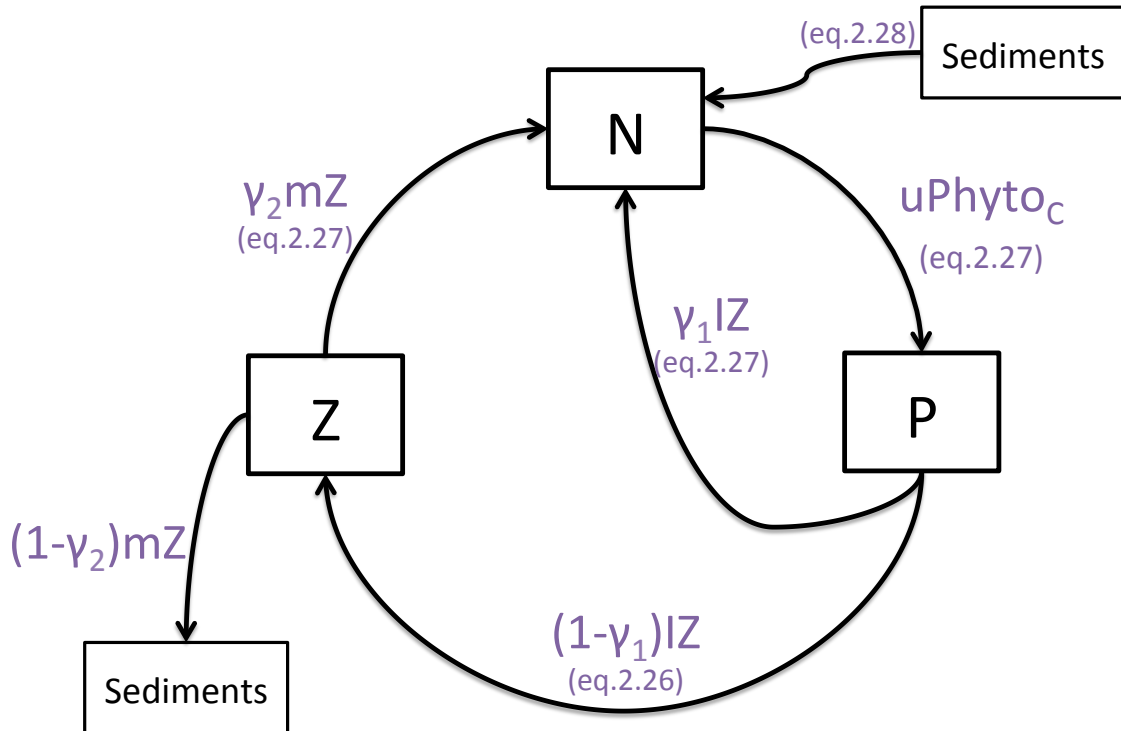


Figure 2.6: Schematic representation of the biological part of the S2P3-NPZ model illustrating the NPZ framework.

Variables	Definition	Units
I	Ingestion rate of phytoplankton	d^{-1}
N	External DIN concentration	mmol N m^{-3}
N_1	Dissolved nitrogen in the bottom grid cell of the water column	mmol N m^{-3}
$Phyto_C$	Phytoplankton biomass in carbon currency	mg C m^{-3}
$Phyto_{chl}$	Phytoplankton biomass in chlorophyll currency	mg Chl m^{-3}
$Phyto_N$	Phytoplankton biomass in nitrogen currency	mmol N m^{-3}
Q	Cellular nutrient quota	$\text{mmol N (mg Chl)}^{-1}$
u	Uptake rate of external DIN	$\text{mmol N (mg Chl)}^{-1} \text{d}^{-1}$
Z	Zooplankton biomass	mmol N m^{-3}
μ	Phytoplankton growth rate	d^{-1}
μ_m	Maximum growth rate of phytoplankton	d^{-1}

Table 2.5: List of variables, with their definitions and units, for the biological part of the S2P3-NPZ model.

2.2.3 S2P3-Photoacclim

A new version of the S2P3 v7.0 model was developed here, based on Geider's model (Geider et al., 1998), which allows phytoplankton to photo-acclimate to changes in light and, therefore, the ratios of Chl:C:N can vary, contrary to the S2P3 v7.0 where only the N:Chl quota (Q) could vary and the Chl:C quota was a fixed value. Therefore, in this model the dynamics of $Phyto_{chl}$ can be different to that for $Phyto_N$. This new version of the model is called S2P3-Photoacclim and allows direct comparison to physiological data.

The biological part of the S2P3-photoacclim model uses three currencies of phytoplankton biomass: carbon ($Phyto_C$; mg C m^{-3}), nitrogen ($Phyto_N$; mg N m^{-3}), and chlorophyll ($Phyto_{chl}$; mg Chl m^{-3}). The S2P3-photoacclim model is based on the Geider et al. (1998) model, with phytoplankton growth being proportional to both nitrogen assimilation and carbon fixation (i.e. variable Chl:N and Chl:C ratios).

Changes in phytoplankton biomass ($Phyto_C$) over time can then be described by:

$$\frac{\partial Phyto_C}{\partial t} = \frac{\partial}{\partial z} \left(K_Z \frac{\partial Phyto_C}{\partial z} \right) + Phyto_C (\mu - R_C T_{function} - u\zeta - G). \quad (2.32)$$

Parameters	Definition	Units	Value
f_N	Seabed nitrogen flux	mmol m ² d ⁻¹	10.0
k_u	Nitrate uptake half-saturation concentration	mmol N m ⁻³	0.3
m	Loss rate of zooplankton due to predation and physiological death	d ⁻¹	0.05
N_0	Seabed nitrogen concentration	mmol N m ⁻³	7.0
Q_m	Maximum cellular quota of N:Chl	mmol N (mg Chl) ⁻¹	1.0
Q_{sub}	Subsistence cell nutrient quota	mmol N (mg Chl) ⁻¹	0.2
r^B	Reference respiration rate	mg C (mg Chl) ⁻¹ d ⁻¹	3.5
R_m	Maximum ingestion rate of phytoplankton	d ⁻¹	2.5
rQ_{10}	Q_{10} exponent for respiration	dimensionless	1.0
rT_o	Reference temperature for respiration rate	°C	15.0
u_m	Maximum nitrate uptake rate	mmol N (mg Chl) ⁻¹ d ⁻¹	2.0
α	Maximum light utilisation coefficient	mg C (mg Chl) ⁻¹ d ⁻¹ (W m ⁻²) ⁻¹	4.0
γ_1	Grazing inefficiency or 'messy feeding' (0.0-1.0), returns a fraction of grazed material back into the DIN pool	dimensionless	0.2
γ_2	Fraction of dead zooplankton that goes into the sediments	dimensionless	0.5
θ	Chl:C	mg Chl (mg C) ⁻¹	0.03
λ	Rate at which saturation is achieved with increasing food levels	(mmol N m ⁻³) ⁻¹	0.75

Table 2.6: List of all the parameters, with their respective definitions, initialised values, and units, in the biological part of the S2P3-NPZ model. This includes the new variables used to simulate the new grazing rate by using zooplankton biomass, including: m , γ_1 , γ_2 , R_m , and λ . Parameter values of the newly added NPZ parameters are taken from different sources of the literature and they are specified in Chapter 4, Table 4.2.

The change of $Phyto_C$ over time is due to the net effect of vertical turbulent transport of biomass, growth of phytoplankton ($\mu Phyto_C$), losses due to respiration (R_C), the cost associated with biosynthesis ($u\zeta$; Geider et al., 1998; Geider, 1992; Penning De Vries et al., 1974), and grazing (G).

Phytoplankton biomass is also modelled in terms of internal nitrogen, P_N . The S2P3-photoacclim model calculates $Phyto_N$ as:

$$\frac{\partial Phyto_N}{\partial t} = \frac{\partial}{\partial z} \left(K_Z \frac{\partial Phyto_N}{\partial z} \right) + uPhyto_C - Phyto_N(R_n T_{function} + G). \quad (2.33)$$

The rate of change of $Phyto_N$ is due to the net effect of vertical turbulent transport of biomass, nitrate uptake ($uPhyto_C$), and losses due to nitrogen remineralisation (R_n) and grazing (G).

The rate of change of phytoplankton biomass in terms of chlorophyll ($Phyto_{chl}$) is described by:

$$\frac{\partial Phyto_{chl}}{\partial t} = \frac{\partial}{\partial z} \left(K_Z \frac{\partial Phyto_{chl}}{\partial z} \right) + u\rho_{chl}Phyto_C - Phyto_{chl}(R_{chl}T_{function} + G), \quad (2.34)$$

where changes in phytoplankton chlorophyll content are regulated by the net effect of vertical turbulent transport of biomass; a coefficient of chlorophyll synthesis (ρ_{chl}), which reflects the ratio of energy assimilated to energy absorbed (Geider & MacIntyre, 1996). The losses of $Phyto_{chl}$ include a term for chlorophyll degradation rate (R_{chl}) and grazing (G).

The change in time of external DIN is calculated as:

$$\frac{\partial N}{\partial t} = \frac{\partial}{\partial z} \left(K_Z \frac{\partial N}{\partial z} \right) + \gamma G Phyto_N - uPhyto_C, \quad (2.35)$$

where the cycle of inorganic nitrogen is given by imbalances due to a fraction of grazed phytoplankton added to the DIN pool (i.e. messy eating or inefficient grazing, γG) and losses due to nitrogen assimilation by phytoplankton ($uPhyto_C$).

In the S2P3-photoacclim model the carbon-specific, light-saturated photosynthetic rate depends on the internal nitrogen of phytoplankton described as an f-ratio (f) based on the work of Moore et al. (2001):

$$P_m = P_{max}f, \quad (2.36)$$

where

$$f = \frac{Q - Q_{min}}{Q_m - Q_{min}}.$$

Nitrogen assimilation is calculated as a Michaelis-Menten function based on the development of the f-ratio:

$$u = u_m \left(\frac{1 - f}{1.015 - f} \right) \left(\frac{N}{k_n + N} \right), \quad (2.37)$$

The carbon-specific photosynthesis is a saturating function of irradiance and it is calculated as:

$$\mu = P_m \left(1 - e^{-\left(\frac{\alpha I_{PAR} \theta}{P_m} \right)} \right), \quad (2.38)$$

where P_m is assumed to be a linear function of the ratio $\text{Phyto}_N : \text{Phyto}_C$ as shown in Figure 2.2.

Finally, chlorophyll-*a* synthesis depends on the rates of photosynthesis and light absorption

$$\rho_{chl} = \theta_{max}^N \left(\frac{\mu}{\alpha I_{PAR} \theta} \right). \quad (2.39)$$

Note that in this model, the following condition is met: $R_C = R_N = R_{Chl} = R_{ref} T_{function}$, where R_{ref} (d^{-1}) is a degradation rate constant at a reference temperature.

A list of biological variables and parameters are shown in Tables 2.7 and 2.8.

Variables	Definition	Units
N	External DIN concentration	mg N m ⁻³
$Phyto_C$	Phytoplankton biomass in carbon currency	mg C m ⁻³
$Phyto_{chl}$	Phytoplankton biomass in chlorophyll currency	mg Chl m ⁻³
$Phyto_N$	Phytoplankton biomass in nitrogen currency	mg N m ⁻³
P_m	Carbon-specific rate of photosynthesis	d ⁻¹
Q	Cellular nutrient quota (N:C)	mg N (mg C) ⁻¹
u	Phytoplankton carbon-specific nitrate uptake rate	mg N (mg C) ⁻¹ d ⁻¹
θ	Chlorophyll : phytoplankton carbon ratio	mg Chl (mg C) ⁻¹
μ	Carbon-specific rate of photosynthesis	d ⁻¹
ρ_{chl}	Chlorophyll synthesis regulation term	mg Chl (mg N) ⁻¹

Table 2.7: List of variables, with their definitions and units, for the biological part of the S2P3-photoacclim model.

2.2.4 S2P3 v8.0

Finally, this section describes a new version of the S2P3 v7.0 model where the zooplankton and photo-acclimation components were combined in order to provide a more realistic representation of the ecosystem dynamics. This new version of the model is called S2P3 v8.0.

The biological part of the S2P3 v8.0 model calculates changes in phytoplankton carbon biomass ($Phyto_C$) over time as:

$$\frac{\partial Phyto_C}{\partial t} = \frac{\partial}{\partial z} \left(K_Z \frac{\partial Phyto_C}{\partial z} \right) + Phyto_C (\mu - R_C T_{function} - u\zeta) - I \frac{Z}{Q_P}. \quad (2.40)$$

Phytoplankton biomass is also modelled in terms of internal nitrogen, $Phyto_N$. S2P3 v8.0 calculates $Phyto_N$ as:

$$\frac{\partial Phyto_N}{\partial t} = \frac{\partial}{\partial z} \left(K_Z \frac{\partial Phyto_N}{\partial z} \right) + u Phyto_C - Phyto_N (R_N T_{function}) - IZ. \quad (2.41)$$

The rate of change of phytoplankton biomass in terms of chlorophyll ($Phyto_{chl}$) is described by:

Parameters	Definition	Units	Value
k_n	Half-saturation constant for nitrate uptake	mg N m ⁻³	0.2
P_{max}^{chl}	Maximum value of the carbon-specific rate of photosynthesis	d ⁻¹	1.2
Q_m	Maximum value of the cellular nutrient quota	mg N (mg C) ⁻¹	0.2
Q_{min}	Minimum value of the cellular nutrient quota	mg N (mg C) ⁻¹	0.05
R_C	Respiration rate constant	d ⁻¹	0.1
R_{chl}	Chlorophyll degradation rate constant	d ⁻¹	0.1
R_n	Nitrate remineralisation rate constant	d ⁻¹	0
u_m	Maximum value of the phytoplankton carbon-specific nitrate uptake rate	mg N (mg C) ⁻¹ d ⁻¹	0.6
α^{chl}	Chlorophyll-specific initial slope of the photosynthesis-light curve	mg C (mg Chl) ⁻¹ d ⁻¹ ($\mu\text{E m}^{-2} \text{s}^{-1}$) ⁻¹	1.0x10 ⁵
ζ	Cost of biosynthesis	mg C (mg N) ¹	0
θ_{max}^N	Maximum value of the chlorophyll : phytoplankton nitrogen ratio	mg Chl (mg N) ⁻¹	0.4
$T_{function}$	Temperature-response function	dimensionless	1.0

Table 2.8: List of all the parameters, with their respective definitions, initialised values, and units, in the biological part of the S2P3-photoacclim model. Parameter values of the newly added photo-acclimation parameters are taken from different sources of the literature and they are specified in Chapter 4, Table 4.2.

$$\frac{\partial \text{Phyto}_{chl}}{\partial t} = \frac{\partial}{\partial z} \left(K_Z \frac{\partial \text{Phyto}_{chl}}{\partial z} \right) + u \rho_{chl} \text{Phyto}_C - \text{Phyto}_{chl} (R_{chl} T_{function}) - I \frac{Z}{Q_z} \quad (2.42)$$

The change in time of external DIN is calculated as:

$$\frac{\partial N}{\partial t} = \frac{\partial}{\partial z} \left(K_Z \frac{\partial N}{\partial z} \right) + \gamma_1 IZ + \gamma_2 mZ + \text{Phyto}_N (R_n T_{function}) - u \text{Phyto}_C. \quad (2.43)$$

As described by Franks (2002), zooplankton grazing on phytoplankton response depends on a Holling Type II or Ivlev grazing, with the ingestion rate of zooplankton (I) described as:

$$I = R_m (1 - e^{(-\lambda \text{Phyto}_N)}),$$

where R_m is the maximum ingestion rate (d^{-1}) and λ is the rate at which saturation is achieved with increasing food levels (mmol N m^{-3}) $^{-1}$.

Zooplankton biomass is, therefore, modelled as:

$$\frac{\partial Z}{\partial t} = \frac{\partial}{\partial z} \left(K_Z \frac{\partial Z}{\partial z} \right) + (1 - \gamma_1) IZ - mZ. \quad (2.44)$$

Finally, Figure 2.7 illustrates and summarises each version of the model developed in this work.

		Explicit zooplankton?	
		NO	YES
Photo-acclimation?	NO	S2P3 v7.0	S2P3-NPZ
	YES	S2P3-Photoacclim	S2P3 v8.0

Figure 2.7: Schematic illustration of each version of model development.

Tables 2.9 and 2.10 show the biological variables and parameters of the S2P3 v8.0 model.

Variables	Definition	Units
N	External DIN concentration	mmol N m^{-3}
P_C	Phytoplankton biomass in carbon currency	mg C m^{-3}
P_{chl}	Phytoplankton biomass in chlorophyll currency	mg Chl m^{-3}
P_N	Phytoplankton biomass in nitrogen currency	mmol N m^{-3}
Z	Zooplankton biomass in nitrogen currency	mmol N m^{-3}
I	Ingestion rate of phytoplankton	d^{-1}
P_m	Carbon-specific rate of photosynthesis	d^{-1}
u	Phytoplankton carbon-specific nitrate uptake rate	$\text{mmol N (mg C)}^{-1} \text{d}^{-1}$
Q_P	Cellular nutrient quota (N:C)	$\text{mmol N (mg C)}^{-1}$
Q_Z	Internal nitrogen : phytoplankton chlorophyll ratio	$\text{mmol N (mg Chl)}^{-1}$
θ	Chlorophyll : phytoplankton carbon ratio	$\text{mg Chl (mg C)}^{-1}$
μ	Carbon-specific rate of photosynthesis	d^{-1}
ρ_{chl}	Chlorophyll synthesis regulation term	$\text{mg Chl (mmol N)}^{-1}$

Table 2.9: List of variables, with their definitions and units, for the biological part of the S2P3 v8.0 model.

Parameters	Definition	Units	Value
k_n	Half-saturation constant for nitrate uptake	mmol N m ⁻³	0.014
P_{max}^{chl}	Maximum value of the carbon-specific rate of photosynthesis	d ⁻¹	1.2
Q_m	Maximum value of the cellular nutrient quota	mmol N (mg C) ⁻¹	0.014
Q_{min}	Minimum value of the cellular nutrient quota	mmol N (mg C) ⁻¹	0.0035
R_C	Respiration rate constant	d ⁻¹	0.1
R_{chl}	Chlorophyll degradation rate constant	d ⁻¹	0.1
R_n	Nitrate remineralisation rate constant	d ⁻¹	0
u_m	Maximum value of the phytoplankton carbon-specific nitrate uptake rate	mmol N (mg C) ⁻¹ d ⁻¹	0.004
α^{chl}	Chlorophyll-specific initial slope of the photosynthesis-light curve	mg C (mg Chl) ⁻¹ d ⁻¹ (W m ⁻²) ⁻¹	1.99x10 ⁻⁶
ζ	Cost of biosynthesis	mg C (mmol N) ⁻¹	0
θ_{max}^N	Maximum value of the chlorophyll : phytoplankton nitrogen ratio	mg Chl (mmol N) ⁻¹	5.6
$T_{function}$	Temperature-response function	dimensionless	1.0
m	Loss rate of zooplankton due to predation and physiological death	d ⁻¹	0.05
R_m	Maximum ingestion rate of phytoplankton	d ⁻¹	2.5
γ_1	Grazing inefficiency or 'messy feeding' (0.0-1.0), returns a fraction of grazed material back into the DIN pool	dimensionless	0.2
γ_2	Fraction of dead zooplankton (0.0-1.0) that goes into the sediments	dimensionless	0.5
λ	Rate at which saturation is achieved with increasing food levels	(mmol N m ⁻³) ⁻¹	0.053

Table 2.10: List of all the parameters, with their respective definitions, initialised values, and units, for the biological part of the S2P3 v8.0 model.

2.3 Meteorological forcing

Daily meteorological data, provided by the National Centers for Environmental Predictions (NCEP) Reanalysis data (<http://www.esrl.noaa.gov/psd>) was used to force the model at the CCS site, located at $49.4^{\circ}N$, $8.6^{\circ}W$. The data is provided in a 2.5° global mesh, where one grid square is used for the CCS location and taken from 1st January 1965 to 31st December 2015 (Figure 2.8). Wind speed (m s^{-1}), cloud coverage (%), air temperature ($^{\circ}\text{C}$), and relative humidity (%) variables from this dataset were all used to force each model version. This dataset has been used by Marsh et al. (2015) using this same model in different temperate shelf sea locations, showing a reasonable agreement with observations in those locations, with differences accounted, but suggested to be due to the photo-acclimation process not being included, influence of riverine inputs (East China and Yellow Seas), and advective fluxes being relevant in some of those locations (e.g. English Channel). Therefore, the use of the NCEP Reanalysis data has demonstrated to be a good input of forcing for the S2P3 v7.0 model. However, here it is suggested that in future research, this dataset could be downscaled into higher resolution to, specially, account for the local changes of wind speed, air temperature, and relative humidity. Local sources of observations to be compared with this dataset could be obtained from the Western Channel Observatory (https://www.westernchannelobservatory.org.uk/pml_weather_station/).

In the meteorological data there is daily to seasonal to inter-annual variability, as shown in Figure 2.9. Wind speed (Figure 2.9a) shows seasonal variability with higher values during wintertime and a slight decrease in frequency and magnitude of extreme events from the start of spring and during summer. Cloud coverage (Figure 2.9b) shows a decrease during springtime, ranging from $\sim 50\%$ to $\sim 40\%$ at the beginning of the year and increasing towards the end of the year ($\sim 60\%$) with more cloudy days. Air temperature shows a strong seasonality (Figure 2.9c), which it is repeated each year with an increase close to spring (approximately 15°C) and lower values from the start of autumn, reaching $\sim 9^{\circ}\text{C}$ at the end of the year. This strong seasonality found only in air temperature might be due to wind speed, cloud cover, and relative humidity are driven by variables of the weather system that are highly variable, contrary to the main driver of air temperature which is the Sun, also showing a marked seasonality throughout the year. Finally, relative humidity (Figure 2.9d) shows daily variability but there is only a weak observable seasonal pattern

for this parameter, maintaining an almost constant level throughout the year.

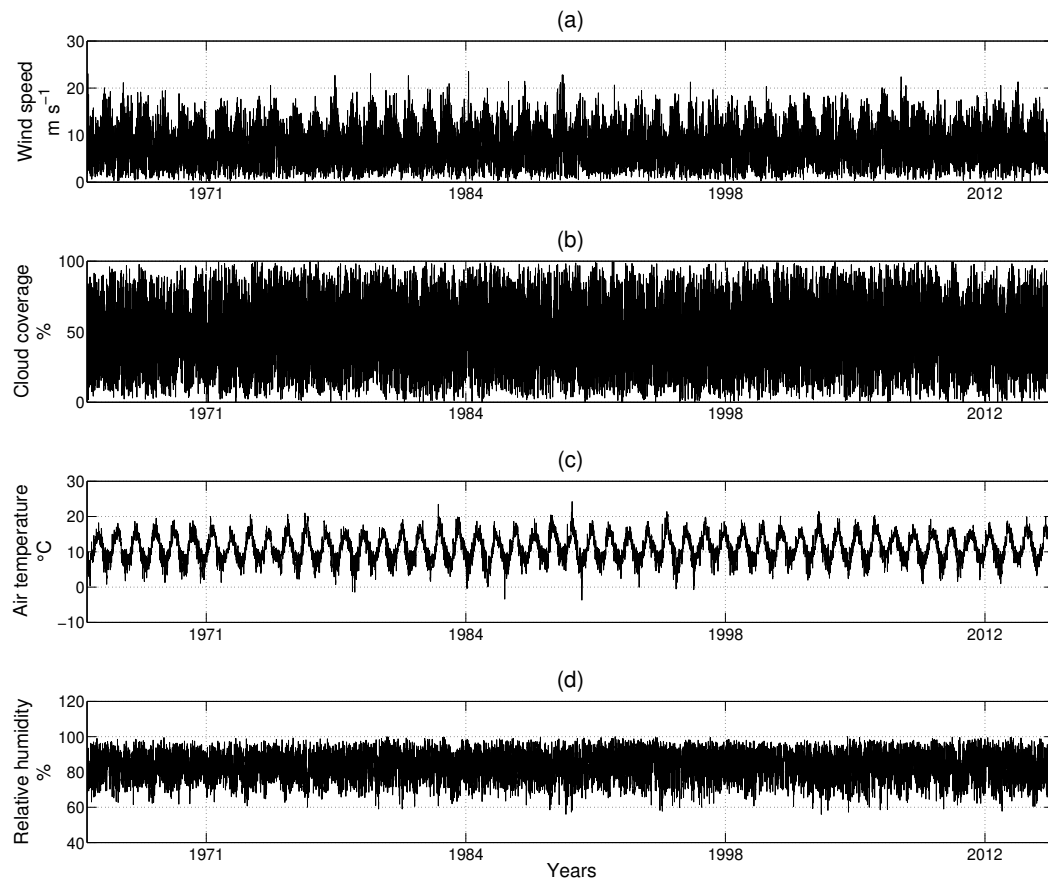


Figure 2.8: Whole record of the meteorological forcing used in the S2P3 model from the start of the year 1965 to the end of the year 2015, showing (a) wind speed, (b) cloud coverage, (c) air temperature, and (d) relative humidity.

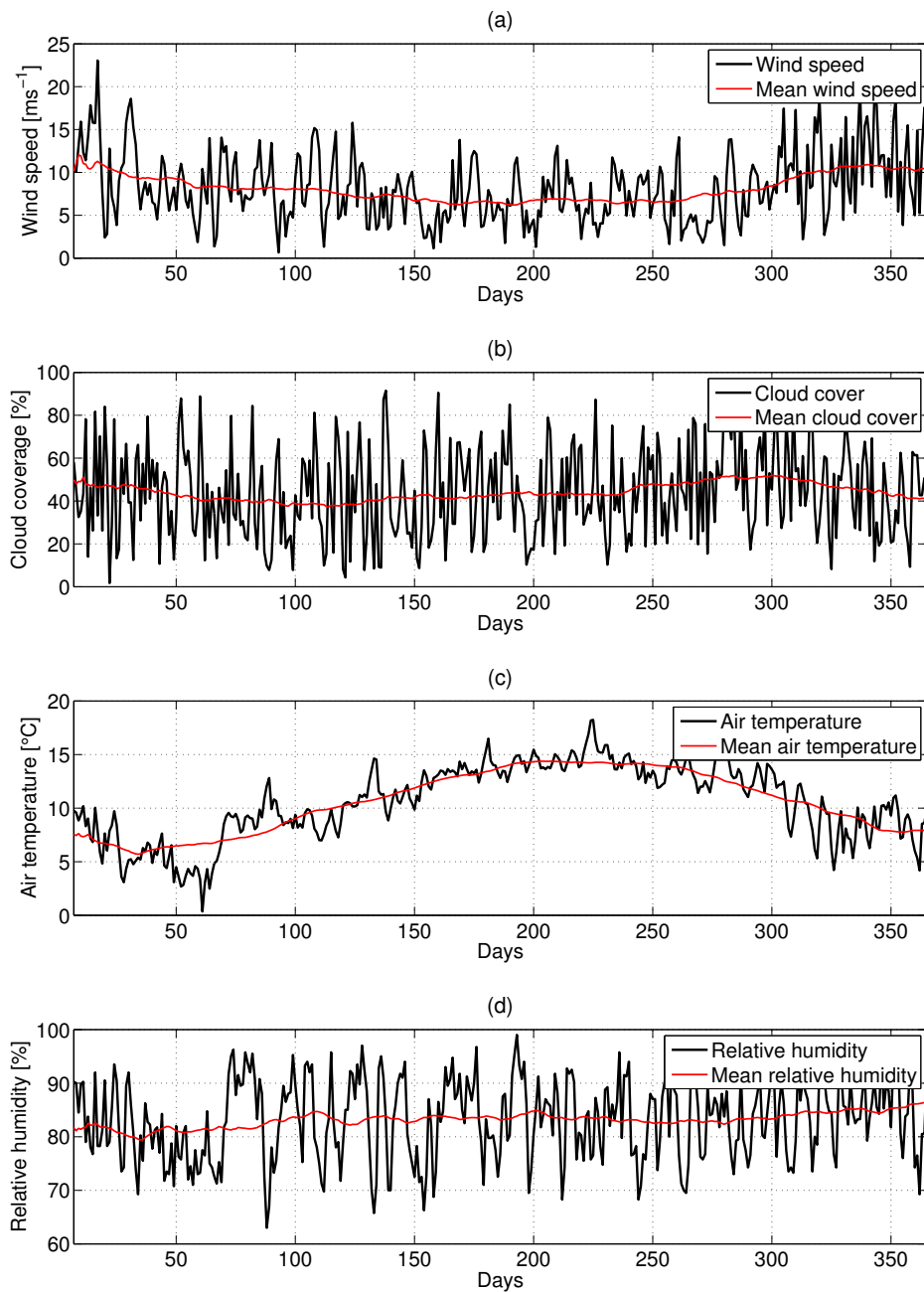


Figure 2.9: Seasonal variability of daily time-series for meteorological forcing (black line) and a running mean (red line) with a span of 80 days in every case. Time-series representing the year 1965 as an example for: (a) wind speed (m s^{-1}), (b) cloud coverage (%), (c) air temperature ($^{\circ}\text{C}$), and (d) relative humidity (%).

Annual means were calculated from 1965 to 2015 in order to observe the inter-annual variability of each meteorological variable (Figure 2.10). A linear regression was performed to estimate trends over time, and a Pearson correlation coefficient was calculated (with 95% confidence interval), between the annual mean of each meteorological variable and time. It was found that wind speed increases over time at a rate of $0.0145 \text{ m s}^{-1} \text{ yr}^{-1}$ ($r^2=0.2422$, $p < 0.05$; Figure 2.10a) with strong variability during the years 1970 to 1975. Air temperature also increases over time at a rate of $0.0143 \text{ }^\circ\text{C yr}^{-1}$ ($r^2=0.2273$, $p < 0.05$; Figure 2.10c), ranging from an initial value of $\sim 10.5 \text{ }^\circ\text{C}$ (year 1965) to $\sim 12 \text{ }^\circ\text{C}$ (year 2015). On the other hand, there are no significant trends over time for either cloud coverage ($r^2=0.0033$, $p > 0.05$; Figure 2.10b) or relative humidity ($r^2=0.0004$, $p > 0.05$; Figure 2.10d).

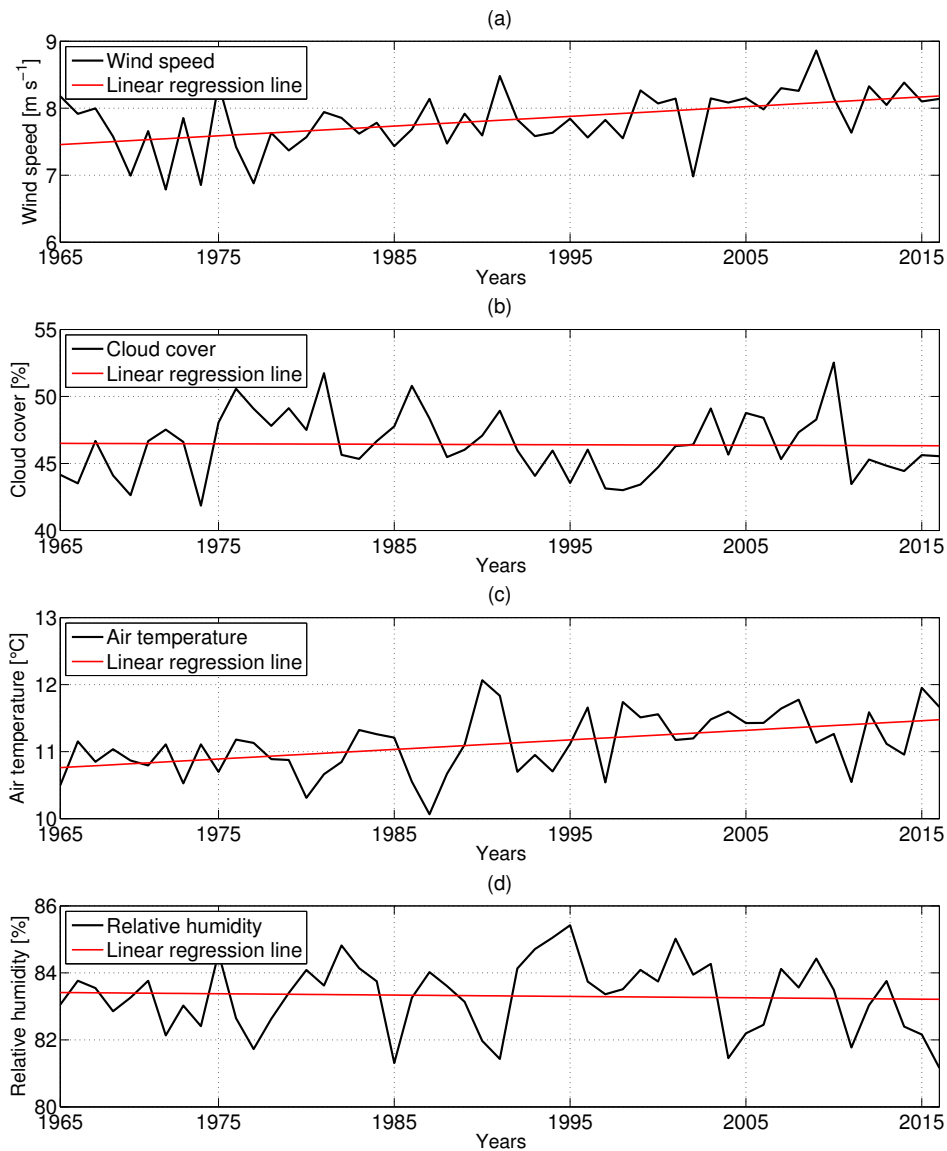


Figure 2.10: Annual means from daily data showing inter-annual variability throughout 1965 to 2015 for each meteorological variable (black lines) and a linear regression line (red lines) fitted in each case for (a) wind speed (m s^{-1}), (b) cloud coverage (%), (c) air temperature ($^{\circ}\text{C}$), and (d) relative humidity (%).

2.4 Model setup for the CCS location

The model setup consists of defining a local depth and tidal currents. The tidal components consists of the u-component (semi-major axis) and the v-component (semi-minor axis) for the M_2 , S_2 , and N_2 tidal constituents (see Table A.1). This data was obtained from a fine mesh (12km horizontal resolution) covering the UK shelf. Tidal currents are predicted using the Proudman Oceanographic Laboratory Coastal Ocean Modelling Systems (POLCOMS) 3-D shelf model using 42 vertical levels in s-coordinates to allow increased resolution near the surface and bed in deeper water (Holt et al., 2009; Wakelin et al., 2009), with an output extracted for the CCS location. Tide components included in the S2P3 v7.0 model will, therefore, simulate the spring-neap tidal cycle by using the u and v components of each tidal constituent, however, the tidal phases are set to zero, which is not doing a well representation of tides in the shelf sea, which could produce changes in the timing of stratification or the spring bloom from up to a week.

The model is initialised on 1st January of the first year of simulation with a temperature of 10.10 °C at all depths, and water column presumed mixed throughout. The setup of initial values for physical and biological parameters in this study is consistent with former studies in UK shelf seas (Marsh et al., 2015) but using tide and water depth information specific to the CCS location. These initial values are only set up at the start of each simulation and do not reset in between years.

2.5 Spin-up and resolution of the model

Spin-up is the time taken for a model to reach a state of statistical equilibrium under the applied forcing. The S2P3 model shows a stabilisation time of five years (Figure 2.11). This is why five climatological years were added to each meteorological variable prior the start of the year 1965. Therefore, experiments were run during the years 1960 - 2015 but every analysis of the output starts from 1965 so the spin-up time is neglected.

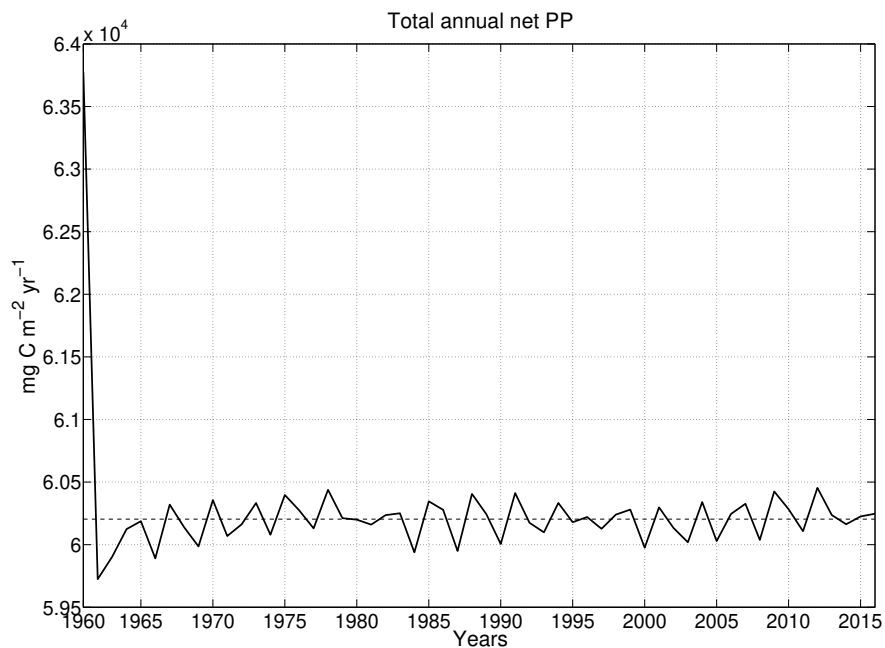


Figure 2.11: Total annual NPP ($\text{mg C m}^{-2} \text{ yr}^{-1}$) calculated from the start of the year 1960 to the end of the year 2015. First five years show the spin-up of the S2P3 v7.0 model. Dashed black line represents the mean of the time-series from 1965 to 2015 (i.e. spin-up is not included).

In terms of the model resolution, experiments were conducted with the same model set up as in the S2P3 v7.0 model but with different depth resolutions. Four model experiments of 1m, 2m, 7m, and 14m depth resolutions can be taken as examples (Figure 2.12). As shown in Figure 2.12, when the model is run with a coarser resolution, the total annual NPP ($\text{mg C m}^{-2} \text{ yr}^{-1}$) is higher. Therefore, it is important to choose an appropriate vertical resolution as it can alter the dynamics of vertical processes in the shelf sea. For example, if the model has a vertical resolution of 14m, each grid cell can overestimate some processes and features in the water column such as the mixed layer depth (MLD), with higher productivity being modelled for an unrealistically deep MLD. Furthermore, Figure 2.12 shows that there are differences between total annual NPP values when the model is set with different vertical resolution, showing that differences with the finest resolution (1m) are less when a 2m vertical resolution is chosen in comparison to coarser resolutions (e.g. 7m, 14m) that show larger differences. However, there are still observable differences in NPP between the 1m and 2m vertical resolution. Therefore, a depth resolution of 1m is

considered for every experiment developed in this work, which is also the highest resolution that can be calculated without blowing-up the model (see CFL condition, eq. 2.16).

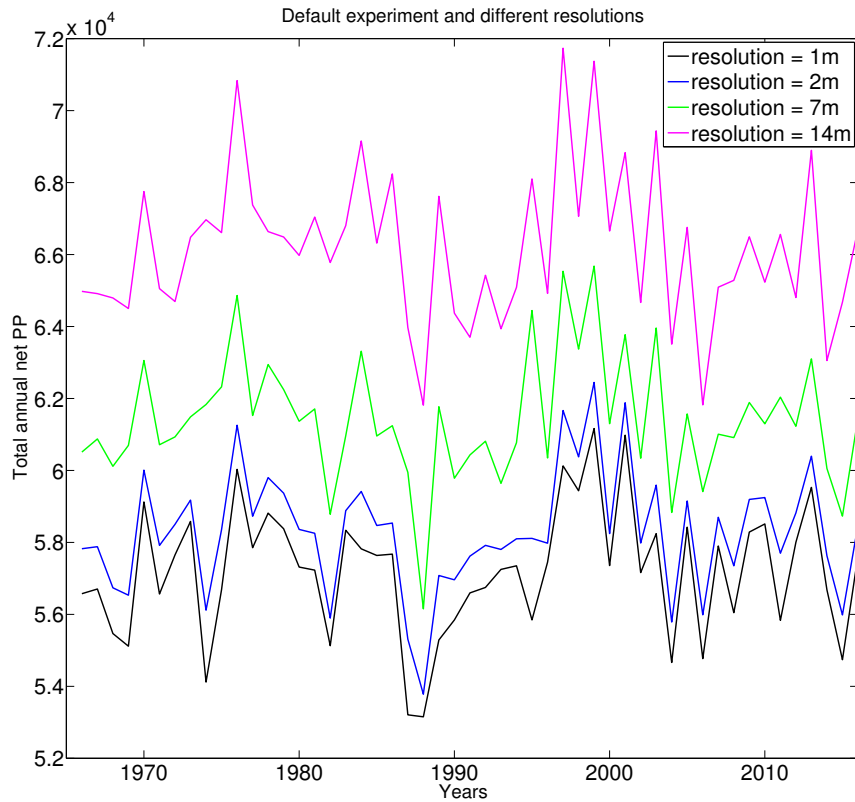


Figure 2.12: Total annual NPP ($\text{mg C m}^{-2} \text{ yr}^{-1}$) calculated from daily time-series during the years 1965 to 2015 with four different resolutions: black line for 1m, blue line for 2m, green line for 7m, and magenta line for 14m.

Chapter 3

Meteorological controls on inter-annual variability in onset and duration of the spring bloom and summer growth in the Central Celtic Sea using a single 1-D model

3.1 Abstract

A single one-dimensional biological and physical coupled model (S2P3 v7.0) is used to explore the effect of meteorology on PP in the CCS, a temperate shelf sea of the NW European Shelf. A default simulation was conducted using observational data to force the model including air temperature, cloud coverage, wind speed, and relative humidity. The model was run between the years 1965 - 2015 and a mean total annual NPP of $\sim 61 \text{ g C m}^{-2} \text{ yr}^{-1}$ was found over those 51 years, with results showing that meteorological forcing produces inter-annual variability in phytoplankton production. Therefore, targeted experiments and a control experiment (i.e. no inter-annual variability of meteorological forcing) were performed. The model experiments provide an understanding of the effects of each meteorological variable, showing that over the 51 years of simulation, wind speed has the largest effect on the inter-annual variability of total annual NPP. Based on these results, a knockout wind experiment was performed to investigate how wind speed affects the timing, magnitude, and duration of the spring phytoplankton bloom as well as summer growth. Wind speed produces variability in the onset of thermal stratification and, consequently, on the timing of the spring phytoplankton bloom, showing that in a long-time scale (1965 - 2015), the high-frequency variability of wind speed is delaying the spring phytoplankton bloom, driving 2 -3 times more NPP variability than the other meteorological variables. A significant correlation between the total spring NPP and the onset of the spring phytoplankton bloom was found ($r^2 = -0.73$, $p < 0.05$), suggesting that a later spring bloom will also

be less productive, being primarily a consequence of the inter-annual variability in wind speed.

3.2 Introduction

This chapter is divided into four sections. The first section is an introduction that provides background knowledge about the effects of meteorological variability in temperate shelf seas and their observed relationship with inter-annual variability of PP, timing, magnitude, and duration of the spring bloom, as well as summer production. The second section describes the model experiments developed to analyse the main questions of this chapter, providing information about the validation of the model in the CCS location over the years 1965 to 2015. The third section is a description of the results found. Finally, the last section provides a discussion and conclusions from the main results, stating the open questions to be studied in future research.

3.2.1 Spring bloom and meteorological drivers

To understand the effect that meteorology plays on the spring phytoplankton bloom, it is necessary to have an understanding of the annual and inter-annual cycles of the processes that drive seasonal stratification and, therefore, the spring bloom. As explained in Chapter 1, seasonal stratification in temperate shelf seas is modulated by a competition between buoyancy inputs due to surface heating and cooling (or freshwater inputs in areas near to land) and mixing by tides and winds.

In temperate shelf seas, the initiation, development, and termination of the spring phytoplankton bloom are controlled by various factors (Sverdrup, 1953; Riley, 1946, 1942). One of these factors is the different heat fluxes that combined create a vertical heat flux at the sea surface, which varies over the year. Its primary driver is the input of short wavelength radiation from the sun (Q_{SW}), with a fraction being reflected and another being absorbed in the ocean, allowing heating of the surface waters, but ultimately returned back to the atmosphere through the surface as long wave back radiation (Q_{LW}), or as a combination of heat fluxes due to evaporation (Q_{lat}) and sensible heat transfer by conduction (Q_{sens} ; Figure 3.1).

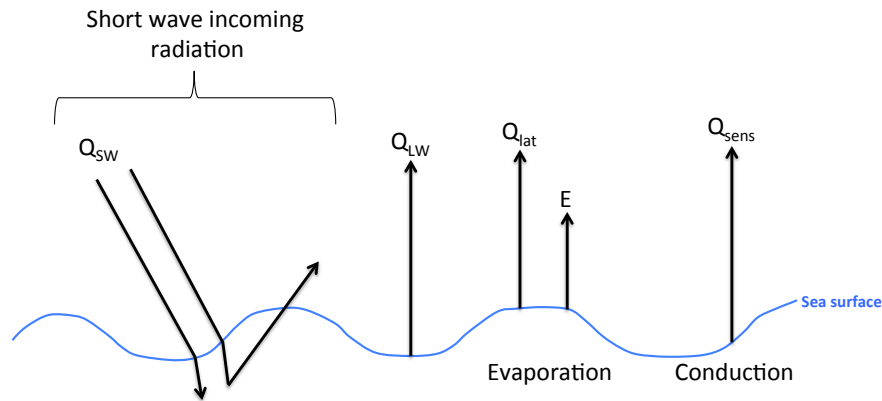


Figure 3.1: Heat fluxes across air-sea boundary showing the incoming short wave radiation (Q_{SW}) representing absorbed and scattered photons. There is long wave radiation (Q_{LW}) emitted from the sea surface, evaporation (E) is related to contributions from latent heat flux (Q_{lat}), and exchange of heating by conduction (Q_{sens}). Diagram adapted from Simpson & Sharples, 2012.

The combination of each heat flux component in temperate latitudes determines the net heat flux which will vary seasonally (Figure 3.2), with an increase in the heat input (Q_{SW}) during summer months and a minimum over winter. Q_{LW} , on the other hand, does not show strong seasonality because it is proportional to the small changes of the sea surface temperature (in Kelvin units) in comparison to the changes of temperature in the atmosphere. The contribution of the evaporation and conduction components to the net heat flux is small but tends to reach larger values in winter months when winds are generally stronger (Simpson & Sharples, 2012).

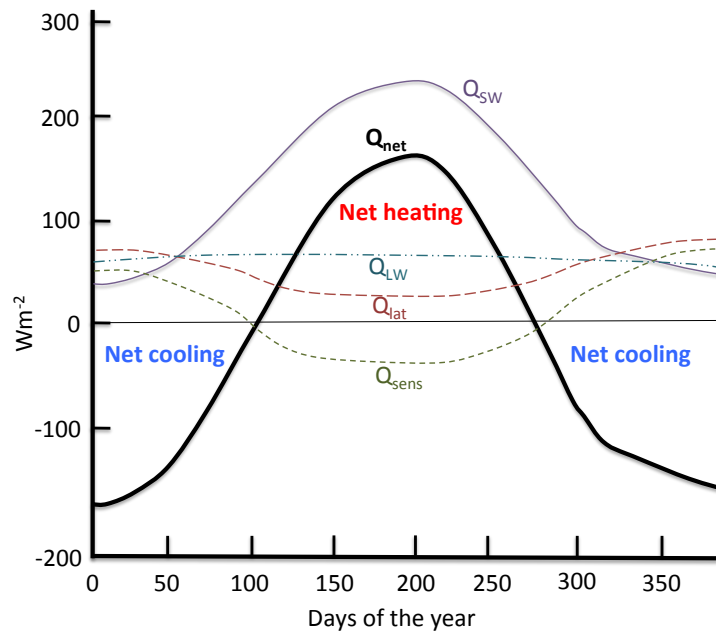


Figure 3.2: Idealized seasonal cycles of vertical heat fluxes at temperate latitudes over one year, showing each component of the net heat flux (units of W m^{-2}), with net cooling periods during winter months, and net heating over spring and summer months.

At the start of the year, the water column is completely mixed but towards spring the increase of solar radiation heats the surface waters, making them more stable by lowering the density of the water at the surface and reducing the convective mixing (Taylor & Stephens, 1993). The vertical net heat flux becomes positive in early spring, producing a state of net heating in the surface waters, stabilising the water column and allowing the start of thermal stratification, intensifying the net growth rate of phytoplankton due to increased irradiance and initiating the spring phytoplankton bloom (Kanda et al., 1989). The spring phytoplankton bloom will terminate because of the depletion of inorganic nutrients at the surface and due to grazing by zooplankton. Finally, thermal stratification is destroyed in late autumn by convective overturning and increasing wind speeds, which together force vertical mixing of the upper water column resulting in a supply of nutrients to the photic zone. However, long and frequent wind events inhibit the phytoplankton bloom from continuing (Kasai et al., 1997). Besides, during the winter period, the mixed layer is relatively deep and phytoplankton spend a large proportion of their time in waters with insufficient

light to support photosynthesis (Smith et al., 2015).

The key physical drivers of phytoplankton production include tidal and wind forcing, and surface buoyancy fluxes from the atmosphere. These factors affect the physical environment by altering stratification, TKE, SST, and the MLD (Barton et al., 2014). These physical drivers impact the light and nutrients received by phytoplankton in the ocean surface (Follows & Dutkiewicz, 2001; Sverdrup, 1953). The interactions and imbalances in the predator-prey relationship between zooplankton and phytoplankton will also be affected by atmospheric forcing (Behrenfeld & Boss, 2014; Behrenfeld, 2010). Grazing by zooplankton is also an important loss factor for phytoplankton biomass (Kasai et al., 1997; Frost, 1987; Sverdrup, 1953; Riley, 1946), yet there is a limited understanding about the impacts of long-term variability in meteorology. Hence, variability in the timing and intensity of the spring phytoplankton bloom will affect the population dynamics of higher trophic levels, and the effects will persist beyond the bloom period. It is necessary to understand the processes regulating the dynamics of the spring phytoplankton bloom to quantify and model the dynamics of pelagic ecosystems (Waniek, 2003).

This chapter aims to investigate the relationship between phytoplankton production in the CCS and meteorological processes. This will be achieved by using a 1-D model (S2P3 v7.0), with different experiments developed to compare and to quantify the importance of meteorological variables in terms of PP variability. The main focus of this study is a seasonally stratified shelf sea, therefore observations from this location are used to validate the model.

The general hypothesis of this work is:

- PP varies between years due to inter-annual variability in meteorological forcing.

The sub-hypotheses of this work are:

- Wind speed has the largest effect on inter-annual variability of total annual PP.
- Wind speed impacts PP moderating the timing, duration, and extent of the spring bloom.
- Variations in wind speed produce inter-annual variability in summer stratification and the SCM.

Following these hypotheses, the main objective is:

- Use a 1-D model forced using meteorological data from 1965 to 2015 to find correlations between each component of the meteorology and the total annual NPP.
- Use a 1-D model forced using meteorological data from 1965 to 2015 and simulate targeted experiments to identify the importance and role of each of the four components of meteorological forcing (wind speed, air temperature, cloud coverage, and relative humidity) on PP.
- Find the direct and indirect control, in terms of physics, on PP and how do they operate.

3.3 Methods

This section describes each experiment, simulated by the S2P3 v7.0 model at the CCS location from 1965 to 2015, used to investigate the effect of meteorological forcing on the inter-annual variability of PP. The model simulations section is divided into three parts, the first one describing a “default simulation” used to address the main hypothesis of this project by comparing the effects of each meteorological variable in terms of the onset of the spring phytoplankton bloom and NPP. The second part describes a series of simulations called “control-based experiments”, which consider meteorological forcing without inter-annual variability to understand which of wind speed, cloud cover, air temperature, or relative humidity has the largest effect on phytoplankton production. The third part explains a final simulation called the “knockout-wind experiment”, based on the sub-hypothesis that wind speed has the largest effect on total annual NPP inter-annual variability. Finally, there is a section that validates the model with CTD and time-series observations.

3.3.1 Model simulations

All the experiments use tidal forcing calculated from the POLCOMS model (Artioli et al., 2012; Holt et al., 2012; Wakelin et al., 2012; Holt et al., 2009; Wakelin et al., 2009) and meteorological forcing between the years 1965 - 2015 at the CCS location. Values for the tidal components used in the simulations are listed in Table A1.

3.3.1.1 Default simulation

A default simulation was calculated with the S2P3 v7.0 model using meteorological forcing (see Chapter 2, section 2.3) with variability at a range of temporal scales. For Figure 3.3, black arrows represent the modal value (tallest bar in each histogram); these values are different from the mean (red arrow) and median (green arrow) of the data. Wind speed (Figure 3.3a) shows a typical Weibull distribution, emphasising that during the year strong gale force winds are rare, while moderate and fresh winds are quite common. Cloud cover (Figure 3.3b) shows a similar distribution than wind speed (right-skewed distribution), with completely cloudy days being more rare than partially clouded days. On the other hand,

air temperature shows a normal distribution during the year (Figure 3.3c) and relative humidity shows a left-skewed distribution, i.e. there are a higher proportion of days during the period with higher values of relative humidity (Figure 3.3d). The statistical test used to check each meteorological variable was the Lilliefors test (Lilliefors, 1967), which tests the closeness of fit to a normal distribution ($\alpha = 0.05$ in every experiment tested).

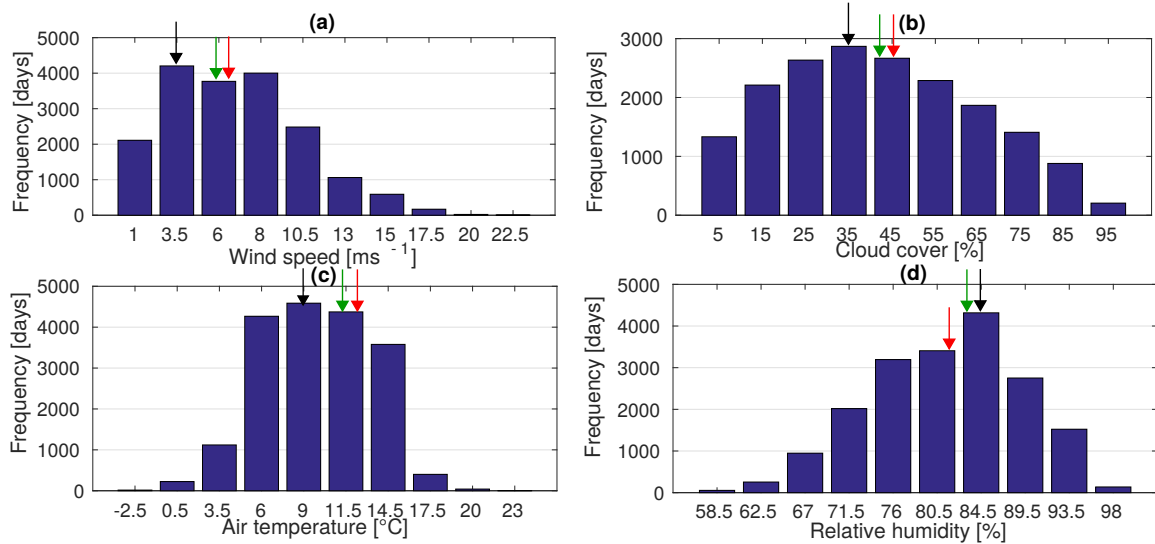


Figure 3.3: Histograms of daily meteorological data taken from the NCEP Reanalysis. Each meteorological variable is taken from the start of the year 1965 to the end of the year 2015. The black arrows represent the modal value in each histogram, the green arrows are the median, and the red arrows are the mean for (a) wind speed (m s^{-1}), (b) cloud coverage (%), (c) air temperature ($^{\circ}\text{C}$), and (d) relative humidity (%).

3.3.1.2 Control-based experiments

A “control experiment” was simulated, including climatological wind speed, air temperature, cloud coverage, and relative humidity. To obtain the climatology of every meteorological variable, a seasonal cycle was considered from 1st January to 31st December from 1965 to 2015 and a mean of the seasonal cycle was calculated over those years to remove inter-annual variability in the forcing of the model.

The control experiment was compared to the other four control-based experiments for which the effect of each meteorological component was identified in turn. The “wind-only experiment” involves only inter-annual variability for wind speed, but all the other meteorological

variables are the same as in the control experiment. The three other experiments follow the same procedure but for each of the three remaining variables, where the “cloud-only experiment” only considers inter-annual variability of cloud cover in the meteorological forcing; the “temperature-only experiment” has only inter-annual variability for the air temperature; and finally, the “humidity-only experiment” considers only inter-annual variability for relative humidity (Table 3.1). In each case, the remaining meteorological components were the same as the control experiment (i.e. had no inter-annual variability).

With the default experiment, control experiment and the other four control-based experiments, it is possible to compare their PP to understand which meteorological variable has a greater effect on phytoplankton productivity at the CCS location.

3.3.1.3 Knockout-wind experiment

Following the main hypothesis of this project and the different sub-hypotheses developed, this simulation was created to analyse the effect of wind speed on the seasonal and inter-annual variability of PP. The “knockout-wind experiment” considers wind speed without inter-annual variability (climatology), while all the other meteorological variables (cloud coverage, air temperature, and relative humidity) are the same as in the observations used to force the default experiment.

Table 3.1 illustrates how each experiment in this chapter has been developed in terms of the meteorological forcing including wind speed, cloud coverage, air temperature, and relative humidity. Climatological variables are represented in red, while the meteorological variables from the NCEP Reanalysis data are represented in blue as observed variables.

Run name	Wind speed	Cloud cover- age	Air tempera- ture	Relative Hu- midity
Default	Observed	Observed	Observed	Observed
Control	Climatology	Climatology	Climatology	Climatology
Wind-only	Observed	Climatology	Climatology	Climatology
Cloud-only	Climatology	Observed	Climatology	Climatology
Temperature-only	Climatology	Climatology	Observed	Climatology
Humidity-only	Climatology	Climatology	Climatology	Observed
Knockout-wind	Climatology	Observed	Observed	Observed
M2-only	Climatology	Climatology	Climatology	Climatology
Spring-neap	Climatology	Climatology	Climatology	Climatology

Table 3.1: List of each experiment developed with the S2P3 v7.0 and the differences for the meteorological forcing.

3.3.2 Validation of the model

Experiments from the S2P3 model have been conducted in former studies in UK shelf seas. Sharples et al. (2006), validated this model in the NW North Sea using short- and long-term datasets from mooring deployments. The model was found to correctly simulate the onset of stratification during 2001. The model was also compared to data from the International Council for the Exploration of the Sea (ICES) during 1974 - 2003, finding that the surface temperature calculated from the model and the ICES data is strongly correlated ($r^2 = 0.80$, $p < 0.05$), with warmer modelled temperatures than ICES data during summer but a good agreement in modelled winter temperatures: the mean annual rate of change of winter temperature produced by the model (0.05 ± 0.01 °C yr⁻¹) is consistent with that from the ICES observations (0.04 ± 0.01 °C yr⁻¹). On the other hand, the model tends to under-predict the bottom water temperature in late summer, due to the influence of local advection in the North Sea, as this has not been taken into consideration in the model.

Marsh et al. (2015) validated the S2P3 model in two different locations in the Western English Channel using weekly and monthly time-series from the Western Channel Observatory. There was good agreement between the model and observations for surface temperature and bottom temperature, although some differences were found due to the influence of freshwater in the Western English Channel because the model does not consider salinity as a state variable, being constant throughout depth and across the time series.

In this chapter, the model was validated for the CCS location using the default experi-

ment and available observations from buoys and CTD casts from the UK SSB programme (<https://www.uk-ssb.org>). Observations were collected throughout the NW European shelf during the spring of 2014 and 2015 as part of the research cruise expeditions DY029 (Poulton, 2015) and DY033 (Humphreys & Moore, 2015) (Figure 3.4). Samples were collected in the CCS location during the pre-bloom, peak bloom, and post-bloom conditions of the area (Figure 3.4a). Time-series of surface temperature ($^{\circ}\text{C}$) and surface chlorophyll-*a* concentrations (mg Chl m^{-3}) from long-term mooring deployments including the CCS Carbon and Nutrient Dynamics and Fluxes over Shelf Systems (CaNDyFloSS; Hull et al., 2017) and Smartbuoy (Mills et al., 2003) were also collected. The phytoplankton community fluorescence from the water samples was calculated as a proxy for chlorophyll-*a* and were calibrated taking into account photochemical quenching. Photochemical quenching occurs when applying light to the samples; the chlorophyll fluorescence has an initial rise but then it declines (within less than a second) and finally increases again over a period of several minutes. For this study, day time data was removed.

CTD (stainless and titanium) casts were performed in the different locations of the NW European shelf from the CCS location to the shelf break (Figure 3.4b,c), with discrete samples of temperature, DIN, and chlorophyll-*a*. In the CCS location, the CTD samples were collected from pre-dawn to midday with a 1m vertical resolution over the whole water column (~ 140 m depth). CTD casts for the CCS location were chosen to validate the model during spring and summer.

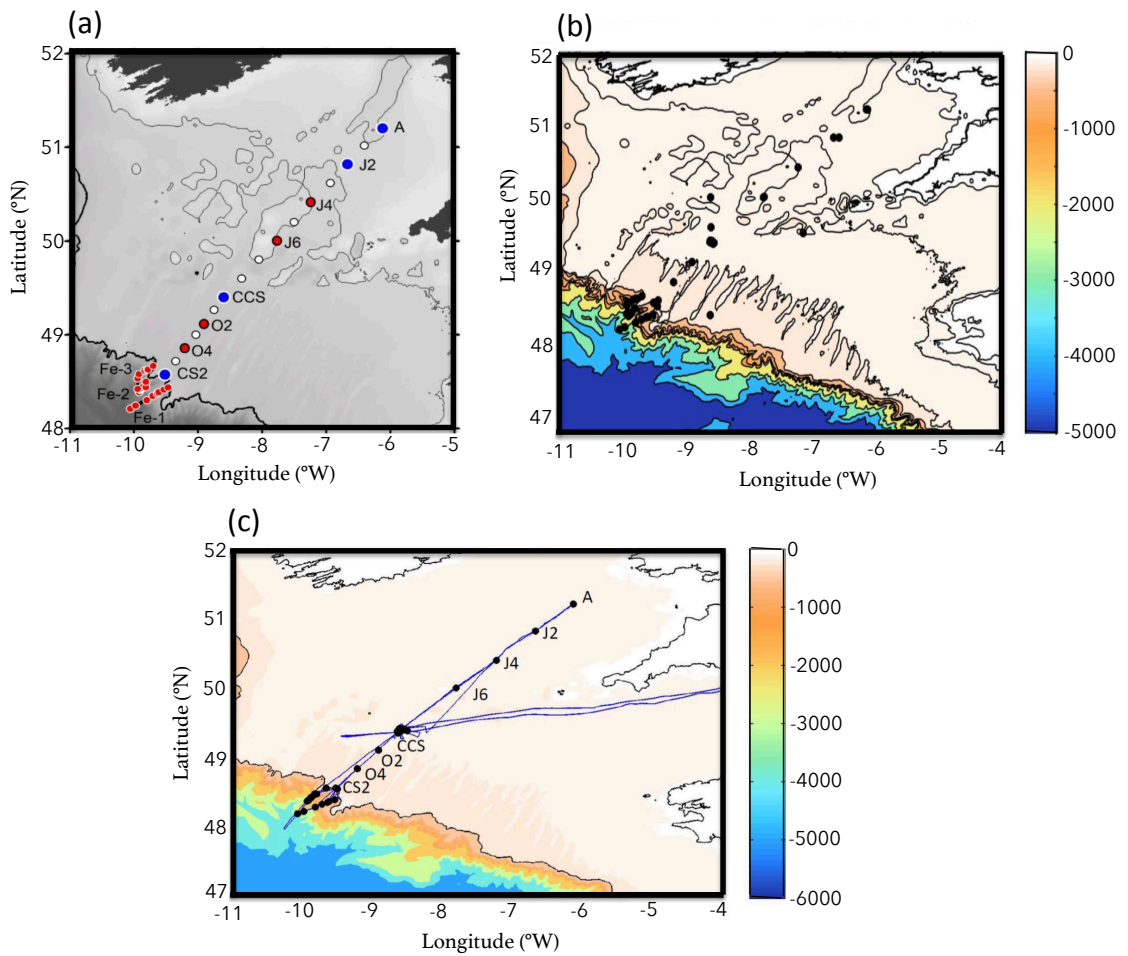


Figure 3.4: (a) DY029 cruise sampling sites, (b) Map of all CTD cast locations (black dots) from DY029 cruise and bathymetry, and (c) DY033 cruise track (blue line), CTD sampling stations (black dots), and bathymetry of the Celtic Sea.

As part of the SSB research programme, buoys (Candyfloss Smartbuoy) were set up at the CCS location (49.4°N, 8.6°W, depth 145.8 m), gathering data for 5 minutes every 30 minutes, with sensors validated against in-situ samples during deployment and recovery (Hull et al., 2017). For this work, measurements of surface temperature and surface chlorophyll-*a* obtained from the buoy were compared to the model, showing good agreement with the physical model (Figure 3.5a) and a strong correlation with surface temperature (Figure 3.5b; $r^2 = 0.91, p < 0.05$), although showing that the model calculates a lower sea surface temperature than the buoy observations during spring and summer months of the year 2014 with a difference of approximately 2° C. The magnitude of surface chlorophyll-*a* during spring are well represented by the model (Figure 3.5c), but there is not significant corre-

lation found between the model and observations for surface chlorophyll-*a* (Figure 3.5d; $r^2 = 0.06$, $p > 0.05$). However, this lack of correlation can be driven by the differences in the timing of the spring phytoplankton bloom, with the model having later blooms than the observations (Figure 3.5c). Therefore, a correlation is applied for a lagged time-series observations, finding that if the buoy is lagged by 30 days, then observations and the model are significantly correlated in terms of surface chlorophyll ($r^2 = 0.13$, $p < 0.05$), although this correlation is weak. Moreover, for a 45 day lag, correlations are significant and stronger $r^2 = 0.31$, $p < 0.05$. Another reason for the mismatch in terms of the timing of the spring bloom between the model and the buoy data is that S2P3 v7.0 is using tidal constituents with their phases set to zero, which is not what actually happens in reality. This calculation of the tides in the model will produce some differences in the onset of thermal stratification and, therefore, in the onset of the spring bloom, accounting for an error that might vary from a day up to a week. Consequently, the onset of the spring phytoplankton bloom plays a role in the comparison to buoy observations, but differences between winter months remain. The model also shows a good representation of the vertical structure of the CCS location (Figure 3.6) during spring and summer. During spring, observations show a later development of the stratified period (Figure 3.6a), a later onset of the spring phytoplankton bloom (Figure 3.6b; ~ 15 days), and a later depletion of DIN at the surface (Figure 3.6c). During summer, temperature profiles from observations show a clear increase in surface temperature but this is less marked in the model (Figure 3.6d). The development of an SCM is shown in the observations while in the model there seem to be high values of chlorophyll-*a* at the surface (Figure 3.6e). On the other hand, there is a depletion of nutrients at the surface shown by both the CTD observations and the model (Figure 3.6f).

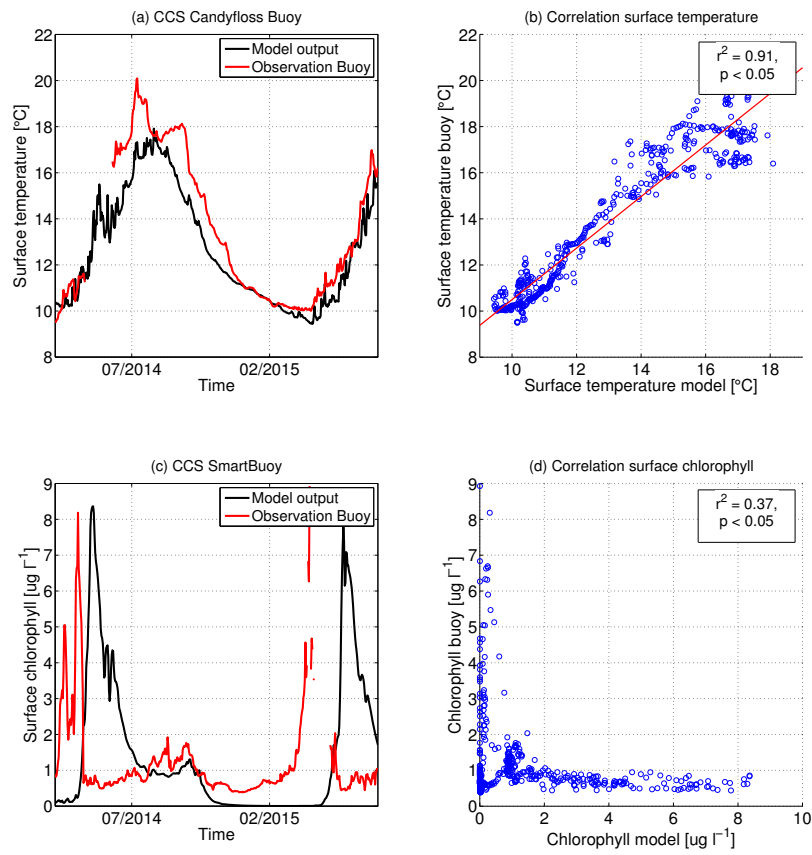


Figure 3.5: Comparison to data of the S2P3 v7.0 model using the output of the default experiment for the CCS location (black lines) and time-series from buoy observations (red lines) from April 2014 to August 2015 for (a) surface temperature (°C) and (c) surface chlorophyll-*a* ($\mu\text{g Chl l}^{-1}$). Scatter plots during the period of validation with significance at 95% confidence level (*p*-value is less than 0.05). The red line represents the regression line of correlation between (b) surface temperature of the default experiment and surface temperature from buoy observations, and (d) surface chlorophyll-*a* of the default experiment and surface chlorophyll-*a* from buoy observations.

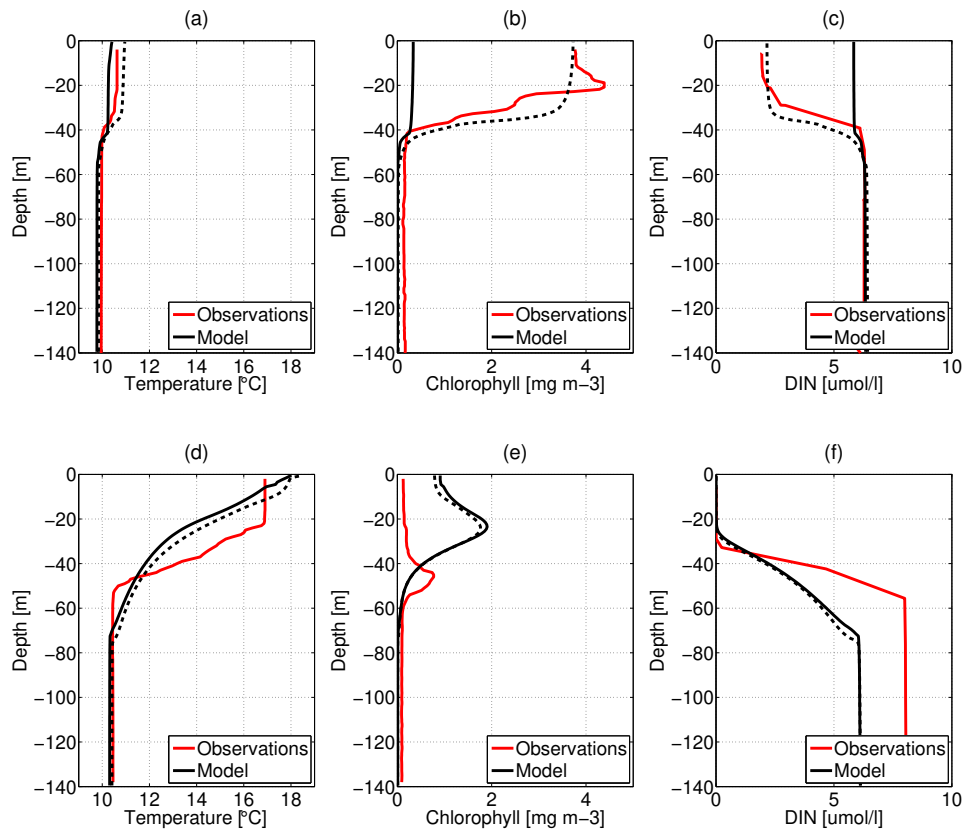


Figure 3.6: CTD validation of the S2P3 v7.0 model in the CCS location (black lines) using observations taken from the UK SSB programme available data (red lines). Validation made in spring during 20/04/2015 for (a) Temperature ($^{\circ}\text{C}$), (b) Chlorophyll-*a* (mg m^{-3}), and (c) DIN ($\mu\text{mol l}^{-1}$) and during summer for day 24/07/2015 for (d) Temperature ($^{\circ}\text{C}$), (e) Chlorophyll-*a* (mg m^{-3}), and (f) DIN ($\mu\text{mol l}^{-1}$). Black dashed lines represent profiles of the model fifteen days later over spring and summer for both dates (05/05/2015 and 08/08/2015, respectively).

The differences in surface temperature between the model and observations suggest that advective fluxes from the North Atlantic might be affecting the area of study in the CCS. The discrepancies in biology between observations and the model, specially a change in magnitude and delay in onset of the spring phytoplankton bloom, could result from a poorly represented predator-prey relationship between phytoplankton and zooplankton, as a constant grazing rate (G). An NPZ framework should be considered as an improvement of the S2P3 v7.0 model in further research. On the other hand, the addition of photo-

acclimation, could improve modelled phytoplankton production during summer months. This hypotheses are considered to be tested in Chapter 4 and Chapter 5 of this work.

Information with relevant information about dates and positions from other CTD casts taken during spring and summer of the year 2015 are listed in Table 3.2. CTD casts chosen to compare the S2P3 v7.0 model are marked in red in Table 3.2.

Cruise name	Date	Latitude (°N)	Longitude (°W)	Depth (m)
DY029	03/04/2015	49.38	8.59	147
DY029	04/04/2015	49.38	8.59	146
DY029	05/04/2015	49.38	8.59	146
DY029	06/04/2015	49.4	8.58	147
DY029	11/04/2015	49.39	8.58	145
DY029	15/04/2015	49.4	8.59	147
DY029	20/04/2015	49.4	8.6	147
DY029	21/04/2015	49.4	8.62	148
DY029	25/04/2015	49.4	8.59	148
DY029	26/04/2015	49.4	8.58	146
DY029	28/04/2015	49.4	8.58	146
DY033	13/07/2015	49.43	8.59	144
DY033	14/07/2015	49.42	8.54	144
DY033	15/07/2015	49.37	8.61	145
DY033	24/07/2015	49.36	8.62	145
DY033	25/07/2015	49.41	8.59	148
DY033	29/07/2015	49.42	8.57	147
DY033	30/07/2015	49.4	8.57	148
DY033	01/08/2015	49.38	8.58	146

Table 3.2: List of relevant CTD casts for the CCS location from DY029 and DY033 cruises considering the date, location (latitude and longitude), and depth. CTD casts in red are the ones chosen in this work to validate the S2P3 v7.0 model during spring and summer.

3.3.3 Statistical analysis

A common statistical analysis was performed in this chapter. Correlations were calculated to understand the relationship between quantitative variables, or time-series in the context of this work. A Pearson correlation coefficient was also calculated (r^2) to test the linear relationship between the data (i.e if it has a positive or negative correlation) and to quantify the strength of this relationship. All correlations were considered significant when p-value < 0.05 (i.e. 95% confidence interval).

An RMSD (eq. 3.1) calculation was performed to measure the differences between total annual NPP for the control experiment and each control-based experiment. Higher values of RMSD mean that there is a large difference between the two variables being compared.

$$RMSD = \sqrt{\frac{\sum_{t=1}^n (x_{1,t} - x_{2,t})^2}{n}}, \quad (3.1)$$

$x_{1,t}$ and $x_{2,t}$ represents two time-series and n is the number of observations. In this study, the two time-series used are the total annual NPP from (1) the control experiment and (2) from each control-based experiment.

Standard deviations (STD) were calculated for the yearly RMSD in each control-based experiment to quantify the amount of variation or dispersion of those sets of data values during the 51 years (1965 - 2015).

$$STD = \sqrt{\frac{1}{N-1} \sum_{i=1}^N (x_i - \bar{x})^2},$$

where N is the number of observations of the time-series, $x_i = \{x_1, x_2, \dots, x_N\}$ are the observed values of the time-series, and \bar{x} is the mean values of those observations.

3.4 Results

This section is divided into three parts that explain the different results found. To address the main hypothesis of this chapter, the first part presents results from the default simulation. The second part presents results that involve the control experiment and control-based experiments to understand the importance of each meteorological variable and their effect on PP inter-annual variability. Finally, the third part investigates the knockout-wind experiment to understand the effects of wind speed during the spring phytoplankton bloom and summer growth.

3.4.1 Analysis of the default simulation

Surface chlorophyll-*a*, bottom temperature, and surface temperature exhibit seasonal variability (Figure 3.7a). With the year 1965 used as an example, during the first ~ 90 days, the surface chlorophyll-*a* remained at a minimum value (~ 0 mg Chl m^{-3}) while bottom and surface temperatures appeared to be the same and thermal stratification did not develop during this period. As soon as springtime starts, surface temperature increases due to higher irradiance and the water column stratifies, trapping phytoplankton at the surface and leading to an increase in the surface chlorophyll-*a*, reaching a peak for the year (spring phytoplankton bloom). Near the start of autumn, surface temperature decreases and the water column becomes mixed (surface and bottom temperatures are equal). As a consequence, surface chlorophyll-*a* decreases to a near minimum value.

The default simulation showed that meteorology also produces inter-annual variability in the surface chlorophyll-*a*, being approximately 30% of the mean. There is also inter-annual variability in the thermal stratification (bottom and surface temperature), affecting the timing, extent, and magnitude of the stratified period (Figure 3.7b).

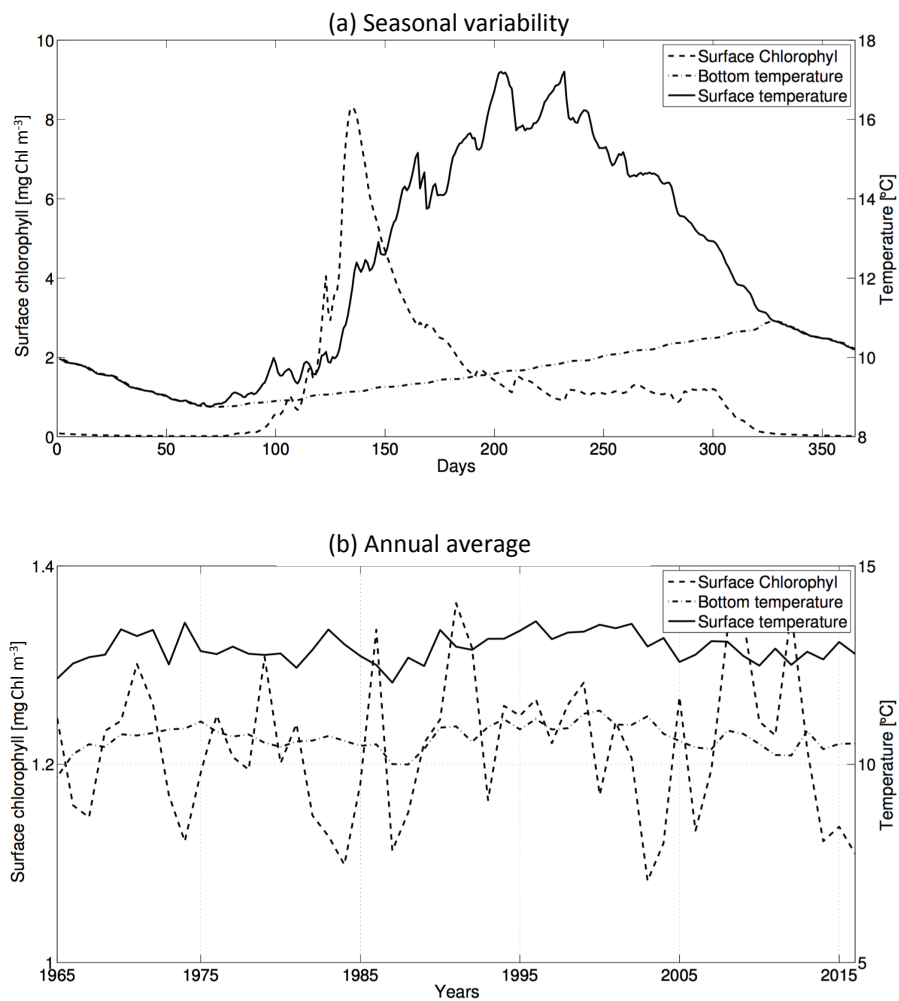


Figure 3.7: (a) Daily time-series showing the seasonal cycle for the default experiment during the year 1965 for the surface chlorophyll-*a* (black dashed line, mg Chl m⁻³), bottom temperature (black dash-dot line, °C), and surface temperature (black solid line, °C), (b) Annually averaged surface chlorophyll-*a* (black dashed line, mg Chl m⁻³), bottom temperature (black dash-dot line, °C), and surface temperature (black solid line, °C) from 1965 to 2015 for the default experiment.

3.4.2 Analysis of control-based experiments

The default simulation showed that meteorology affects phytoplankton production, producing inter-annual variability. Nevertheless, the control-based experiments do not show significant correlations between the total annual NPP and each meteorological variable from 1965 - 2015 (Figure A2). Despite that, some control-based experiments showed sig-

nificant correlations between the meteorological variables and the total annual NPP during the spring months (Table A.2), although these correlations are significant they explain very little of the variability in NPP.

A deeper analysis was undertaken to understand the link between total annual NPP and meteorological variables. From the control experiment, it was noted that there is small inter-annual variability of total annual NPP (Figure 3.8; red solid lines), although there is no inter-annual variability in the meteorological forcing of this simulation. This variability was further investigated using the experiments M2-only and Spring-neap (see Table 3.1), finding that the spring-neap tidal cycle have a contribution in the observed inter-annual variability of total annual NPP. The percentage of a bias between the total annual NPP of a control experiment that includes spring-neap tidal cycle and a control experiment that includes only the M₂ tidal constituent was calculated, showing that the spring-neap tidal cycle contributes 3% to the inter-annual variability of total annual NPP, producing less NPP on average from 1965 to 2015.

For the wind-only experiment, the total annual NPP showed abrupt changes from one year to another and was typically lower than in the control experiment (Figure 3.8a). In addition, the cloud-only experiment also showed inter-annual variability in total annual NPP with lower values than in the control experiment (Figure 3.8b), due to the effect that cloud have on heating of the water column (see eq. 2.12). Similar results were found for the temperature-only experiment, with inter-annual variability of NPP and increasing values over the 51 years (Figure 3.8c). Finally, for the humidity-only experiment, inter-annual variability of total annual NPP was observed as well as decreasing values over time (Figure 3.8d). A standard deviation (STD) was calculated to quantify the variability of total annual NPP of each experiment from 1965 to 2015, with the wind-only experiment showing higher variability of $\pm 1448.5 \text{ mg C m}^{-2} \text{ yr}^{-1}$, followed by the temperature-only experiment with $\pm 1060.4 \text{ mg C m}^{-2} \text{ yr}^{-1}$, cloud-only experiment with $\pm 977.9 \text{ mg C m}^{-2} \text{ yr}^{-1}$, and, finally, humidity-only experiment with $\pm 859.9 \text{ mg C m}^{-2} \text{ yr}^{-1}$ showing the lowest effect on inter-annual variability of total annual NPP over the 51 years.

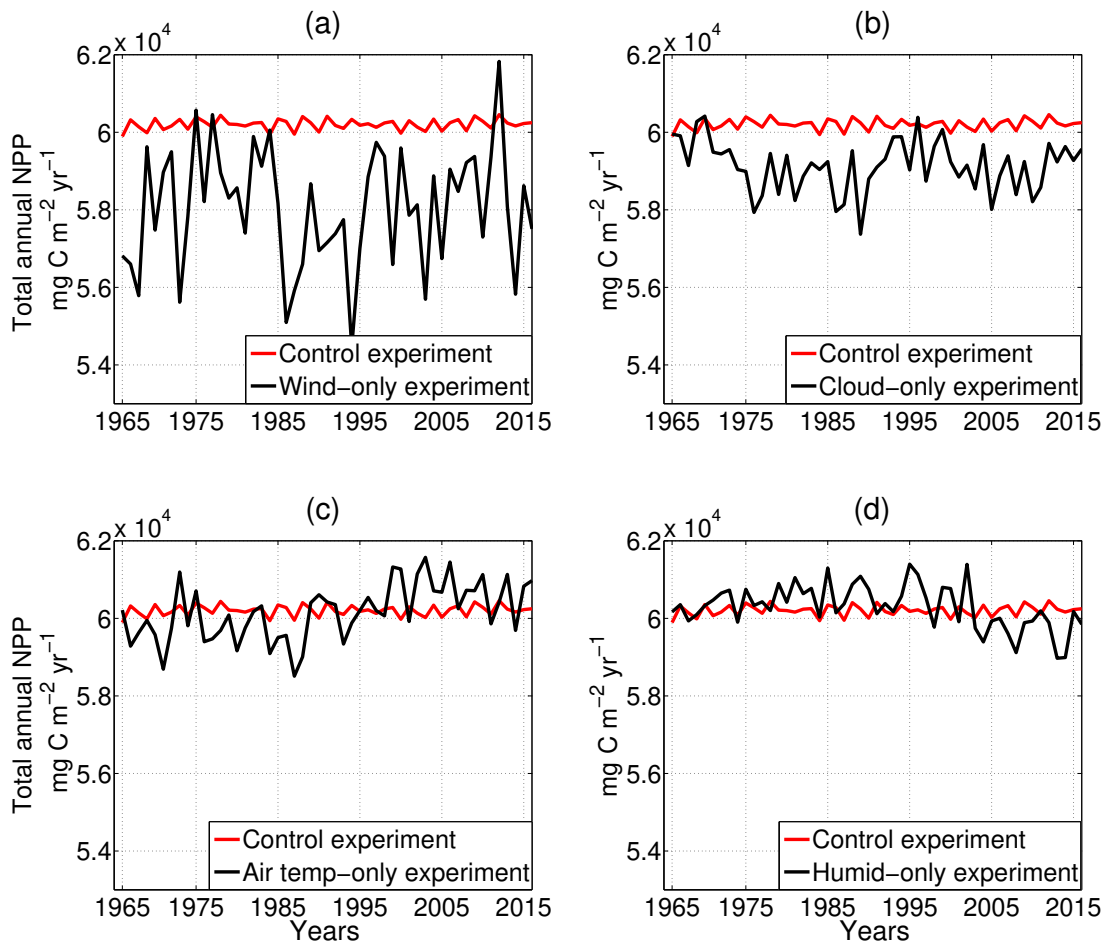


Figure 3.8: Total annual NPP ($\text{mg C m}^{-2} \text{yr}^{-1}$) time-series calculated from 1965 to 2015 for the control experiment (red line) and for (a) wind-only experiment, (b) cloud-only experiment, (c) temperature-only experiment, and (d) humidity-only experiment.

Figure 3.8 shows that meteorology is causing inter-annual variability of NPP and which meteorological variable is most significant for that variability. To quantify this, an RMSD was calculated for the total annual NPP between each control-based experiment and the control experiment (Figure 3.9). Over the 51 years of simulation, it was found that the highest value in the RMSD was for the wind-only experiment ($2635 \text{ mg C m}^{-2} \text{yr}^{-1}$), followed by the cloud-only experiment ($1257 \text{ mg C m}^{-2} \text{yr}^{-1}$), temperature-only experiment ($728 \text{ mg C m}^{-2} \text{yr}^{-1}$), and the lowest RMSD value was given by the humidity-only experiment ($580 \text{ mg C m}^{-2} \text{yr}^{-1}$; Figure 3.9a). This suggests that the largest difference of total annual NPP between the control experiment and the control-based experiments is driven

by the inter-annual variability of wind speed. Moreover, in order to assess variability of the RMSD during the 51 years, an RMSD is calculated every year from 1965 to 2015 (Figure 3.9b), showing inter-annual variability of the RMSD for each meteorological component, however, the strongest year-to-year variability can be observed for the wind-only experiment (STD=1427), followed by the cloud-only experiment (STD=623.9), temperature-only experiment (STD=424), and humidity-only experiment (STD=346). The wind-only experiment presents the larger RMSD every year for $\sim 75\%$, 89% , and $\sim 90\%$ more in comparison to the cloud-only, temperature-only, and humidity-only experiments, respectively.

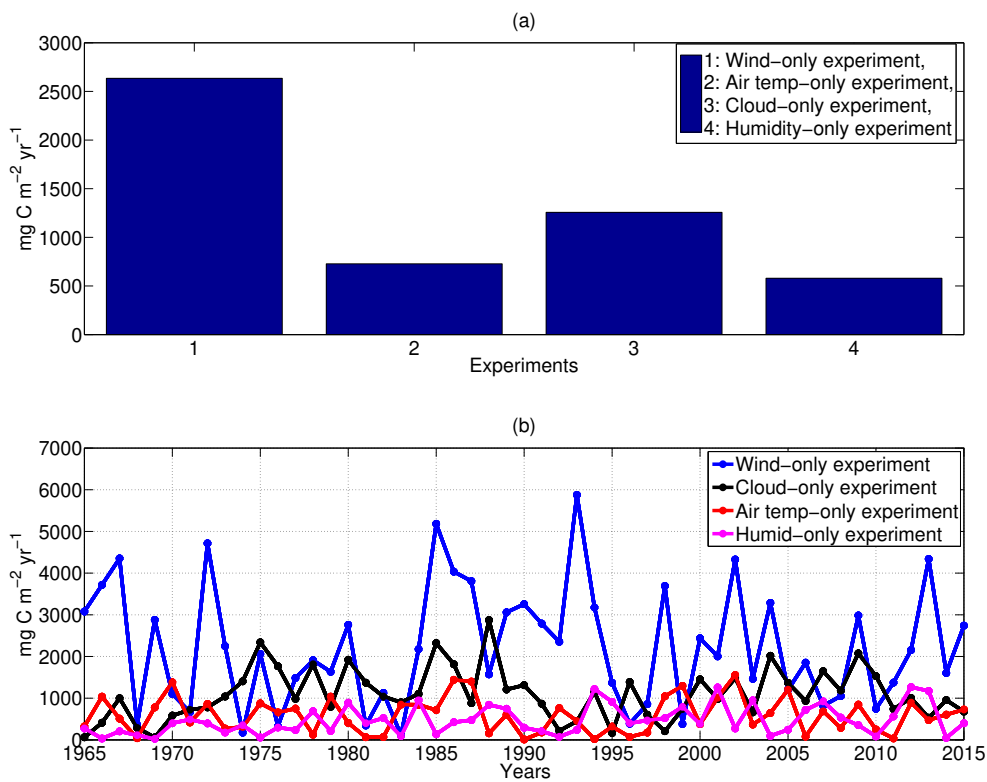


Figure 3.9: (a) An RMSD for the total annual NPP ($\text{mg C m}^{-2} \text{ yr}^{-1}$) calculated between the control experiment and 1: wind-only experiment, 2: temperature-only experiment, 3: cloud-only experiment, and 4: humidity-only experiment. (b) RMSD calculated for the wind-only experiment (blue solid line), cloud-only experiment (black solid line), temperature-only experiment (red solid line), and humidity-only experiment (magenta solid line) for every year. The RMSD for (a) and (b) were calculated throughout 1965 and 2015.

3.4.2.1 Insights for the spring bloom

Meteorological forcing have shown to have an effect in the inter-annual variability of total annual NPP, therefore, it is important to understand the main processes that can influence the annual phytoplankton production. One of these processes to be considered is the spring phytoplankton bloom and the characteristics that define it.

This section shows a preliminary analysis of the spring phytoplankton bloom in terms of the inter-annual variability of its magnitude driven by meteorological forcing. Phytoplankton production generated during spring is a significant percentage of the total annual NPP (Joint et al., 2001; Townsend et al., 1994). Therefore, it is relevant to know the contribution that the timing, magnitude, or duration of the spring bloom has on the inter-annual variability of NPP.

Wind speed is the meteorological variable with the largest effect on inter-annual variability of NPP. To investigate how wind speed is controlling the phytoplankton production variability, the spring phytoplankton bloom was further studied. The day that total annual NPP has the highest value each year from 1965 to 2015 (day of maximum NPP) was calculated for the control experiment and each control-based experiment (Figure 3.10).

Moreover, a boxplot was calculated for the timing of the peak bloom NPP (day), to show the distribution of this characteristic for each model based on their minimum (lower whisker), first quartile (lower side of the box), median (middle line of the box), third quartile (upper side of the box), and maximum (upper whisker), also showing outliers and their values (red cross). As expected, the box plot (from the minimum to the maximum values) shows that the control experiment has low variability for the day of maximum NPP, varying between days 123 and 126 throughout the years 1965 - 2015. For the wind-only experiment, the day of maximum NPP showed the widest range (between days 120 and 143). The cloud-only experiment showed a smaller range (between days 120 and 134), followed by the temperature-only experiment range (between days 118 and 132), where the peak of NPP appeared to be at an earlier stage during the year, and finally, the humidity-only experiment showed a less variable range between the days 120 and 131.

Significant and negative correlations between the day of maximum NPP and the total

annual NPP for the wind-only experiment ($r^2 = -0.3643$, $p < 0.05$), cloud-only experiment ($r^2 = -0.5301$, $p < 0.05$), temperature-only experiment ($r^2 = -0.5666$, $p < 0.05$), and for the humidity-only experiment ($r^2 = -0.2839$, $p < 0.05$) were found (Figure A3). These correlations suggest that the earlier the day of maximum NPP during the spring phytoplankton bloom, more total annual NPP will be in a given year.

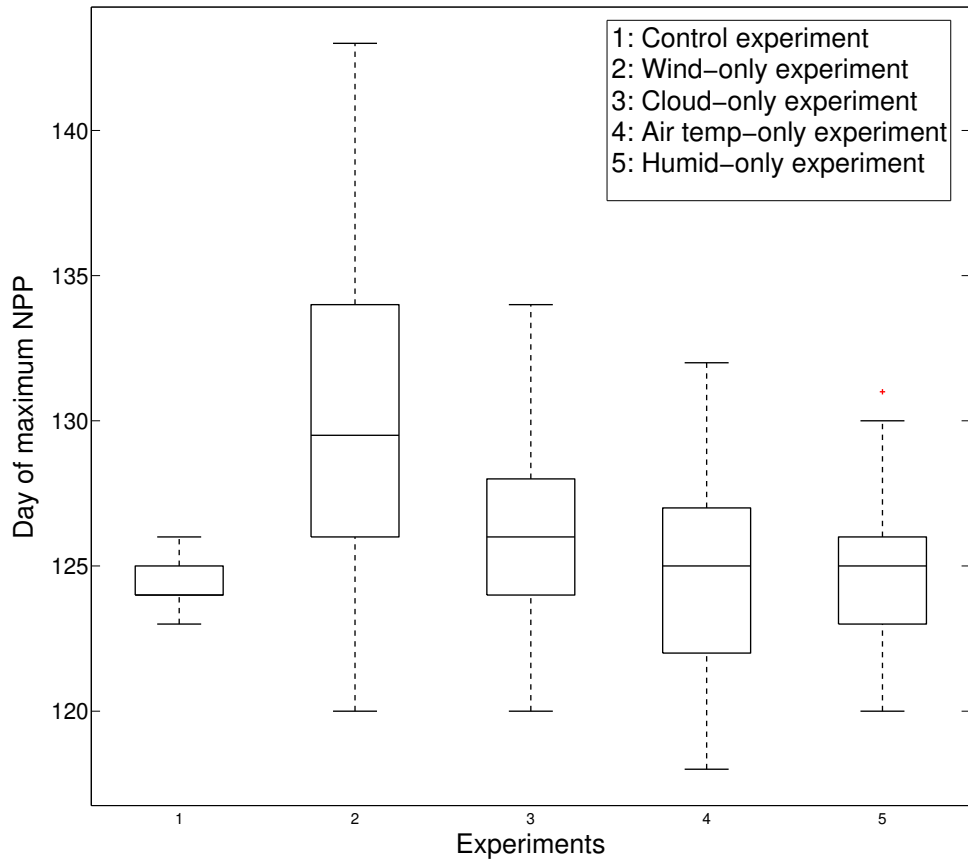


Figure 3.10: Boxplot for the timing of the peak bloom NPP (days) calculated from daily NPP ($\text{mg C m}^{-2} \text{ day}^{-1}$) from 1965 to 2015 for 1: control experiment, 2: wind control-based experiment, 3: cloud control-based experiment, 4: temperature control-based experiment, and 5: humidity control-based experiment.

3.4.3 Analysis of knockout-wind experiment

Results have shown inter-annual variability in the total annual NPP and the spring phytoplankton bloom driven by the different meteorological variables, with wind speed being

the variable that has demonstrated to have the largest effect in this variability. Following the sub-hypothesis of this chapter that states that wind speed impacts PP moderating the timing, duration, and extent of the spring phytoplankton bloom, the knockout-wind experiment was developed. To address this hypothesis, the results of the knockout-wind experiment are shown in this section. Comparison between this experiment and the default simulation might provide insight into the effects of the variability of wind speed on summer stratification and the SCM and, therefore, its impact on spring and summer phytoplankton blooms.

In order to assess the results obtained from Figure 3.11, it is necessary to first define how is the start of the stratified period defined: the start of the stratified period in a given year is defined by the difference between the surface temperature and the bottom temperature in the water column being more than 0.5°C (Figure 3.11b). The default simulation and the knockout-wind experiment were compared during the 51 years of simulation, but for simplicity only the year 1965 is shown in Figure 3.11. Figure 3.11a shows the observations of wind speed, with high-frequency variability and the seasonal cycle (black solid line); less extreme events were observed towards spring and summer in comparison to winter. Additionally, the wind speed control observations do not show high-frequency variability but only the average seasonal cycle of wind speed (Figure 3.11a; black dash-dotted line). These observed differences in the wind speed appear to produce less variability in the knockout-wind experiment regarding thermal stratification (Figure 3.11b; black dash-dotted line), showing that the onset of the stratified period was delayed in the case of the default experiment (Figure 3.11b; black solid line) and with observable pulses producing more seasonal variability. Because of this lag at the start of thermal stratification, the spring phytoplankton bloom is delayed in the default simulation (Figure 3.11c; black solid line) in comparison to the knockout-wind experiment (Figure 3.11c; black dash-dotted line). With these results, it was concluded that inter-annual variability and high-frequency variability of wind speed is affecting the timing of the spring phytoplankton bloom.

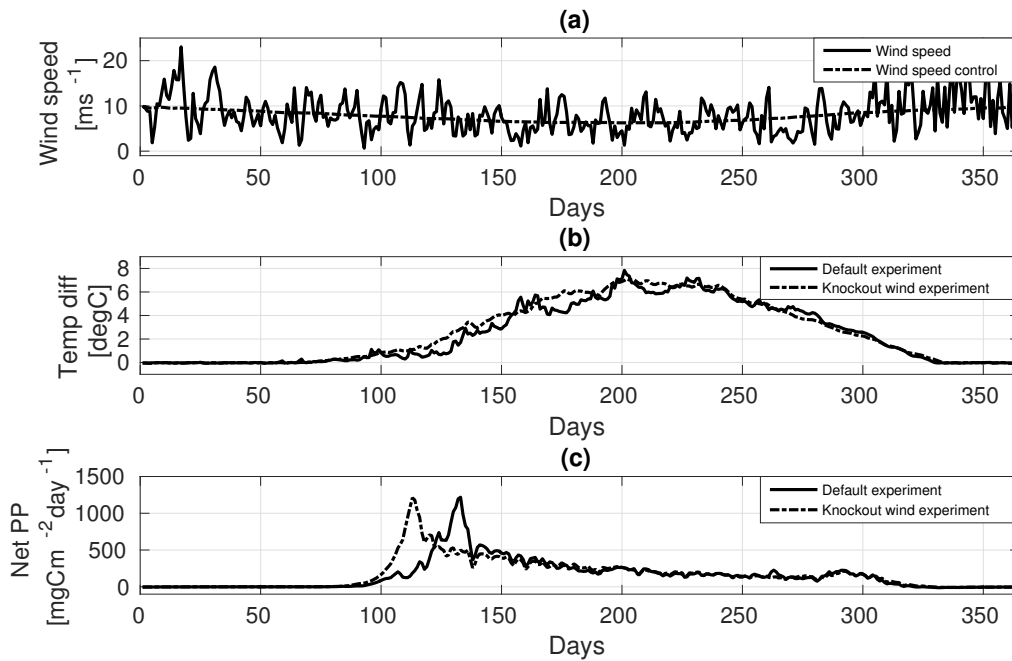


Figure 3.11: Time-series from the output of the default experiment (black solid line) and from the knockout wind experiment (black dashed line) using the year 1965 as an example for (a) Daily wind speed (black solid line) and daily wind speed control (black dashed line, m s^{-1}), (b) daily temperature difference (surface temperature minus bottom temperature, $^{\circ}\text{C}$) for the default experiment (black solid line) and the knockout wind experiment (black dashed line), and (c) daily NPP ($\text{mg C m}^{-2} \text{day}^{-1}$) for the default experiment (black solid line) and the knockout wind experiment (black dashed line).

To assess the overall effects of wind speed throughout the year and the whole water column, the knockout-wind experiment was compared to the default simulation. A difference for daily profiles between the knockout-wind experiment and the default simulation was calculated for temperature, chlorophyll-*a*, and DIN for each year from 1965 to 2015. Each year showed differences and these were averaged over the 51 years for each variable (Figure 3.12), showing information about the overall contribution of wind speed, although losing year-to-year information about wind influence.

During the mixed period of the water column (winter months), the default experiment has higher temperature values than the knockout-wind experiment (Figure 3.12a). To-

wards spring there are some features suggesting that wind speed is affecting the start of the thermally stratified period, while during summer there are differences at the surface, probably affected by the spring-neap tidal cycle in periods of mixing and remixing of the water column. There are changes at the end of the stratified period with higher values of temperature in the sub-surface for the knockout-wind experiment.

Chlorophyll-*a* profiles during the year are also affected by wind speed inter-annual variability showing negative values at the start of spring, which suggests that there are differences in the timing of the spring phytoplankton bloom between both experiments (Figure 3.12b). For the 51 years of simulation, the default experiment tends to show earlier spring phytoplankton blooms than the knockout-wind experiment. Higher values are shown during summer at the surface, with more phytoplankton production in the knockout-wind experiment than the default simulation.

Inter-annual variability seems to also affect DIN, showing fewer nutrients available during springtime for the default simulation and differences in the sub-surface during summer (Figure 3.12c). Variability of DIN happens at the end of the stratified period, with the depletion of nutrients at the surface and more nutrients available below the thermocline for the default simulation in comparison to the knockout-wind experiment.

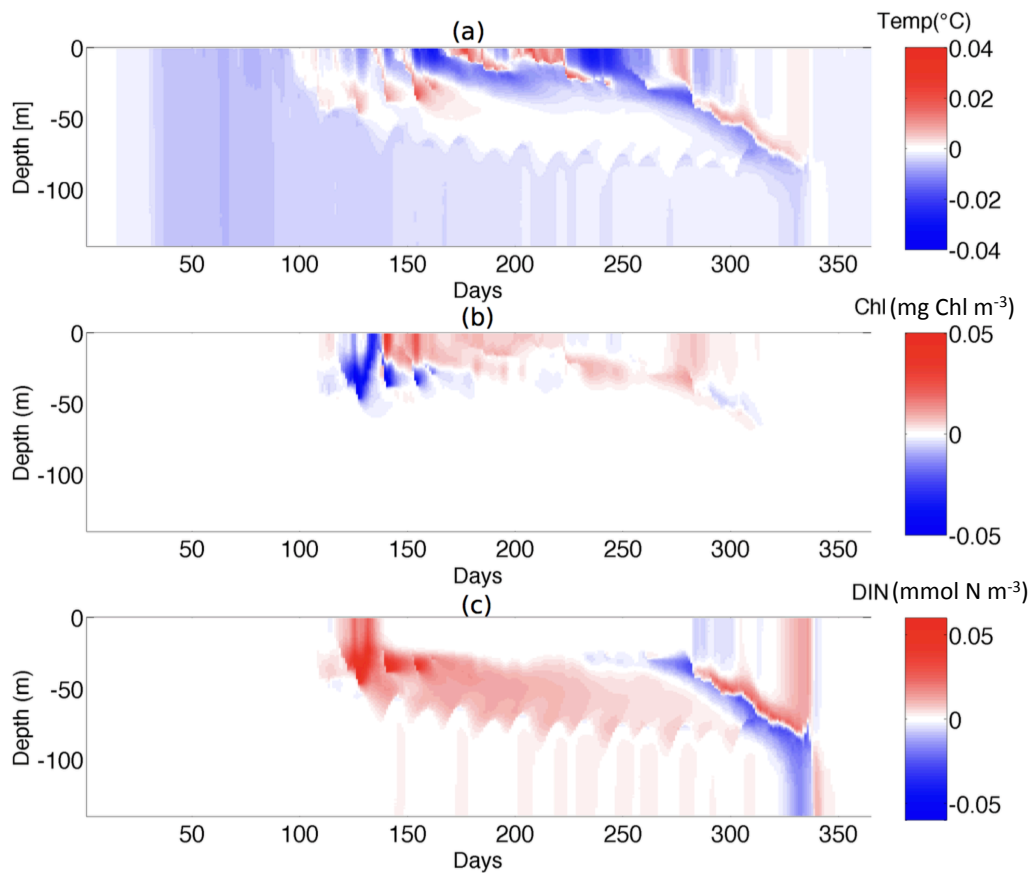


Figure 3.12: Contour plots of mean daily difference between the knockout-wind experiment and the default experiment during 1965 and 2015 along the whole water column with a maximum depth of 140m. (a) Temperature ($^{\circ}\text{C}$), (b) Chlorophyll-*a* (mg Chl m^{-3}), and (c) DIN (mmol N m^{-3}). The red colour represents positive values and the blue colour represents negative values.

3.4.3.1 Spring phytoplankton bloom

The following results are focused on the analysis of the spring phytoplankton bloom period using the knockout-wind experiment and comparing it to the default simulation.

As explained in Chapter 1, section 1.2.2, there are multiple definitions of the start of the spring bloom used in the literature. In this section, a spring phytoplankton bloom period is defined using the following criteria: the onset of thermal stratification, was defined as

the first julian day (JD) each year when the temperature difference is more than 0.5 °C for a period of at least ten days, so seasonal stratification was well established (Figure A4a). This definition comes from the observed time-series of surface and bottom temperatures, and surface chlorophyll in the North Sea where stratification begins to be established when the surface-bed temperature differences is more than 0.5°C (Simpson & Sharples, 2012). However, two more definitions for the start of the spring bloom were also tested using surface chlorophyll thresholds (1.5 and 2 mg Chl m⁻³), showing significant correlations for the default experiment between the definition used with temperature differences of $r^2=0.58$ ($p<0.05$), $r^2=0.56$ ($p<0.05$) compared to surface chlorophyll thresholds of 1.5 and 2 mg Chl m⁻³, respectively. Similar results are found for the knockout-wind experiment: $r^2=0.57$, $p<0.05$ (between threshold of temperature difference and 1.5 mg Chl m⁻³ surface chlorophyll threshold) and $r^2=0.58$, $p<0.05$ (between threshold of temperature difference and 2 mg Chl m⁻³ surface chlorophyll threshold). Between these three definitions of the timing of the spring bloom, only small differences were found in the results of this section, producing slightly changes in the magnitude of the correlations found. Consequently, in order to study the effects of meteorology between the knockout-wind and default experiment, it has been chosen the temperature difference proxy to define the spring bloom as meteorology is directly affecting the physics of the model (temperature field) and it is assumed that the spring bloom only develops once stratification is present.

The end of this spring phytoplankton bloom period is defined as when surface chlorophyll-*a*, reaches a typical summer value equal to 1.5 mg Chl m⁻³ (Figure A4c). With this period defined (Figure A4b), the effect of wind speed on the timing and magnitude of the spring phytoplankton bloom was studied.

A positive and significant correlation was found for the timing of the spring phytoplankton bloom between the default simulation and the knockout-wind experiment (Figure 3.13a; $r^2 = 0.23$, $p < 0.05$). On the other hand, no significant correlation was found between both experiments for the total spring NPP (Figure 3.13b; $r^2 = 0.0002$, $p > 0.05$). Despite Figure 3.13a showing a significant correlation, the strength of such correlation is weak, explaining only 23% of the variability in the timing of the spring phytoplankton bloom between both experiments. Therefore, Figure 3.13a,b are showing that wind variability is not only affecting the timing of the spring phytoplankton bloom but also its magnitude

and duration. Additionally, there is a negative and weak correlation found for the onset of thermal stratification and the total spring NPP in the default experiment (Figure 3.13c; $r^2 = -0.15, p < 0.05$), suggesting that in 15% of the years studied it is found that the later the onset of thermal stratification then the lower the total production during that period. This is also observed for the knockout-wind experiment although the relationship is much stronger (Figure 3.13d; $r^2 = -0.73, p < 0.05$).

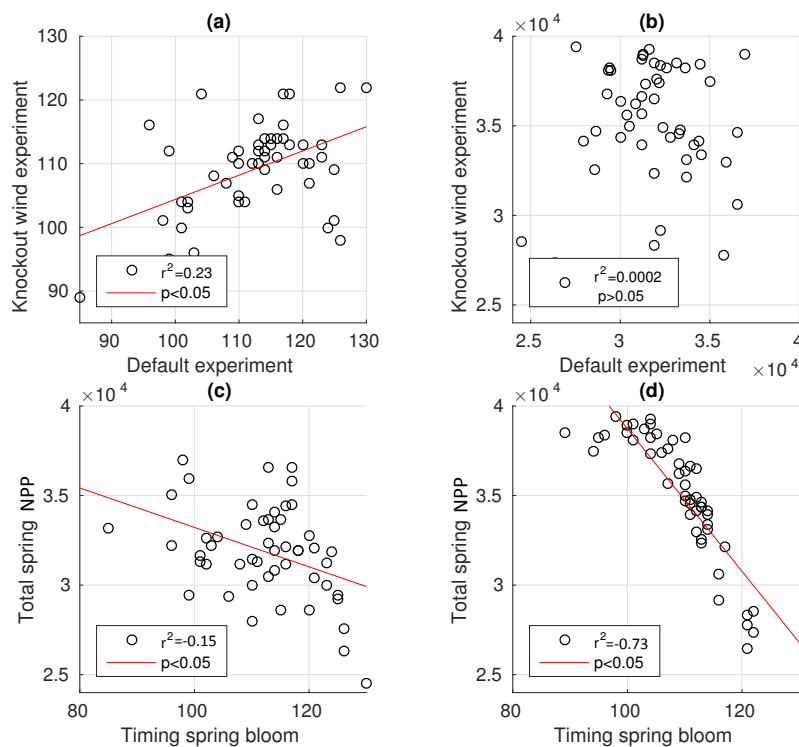


Figure 3.13: Scatter plots of model output for 1965 to 2015. The red line represents the regression line of the correlations between (a) Timing of the spring phytoplankton bloom (*days*) for the default experiment and the knockout-wind experiment, (b) Total spring NPP ($\text{mg C m}^{-2} \text{ day}^{-1}$) for the default experiment and knockout-wind experiment, (c) timing of the spring phytoplankton bloom (*days*) and total spring NPP ($\text{mg C m}^{-2} \text{ day}^{-1}$) for the default experiment, and (d) timing of the spring phytoplankton bloom (*days*) and total spring NPP ($\text{mg C m}^{-2} \text{ day}^{-1}$) for the knockout-wind experiment.

Another feature in the water column during spring which could still be affected by wind forcing and contributes to the inter-annual variability of PP is the depth at which phytoplankton is able to grow linked to temperature and which shows inter-annual variability (Figure 4A), defined here as the surface of the bottom mixed layer (BML). A criteria to find the surface BML for the default experiment and the knockout-wind experiment considered mean vertical daily profiles of water temperature during the spring period (calculated according to the same criteria used for the spring phytoplankton bloom period) with 51 profiles showing the spring vertical temperature and their gradient (Figure A4; black solid lines). The surface BML is calculated when the gradient of temperature is equal to zero (i.e. depth below the thermocline), and shows higher variability in the case of the default simulation.

No significant correlation was found between the timing of thermal stratification and the surface BML for the default simulation (Figure 3.14a; $r^2 = -0.04, p > 0.05$) but significant negative correlations can be observed for the knockout-wind experiment (Figure 3.14b; $r^2 = -0.339, p < 0.05$). This could imply that a deeper BML would lead to a later onset of the spring bloom. On the other hand, there is a significant and negative correlation between the total spring NPP and the surface BML for the default simulation (Figure 3.14c; $r^2 = -0.176, p < 0.05$), while in the case of the knockout-wind experiment, this correlation is significant and positive (Figure 3.14d; $r^2 = 0.174, p < 0.05$). However, these significant correlations found are weak and, therefore, the inter-annual variability of the BML only explains a small percentage of the inter-annual variability of the timing and magnitude of the spring phytoplankton bloom (no more than 30%).

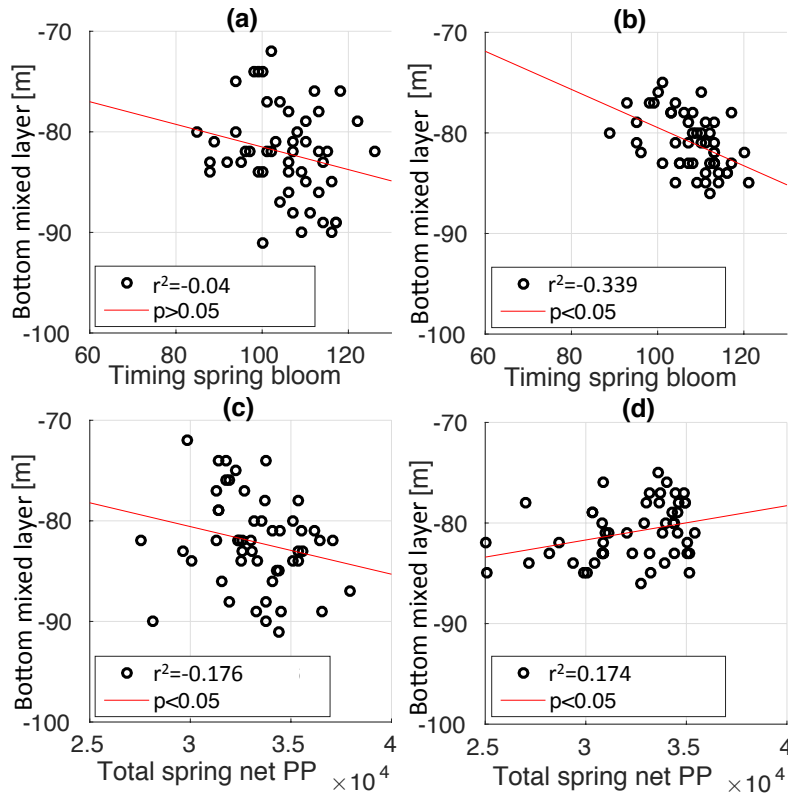


Figure 3.14: Scatter plots of model output for the period 1965 and 2015. The red line represents the regression line of the correlations between (a) timing of the spring phytoplankton bloom (*days*) and surface BML (*m*) for the default experiment, (b) timing of the spring phytoplankton bloom (*days*) and surface BML (*m*) for the knockout-wind experiment, (c) total spring NPP ($\text{mg C m}^{-2} \text{ day}^{-1}$) and surface BML (*m*) for the default experiment, and (d) total spring NPP ($\text{mg C m}^{-2} \text{ day}^{-1}$) and surface BML (*m*) for the knockout-wind experiment.

3.4.3.2 Summer growth

The spring phytoplankton bloom is one of the characteristics that have been studied in this chapter to understand the effects that meteorology has in the inter-annual variability of total annual NPP, but there is another seasonal feature that can contribute to the annual production and it is the growth of phytoplankton during summer.

In this section, a summer growth period was calculated; the start defined as the end of the spring phytoplankton bloom and the end defined by when thermal stratification becomes

less than 0.5°C . Further analysis during summer was done, finding that the length of the stratified period is positively correlated with the total summer net production in the default experiment ($r^2 = 0.1571$, $p < 0.05$; Figure 3.15a) and the knockout-wind experiment ($r^2 = 0.4438$, $p < 0.05$; Figure 3.15b); this means that the longer the stratification, the greater the production will be in summer. Positive and significant correlations between the total summer NPP with the length of the summer period were found for the default experiment ($r^2 = 0.7009$, $p > 0.05$; Figure 3.15c) and for the knockout-wind experiment ($r^2 = 0.6344$, $p < 0.05$; Figure 3.15d). It is important to note that the results do not show significant correlations between the total annual NPP and the total spring NPP for the default experiment ($r^2 = 0.0002$, $p > 0.05$) and for the knockout-wind experiment ($r^2 = 0.0015$, $p > 0.05$); on the other hand, significant correlations were found between the total summer NPP for the default experiment ($r^2 = 0.0293$, $p < 0.05$) and for the knockout-wind experiment ($r^2 = 0.2931$, $p < 0.05$).

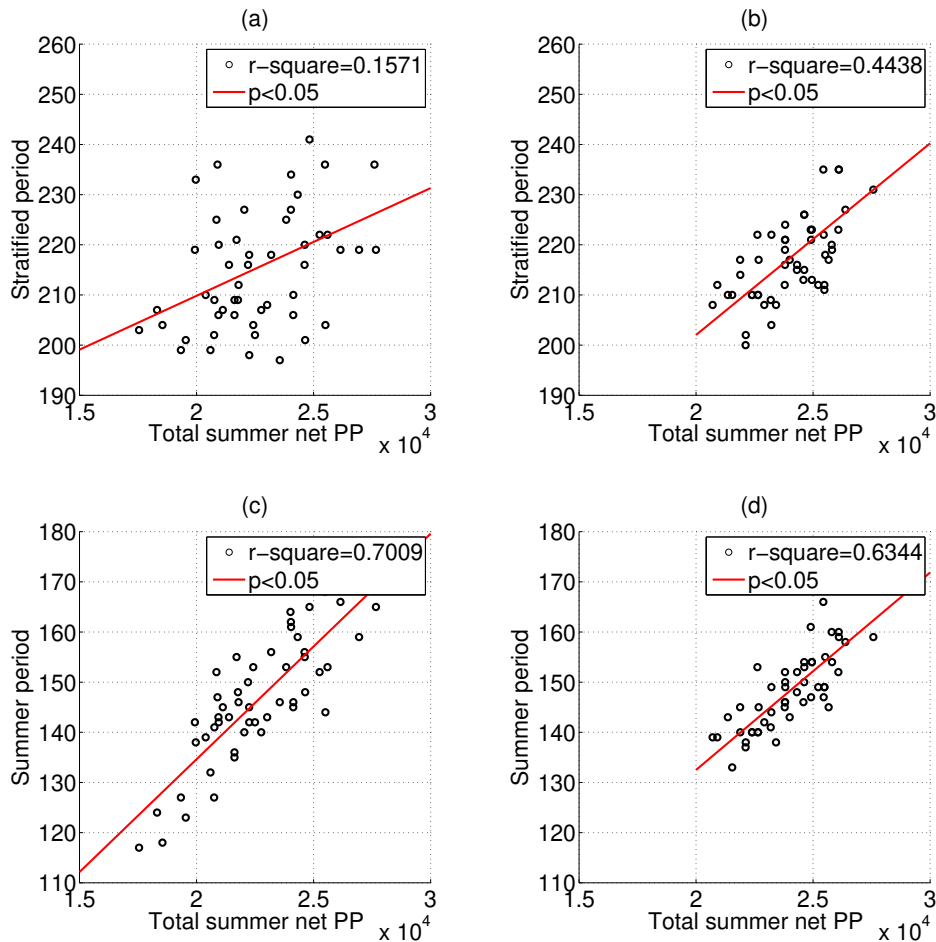


Figure 3.15: Scatter plots calculated for the period 1965 and 2015. Red line represents the regression line of the correlations between (a) length of the stratified period (days) and the total summer NPP ($\text{mg C m}^{-2} \text{ day}^{-1}$) for the default experiment, (b) length of the stratified period (days) and the total summer NPP ($\text{mg C m}^{-2} \text{ day}^{-1}$) for the knockout-wind experiment, (c) total summer NPP ($\text{mg C m}^{-2} \text{ day}^{-1}$) and the length of the summer period (days) for the default experiment, and (d) total summer NPP ($\text{mg C m}^{-2} \text{ day}^{-1}$) and the length of the summer period (days) for the knockout-wind experiment.

Negative values of NPP were found during the winter months due to values of phytoplankton cellular respiration exceeding gross photosynthesis. This explains the findings that some years there is less total annual NPP than total spring + summer NPP in the default simulation (Figure 3.16a). There is a stronger inter-annual variability found in the total annual NPP for the default experiment than in the knockout-wind experiment, although

stronger inter-annual variability of the total spring + summer net production can be observed in the knockout-wind experiment (Figure 3.16b).

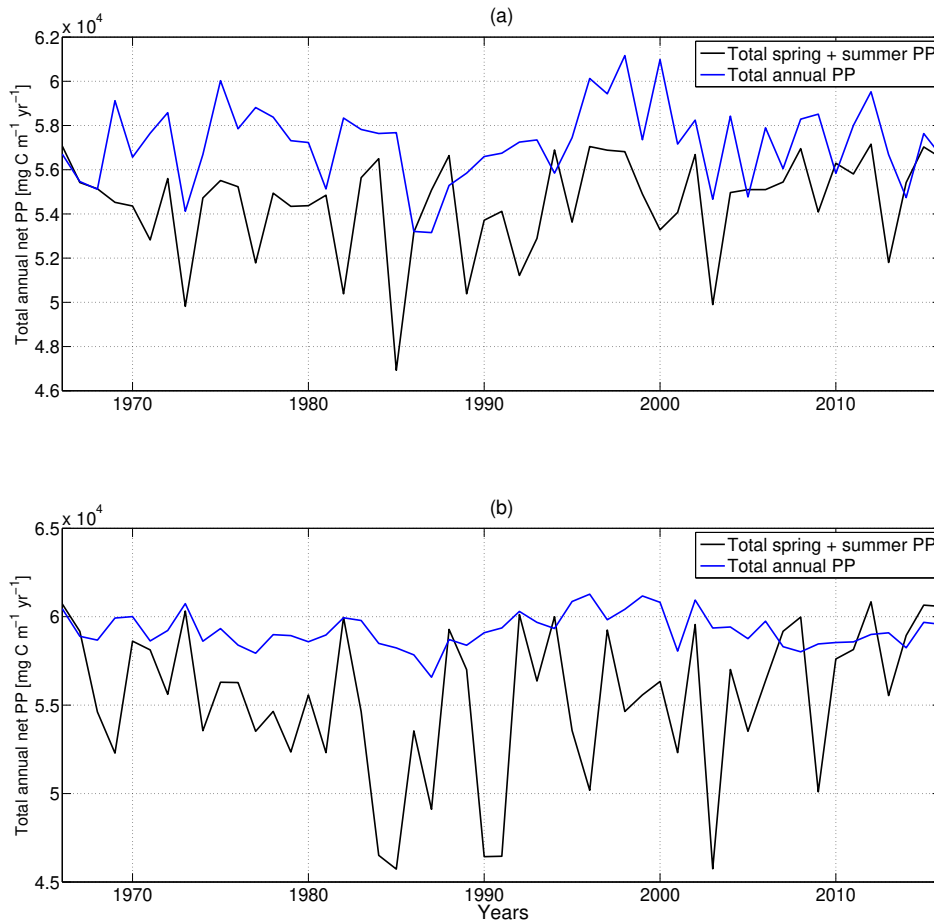


Figure 3.16: (a) Time-series of total annual NPP (black solid line; mg C m⁻² yr⁻¹) and total spring + summer NPP (blue solid line; mg C m⁻² yr⁻¹) for the default experiment throughout 1965 to 2015. (b) Time-series of total annual NPP (black solid line; mg C m⁻² yr⁻¹) and total spring + summer NPP (blue solid line; mg C m⁻² yr⁻¹) for the knockout-wind experiment from 1965 to 2015.

3.5 Discussion

The results show the effects of each meteorological variable on the inter-annual variability of PP, based on the different model run experiments. This chapter is divided into three sections. The first part considers the default simulation to address the main hypothesis of this work. The second part will discuss the different results obtained from the control-based experiments and the importance of each meteorological variable to produce inter-annual variability of PP. The third and final part will analyse the importance of wind speed and its effect on different vertical processes of the water column during spring and summer.

3.5.1 Default simulation and inter-annual variability of stratification

A comparison between the modelled production rate of the default simulation and former studies in the CCS, as well as typical observations, has been made. The average total annual NPP over the 51 years of simulation obtained for the default experiment was $\sim 61 \text{ g C m}^{-2}$, while a value of 109 g C m^{-2} was found for the GPP calculated by the model. These results of PP compare to the ones found by Sharples (2008) for the Celtic Sea (in a seasonally stratified area of the shelf) of $\sim 70 \text{ g C m}^{-2}$. Additionally, Joint & Groom (2000) estimated PP in the CCS location during April to September based on in-situ incubations of 80 g C m^{-2} , which is lower to the same estimates found using the sea-viewing wide field-of-view (SeaWiFS) ocean colour sensor, which found the PP to be 102 g C m^{-2} in 1998 and 93 g C m^{-2} in 1999. Moreover, the work of Joint et al. (1986) reported measurements of size fractionated PP made in all seasons over a 2 years period (1982 - 1983) in the Celtic Sea (CS2 location at 50° 3N , 7°W), estimating an annual production of $102.81 \text{ g C m}^{-2}$, with 37.89 g C m^{-2} corresponding to phytoplankton $>5\mu\text{m}$, from which half of this occurred only during April (i.e. $18.45 \text{ g C m}^{-2} \text{ mo}^{-1}$). Therefore, the capability of the S2P3 v7.0 model to accurately represent the rates of PP is comparable to results found in the literature, reflecting the models capability to simulate the CCS location and support the use of the 1-D framework of the S2P3 model. Differences found between the model and estimated values of PP could be given by different reasons ranging from inter-annual variability of PP which might not be represented in the observations if they only calculate for one or two years, while the model is calculating PP over the last 51 years; the methodology used to calculate phytoplankton production can also imply differences in the estimates; and, finally, it is important to recognise that some of the assumptions in

the S2P3 v7.0 model such as a fixed grazed of zooplankton, no inclusion of size-fractioned phytoplankton, and the slower rates of nitrate remineralisation in the model might be one of the sources for different estimates of PP.

The results of the default model simulation show that alongside the development of the stratified period, a spring phytoplankton bloom developed. Inter-annual variability in thermal stratification was also found to affect the extent and timing of the onset of the spring phytoplankton bloom. This variability is related to the meteorological variables: wind speed, air temperature, cloud cover, and relative humidity. One interesting finding was that there were no significant correlations between the total annual NPP and each meteorological variable between 1965 and 2015 including wind speed ($r^2 = 0.048$, $p > 0.05$), cloud cover ($r^2 = 0.045$, $p > 0.05$), air temperature ($r^2 = 0.034$, $p > 0.05$), and relative humidity ($r^2 = 0.004$, $p > 0.05$). Phytoplankton production during the meteorological spring months (April, May, and June) shows significant and positive correlations with mean spring values of wind speed, air temperature, and cloud cover (Table A.2). It is important to note that wind speed is correlated to total annual NPP during the whole spring period. However, these significant correlation during spring only explain a small percentage of the inter-annual variability of NPP due to meteorological forcing, therefore, it is important to consider that the effects of wind speed, air temperature, and cloud cover could not be well represented with a correlation, possibly due to a lag in the response of the water column and phytoplankton to meteorological variability possibly due to complex feedbacks between existing between plankton communities and changes in their physical environment.

3.5.2 Model experiments

3.5.2.1 Control-based experiments: inter-annual variability of phytoplankton production and meteorological controls

Wind speed produces a greater contribution to inter-annual variability of total annual NPP than any other meteorological variable (Figure 3.8). Sharples et al. (2006) showed that wind stress variability has the greatest effect on the timing of the spring phytoplankton bloom before the decade of 1990 in the NW North Sea, with spring air temperature playing a major role after the decade of 1990. Changes in wind stress over long-time scales can cause significant variations in phytoplankton production, inhibiting the start of the spring

phytoplankton bloom due to mixing in the water column. This is related to the PEA theory that states that different buoyancy inputs play a role in the development of thermal stratification, considering mixing by tides (Kobayashi et al., 2006) and winds (Williams et al., 2013) competing with surface heating (Sharples, 2008).

to an abnormally cold spring followed by a warm summer in the UK (Marsh et al., 2015), and stronger stratification producing a delayed spring phytoplankton bloom.

Inter-annual variability of total annual NPP was observed in every control-based experiment (Figure 3.8). There was an increase of annual phytoplankton production after the 1990s in the case of the temperature-only experiment (Figure 3.8c), which can be related to the increase of air temperature over time (Figure 2.10) and the effect that this has on the sensible heat flux, suggesting that the increased total annual NPP after the 1990s corresponds to a weaker cooling, affecting the MLD and thermocline. These results can be compared with those of Elliott & Clarke (1991), which showed that anomalous hotter years can also produce an effect on the water column temperature during the next year, but in the case of the temperature-only experiment, air temperature seems to steadily increase over time (Figure 2.11c). An opposing pattern was observed for the humidity-only experiment, where up to 1990 the total annual NPP was lower than in the control simulation. This is an interesting result because relative humidity does not show a tendency to increase or decrease over time (Figure 2.11d) so the decrease of total annual NPP must be caused by factors other than the lack of a long-term trend for relative humidity. For example, relative humidity could be impacting other processes indirectly (e.g. air-sea fluxes interaction, see eqs. 2.11 - 2.15) and feedbacks between them can involve more complexity and non-linear responses to be analysed only with a direct comparison between trends of NPP and relative humidity. Moreover, a 51 years trend of relative humidity is not showing information about short term variability (e.g. seasonal or decadal), and this also may have a role to play. These hypotheses suggested imply that further work needs to be done to address them.

The cloud-only experiment shows that the total annual NPP was less than in the control experiment (Figure 3.8b). Cloud cover affects the surface irradiance which is considered one of the controls of phytoplankton growth. Shi et al. (2017) demonstrated that earlier phytoplankton blooms can occur as a result of favourable weather conditions, and hence,

PP will increase over spring. However, the effect of cloud cover can produce later spring phytoplankton blooms because it will inhibit the heating in the surface of the water column (see eqs. 2.8, 2.12), producing less total annual NPP due to this delay. On the other hand, phytoplankton can grow in the SCM during summer and the effect of cloudiness can also produce lower levels of PP over this period because cells are very sensitive to meteorological changes in the SCM region due to light limitation (Sharples et al., 2001), with photo-acclimation of phytoplankton playing a role in the production of biomass (Moore et al., 2006). The S2P3 v7.0 model does not include photo-acclimation, therefore, it will require model development and this will be revisited in Chapters 4 & 5 of this work.

Of all the meteorological variables, results showed that wind speed has the largest effect on the inter-annual variability of PP (Figure 3.9). Control-based experiments suggest that wind variability plays a major role in the changes in phytoplankton production from one year to another.

3.5.2.2 Insights into the spring phytoplankton bloom

A feature of the spring phytoplankton bloom that was analysed corresponds to the day of maximum NPP. Figure 3.10 shows that wind speed is the meteorological variable with the highest range in the timing of the spring bloom peak. This means that mixing at the surface of the water column can lead to a larger variability in the timing of the spring phytoplankton bloom than cloud cover, air temperature, or relative humidity. It has also been found that wind speed produces less total annual NPP than the control experiment (Figure 3.8a), which means that despite a later day of maximum NPP during spring, total annual NPP will not necessarily be more in a given year. These results are supported by significant and negative correlations between the day of peak bloom and the total annual NPP (Figure A3), although Figure A3a does not explain a high percentage (only $\sim 37\%$) about the inter-annual variability between later days of maximum NPP resulting in less total annual NPP for the wind-only experiment. The effect of wind speed will create a deeper MLD in late winter due to vertical mixing of the water column, leading to later blooms during spring (Zhao et al., 2013), and at the same time, the inter-annual variability of the magnitude of the spring bloom has been attributed to changes in the depth of winter mixing (driven by wind speed and net heat fluxes), and hence enhancing concentrations of nutrients available in spring (Koeve, 2001). Therefore, the responses of the maximum day

of NPP during spring and the total annual NPP to inter-annual variability of wind speed will be produced due to different feedbacks that are not clearly represented with a Pearson correlation and further analysis should be done to understand the direct mechanisms that wind speed play in driving seasonal and inter-annual variability of NPP. Additionally, as shown in Figure 3.10, air temperature variability will produce an earlier peak bloom than wind speed variability because the mechanistic effect of higher temperature is to induce earlier blooms by causing thermal stratification, which results in high light intensities in a shallow mixed layer (Sommer et al., 2012). Finally, cloud cover has an important effect on the timing of the spring phytoplankton bloom: more cloud cover can delay the stratified period but this does not mean that the total annual NPP will necessarily be more in a given year (Figure A3b).

3.5.3 Knockout wind experiment: analysis of the spring phytoplankton bloom and summer growth

Inter-annual variability of wind speed changes thermal stratification, with observable pulses of temperature in the thermocline, suggesting that extreme events of wind (i.e. storms or calm days) are the main cause (Figure 3.12). Wind stress mixes the vertical water column inhibiting thermal stratification and, therefore, affecting the timing of the spring phytoplankton bloom by delaying it. The differences in the timing of the spring phytoplankton bloom between the knockout-wind experiment and the default simulation (Figure 3.11c, Figure 3.12b) are because the knockout-wind experiment uses a climatological wind speed as meteorological forcing. An important consideration in this experiment is that the smoothing process used to create the climatological wind forcing leads to the removal of daily variability. Daily variability is likely to be of importance when investigating meteorology, particularly in how this affects the spring phytoplankton bloom. For example, in temperate shelf seas, strong wind forcing can be important during post-spring bloom periods, because it has been linked to vertical transport of nutrients towards the surface (Rippeth et al., 2009). This implies that the effect of wind speed on the results is associated with extreme events (e.g. storms) alongside seasonal variability so these factors need to be identified and investigated in further work. Therefore, in order to explore this hypothesis is suggested that the occurrence of storms is defined, specially in late winter/early spring and summer months to understand the effect of these extreme events have on the timing and magnitude of the spring bloom, and on summer growth related to nutrient entrainment

from below the thermocline.

Wind speed variability is affecting processes in the whole water column as shown in Figure 3.12. There is, on average, a higher temperature for the default experiment during the years 1965 - 2015 when the water column is mixed in winter. The mixing effect produced by wind variability in the water column allows heat from shallower layers to reach deeper and, therefore, disperses more of that heat through the whole water column after summer when irradiance has reached its seasonal peak. Sharples et al. (2006) discussed that the inter-annual variability of the timing of the spring stratification and bloom is also linked to the phase of the spring-neap tidal cycle. These results can be observed in the case of temperature profiles during the year (Figure 3.12a), with pulses of higher temperature during spring in the thermocline relative to the default experiment over a period of ~ 15 days. Additionally, results from the M2-only and Spring-neap experiments showed that the spring-neap tidal cycle is contributing 3% to the inter-annual variability of total annual NPP, which could be related to tidal stirring changing the timing of thermal stratification and related start of the spring bloom. Therefore, here it is suggested that further investigation needs to be done to understand the combined effects of wind speed and the spring-neap tidal cycle in the thermocline.

It is also interesting to note a contradiction in the results. From earlier calculations, it was found that wind speed delays the spring phytoplankton bloom during the example year 1965 (Figure 3.11), but a general overview of the water column, and throughout the 51 years of simulation, demonstrates that, on average, wind speed variability is producing earlier blooms (Figure 3.12b). Figure 3.12c shows a depletion of nutrients at the surface at the start of the spring phytoplankton bloom for the default experiment and leads to a new hypothesis about the climatological wind as a forcing. As the smoothing process of wind is done yearly from 1965 to 2015, daily variability is lost but due to the skewed distribution of values (Figure 3.3a) probably this new forcing has higher values than more than half of the years during that period. Prestidge & Taylor (1995) used a model to understand thermal stratification and phytoplankton abundance in the Irish Sea, showing that when simulations used wind speed data smoothed over a short term period (11 days), the reduction of mixing energy produced earlier and slightly more intense spring and autumn blooms. This proves that wind speed is relevant in the CCS location for the inter-annual variability of PP and

that the smoothing process of wind speed in the knockout-wind experiment over a whole year can be one of the reasons for these opposing results. Further work needs to be done to understand how different calculations of non-inter-annually varying forcing is the cause of earlier blooms.

3.5.3.1 Spring phytoplankton bloom

The onset of thermal stratification is related to the competition of buoyancy inputs, which are affected by surface heating (Sharples, 2008), as well as stirring by tides (Kobayashi et al., 2006) and wind stress (Williams et al., 2013). In many cases, the most dominant mechanical forcing of the shelf seas is the result of momentum and energy inputs from the tides (Simpson & Sharples, 2012). The default simulation and the knockout-wind experiment differ in the timing and magnitude of the spring phytoplankton bloom, showing that wind variability modulates these features (Figure 3.12a,b). Wind speed produces larger variability in the default simulation for the onset of the spring phytoplankton bloom, but the timing and total spring NPP shows lower correlation (Figure 3.13c) than in the knockout-wind experiment (Figure 3.13d). On the other hand, the timing of the spring phytoplankton bloom has been shown to be sensitive to changes in the grazing rate (Behrenfeld et al., 2013; Behrenfeld, 2010), therefore, the effects of zooplankton in the timing of the spring phytoplankton bloom need to be investigated.

A delayed bloom is often indicative of deeper mixed layers and increased surface nutrient concentrations. Despite no significant correlations found between the timing of the spring bloom and the BML for the default experiment (Figure 3.14a), the knockout-wind experiment (Figure 3.14b) can explain $\sim 34\%$ of the inter-annual variability in the timing of the spring bloom due to changes in the BML. Therefore, it can be concluded that the results show that the surface BML is influenced by wind speed, through mixing in the water column, producing larger variability, with the wind not only affecting the surface layer but the whole thermocline. However, the effects of wind speed are not explained by the correlations in Figure 3.14, suggesting again about the lag and non-linearity of the responses of the physical and biological parts of the ecosystem to changes in wind. Additionally, it is important to note that this analysis considers averaged temperature profiles during spring (Figure A4) and a deeper understanding of the role that surface BML variability plays in the total annual NPP should consider daily profiles of the BML to understand

high-frequency variability that is being lost.

3.5.3.2 Summer growth

With a defined period for the spring phytoplankton bloom (Figure A1) and for summer growth, results show that there are no significant correlations found between the total spring NPP and total annual NPP, or between the total summer NPP and total annual NPP, which is interesting considering that the spring production alone reaches about 50% of the total annual NPP every year (Figure 3.15). Therefore, it is important to consider other processes during spring or summer (such as timing and magnitude of the spring phytoplankton bloom, development of an SCM, or nutrient entrainment to surface layers during summer) that might provide a large contribution to the annual variability of NPP, but investigating other seasons of the year such as autumn and winter can also be a matter of discussion in future work and it is suggested that all seasons be studied to analyse their contribution to the annual variability of NPP.

The turbulent dissipation at the base of the thermocline is responsible for nutrient entrainment into the thermocline from the BML (Richardson et al., 1998). Therefore, this nutrient flux will play an important role in the maintenance and production of an SCM, driven by energy dissipated at the base of the thermocline due to wind speed (Williams et al., 2013) and tidal periodicity (Sharples et al., 2001). The future study of an SCM and vertical processes in the CCS is important to improve the understanding of the effects of meteorology during summer months.

3.5.4 Concluding remarks

The S2P3 v7.0 model is used in a series of experiments to investigate the effects of meteorology on the inter-annual variability of NPP. Inter-annual variability of phytoplankton growth is associated with a sequence of processes through the seasonal cycle. The onset of thermal stratification in spring influences the timing, magnitude, and duration of the spring bloom. This is followed by summer growth associated to the SCM. A simple 1-D model is demonstrated to be an efficient tool at a low computational cost and showing a reasonable representation of the CCS shelf sea ecosystem based on comparison with obser-

variations from the SSB programme.

It is important to mention that all ecosystem models are a simplification of the natural ecosystems (Behrenfeld et al., 2013). For example, from the most relevant assumptions of the S2P3 v7.0 is the no consideration of advective fluxes, therefore, to study a location close to the shelf edge or to the continental margins that are considered ROFIs, it would pose an issue for a realistic representation of that particular ecosystem with this 1-D model. Nevertheless, this chapter have shown that the S2P3 v7.0 model can make a good representation of the CCS location, by being validated with buoy and CTD observations, as well as compared with PP estimates from literature values for the Celtic Sea. However, another assumption from the S2P3 v7.0 model is the oversimplification of zooplankton populations, by calculating the grazing rate solely as a fraction of phytoplankton biomass removed each time step to be recycled back into the available pool of water column DIN. But there is evidence that the spring bloom marks the beginning of zooplankton production in temperate marine systems (Friedland et al., 2015; Longhurst, 1995) and that the timing and duration of phytoplankton blooms can be influenced by the grazing activity (Behrenfeld et al., 2013; Behrenfeld, 2010) of micro-zooplankton (Chen et al., 2013) and meso-zooplankton (Hlaili et al., 2014). Consequently, improvements in the S2P3 v7.0 model need to be considered for further analysis of the CCS location and the meteorological drivers that produce inter-annual variability on phytoplankton PP. This model development should include a realistic zooplankton grazing, allowing to vary over time as in models that consider an NPZ framework. This could provide more confidence in the results found and better insights in phytoplankton growth variability by representing the predator-prey relationship between zooplankton and phytoplankton.

Additionally, another process that should be taken into consideration is the photo-acclimation of phytoplankton, which will give more complexity to the model but will also resolve the phenotypic changes of phytoplankton to changes in light (MacIntyre et al., 2002; Falkowski & LaRoche, 1991; Falkowski, 1980). Phytoplankton photo-acclimation addition to the S2P3 v7.0 model could act to compensate for irradiance changes over period of days (Falkowski & Raven, 1997), meaning that the shape and magnitude of the phytoplankton growth dependency on light availability (or PE curve, Figure 2.4) will reflect underlying biophysical, biochemical, and metabolic processes that regulate photosynthesis

(Falkowski, 1992), with changes in the PE curve and variability of the Chl : C : N ratio to assess photo-acclimation. Consequently, because inter-annual and decadal variability in the annual phytoplankton production is a response to the variability of the different environmental drivers and to the changes that occur inside the algal cells, modelling the response of phytoplankton to the variability of local weather conditions can have wider implications in the marine shelf sea modelling, providing insights into the effects that future changes in weather and climate will have on plankton communities.

Chapter 4

Constraining the response of phytoplankton to zooplankton grazing and photo-acclimation in a 1-D model

4.1 Abstract

The numerical model used in the previous chapter has been developed into three different new models: S2P3-NPZ which includes an NPZ framework, where the grazing rate is no longer constant, but instead varies over time depending on different functions chosen to represent the predator-prey relationship between phytoplankton and zooplankton; S2P3-Photoacclim which includes a representation of the process of photo-acclimation in phytoplankton; and S2P3 v8.0 which combines the NPZ framework and the photo-acclimation of phytoplankton at the same time. Each of these models is compared to buoy and CTD observations, as well as zooplankton biomass and in situ physiological parameters taken in the CCS location as components of the SSB programme. In this chapter, each new model is calibrated by comparison to observations of the timing and magnitude of the spring phytoplankton bloom, magnitude of the spring zooplankton bloom, and physiological parameters throughout the water column. A sensitivity study was also performed for each model, based on parameter values found in the literature, to understand the effects of each parameter on model dynamics. Results demonstrate that the best agreement with biological observations is obtained with the addition of photo-acclimation and grazing.

4.2 Introduction

This section provides an introduction and is divided into two main subsections. The first subsection provides a background of general knowledge and description of NPZ models, their importance and advantages. The second subsection provides information about light and photosynthesis and how the photo-acclimation of phytoplankton influences cellular composition and physiology. The aims of this chapter are stated in the final part of this section.

4.2.1 NPZ models and S2P3 v7.0: S2P3-NPZ

The development and management of shelf sea ecosystems depend on the level of understanding of factors that influence the communities of resident organisms. Ecosystem models can provide a useful tool to explore these processes.

To study plankton dynamics in the ocean and, in particular, in a temperate shelf sea (as the main focus of this work), different models have been developed, ranging from very simple ones (e.g. the Lotka-Volterra competition model; Lotka, 1932; Volterra, 1926) to more sophisticated ones, adding more degrees of complexity by including advection, diffusion, or size structure (e.g. NEMO-ERSEM model; Edwards et al., 2012). Although complexity can be useful for describing the interacting behaviour of multiple system components incomplete understanding of the ecology and key processes of the organisms, and the lack of data for validation (Anderson, 2005) can reduce the reliability of predictions and also demands a higher computational cost. On the other hand, simpler models using an NPZ or NPZD framework, with the use of nutrients, phytoplankton, zooplankton, and detritus as the main model structure (e.g. Anderson, 2005; Wroblewski et al., 1988; Steele, 1974) have shown good agreement with observations in terms of chlorophyll and PP, by simulating the timing and magnitude of the spring bloom in different regions of the ocean.

NPZ models were first proposed by Riley in 1946 (Riley, 1946; Figure 4.1), to explicitly represent the first assumptions for the rate of change of phytoplankton over time, based on environmental factors and a grazing rate by zooplankton. In terms of environmental factors, it is known that phytoplankton growth depends on light, nutrients, and temperature

(Eppley, 1972; Jassby & Platt, 1976; Droop, 1983). These relationships define the seasonal cycle of phytoplankton in the S2P3 v7.0 model and in temperate shelf seas through thermal stratification of the water column, affecting the availability of inorganic nutrients in the surface layers where phytoplankton can produce organic matter via photosynthesis. In an NPZ model, these primary producers are grazed by zooplankton where a fraction of the ingested phytoplankton will be excreted and lost to the environment and added to sediments due to sinking, while another fraction will be remineralised through zooplankton mortality and added back into the inorganic nutrient pool (see Figure 2.6).

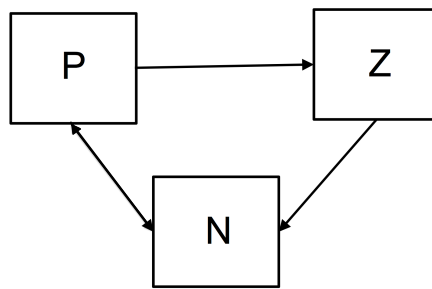


Figure 4.1: Conceptual view of NPZ models. The arrows represent the nutrient flow pathways between P (phytoplankton), Z (zooplankton), and N (DIN).

Simplistic biogeochemical models have been used to understand the dynamics of the NPZD cycle (Yool et al., 2011; Palmer & Totterdell, 2001; Six & Maier-Reimer, 1996; Sarmiento et al., 1993). Nowadays, it is known that the ecosystem community structure is regulated by a variety of factors including: physical conditions, predation, competition for resources, and environmental variability (Follows et al., 2007; Pedrós-Alió, 2006; Tilman, 1977; Margalef, 1968).

Despite their relative simplicity, NPZ models can be a better option to approach an understanding of the physics and biology of an ecosystem essentially depending about the question being asked. In this chapter, the S2P3 v7.0 model has been developed from the simplest assumption previously adopted where a fixed proportion of phytoplankton being grazed and remineralised into the DIN pool (grazing rate, G), to an NPZ framework (S2P3-NPZ) to capture the dominant dynamics of the biological system of the CCS location. This new development of the S2P3 v7.0 model will allow to understand how the predator-prey

relationship between zooplankton and phytoplankton is affected by meteorological forcing with stronger confidence that the model is making a better representation of the ecosystem.

4.2.2 Light, nutrients, and photosynthesis

This subsection provides an introduction to light, photosynthesis, and the photo-acclimation process of algal cells. It provides information about the S2P3 v7.0 model development into S2P3-photoacclim which represents the process of photo-acclimation and associated influences on cellular composition and physiology.

In previous chapters, it was explained how phytoplankton growth depends on different environmental factors, including temperature, nutrients, and irradiance. In this chapter, the analysis is focused on the influences that these three environmental factors play on phytoplankton growth and PP.

Light is fundamental to phytoplankton and photosynthesis, but phytoplankton growth can also be constrained by nutrient availability and temperature, affecting growth rates, making it necessary to understand the effects that each of these factors has on the seasonal cycle of PP. The temperature-dependence of growth rate can be explained as an exponential dependence according to Eppley (1972) as described in Chapter 2, section 2.2 (see Figure 2.3). On the other hand, availability of inorganic nutrients can also modify the nutrient quota (N:Chl), showing a maximum phytoplankton growth rate when N:Chl is maximum (see Figure 2.2). Moreover, it is necessary to understand the effects that irradiance has on algal cells and to learn about the way light penetrates in the water column and how it is absorbed by phytoplankton. Underwater light is commonly measured as irradiance or as photosynthetically available radiation (PAR; Wm^{-2}), a parameter that provides information about how much light is available for photosynthesis in the water column, including only photons in the visible spectrum with wavelengths between 400 and 700 nm and which usually correspond to the 45% of the total incident radiation (Kirk, 1994). In S2P3 v7.0, PAR decays exponentially through the water column (see Chapter 2, eq. 2.10), simulating the absorption and scattering of light in the ocean due to the interaction with water molecules, detrital matter, coloured dissolved organic matter, and phytoplankton (Dutkiewicz et al., 2015).

To understand the photo-acclimation process it is necessary to study two factors: (1) the relationship between photosynthesis and irradiance (PE curve; Figure 2.4), which provides information about the biophysical, biochemical, and metabolic processes that regulate photosynthesis. Also because the chemical composition of cell changes in response to light and nutrients variability, it is necessary to consider (2) the Chl:C and Chl:N ratios (Cloern et al., 1995; Langdon, 1988; Geider, 1987), where chlorophyll production is proportional to carbon fixation and nitrogen assimilation (Geider et al., 1998; Droop, 1983). On time scales from hours to days, phytoplankton adjust their physiological responses to variations in light intensity and nutrients, including variations in the amounts and ratios of photosynthetic pigments, gross chemical composition (e.g. C:N ratios), cell volume, and dark respiration rates (Falkowski, 1980).

In the Celtic Sea, stratification develops in spring (April; Hickman et al., 2012), triggering a phytoplankton bloom that depletes the surface mixed layer (SML) of nitrate (Fasham et al., 1983; Pingree et al., 1976). During the summer months, surface waters are relatively warm and nutrient depleted, with low concentrations of chlorophyll-*a* (Hickman et al., 2012). Low pigment standing stocks resulting from lack of nitrate in the SML hence permit light penetration to the thermocline, which will be determined by the competition between buoyancy input from solar heating and mixing caused by tidally generated turbulence at the seabed and wind at the surface (Simpson & Hunter, 1974). During this period, the thermocline will represent a barrier to transport between high-light surface waters and the low-light sub-surface chlorophyll maximum (SCM) (Sharples et al., 2001), contrary to winter months when a mixed water column is present and can be characterised by the rapid movement of phytoplankton between high and low light (Moore et al. 2003). Therefore, to understand the interactions of physical forcing and biological response of phytoplankton in the Celtic Sea, it is relevant to consider the photo-acclimation process of phytoplankton (S2P3-photoacclim model). This new version can model the light-, nutrient-, and temperature-dependencies of phytoplankton growth rate at the same time, by adding prognostic Chl:C, C:N, and Chl:N ratios based on Geider et al. (1998) model as described in Chapter 1, section 1.3.2.

4.2.3 Combining S2P3-NPZ and S2P3-photoacclim: S2P3 v8.0

The chapter aims to build on the findings of Chapter 3, where it was suggested that the differences in the timing of the spring bloom between buoy observations and CTD data during the years 2014 and 2015 in the CCS location were probably a consequence of the fixed grazing rate in the S2P3 v7.0 model or the non-inclusion of the photo-acclimation process. Further questions that remained from Chapter 3 (e.g. effect of the spring-neap tidal cycle, tendency of NPP in the humidity-only experiment, etc), could be analysed in future work with the newly developed model (S2P3 v8.0) to give more robust answers due to a more realistic representation of the CCS location as some relevant processes to temperate shelf seas can be represented in this model (e.g. zooplankton, photo-acclimation). Therefore, S2P3-NPZ and S2P3-photoacclim are developed into a new model called S2P3 v8.0 that combines both models in order to study the role of grazing and physiological flexibility on the dynamics of PP in the CCS location, by having a more realistic 1-D model. For this reason, the main objective of this chapter is to calibrate each model based on *in situ* observations and to analyse the effects of each parameter on the model dynamics and the associated relative sensitivities.

4.3 Methods

This section is divided into three different subsections: a description of the multiple data and observation types used to simultaneously constrain and validate the S2P3-NPZ, S2P3-Photoacclim, and S2P3 v8.0 model behaviours; a section calibrating each model and, also a sensitivity analysis for the CCS location.

The physical part of each model is the same as in the S2P3 v7.0 model and it is not described in this chapter (for more information see Chapter 2, section 2.1).

4.3.1 Validation of the model

S2P3-NPZ, S2P3-Photoacclim, and S2P3 v8.0 are calibrated and validated using the CTD observations and time-series from the Smartbuoy and CaNDyFloSS moorings described in Chapter 3, section 3.3.2. For S2P3-NPZ, zooplankton biomass was used to validate this model in the CCS location. Similarly, physiological observations were used to validate the S2P3-Photoacclim model.

4.3.1.1 Zooplankton biomass

Zooplankton biomass samples were collected during the cruises DY026, DY018, DY029, and DY033 across the Celtic Sea (Figure 4.2) at three main stations: the Shelf Edge near the shelf break (CS2 site; $48^{\circ}34$ N, $9^{\circ}30$ W, ~ 200 m water depth), the Central Site or CCS location ($49^{\circ}25$ N, $8^{\circ}35$ W, ~ 150 m water depth); and the Celtic Deep near the coast ($\sim 51^{\circ}10$ N, $6^{\circ}20$ W, ~ 100 m water depth). These cruises were undertaken during four periods: 5th - 12th August 2014, 10th - 29th November 2014, 3rd - 28th April 2015, and 13th - 31st July 2015 (Giering et al., 2018). For this work, only the CCS site data is considered for analysis because this location is directly comparable to buoy observations.

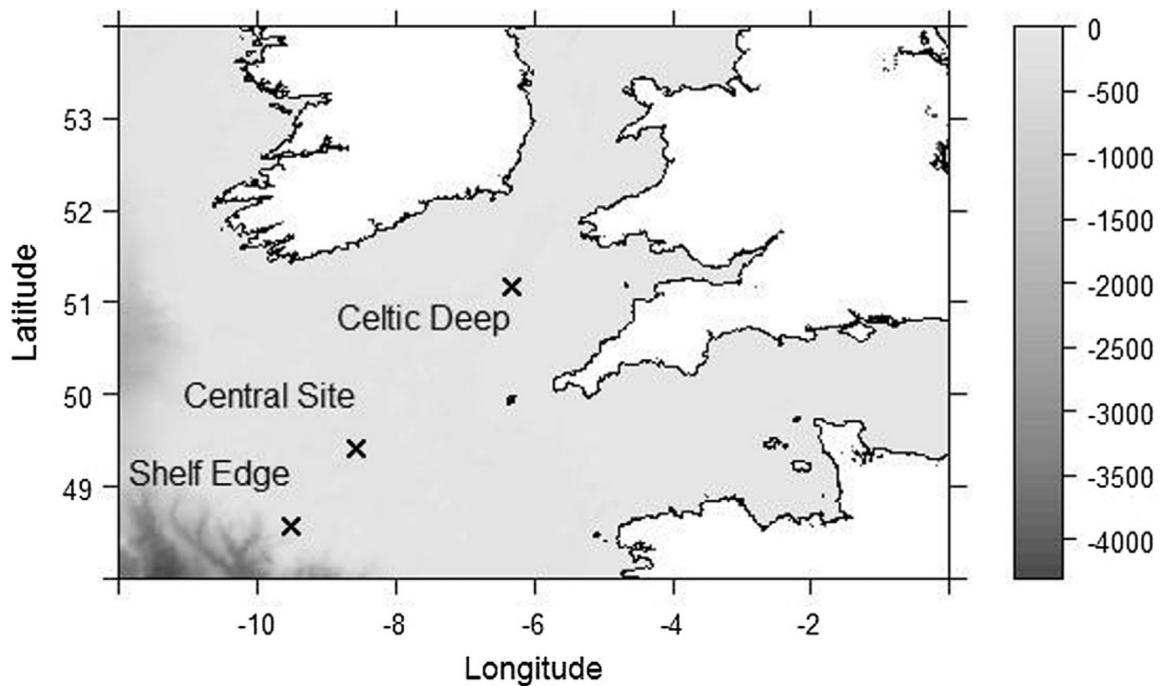


Figure 4.2: Map of the three main stations across the Celtic Sea for the cruises DY026, DY018, DY029, and DY033. The sampling sites are represented by crosses and include the Celtic Deep, the Central Site (or CCS site), and the Shelf Edge. Grey scale shows the bathymetry (in m). Image taken from Giering et al., 2018.

For zooplankton biomass samples, net rings of 57 cm diameter were used and fitted with two different mesh sizes of 63 μm and 200 μm . The nets had a closing mechanism when deployed, sampling zooplankton biomass during daytime and night-time at different depth: above and below the thermocline, and, when existing, across the deep chlorophyll maximum (DCM; determined based on fluorescence measurements). The thermocline and DCM were determined from CTD casts immediately prior to the net deployments. The 63 μm and 200 μm mesh nets were hauled at 0.2 m s^{-1} and 0.5 m s^{-1} , respectively. See Table 4.1 for more details about net deployments in each site, depth, and date.

Zooplankton were fractionated into microplankton, small mesozooplankton, and large mesozooplankton by using different mesh sizes. For this work, only mesozooplankton biomass at the CCS location was considered due to the small contribution that microzooplankton has in this location, contributing only $\sim 1.3\%$, $\sim 2.3\%$, and $\sim 0.8\%$ of the total zooplankton biomass for the measurements done in November, April, and July, respectively

(Giering et al., 2018). Furthermore, microzooplankton was not directly measured but their biomass values were inferred from FlowCam images. Mesozooplankton consist in a community composition that included: amphipods, appendicularian, chaetogratha, copepods, euphausiacea, polychaeta, and others (e.g. cladocerans, dinoflagellates, echinoderm, eggs, foraminifera, gymnosomata, unidentified larvae, nauplii, ostracods and radiolarian, all of which contributed < 3% in all samples). A FlowCam (Fluid Imaging Technologies Inc.) and a ZooScan were used to scan zooplankton individuals images processed using ZooProcess 7.19 and Plankton Identifier 1.3.4 softwares (Gorsky et al., 2010). From the images the biovolume spectra were calculated and converted into image-derived dry weight (DW). The total 246 net hauls collected for biomass samples (Figure 4.3) provided 44 vertical depth profiles, integrating zooplankton biomass typically between 0 and 120 m at the CCS location. The complete data set can be obtained from the British Oceanographic Data Centre (BODC), <http://www.bodc.ac.uk/data>.

Date	Net opened at day	Net opened at night	Shallow depth (in m)	SCM depth* (in m)	Deep depth (in m)	Integrated depth (in m)
05/08/2014	13:41	21:29	0-30		30-120	0-120
10/11/2014	14:01	20:24	0-50		50-130	0-130
12/11/2014	13:31	03:11	0-50		50-130	0-130
25/11/2014	14:02	20:55	0-60		60-130	0-130
04/04/2015	16:19	23:59	0-80		80-120	0-120
05/04/2015	16:20	00:06	0-60		60-140	0-140
10/04/2015	NA	21:38	0-60		60-120	0-120
11/04/2015	15:20	21:34	0-50		50-120	0-120
15/04/2015	14:12	21:27	0-20		20-120	0-120
16/04/2015	11:24	20:04	0-40		40-120	0-120
20/04/2015	14:15	21:00	0-50		50-120	0-120
21/04/2015	11:16	20:20	0-50		50-120	0-120
25/04/2015	14:12	21:44	0-50		50-120	0-120
28/04/2015	NA	00:17	0-50		50-120	0-120
13/07/2015	13:40	23:50	0-60		60-120	0-120
14/07/2015	13:33	21:46	0-30	30-70	70-120	0-120
25/07/2015	12:43	NA	0-30	30-70	70-130	0-130
29/07/2015	12:23	22:02	0-30	30-50	50-130	0-130
30/07/2015	12:29	22:26	0-30	30-70	70-130	0-130

Table 4.1: Net deployments at the CCS locations including date, time during the day and night, and depth horizons. *SCM depth sampled when SCM present. Information obtained from Giering et al., 2018.

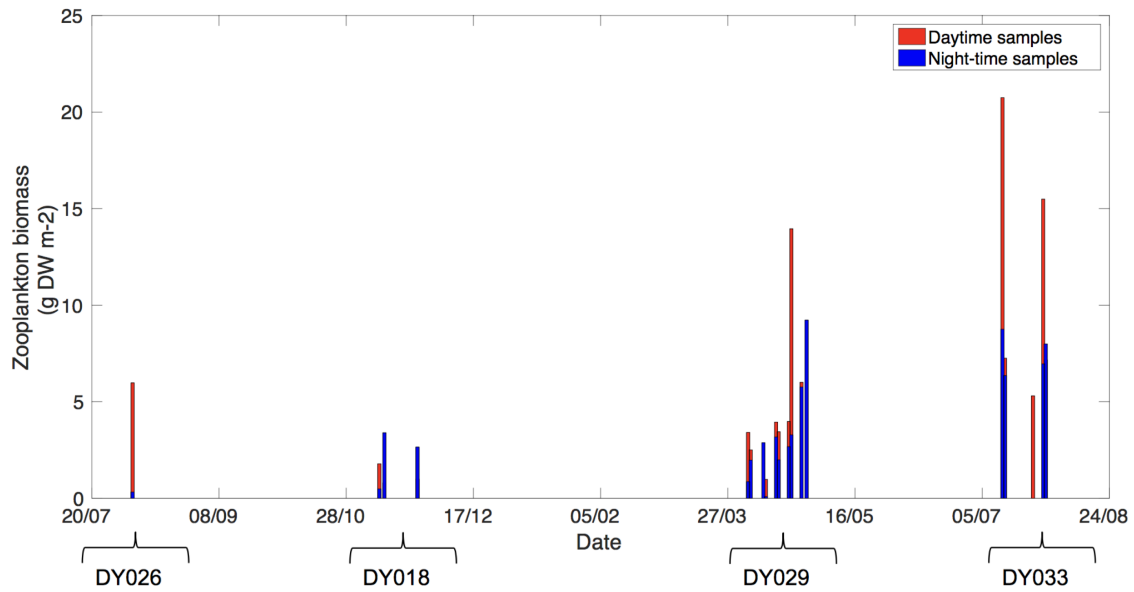


Figure 4.3: Depth-integrated zooplankton biomass for daytime and night-time samples at the CCS location, including different species of mesozooplankton from the cruises DY026, DY018, DY029, and DY033.

Observations from the four different cruises of depth-integrated zooplankton biomass (g DW m^{-2}) were obtained over the years 2014 and 2015. Note that there is usually more zooplankton biomass during daytime over the whole water column and a seasonal cycle of zooplankton can also be observed (Figure 4.3), with lower values during November 2014 (winter) and highest values during July 2015 (summer). This dataset allows comparison with the S2P3-NPZ model not only in terms of phytoplankton biomass, but also in terms of the seasonal cycle of zooplankton, providing validation of the spring zooplankton bloom and summer growth. However, it is important to note that the S2P3-NPZ model does not account for changes in the community composition of mesozooplankton during the different seasons of the year as it does not differentiate between species, but it does average the total biomass of the different species of mesozooplankton found at the CCS location.

4.3.1.2 Physiological observations

Samples were collected at a number of stations in the Celtic Sea from the cruises JR98 and CD173 (Figure 4.4). The JR98 cruise was undertaken from 24th July to 14 August of 2003. In Figure 4.4 it is shown the different stations, from the Irish Sea to the Celtic Sea

shelf break, ranging from weakly stratified or fully mixed stations (IS1b) to very strong, narrow thermoclines in the southern Celtic Sea (CS1), and to the weak, deep surface layer associated with internal wave mixing at the shelf edge (CS2). The physiological properties (e.g. photoacclimation) and survival strategies of phytoplankton in the SCM determine the efficiency of nutrient assimilation within the thermocline and lead, in turn, to broadly predictable patterns in the density and species composition of the population (Hickman et al., 2012; Hickman et al., 2009). On the other hand, the CD173 cruise was undertaken from 15th July to 6th August of 2005. CD173 was the second cruise from the project "Physical-Biological Control of New Production within the Seasonal Thermocline". This cruise expedition was split into two: from July 15th – July 25th it was primarily focused on the shelf edge of the Celtic Sea, in an investigation of the spring-neap variability in the vertical mixing of nutrients by the breaking internal tide; from July 25th – August 6th it was carried out an investigation of the effects of seabed banks on the generation of internal mixing and the response of the primary producers. Figure 4.4 also shows the sites occupied in this cruise, from the stratified region of the Celtic Sea shelf (stations D2, CS1, CS3, U2, CS1, B2, JB1, OB, P1, ctd16) and shelf break (stations CS2, N1) and at a mixed site within the Irish Sea (station IS1).

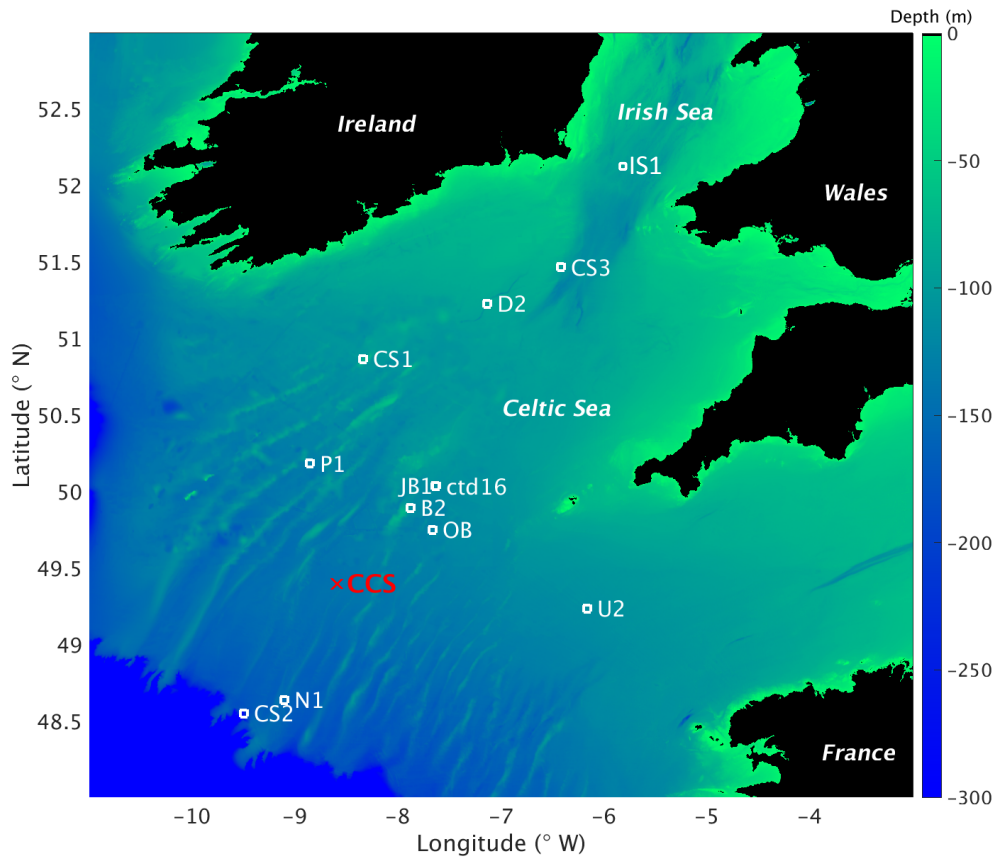


Figure 4.4: Map for study area and stations for the JR98 (stations IS1, CS3, D2, CS1, U2, N1, CS2) and CD173 (stations B2, CS2, JB1, OB, P1, U2, ctd16) cruises, including the CCS location (in red colour). Image created with Matlab using the repository data for gridded bathymetry provided by General Bathymetric Chart of the Oceans (GEBCO). Bathymetric data only considered for the shelf sea region (0 to 300m depth) with open ocean depth neglected (deeper than 300m). Continents considered in black colour (over 0m elevation).

Photosynthesis versus irradiance (P vs E) experiments were conducted in short-term incubations (2 - 4h) using a photosynthetron (Moore et al., 2006). A photosynthetron is a chamber that allows simultaneous incubations of multiple samples over a range of light intensities to provide a P vs E curve (Figure 2.4; Lewis & Smith, 1983). From these P vs E experiments chlorophyll-*a* normalised PP was derived from ^{14}C uptake to obtain the chlorophyll-*a* specific maximum light-saturated photosynthesis rate P_{\max}^{Chl} ($\text{mg C (mg Chl - a)}^{-1} \text{ h}^{-1}$) and the maximum light utilisation coefficient, α^{chl} ($\text{mg C (mg Chl-a)}^{-1}$

h^{-1} ($\mu\text{E m}^{-2} \text{s}^{-1}$)⁻¹) (Hickman et al., 2012; Jassby & Platt, 1976). Water samples were collected before dawn using 10-liter Niskin bottles for four of the sites: CS1, CS2, CS3, and IS1 (Figure 4.4) during 24-h periods on 31st July, 29th July, 05th August, and 2nd August, respectively. Multiple samples were collected in the surface and in deeper layers (in the surface mixed layer (SML) and the SCM) to obtain different phytoplankton populations throughout the photoperiod. Additionally the CS1 and CS3 sites were resampled on 10 and 11 August, respectively. The water samples were then incubated in 73 ml polycarbonate bottles in photosynthetrons at constant temperature corresponding to measured depths in the SML or the SCM. Values of α^{chl} and the light saturation parameter, E_k ($\mu\text{E m}^{-2} \text{s}^{-1}$) (given by $E_k = P_{\text{max}}^{\text{Chl}}/\alpha^{\text{chl}}$) were spectrally corrected to the *in situ* irradiance at the sample depth according to the phytoplankton light absorption (Moore et al., 2006).

For this work, observations from both cruises were used considering only the stations from the seasonally stratified sites (B2, CS1, CS3, D2, JB1, OB, P1, U2, and ctd16) and excluding stations CS2 and N1 because they are in the shelf edge where advective fluxes are more relevant than in the stations nearer to the CCS location. The maximum light utilisation coefficient (α^{chl}) was constrained for the model by finding the mean from all observations ($\alpha^{\text{chl}} = 9.16 \times 10^{-6} \text{ mg C (mg Chl-a)}^{-1} \text{ h}^{-1} (\mu\text{E m}^{-2} \text{s}^{-1})^{-1}$), and therefore, the values of $P_{\text{max}}^{\text{Chl}}$ and E_k were used as variables for comparison with equivalent modelled values (Figure 4.5). Figure 4.5 shows that near the sea surface where there is high light photo-acclimation of phytoplankton, values of $P_{\text{max}}^{\text{Chl}}$ and E_k are higher than in deeper layers of the water column. With the observed $P_{\text{max}}^{\text{Chl}}$ having a range of approximately $0.5\text{-}2.5 \times 10^{-3} \text{ (mg C (mg Chl-a)}^{-1} \text{s}^{-1})$ in the surface waters (first 5m), while this range is smaller and lower in deeper layers ($0\text{-}1.0 \times 10^{-3} \text{ mg C (mg Chl-a)}^{-1} \text{s}^{-1}$) for the 40m depth. Similar variability can be observed with E_k , having lower values in deeper layers of the water column, but the largest variability occurs in the surface layer ($\sim 100\text{-}250 \mu\text{E m}^{-2} \text{s}^{-1}$).

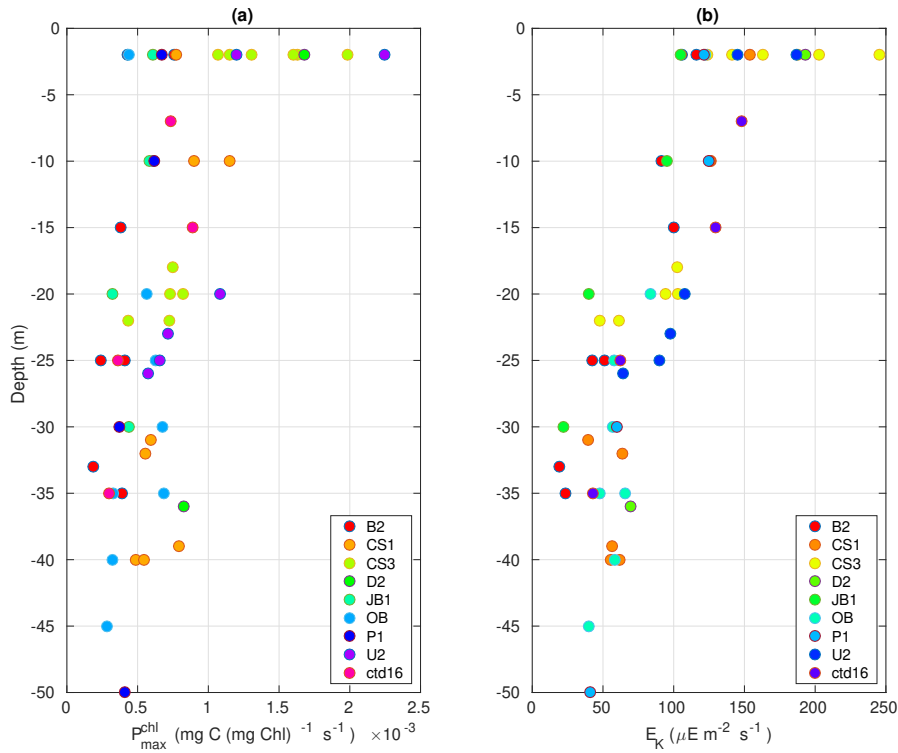


Figure 4.5: Photophysiological parameters obtained from ^{14}C -uptake photosynthesis versus irradiance experiments ($n = 55$) from the JR98 and CD173 cruises. (a) Chlorophyll- a specific maximum light-saturated photosynthesis rate, and (b) Light saturation parameter, spectrally corrected to the *in situ* irradiance at the sample depth (see Moore et al., 2006).

4.3.2 Calibration of the models

This section explains the methodology used to calibrate each version of the S2P3 model developed in this work.

To calibrate or tune a model, there is usually two options: an approach to determine the values of the model parameters is to run the model to equilibrium with many separate sets of parameters and then determine which set provides results that are in best agreement with observations (trial-and-error basis); another alternative would be to undertake a formal parameter optimisation, where each parameter of the model is automatically adjusted until disagreement with the *in situ* observations is minimised. The latter approach requires sophisticated numerical modifications of the code and is computationally expensive, therefore, in this work it was used the first approach. Besides, the first approach also permits

to investigate directly the sensitivity of the model to changes in the parameters.

Calibrating each model developed in this work was performed on a trial-and-error basis, by adjusting the NPZ and physiological parameters based on their agreement with the observations described in this methodology and in Chapter 3, section 3.3.2. Parameter values adjustment were set based on previously published modelling studies (see Table 4.2), with some parameters and variables set and initialised based on the *in situ* observations. It is important to note that the range of parameter values referred in Table 4.2 were obtained through different methodologies (observations, laboratory cultures, and models) and different locations, therefore, the calibrated versions of the S2P3-NPZ, S2P3-Photoacclim, and S2P3 v8.0 models might not necessarily adjust to these parameter ranges. Consequently, not all parameter values from Table 4.2 might be representative for the CCS location, but it is relevant to have an estimate to start the model calibrations.

Parameters	Range	Units	Reference
γ_1	[0.2 - 0.7]	dimensionless	Franks et al. (1986); Raymont (1980)
γ_2	[0.1 - 0.9]	dimensionless	
λ	[0.1 - 2.0]	$(\text{mmol N m}^{-3})^{-1}$	Franks et al. (1986); Checkley (1980); Frost (1972); McAllister (1970)
R_m	[0.16 - 1.5]	d^{-1}	Franks et al. (1986)
m	[0.07 - 1.75]	d^{-1}	Franks et al. (1986); Steele & Henderson (1981); Steele & Frost (1977); Steele (1974)
P_{\max}^C	[3.0 - 5.1]	d^{-1}	Geider et al. (1998) and Sources
Q_m	[0.167 - 0.2]	mg N (mg C)^{-1}	Geider et al. (1998) and Sources
θ_{\max}^N	[0.3 - 0.4]	$\text{mg Chl (mg N)}^{-1}$	Geider et al. (1998) and Sources
$R_C = R_n = R_{\text{chl}}$	[0.0 - 0.025]	d^{-1}	Geider et al. (1998) and Sources
Q_{\min}	[0.04 - 0.04]	mg N (mg C)^{-1}	Geider et al. (1998) and Sources
u_m	[0.5 - 1.0]	mg N (mg C)^{-1} d^{-1}	Geider et al. (1998) and Sources

Table 4.2: Ranges for parameter values for the S2P3-NPZ, S2P3-Photoacclim, and S2P3 v8.0 models. Sources from Geider et al. (1997); Langdon (1988); Falkowski et al. (1985); Cosper (1982); and Yoder (1979) for phytoplankton species: *Skeletonema costatum*, *Thalassiosira pseudonana*, *Isochrysis galbana*, and *Pavlova lutheri*.

4.3.3 Sensitivity analysis

A sensitivity analysis was performed to assess the robustness of the results and conclusions based on the uncertainty of some parameter values for each version of the S2P3 model.

After calibrating/tuning each version of the model, the set of parameters listed in Table 4.2 were analysed taking into account the range of values found in the literature. Model runs with these parameters were compared to observations and to the default version of each model developed (or calibrated version). Each parameter was varied one at a time in order to understand how sensitive the model is to those changes and the effect that they have on the modelled ecosystem dynamics of the CCS location. For every experiment developed to perform these sensitivity analyses, each parameter was varied from the best calibrated value by +50% and -50%.

4.3.3.1 S2P3-NPZ

Sensitivity studies were conducted to study five different parameters in the S2P3-NPZ model to understand the effects on predator-prey dynamics of phytoplankton and zooplankton. This sensitivity analysis included comparisons with observations from the Candyfloss and Smartbuoy time-series of surface chlorophyll-*a*, and CTD data at the CCS site (Chapter 3, section 3.3.2). This model also allowed comparison to the zooplankton biomass observations (Giering et al., 2018).

The procedure of the sensitivity analysis consists of finding the best fit/calibrated version of the S2P3-NPZ model in comparison to *in situ* observations, minimising the differences in terms of the timing and magnitude of the spring phytoplankton bloom, summer chlorophyll-*a*, spring zooplankton bloom magnitude, and chlorophyll-*a* and DIN vertical structures. The calibrated experiment of this model was called 'Control NPZ', which was found by changing the following five parameters: γ_1 , γ_2 , λ , R_m , and m (see Chapter 2, section 2.2.2). Each of these parameters were adjusted from +50% and -50% from their values found in the Control NPZ experiment (Table 4.3).

4.3.3.2 S2P3-Photoacclim

A sensitivity analysis was performed for the S2P3-Photoacclim model to understand the effects of physiological parameters in the ecosystem dynamics. These parameters included: P_{\max}^C , Q_m , θ_{\max}^N , and respiration rates ($R_C = R_n = R_{\text{chl}}$) (see Chapter 2, section 2.2.3). The model did not show to be sensitive to changes in the Q_{\min} and u_m parameters, therefore, they are not shown in this section.

Each experiment of the sensitivity analysis for this model was compared to *in situ* observations, considering the timing and magnitude of the spring phytoplankton bloom, the vertical structure of chlorophyll-*a*, DIN, chlorophyll-*a* specific maximum light-saturated photosynthesis rate, and light saturation parameter. The calibrated experiment of this model was called 'Control Photoacclim'. Each physiological parameter was adjusted from -50% and +50% from their values found in the Control Photoacclim experiment (Table 4.4).

4.3.3.3 S2P3 v8.0

For the S2P3 v8.0 model the procedure for the sensitivity analysis was the same as the one performed for the S2P3-NPZ and S2P3-Photoacclim models. The advantage of this model in comparison to the other versions of the S2P3 model studied in this chapter, is that it is possible to analyse the zooplankton parameters at the same time as analysing the physiological parameters that are involved in the photo-acclimation process. Therefore, the sensitivity analysis for the S2P3 v8.0 model includes experiments that vary each parameters from +50% and -50% based on the values found in the Control NPZPhot experiment, which is the calibrated version of this model in comparison to observations (Table 4.5).

Name of experiments	γ_1	γ_2	λ	R_m	m
Run1	0.1	0.5	0.75	2.5	0.05
Run2	0.3	0.5	0.75	2.5	0.05
Run3	0.2	0.25	0.75	2.5	0.05
Run4	0.2	0.75	0.75	2.5	0.05
Run5	0.2	0.5	0.375	2.5	0.05
Run6	0.2	0.5	1.125	2.5	0.05
Run7	0.2	0.5	0.75	1.25	0.05
Run8	0.2	0.5	0.75	3.75	0.05
Run9	0.2	0.5	0.75	2.5	0.025
Run10	0.2	0.5	0.75	2.5	0.075
Control NPZ	0.2	0.5	0.75	2.5	0.05

Table 4.3: List of experiments developed for the sensitivity studies of the S2P3-NPZ based on the Control NPZ experiment.

Name of experiments	P_{\max}^C	Q_m	θ_{\max}^N	$R_C = R_n = R_{chl}$
Phot1	1.0	0.4	0.3	0.02
Phot2	3.0	0.4	0.3	0.02
Phot3	2.0	0.2	0.3	0.02
Phot4	2.0	0.6	0.3	0.02
Phot5	2.0	0.4	0.15	0.02
Phot6	2.0	0.4	0.45	0.02
Phot7	2.0	0.4	0.3	0.01
Phot8	2.0	0.4	0.3	0.03
Control Photoacclim	2.0	0.4	0.3	0.02

Table 4.4: List of experiments developed for the sensitivity studies of the S2P3-Photoacclim based on the Control Photoacclim experiment.

Name of experiments	P_{\max}^C	Q_m	θ_{\max}^N	$R_C = R_n = R_{chl}$	γ_1	γ_2	λ	R_m	m
NPZPhot1	1.75	0.45	0.15	0.02	0.1	0.4	0.2	3.5	0.02
NPZPhot2	5.25	0.45	0.15	0.02	0.1	0.4	0.2	3.5	0.02
NPZPhot3	3.5	0.225	0.15	0.02	0.1	0.4	0.2	3.5	0.02
NPZPhot4	3.5	0.675	0.15	0.02	0.1	0.4	0.2	3.5	0.02
NPZPhot5	3.5	0.45	0.075	0.02	0.1	0.4	0.2	3.5	0.02
NPZPhot6	3.5	0.45	0.225	0.02	0.1	0.4	0.2	3.5	0.02
NPZPhot7	3.5	0.45	0.15	0.01	0.1	0.4	0.2	3.5	0.02
NPZPhot8	3.5	0.45	0.15	0.03	0.1	0.4	0.2	3.5	0.02
NPZPhot9	3.5	0.45	0.15	0.02	0.05	0.4	0.2	3.5	0.02
NPZPhot10	3.5	0.45	0.15	0.02	0.15	0.4	0.2	3.5	0.02
NPZPhot11	3.5	0.45	0.15	0.02	0.1	0.2	0.2	3.5	0.02
NPZPhot12	3.5	0.45	0.15	0.02	0.1	0.6	0.2	3.5	0.02
NPZPhot13	3.5	0.45	0.15	0.02	0.1	0.4	0.1	3.5	0.02
NPZPhot14	3.5	0.45	0.15	0.02	0.1	0.4	0.3	3.5	0.02
NPZPhot15	3.5	0.45	0.15	0.02	0.1	0.4	0.2	1.75	0.02
NPZPhot16	3.5	0.45	0.15	0.02	0.1	0.4	0.2	5.25	0.02
NPZPhot17	3.5	0.45	0.15	0.02	0.1	0.4	0.2	3.5	0.01
NPZPhot18	3.5	0.45	0.15	0.02	0.1	0.4	0.2	3.5	0.03
Control NPZPhot	3.5	0.45	0.15	0.02	0.1	0.4	0.2	3.5	0.02

Table 4.5: List of experiments developed for the sensitivity studies of the S2P3 v8.0 model based on the Control NPZPhot experiment.

4.4 Results

This section is divided into two main parts. The first part shows the calibrated versions of the S2P3-NPZ, S2P3-Photoacclim, and S2P3 v8.0 models compared to *in situ* observations. The second part of this section shows the sensitivity analysis of each model compared to the calibrated version of each model and to observations.

4.4.1 Calibration

The best fit calibrated version of each model was found through comparison to observations. Seasonal cycles of phytoplankton (Figure 4.6a) and zooplankton (Figure 4.6b) were considered from the start of April of the year 2014 to the end of June of the year 2015. In the case of buoy observations, two spring phytoplankton blooms can be observed in the early spring during March and April of each year (surface chlorophyll-*a*; red line). On the other hand, the lowest values of zooplankton biomass are found during winter (November 2014), while the highest values can be observed during summer (July 2015).

As described in Chapter 2, the physical part of each model is exactly the same as in the S2P3 v7.0 model, therefore, there are no differences in the physical seasonality of the ecosystem and it is not affected by the change of parameter values, therefore, comparison of surface temperature buoy observations was omitted in this chapter.

4.4.1.1 S2P3-NPZ

The S2P3-NPZ model is represented in magenta colour in this chapter. To calibrate this model, it was necessary to test different experiments by changing parameter values of γ_1 , γ_2 , λ , R_m , and m . As a starting point, the values suggested in Table 4.2 were taken into account to set each parameter between those ranges. In a trial-and-error basis, each parameter was changed at one time.

To calibrate this model it was necessary to understand beforehand the effects that each parameter has in the model dynamics. For example, an increase of γ_1 implies more sloppy feeding which would increase the values of surface chlorophyll-*a* due to the increase in

N released by grazed phytoplankton being directly supplied to the DIN pool. A change in γ_2 will modify the amount of dead zooplankton going to sediments or the DIN pool (Figure 2.6), therefore, an increase in γ_2 would increase the amount of N released by dead zooplankton into the DIN pool. On the other hand, changes in λ would play a direct role in the predator-prey relationship and estimating the effects that this parameter has in the model dynamics are more complex to understand; a decrease of λ would weaken the grazing effects of zooplankton on phytoplankton, while stronger predator-prey interactions could be expected when λ is increased. Another parameter that affects the phytoplankton and zooplankton dynamics is R_m , where an increase of this parameter would imply that zooplankton can graze more phytoplankton per unit time and a decrease of R_m will allow phytoplankton to grow more. Finally, zooplankton mortality (m) will modify how much zooplankton dies per unit time, affecting phytoplankton growth through modification of grazing pressure and resupply of zooplankton associated N to the DIN pool.

With the best fit of the S2P3-NPZ model found, differences can be seen in terms of the timing of the spring phytoplankton bloom for the year 2015, with a later bloom from the S2P3-NPZ model, reaching a peak bloom about a month later (Figure 4.6). Additionally, the magnitude of the spring phytoplankton bloom is also higher in the model in comparison to observations. Phytoplankton is able to escape grazing control in April and early May, with the spring zooplankton bloom occurring about a month later. During summer months (June, July, and August) there are low concentrations of chlorophyll-*a* at the surface for the buoy observations and the S2P3-NPZ model as shown in Figure 4.6a. Over winter months (December, January, and February) phytoplankton biomass observations reach a minimum, with surface chlorophyll-*a* decreasing to zero in the model.

CTD observations compared to the calibrated S2P3-NPZ model show that during spring (Figure 4.7b), the model has not yet reached the spring phytoplankton bloom as in the observations, therefore, there are very low chlorophyll-*a* concentrations at the surface and inorganic nutrients have not yet been depleted at this stage. On the other hand, during summer months there is an SCM in the buoy observations and in the model (Figure 4.7e), with a similar magnitude, although this is shallower in the case of the model.

4.4.1.2 S2P3-Photoacclim

The S2P3-Photoacclim model is represented in blue colour in this chapter. To calibrate this model, it was necessary to test different experiments by changing parameter values of P_{\max}^C , Q_m , θ_{\max}^N , and respiration rates ($R_C = R_n = R_{chl}$). As a starting point, the values suggested in Table 4.2 were taken into account to be set between those ranges. In a trial-and-error basis, each parameter was changed at one time.

Similar to the S2P3-NPZ model, understanding the effects of each parameter in the model dynamics was necessary. For example, changes in P_{\max}^C modify the maximum growth of phytoplankton under saturated nutrients and irradiance levels in the P vs E curve described in Figure 2.4, therefore, a change in this parameter is expected to modify the timing and magnitude of the spring phytoplankton bloom. Another parameter that was changed to find the best fit of S2P3-Photoacclim model was Q_m , which will modify the maximum uptake rate of inorganic nutrients and it is likely to modify the concentrations of DIN at the surface and phytoplankton growth. Additionally, under balanced growth conditions, θ_{\max}^N is inversely related to the light-saturation parameter (E_k), which means that an increase of θ_{\max}^N will decrease E_k . Finally, changes in the respiration rates modify the phytoplankton carbon concentrations based on the imbalances with photosynthesis, therefore, it will affect the magnitude and timing of the spring phytoplankton bloom.

Differences can be observed between the calibrated S2P3-Photoacclim model and buoy observations in terms of the timing of the spring phytoplankton bloom (Figure 4.6a). These differences in the timing are complex to constrain because fitting earlier blooms modifies the magnitude of the spring bloom by increasing it to unrealistic levels.

CTD observations compared to the calibrated S2P3-Photoacclim model showed that during spring (Figure 4.7b), the model has not yet reached the spring phytoplankton bloom as in the observations, therefore, there are very low chlorophyll-*a* concentrations at the surface and inorganic nutrients have not yet been depleted at this stage. On the other hand, during summer months there is a marked and shallower SCM than in the CTD observations (Figure 4.7e).

Finally, there is good agreement between physiological observations and the model (Figure

4.8), with sensible values of P_{\max}^{chl} and E_k found through the water column, showing novelty work performed to calibrate this model against physiological data.

4.4.1.3 S2P3 v8.0

The S2P3 v8.0 model is represented in green colour in this chapter. To calibrate this model, it was necessary to change every parameter that was used to constrain the S2P3-NPZ and S2P3-Photoacclim models. With more degrees of freedom due to the larger number of parameters than in any of the other models, it was necessary to develop more experiments on a trial-and-error basis allowing more data constraints.

Figure 4.6a shows that between the three models the best agreement found in comparison to buoy observations correspond to the S2P3 v8.0 model. The timing and magnitude of the spring phytoplankton bloom show some remaining small differences with the buoy observations, with higher concentrations of surface chlorophyll-*a* during spring ($\sim 10 \text{ mg Chl m}^{-3}$). Moreover, the timing of the spring phytoplankton bloom during the year 2014 matches the observations but a delayed bloom is shown during the year 2015. Quantitatively, an RMSD was calculated between the buoy observations and the chlorophyll time-series of the S2P3 v8.0, S2P3-Photoacclim, and S2P3-NPZ, resulting in a difference of $1.67 \text{ mg Chl m}^{-3}$, $2.68 \text{ mg Chl m}^{-3}$, and $2.7 \text{ mg Chl m}^{-3}$, respectively. Correlations between each model and the buoy observations were also calculated between the time-series, with the strongest and significant correlation given for the S2P3 v8.0 model ($r^2=0.23$, $p < 0.05$), followed by the S2P3-NPZ model ($r^2=0.19$, $p < 0.05$), and finally, the S2P3-Photoacclim ($r^2=-0.006$, $p > 0.05$). It is important to note that low correlations between the models and the surface chlorophyll observations can be given due to disagreement with the timing of the spring phytoplankton bloom, specially during the year 2015 where none of the models matched the observed timing and during winter months each model show lower values of surface chlorophyll than the observations. Altogether, the S2P3 v8.0 does have a better agreement with the buoy observations than the S2P3-NPZ and S2P3-Photoacclim models. On the other hand, zooplankton biomass (Figure 4.6b) is higher than in the S2P3-NPZ and the predator-prey relationship is well represented, with the spring zooplankton bloom happening approximately a month later than the spring phytoplankton bloom. However, quantifying the differences between each model and the zooplankton biomass observations

is complex due to the nature of the sampling (discrete values over the seasons), although the S2P3-NPZ and S2P3 v8.0 represent low values of zooplankton during winter months which show agreement with observations having the lowest values sampled for November. Furthermore, the highest values of observed zooplankton biomass occur during July while the models represent high values of zooplankton from late May.

Vertical profiles of chlorophyll-*a* during spring (Figure 4.7b) show higher values at the surface than in the CTD observations, therefore, the concentrations of DIN at the surface are lower than in the observations (Figure 4.7c). On the other hand, during summer months, the SCM of the model has the same magnitude than in the observations but it is shallower (Figure 4.7e).

Finally, the physiological variables from the model have a good agreement with observations through the water column (Figure 4.8), although higher values of P_{\max}^{chl} and E_k are shown in comparison to the ones found in the S2P3-Photoacclim calibrated model.

Table 4.6 shows each parameter that was used to calibrate the S2P3-NPZ, S2P3-Photoacclim, and S2P3 v8.0 models. The chosen values of each parameter are listed along the calibrated version of each model: Control NPZ, Control Photoacclim, and Control NPZPhot.

Parameters	Control NPZ	Control Photoacclim	Control NPZPhot
γ_1	0.2		0.1
γ_2	0.5		0.4
λ	0.75		0.2
R_m	2.5		3.5
m	0.05		0.02
P_{\max}^C		2.0	3.5
Q_m		0.4	0.45
θ_{\max}^N		0.3	0.15
$R_C = R_n = R_{\text{chl}}$		0.02	0.02

Table 4.6: List of parameter values for the Control NPZ, Control Photoacclim, and Control NPZPhot experiments (for parameter units see Table 4.2).

Further quantitative comparison between each newly developed model and the buoy observations were made as shown in Table 4.7. A comparison with the time-series of surface

chlorophyll (Figure 4.6a), shows that the timing of the spring bloom is earlier during 2014 for the S2P3 v8.0 model than in the observations by two days, while during the year 2015, the model shows a later start of the bloom by 24 days. In this context, the S2P3-NPZ and S2P3-Photoacclim models show later timing of the spring bloom than the observations, but these differences are larger than with the S2P3 v8.0 model, while the S2P3-Photoacclim shows the lesser accurate timing based on the observations, with a delayed bloom by 20 days (2014) and 51 days (2015). Moreover, the length of the spring bloom and total spring surface chlorophyll were also calculated but only for the year 2014 due to the lack of data in the observations during the year 2015. The length of the spring bloom shows that the S2P3-Photoacclim model and the S2P3 v8.0 models are the most similar to the observed length of the spring bloom. The total spring surface chlorophyll is higher for the S2P3-NPZ and S2P3-Photoacclim models than the observations, showing that the most accurate value correspond to the S2P3 v8.0 model. Consequently, the S2P3 v8.0 model does a better representation of the CCS location than the S2P3-NPZ and S2P3-Photoacclim models.

Characteristic	Year	Buoy	S2P3-NPZ	S2P3-Phot	S2P3 v8.0
Timing spring bloom	2014	5 th April	14 th April	25 th April	3 rd April
	2015	16 th March	24 th April	6 th May	9 th April
Length spring bloom (days)	2014	35	27	40	40
Total spring chl (mg Chl m ⁻³)	2014	138.4	208.6	224.15	137.7

Table 4.7: Quantitative comparison of observed time-series of surface chlorophyll from buoy samples in terms of the timing and length of the spring bloom, and the total spring surface chlorophyll between the S2P3-NPZ, S2P3-Photoacclim, and S2P3 v8.0 models.

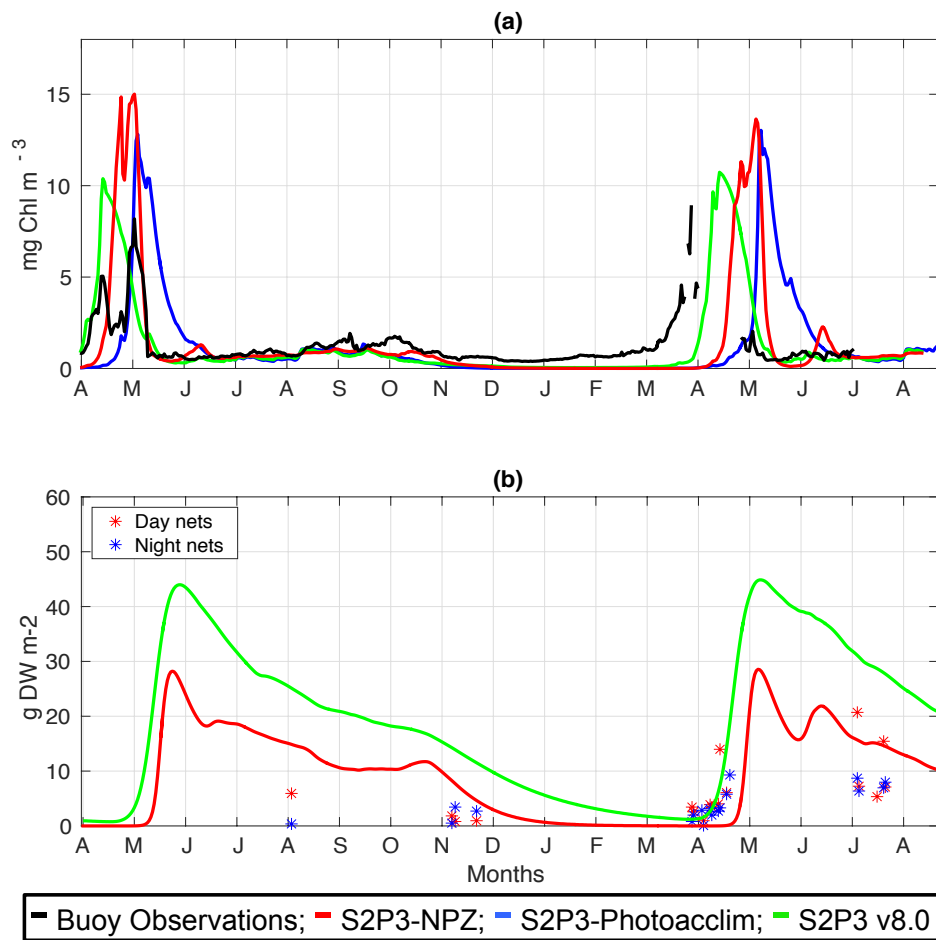


Figure 4.6: SSB observations (black lines) for (a) Surface chlorophyll-*a*, (b) zooplankton biomass along the S2P3-NPZ (red line), S2P3-Photoacclim (blue line), and S2P3 v8.0 (green line) calibrated models.

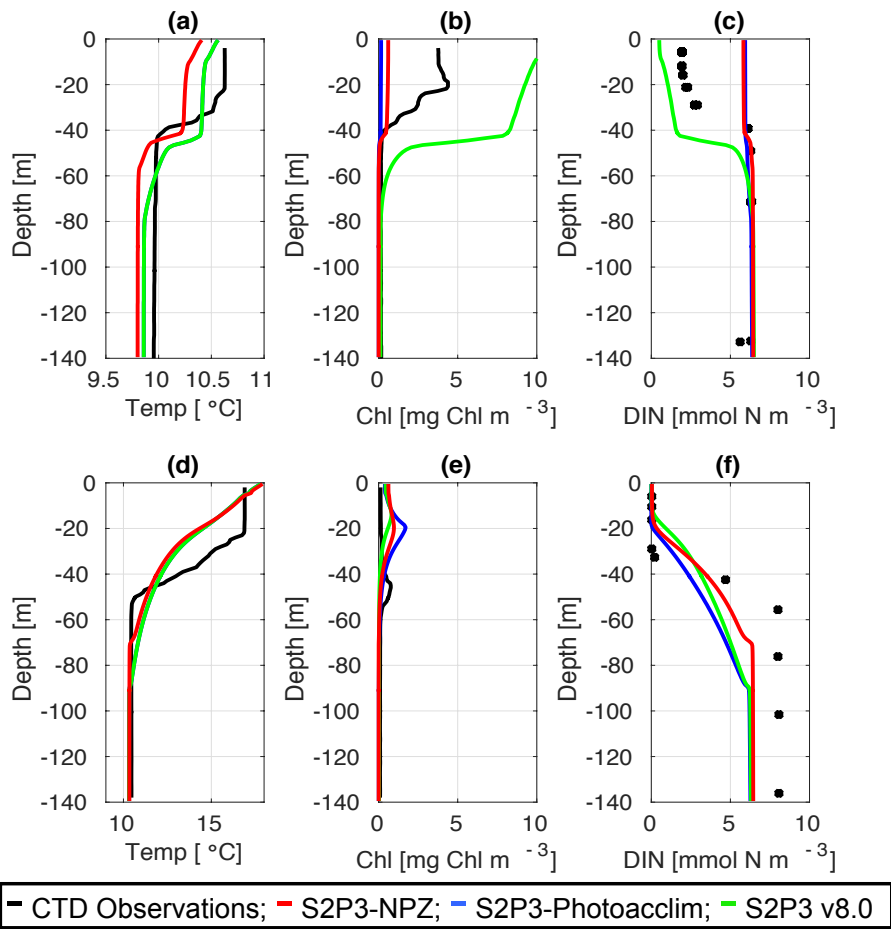


Figure 4.7: CTD observations from the SSB programme including data for: springtime (20/04/2015) (a) temperature, (b) chlorophyll-*a*, and (c) DIN; for summertime (24/07/2015) for (d) temperature, (e) chlorophyll-*a*, and (f) DIN along the S2P3-NPZ (red line), S2P3-Photoacclim (blue line), and S2P3 v8.0 (green line) calibrated models.

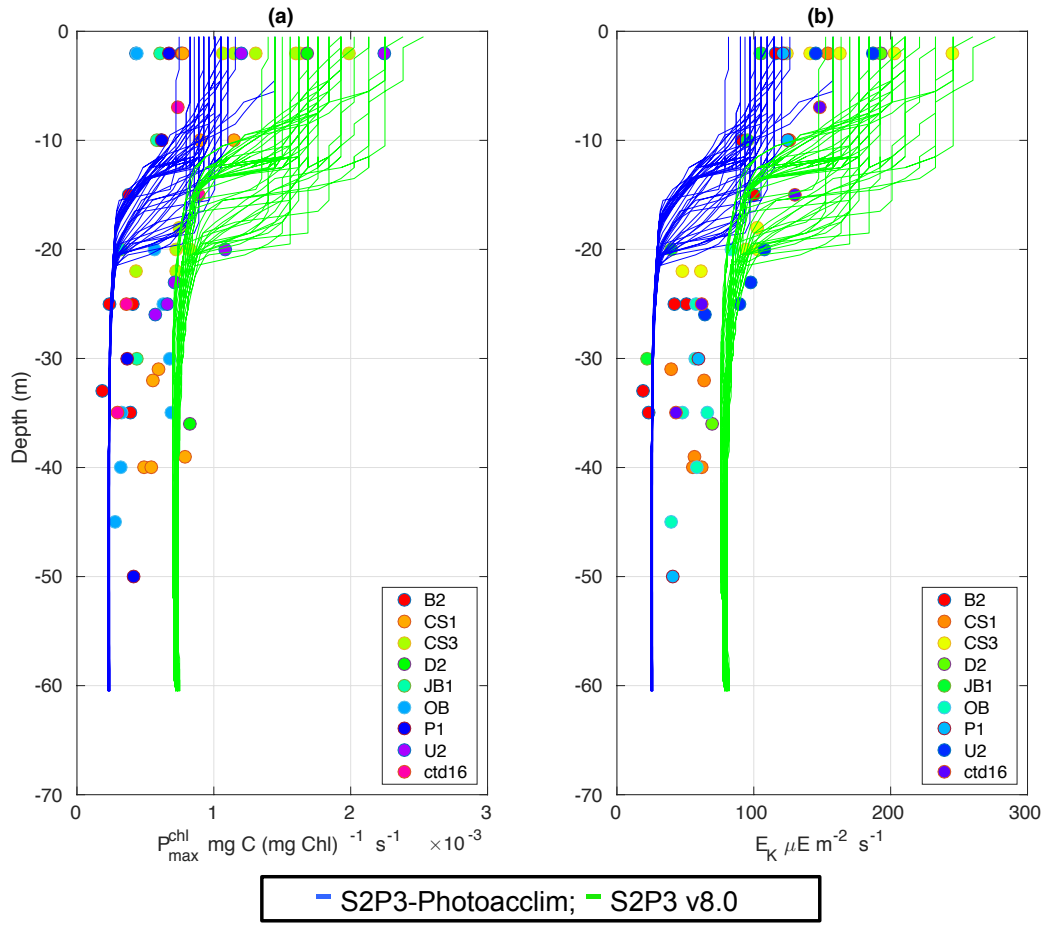


Figure 4.8: Observations from the cruises CD173 and JR98 for:(a) chlorophyll-*a* specific maximum light-saturated photosynthesis rate (P_{\max}^{chl}) in different locations of the Celtic Sea and for the calibrated S2P3-Photoacclim model (blue lines) and the S2P3 v8.0 model (green lines); (b) observations of the light saturation parameter (E_k) for different stations across the Celtic Sea and E_k from the calibrated S2P3-Photoacclim model (blue lines) and the S2P3 v8.0 model (green lines). The data from both models were plotted for the same days that the observations were collected: between 15th July to 6th August of 2003 (JR98 cruise) and between 24th July to 14th August of 2005 (CD173 cruise).

4.4.2 Sensitivity analysis

In this section, a sensitivity analysis for each model was performed. Firstly, the sensitivity analysis of the S2P3-NPZ model is shown by comparing it to the Control NPZ experiment, surface chlorophyll-*a* and zooplankton biomass observations. Moreover, CTD observations for spring and summer months were also used to compare each experiment listed in Table 4.3. Secondly, a sensitivity analysis for the S2P3-Photoacclim model was performed (Table

4.4) and compared to the Control Photoacclim experiment and also to surface chlorophyll-*a* and CTD observations of temperature, chlorophyll-*a*, and DIN; physiological observations were also used to analyse the parameters in this model. Finally, a sensitivity analysis for the S2P3 v8.0 model is shown (Table 4.5) and compared to the Control NPZPhot experiment and to surface chlorophyll-*a*, zooplankton biomass, CTD, and physiological observations.

For each model, a series of features were calculated per experiment performed to quantitatively analyse which parameter causes the model to be the most sensitive to its changes. These features included the timing and magnitude of the spring phytoplankton bloom, and the total annual zooplankton biomass for the S2P3-NPZ and the S2P3 v8.0 models only. The definition of the timing of the spring phytoplankton bloom differs from the criteria calculated in Chapter 3 (Figure A1), where the onset of stratification was considered to be the day when the surface-bed temperature difference was more than 0.5°C (Simpson & Sharples, 2012) during a period of at least ten days. In the context of Chapter 3, the modification of thermal stratification was a good proxy for the timing of the spring phytoplankton bloom because the meteorological forcing was different in each experiment and, therefore, it modified directly the physical part of the model (i.e. thermal stratification), which aided the aim to understand the effects of meteorology in phytoplankton inter-annual variability. However, in this section, the timing of the spring phytoplankton bloom is directly defined with the surface chlorophyll-*a* data (when it reaches more than 1.5 mg Chl m⁻³), because the physical part of S2P3 v7.0 was not modified to develop S2P3-NPZ, S2P3-Photoacclim, and S2P3 v8.0, showing no differences in the physical features (e.g. temperature). Furthermore, in Chapter 3 it was demonstrated that different definitions of the start of the spring bloom when considering a threshold for surface-bed temperature and surface chlorophyll produces differences in the results that could be negligible, differences that can also be neglected for the purposes of this chapter, where the understanding of each parameter to the dynamics of each model will not be dependent on such definition. Consequently, defining the timing of the spring bloom directly based on chlorophyll for the sensitivity analysis, seems more appropriate than based on the temperature profile as the physics of the model does not seem to be affected by changes in the parameter values, while surface chlorophyll seems more sensitive and a good proxy for the timing of the spring bloom in this case to compare behavioural responses in each model according to each parameter.

4.4.2.1 S2P3-NPZ

The assimilation efficiency parameter called γ_1 is tested from a value of 0.2 found in the Control NPZ experiment, ranging from 0.1 (-50%, Run 1) to 0.3 (+50%, Run 2). There are not large changes observed in terms of surface chlorophyll-*a* compared to the Control NPZ experiment or in terms of the timing and magnitude of the spring phytoplankton bloom (Figure 4.9a). A lower value of γ_1 means that there is less nitrogen coming from sloppy feeding into the DIN pool, so when $\gamma_1 = 0.1$, only 10 % of the total phytoplankton N being grazed by zooplankton goes back to the DIN pool. On the other hand, when γ_1 is equal 0.3, surface chlorophyll-*a* is a lot higher than in the buoy observations and in the Control NPZ experiment, while the spring phytoplankton bloom is earlier by 3 days in the year 2014 and by five days in the year 2015 for the Run 2 experiment (Table 4.9).

Table 4.9 shows the differences between the Control NPZ and each model experiment in terms of the timing and magnitude of the spring phytoplankton bloom, and in terms of the total annual zooplankton biomass. In the experiments that negative values can be observed in the difference of the timing, it means that the spring bloom start was delayed in those experiments in comparison to the Control NPZ. On the other hand, negative values of the difference of the magnitude represent experiments with larger spring blooms than in the Control NPZ experiment. Finally, the differences of the total annual zooplankton biomass that have negative values, implies more zooplankton production over the year than in the Control NPZ experiment.

Figure 4.9b shows that when $\gamma_1 = 0.1$, there are small differences between the Control NPZ experiment and Run 1 in terms of the spring zooplankton bloom, although delayed blooms can be observed for Run 2 ($\gamma_1 = 0.3$) including lower total annual zooplankton biomass than in the Control NPZ experiment.

The differences between the Control NPZ experiment and Run 2 can be observed in more detail through the water column in Figure 4.10, where surface chlorophyll-*a* is not high enough in comparison to CTD observations because despite an earlier bloom in Run 2 in comparison to the Control NPZ experiment, it is still later in the year in comparison to the

date of the CTD observations. On the other hand, an SCM can be observed for Run 1 and Run 2 during summer (Figure 4.10e). The SCM exists at the same depth but the magnitude is higher in Run 2 rather than in Run 1, Control NPZ, and in the CTD observations.

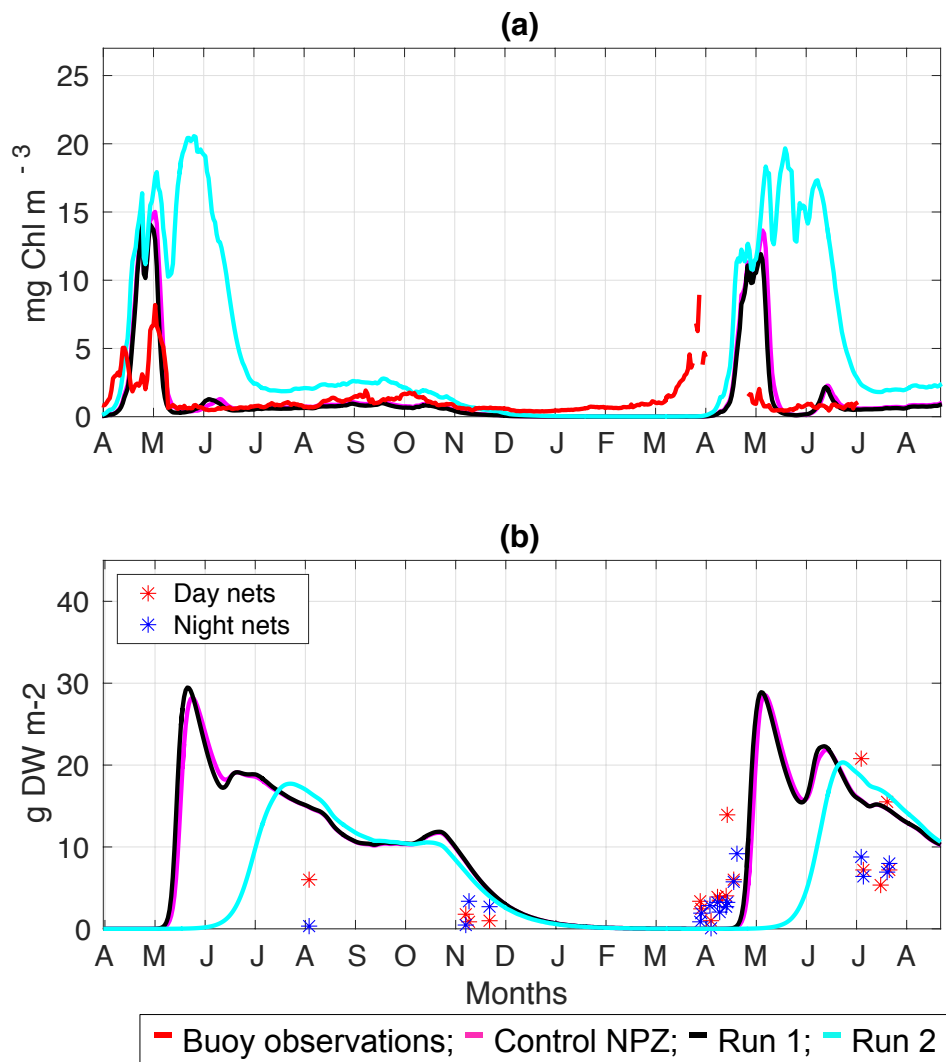


Figure 4.9: SSB buoy observations (red line) from the start of April 2014 to end of June 2015 compared to the Control NPZ (magenta line), Run 1 ($\gamma_1 = 0.1$; black line), and Run 2 ($\gamma_1 = 0.3$; cyan line) shown from start of April 2014 to the end of August 2015 for (a) surface chlorophyll-*a* and (b) zooplankton biomass.

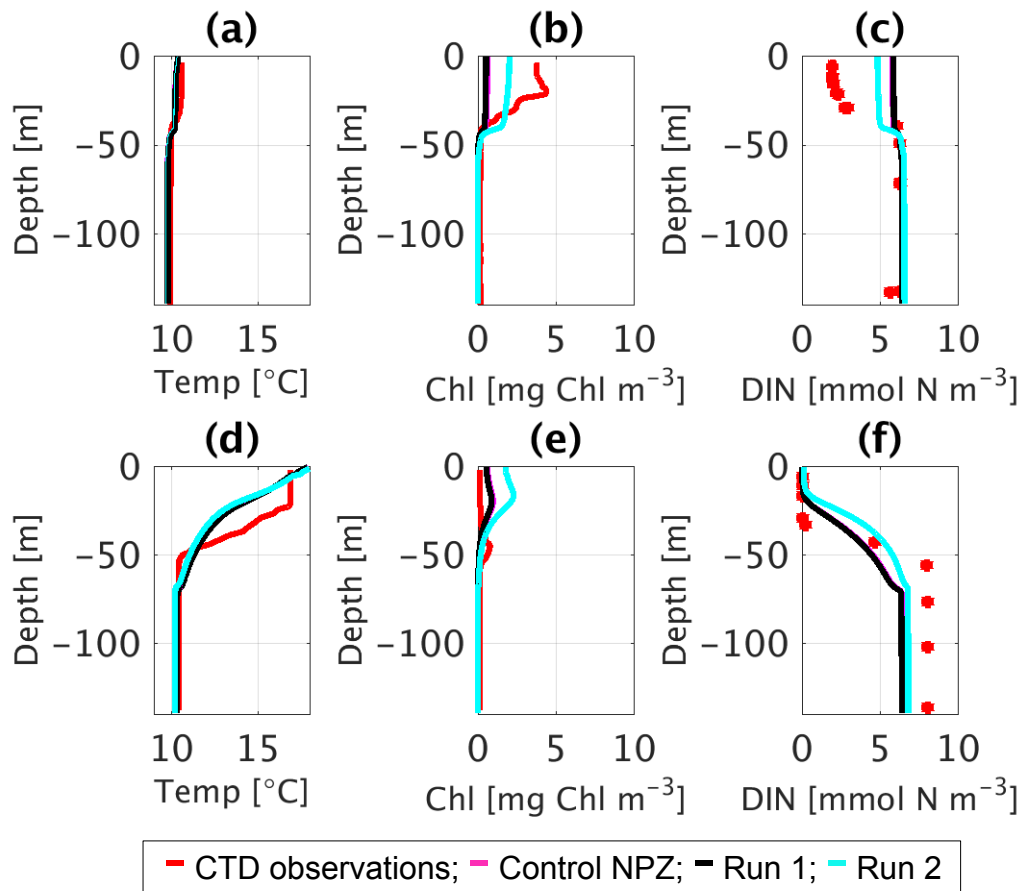


Figure 4.10: CTD observations from the SSB programme (red line) including data for: springtime (20/04/2015) (a) temperature, (b) chlorophyll-*a*, and (c) DIN; for summertime (24/07/2015) for (d) temperature, (e) chlorophyll-*a*, and (f) DIN along the S2P3-NPZ (magenta line), Run 1 ($\gamma_1 = 0.1$; black line), and Run 2 ($\gamma_1 = 0.3$; cyan line).

The next parameter to be analysed is γ_2 , being modified from its default value of 0.5 (Control NPZ) ranging from 0.25 (-50%, Run 3) to 0.75 (+50%, Run 4) as shown in Table 4.3. It is interesting to note that differences between these experiments in terms of surface chlorophyll-*a* are small (Figure 4.11a), with differences in the timing of the spring phytoplankton bloom (Tables 4.8, 4.9). On the other hand, zooplankton biomass shows large differences between each experiment, with secondary blooms in Run 4 when γ_2 is higher than in the Control NPZ experiment.

Vertical profiles of chlorophyll-*a* and DIN during spring do not show large differences between experiments (Figure 4.12b,c), but concentrations of surface chlorophyll-*a* are low in comparison to CTD observations because the spring phytoplankton bloom in the model is delayed. During summer, differences in the SCM and in DIN concentrations at the surface can be observed between experiments, with highest values of DIN in Run 4, because more dead zooplankton N is being directly supplied to the DIN pool rather than going to sediments.

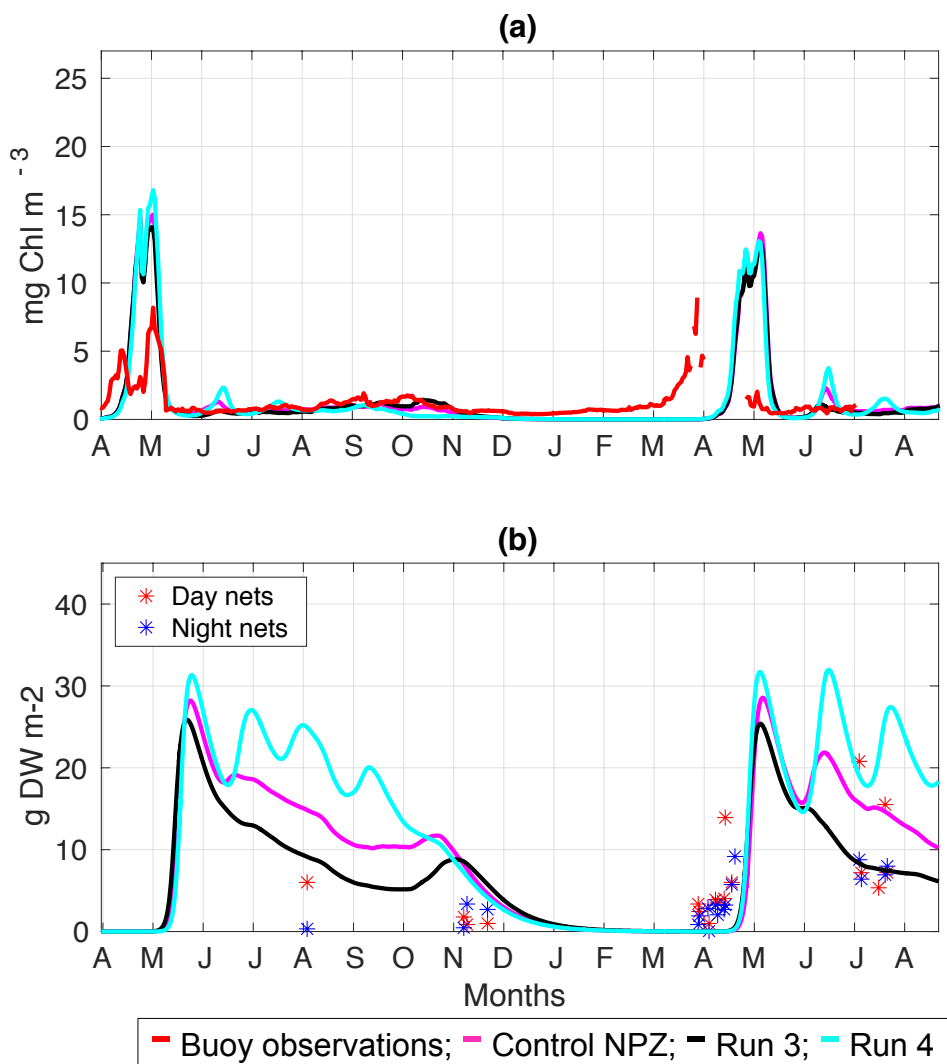


Figure 4.11: SSB buoy observations (red line) from the start of April 2014 to end of June 2015 compared to the Control NPZ (magenta line), Run 3 ($\gamma_2 = 0.25$; black line), and Run 4 ($\gamma_2 = 0.75$; cyan line) shown from start of April 2014 to the end of August 2015 for (a) surface chlorophyll-*a* and (b) zooplankton biomass.

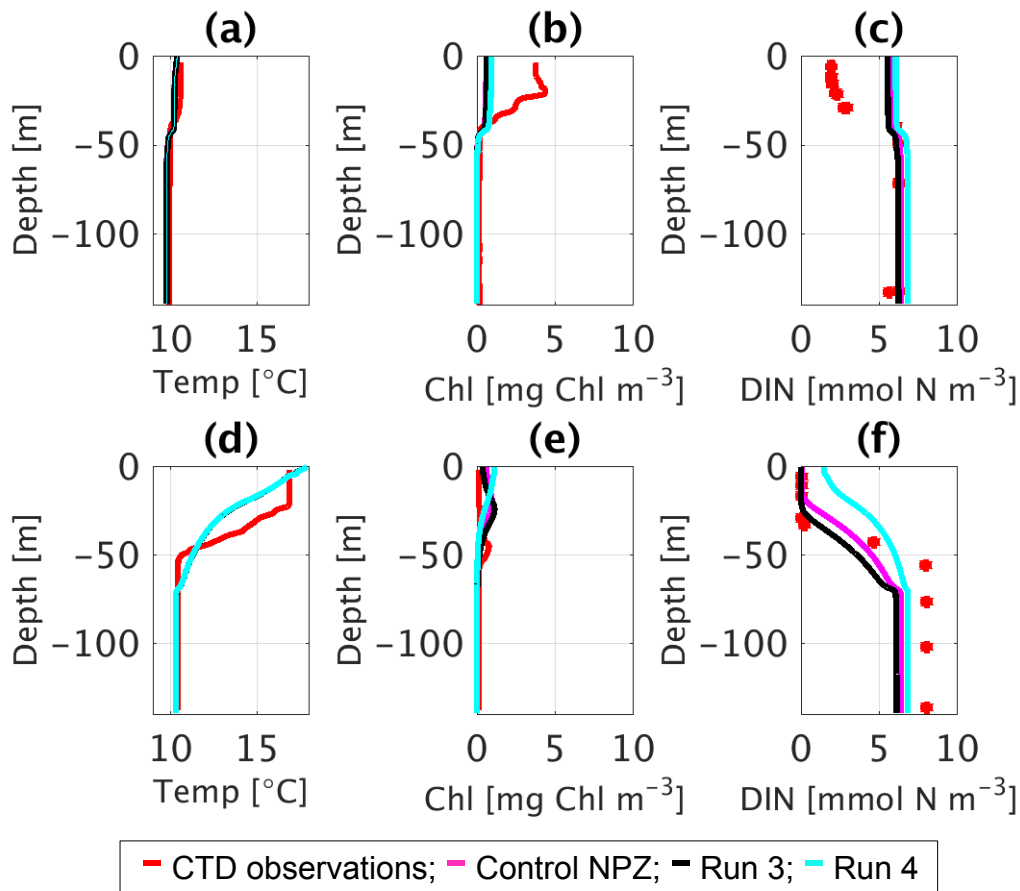


Figure 4.12: CTD observations from the SSB programme (red line) including data for: springtime (20/04/2015) (a) temperature, (b) chlorophyll-*a*, and (c) DIN; for summertime (24/07/2015) for (d) temperature, (e) chlorophyll-*a*, and (f) DIN along the S2P3-NPZ (magenta line), Run 3 ($\gamma_2 = 0.25$; black line), and Run 4 ($\gamma_2 = 0.75$; cyan line).

In this study it was found that, on average, the S2P3-NPZ model is most sensitive to changes in the rate of saturation achieved by grazing (λ) in terms of the magnitude of the spring phytoplankton bloom (marked in red cells in Table 4.9) and in terms of the total annual zooplankton biomass (marked in grey cells in Table 4.9). When λ is equal $0.375 \text{ (mmol N m}^{-3}\text{)}^{-1}$ (Run5; Table 4.3), the predator-prey coupling between phytoplankton and zooplankton is weaker allowing phytoplankton to grow up to unrealistic levels over a sustained period of time (April to December) as shown in Figure 4.13a. On the other hand, Run 6 shows that when λ equals $1.125 \text{ (mmol N m}^{-3}\text{)}^{-1}$ (Table 4.3), the timing of the

spring phytoplankton bloom is delayed only by 2 days (year 2014) and 5 days (year 2015) in comparison to the Control NPZ (Table 4.9), but secondary blooms can be observed during the year.

Zooplankton biomass responds accordingly to surface chlorophyll-*a* dynamics, with zero total annual zooplankton biomass in Run 5 and secondary blooms during the year as a response of the post-blooms of phytoplankton in Run 6 (Figure 4.13b). This is not represented in the vertical profiles of chlorophyll-*a* (Figure 4.14b,e), where small differences can be observed between the Run 6 and the Control NPZ experiments during spring and summer months. On the other hand, high values of surface chlorophyll are observed for Run 5, with depleted inorganic nutrients during spring and summer (Figure 4.14c,f).

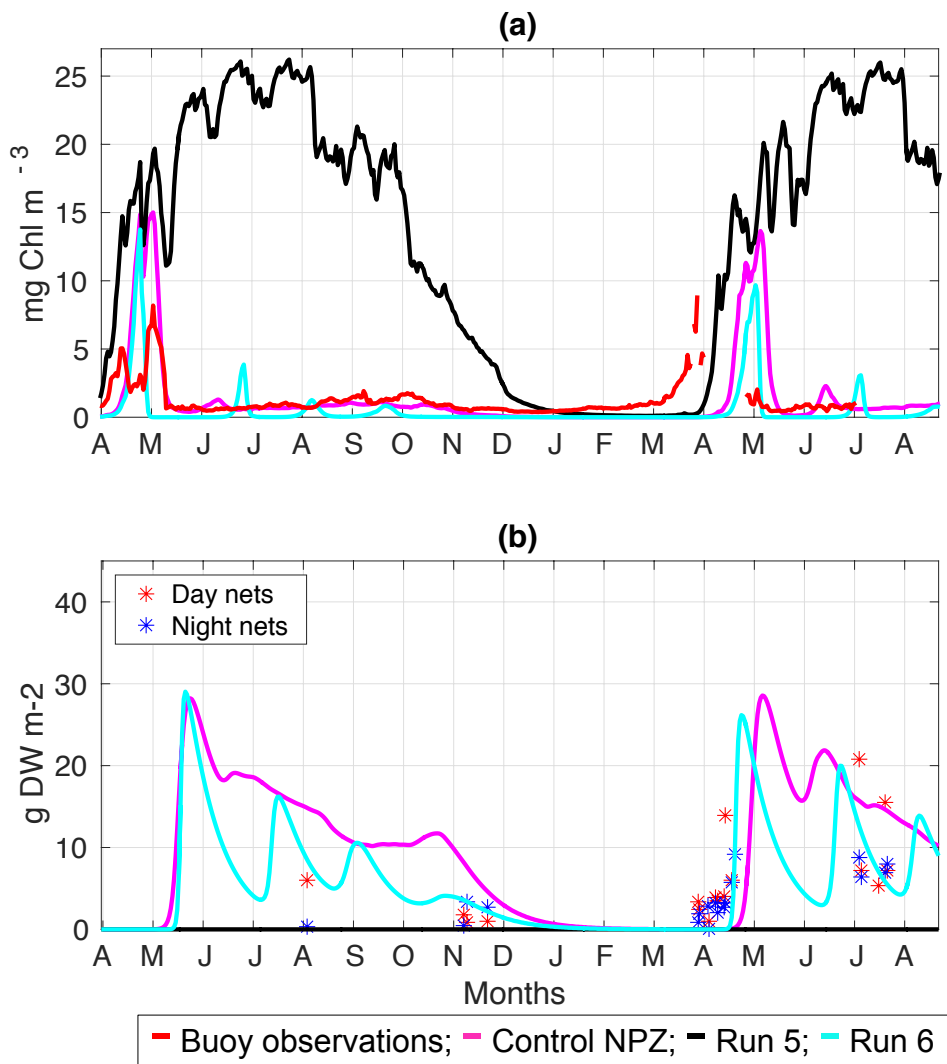


Figure 4.13: SSB buoy observations (red line) from the start of April 2014 to end of June 2015 compared to the Control NPZ (magenta line), Run 5 ($\lambda = 0.375$; black line), and Run 6 ($\lambda = 1.125$; cyan line) shown from start of April 2014 to the end of August 2015 for (a) surface chlorophyll-*a* and (b) zooplankton biomass.

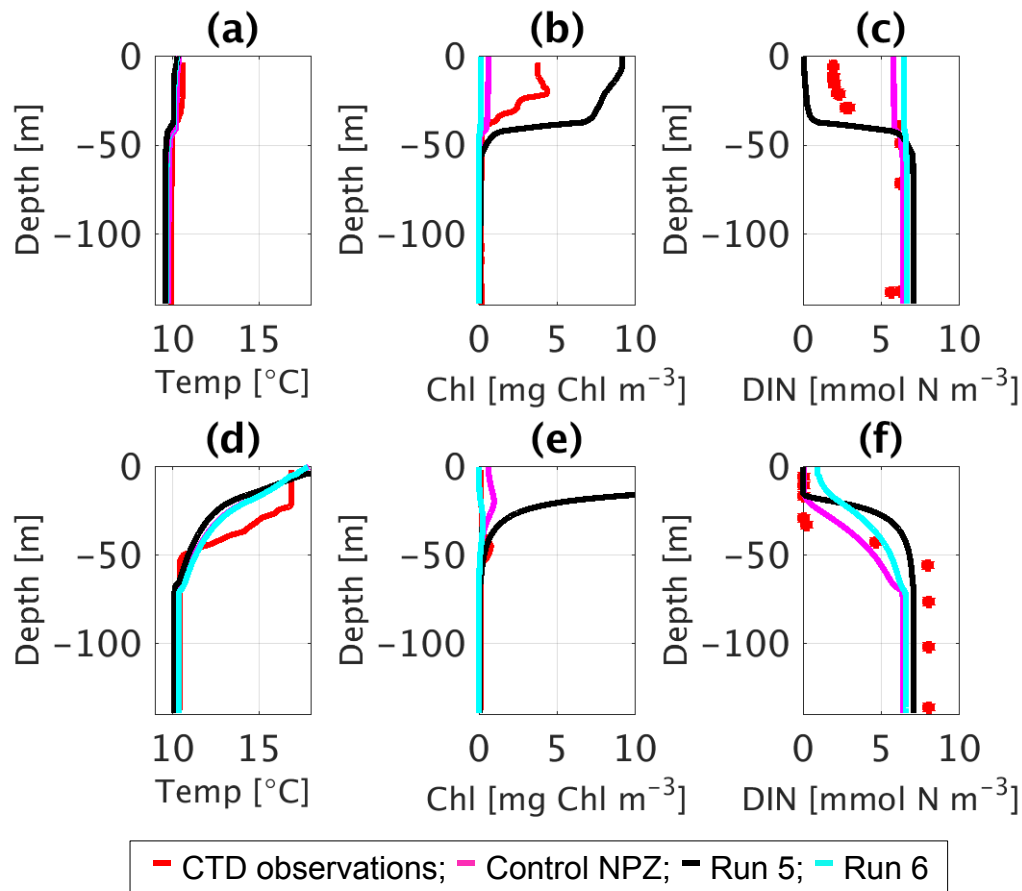


Figure 4.14: CTD observations from the SSB programme (red line) including data for: springtime (20/04/2015) (a) temperature, (b) chlorophyll-*a*, and (c) DIN; for summertime (24/07/2015) for (d) temperature, (e) chlorophyll-*a*, and (f) DIN along the S2P3-NPZ (magenta line), Run 5 ($\lambda = 0.375$; black line), and Run 6 ($\lambda = 1.125$; cyan line).

The maximum ingestion rate of phytoplankton (R_m) was also studied in this section. Changes in R_m imply that different amounts of phytoplankton will be grazed by zooplankton per unit time, therefore a decrease in R_m from its default value of 2.5 d^{-1} to 1.25 d^{-1} (Run 7, Table 4.3) will allow phytoplankton to grow more leading to unrealistic values of surface chlorophyll-*a* (Figure 4.15a) and, consequently, zero total annual zooplankton biomass (Figure 4.15b). On the other hand, a higher value of R_m equal to 3.75 d^{-1} (Run 8), did not produce large differences in the timing or magnitude of the spring phytoplankton bloom (Table 4.9).

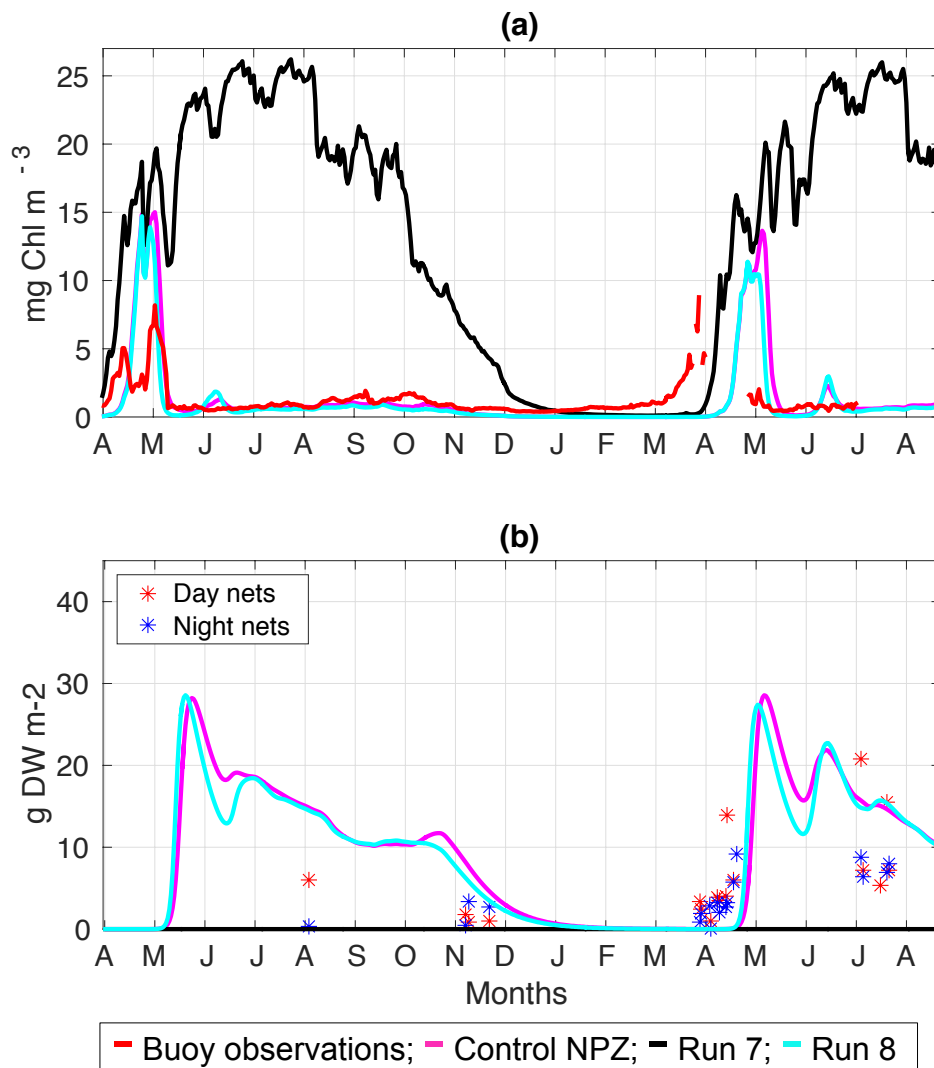


Figure 4.15: SSB buoy observations (red line) from the start of April 2014 to end of June 2015 compared to the Control NPZ (magenta line), Run 7 ($R_m = 1.25$; black line), and Run 8 ($R_m = 3.75$; cyan line) shown from start of April 2014 to the end of August 2015 for (a) surface chlorophyll-*a* and (b) zooplankton biomass.

For the comparison to CTD observations (Figure 4.16), high values of surface chlorophyll-*a* are observed in Run 7 ($R_m = 1.25$; Figure 4.16b,e), while DIN concentrations are set to zero because phytoplankton have consumed it all (Figure 4.16c,f). On the other hand, Run 8 ($R_m = 3.75$) do not show significant differences for vertical profiles of chlorophyll-*a* and DIN in comparison to the Control NPZ experiment.

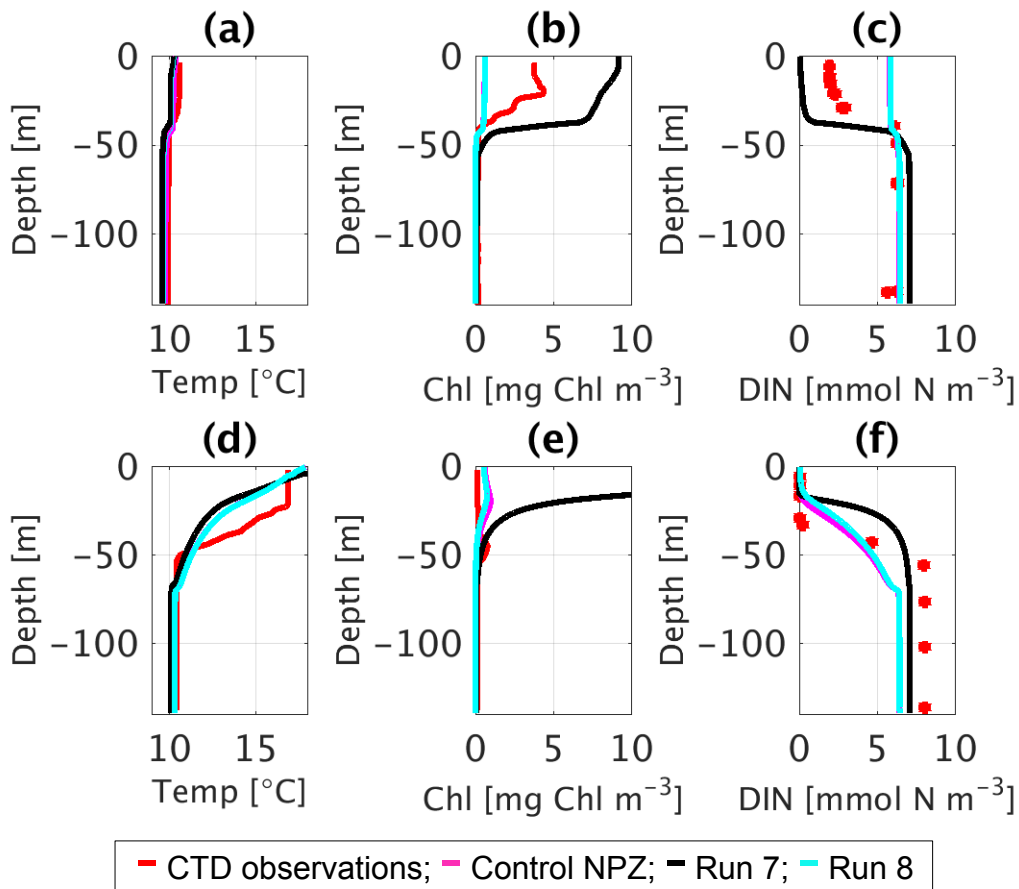


Figure 4.16: CTD observations from the SSB programme (red line) including data for: springtime (20/04/2015) (a) temperature, (b) chlorophyll-*a*, and (c) DIN; for summertime (24/07/2015) for (d) temperature, (e) chlorophyll-*a*, and (f) DIN along the S2P3-NPZ (magenta line), Run 7 ($R_m = 1.25$; black line), and Run 8 ($R_m = 3.75$; cyan line).

Finally, zooplankton mortality rate (m) is analysed in Run 9 ($m = 0.025$) and Run 10 ($m = 0.075$). A lower value of m from its default of 0.05 d^{-1} in the Control NPZ experiment to 0.025 d^{-1} means that zooplankton mortality will be less, therefore, more zooplankton will be able to graze phytoplankton (Figure 4.17a). The S2P3-NPZ model showed to be, on average, the most sensitive to zooplankton mortality in terms of the timing of the spring phytoplankton bloom (marked in orange cells in Table 4.9), showing later blooms when m is lower and earlier blooms when m is higher. Run 10 resulted in the total annual zooplankton biomass being close to zero.

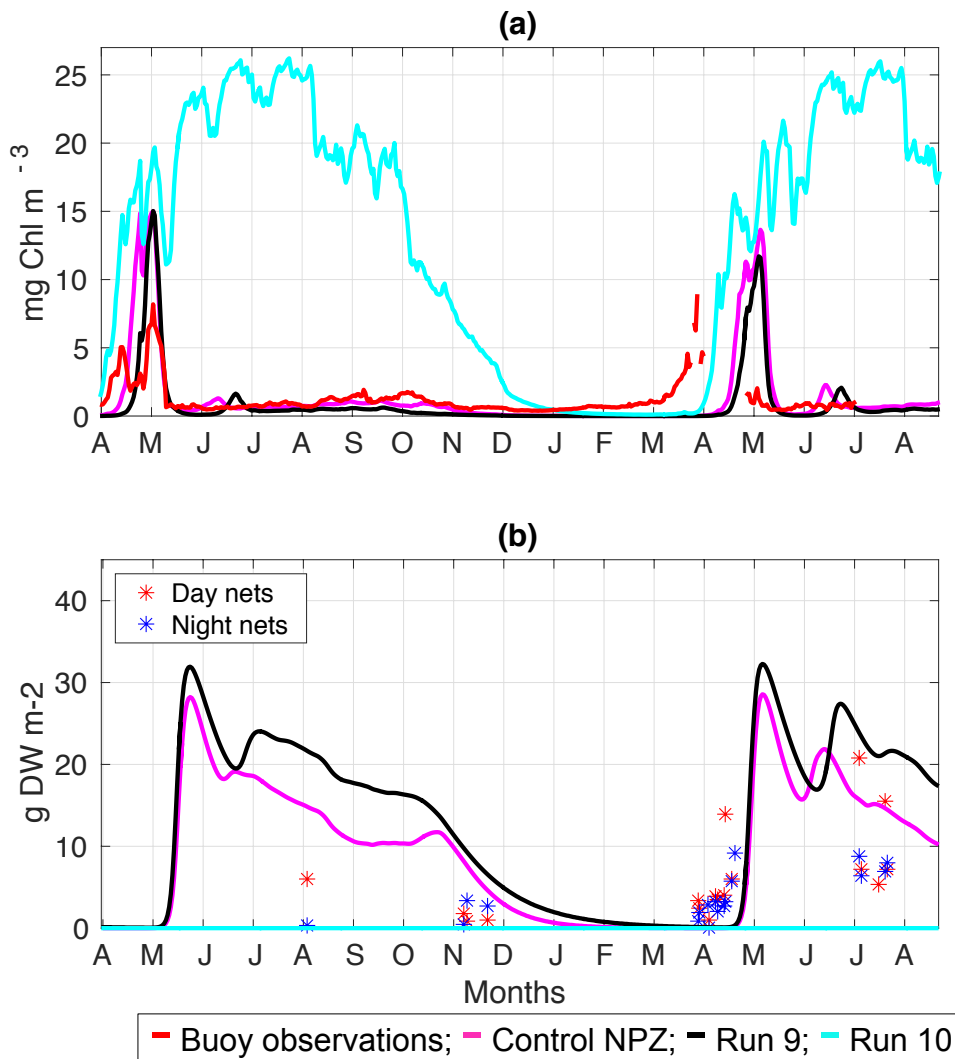


Figure 4.17: SSB buoy observations (red line) from the start of April 2014 to end of June 2015 compared to the Control NPZ (magenta line), Run 9 ($m = 0.025$; black line), and Run 10 ($m = 0.075$; cyan line) shown from start of April 2014 to the end of August 2015 for (a) surface chlorophyll-*a* and (b) zooplankton biomass.

Figure 4.18b,e shows that surface chlorophyll-*a* is high in Run 10 when mortality of zooplankton is higher, depleting DIN concentrations at the surface. On the other hand, small differences through the water column are observed between the Control NPZ experiment and Run 9.

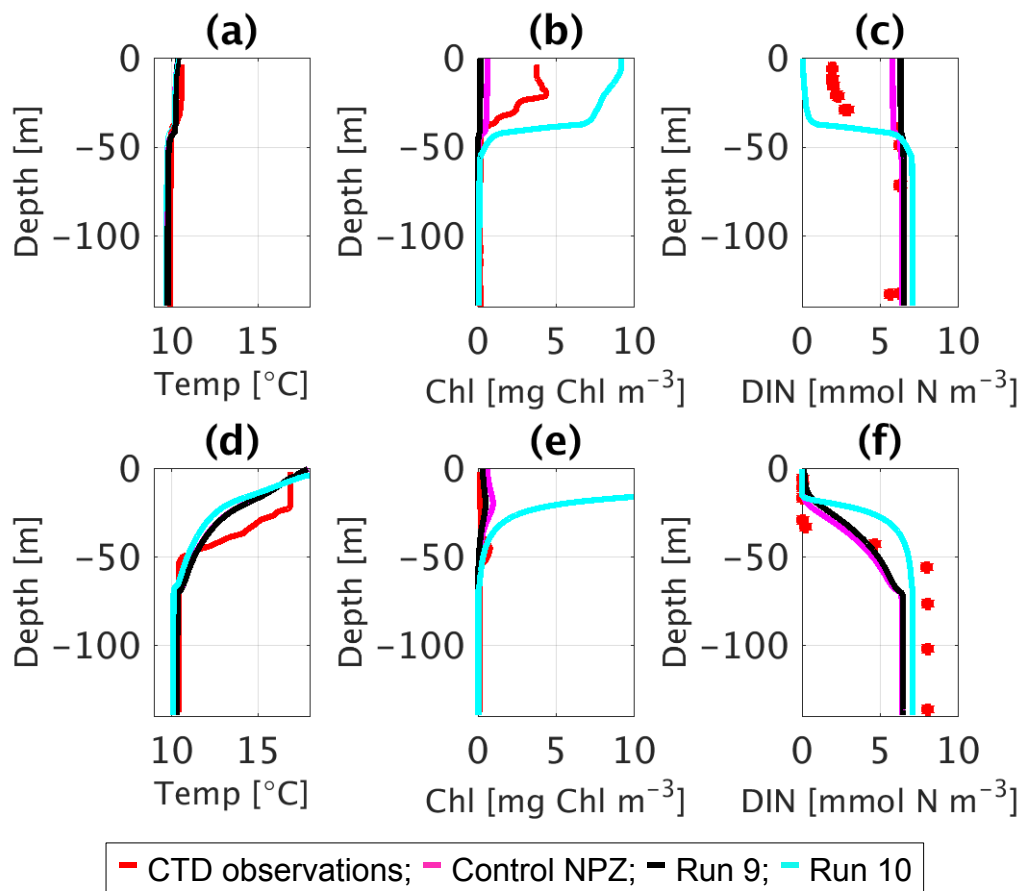


Figure 4.18: CTD observations from the SSB programme (red line) including data for: springtime (20/04/2015) (a) temperature, (b) chlorophyll-*a*, and (c) DIN; for summertime (24/07/2015) for (d) temperature, (e) chlorophyll-*a*, and (f) DIN along the S2P3-NPZ (magenta line), Run 9 ($m = 0.025$; black line), and Run 10 ($m = 0.075$; cyan line).

Experiments	Years	Timing spring phytoplankton bloom (date)	Magnitude spring phytoplankton bloom (mg Chl m⁻³)	Total annual zooplankton biomass (g DW m⁻²)
Run1 ($\gamma_1 \downarrow$)	2014	15 th April	152.6	3158
	2015	24 th April	266.3	3066
Run2 ($\gamma_1 \uparrow$)	2014	11 th April	1430	2062
	2015	19 th April	1425	1986
Run3 ($\gamma_2 \downarrow$)	2014	14 th April	208.5	2337
	2015	24 th April	289.8	2270
Run4 ($\gamma_2 \uparrow$)	2014	15 th April	306.1	4004
	2015	22 nd April	343.9	3744
Run5 ($\lambda \downarrow$)	2014	1 st April	3707	0
	2015	10 th April	3705	0
Run6 ($\lambda \uparrow$)	2014	16 th April	90.6	1943
	2015	29 th April	80.4	1845
Run7 ($R_m \downarrow$)	2014	1 st April	3711	0
	2015	10 th April	3709	0
Run8 ($R_m \uparrow$)	2014	15 th April	226.7	2909
	2015	24 th April	242.1	2835
Run9 ($m \downarrow$)	2014	22 nd April	209	4269
	2015	28 th April	213.5	4065
Run10 ($m \uparrow$)	2014	1 st April	3710	0
	2015	10 th April	3708	0
Control NPZ	2014	14 th April	208.6	3118
	2015	24 th April	315.8	2983

Table 4.8: List of the experiments run for the S2P3-NPZ model including the year of observations, timing and magnitude of the spring phytoplankton bloom, and total annual zooplankton biomass values.

Experiments	Years	Difference timing spring phytoplankton bloom (days)	Difference magnitude spring phytoplankton bloom (mg Chl m ⁻³)	Difference total annual zooplankton biomass (g DW m ⁻²)
Run1 ($\gamma_1 \downarrow$)	2014	-1	56	-40
	2015	0	49.5	-83
Run2 ($\gamma_1 \uparrow$)	2014	3	-1221.4	1056
	2015	5	-1109.2	997
Run3 ($\gamma_2 \downarrow$)	2014	0	0.1	781
	2015	0	26	713
Run4 ($\gamma_2 \uparrow$)	2014	-1	-97.5	-886
	2015	2	-28.1	-761
Run5 ($\lambda \downarrow$)	2014	13	-3498.4	3118
	2015	14	-3389.2	2983
Run6 ($\lambda \uparrow$)	2014	-2	118	1175
	2015	-5	235.4	1138
Run7 ($R_m \downarrow$)	2014	13	-3502.4	3118
	2015	14	-3393.2	2983
Run8 ($R_m \uparrow$)	2014	-1	-18.1	209
	2015	0	73.7	148
Run9 (m \downarrow)	2014	-8	-0.4	-1151
	2015	-4	102.3	-1082
Run10 (m \uparrow)	2014	13	-3501.4	3118
	2015	14	-3392.2	2983

Table 4.9: List of the experiments run for the S2P3-NPZ model including the year of observations, differences in the timing and magnitude of the spring phytoplankton bloom, and differences in the total annual zooplankton biomass values (differences given by the Control NPZ minus each experiment). Orange colour represents the largest difference in terms of the timing of the spring phytoplankton bloom between the Control NPZ and a given experiment; the red colour represents the largest difference in terms of the magnitude of the spring phytoplankton bloom between the Control NPZ and a given experiment; and the grey colour represents the largest difference in terms of the total annual zooplankton biomass between the Control NPZ and a given experiment.

4.4.2.2 S2P3-Photoacclim

The experiment Phot1 and Pho2 (Table 4.4) show the sensitivity of the model to the parameter P_{\max}^C , ranging from its default value of 2 d^{-1} (Control Photoacclim experiment) to 1 d^{-1} (-50%, Phot1) and to 3 d^{-1} (+50%, Phot2). This parameter produces changes in the magnitude and timing of the spring phytoplankton bloom (Figure 4.19). In the Phot1 experiment, it can be observed a delay of the spring phytoplankton bloom by 31 days (year 2014) and by 37 days (year 2015) as shown in Table 4.10, while an increase of P_{\max}^C produces earlier spring blooms. On the other hand, the comparison to CTD observations show that the spring phytoplankton bloom have not been reach yet (Figure 4.20b), therefore, surface chlorophyll-*a* has low values. During summer months, there is an SCM developed for the Phot1 and Phot2 experiments (Figure 4.20e).

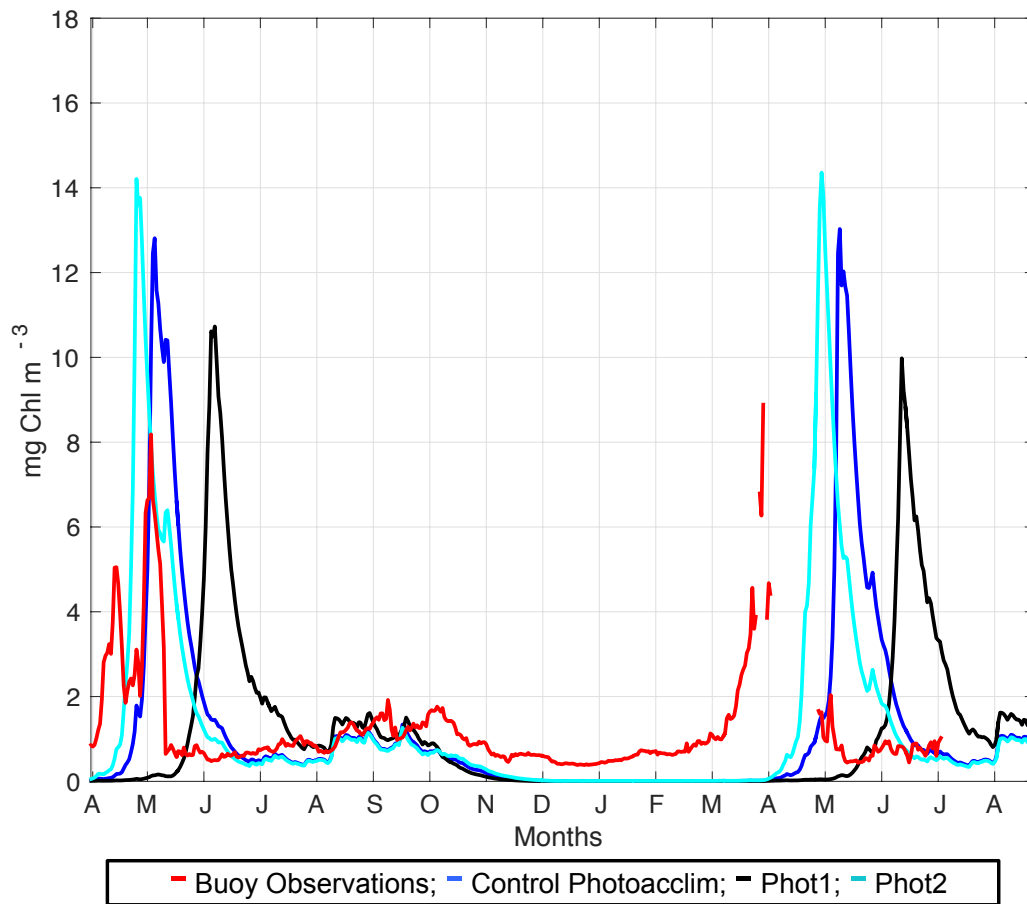


Figure 4.19: SSB buoy observations (red line) from the start of April 2014 to end of June 2015 compared to the Control Photoacclim (blue line), Phot 1 ($P_{\max}^C = 1$; black line), and Phot 2 ($P_{\max}^C = 3$; cyan line) shown from start of April 2014 to the end of August 2015 for surface chlorophyll-*a*.

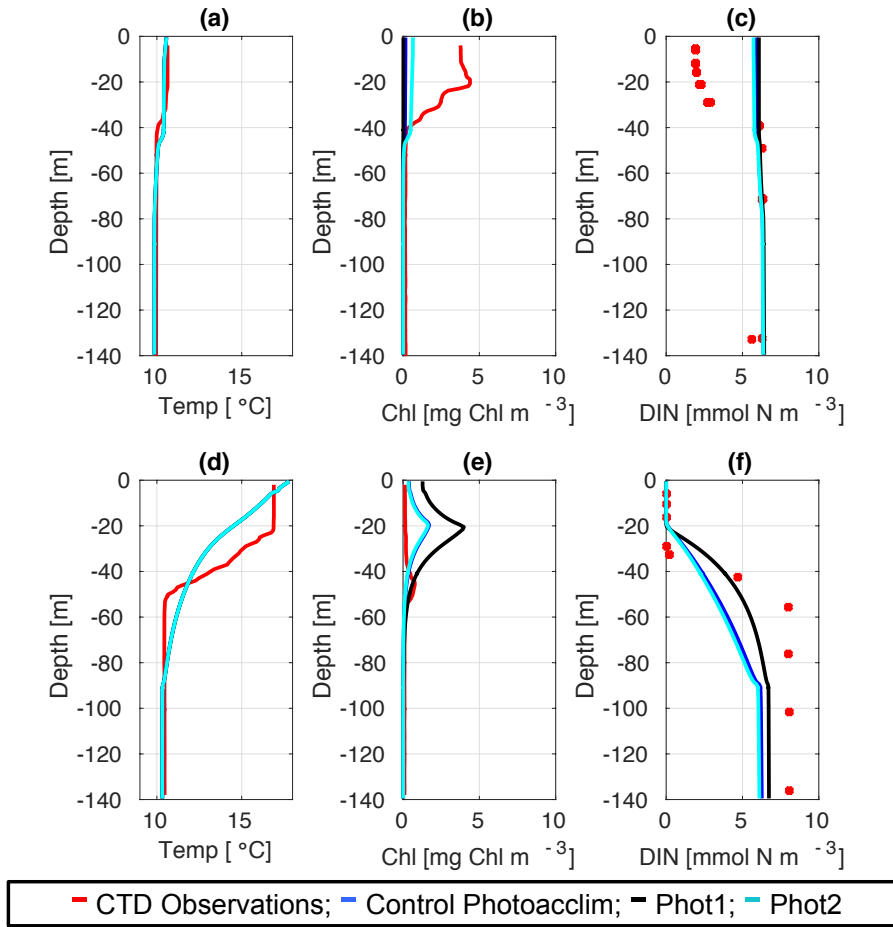


Figure 4.20: CTD observations from the SSB programme (red line) including data for: springtime (20/04/2015) (a) temperature, (b) chlorophyll-*a*, and (c) DIN; for summer-time (24/07/2015) for (d) temperature, (e) chlorophyll-*a*, and (f) DIN along the S2P3-Photoacclim (blue line), Phot 1 ($P_{\max}^C = 1$; black line), and Phot 2 ($P_{\max}^C = 3$; cyan line).

Additionally, P_{\max}^{chl} and E_k are directly affected by changes in P_{\max}^C because:

$$P_{\max}^{\text{chl}} = \frac{P_{\max}^C}{\theta_{\max}^N},$$

$$E_k = \frac{P_{\max}^{\text{chl}}}{\alpha^{\text{chl}}}.$$

In consequence, the Phot1 experiment produces lower values of P_{\max}^{chl} and E_k through the

water column, while a higher value of P_{\max}^C (Phot2 experiment) generates higher values P_{\max}^{chl} and E_k (Figure 4.21), which are not well matched to observations.

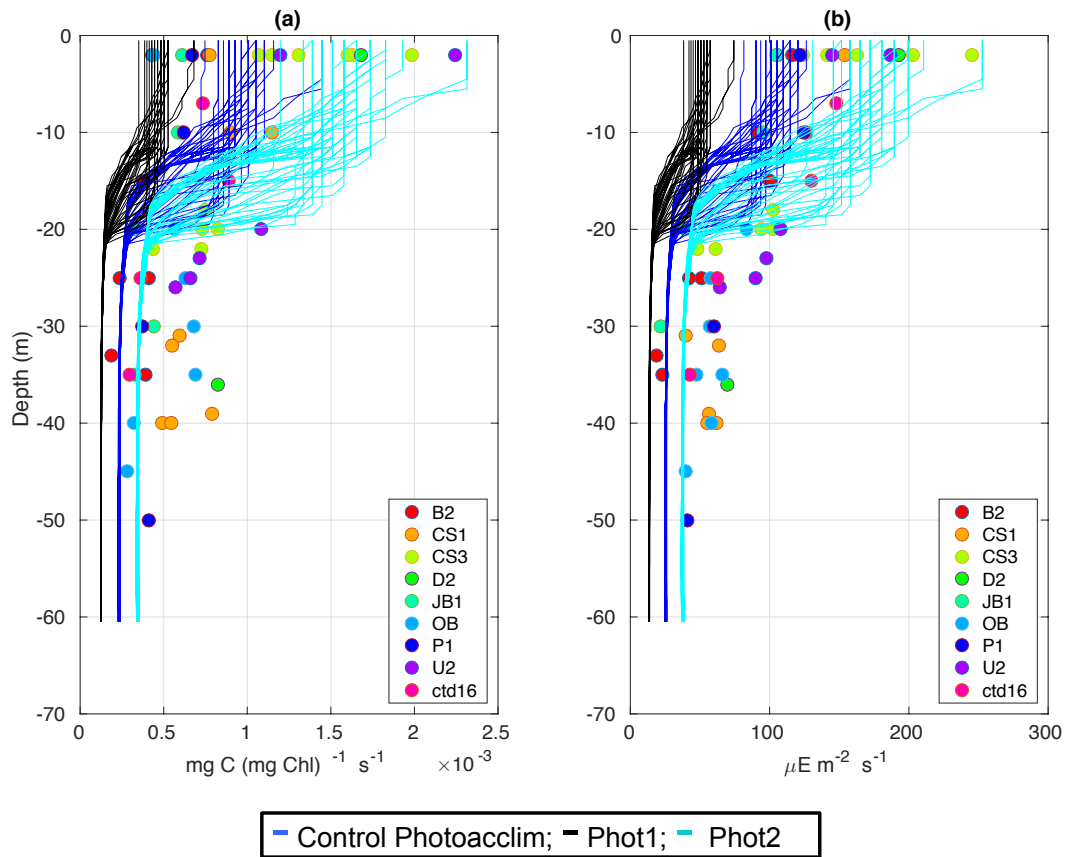


Figure 4.21: Observations from the cruises CD173 and JR98 in different locations of the Celtic Sea, including Control Photoacclim (blue lines), Phot 1 ($P_{\max}^C = 1$; black lines), and Phot 2 ($P_{\max}^C = 3$; cyan lines) for: (a) chlorophyll-a specific maximum light-saturated photosynthesis rate (P_{\max}^{chl}) and (b) light saturation parameter (E_k). The data from the model was plotted during the same days that the observations were collected.

Changes in Q_m produce differences in terms of the timing and magnitude of the spring phytoplankton bloom by delaying it by 33 days (year 2014) and by 40 days (year 2015) in the Phot3 experiment ($Q_m=0.2$, Table 4.4). On the other hand, the Phot4 ($Q_m=0.6$) experiment produces earlier spring phytoplankton blooms.

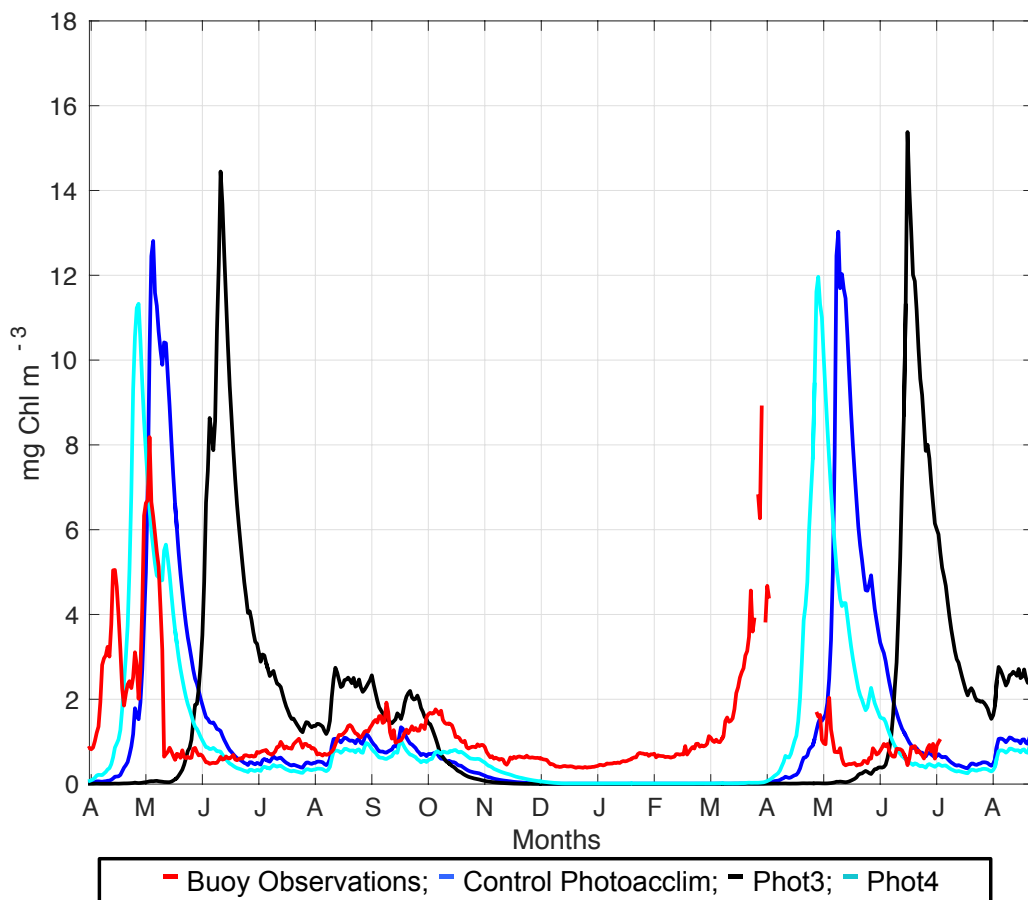


Figure 4.22: SSB buoy observations (red line) from the start of April 2014 to end of June 2015 compared to the Control Photoacclim (blue line), Phot 3 ($Q_m = 0.2$; black line), and Phot 4 ($Q_m = 0.6$; cyan line) shown from start of April 2014 to the end of August 2015 for surface chlorophyll-*a*.

The Phot3 and Phot4 experiments show delayed spring phytoplankton blooms in comparison to the buoy and CTD observations, with low values of surface chlorophyll-*a* (Figure 4.23b) and inorganic nutrients not been depleted yet and, therefore, showing high values of surface DIN during spring (Figure 4.23c). An SCM is shown for the Phot3 and Phot4 experiments, with higher values of the SCM than in the Control Photoacclim experiment for the Phot3 experiment (Figure 4.23e).

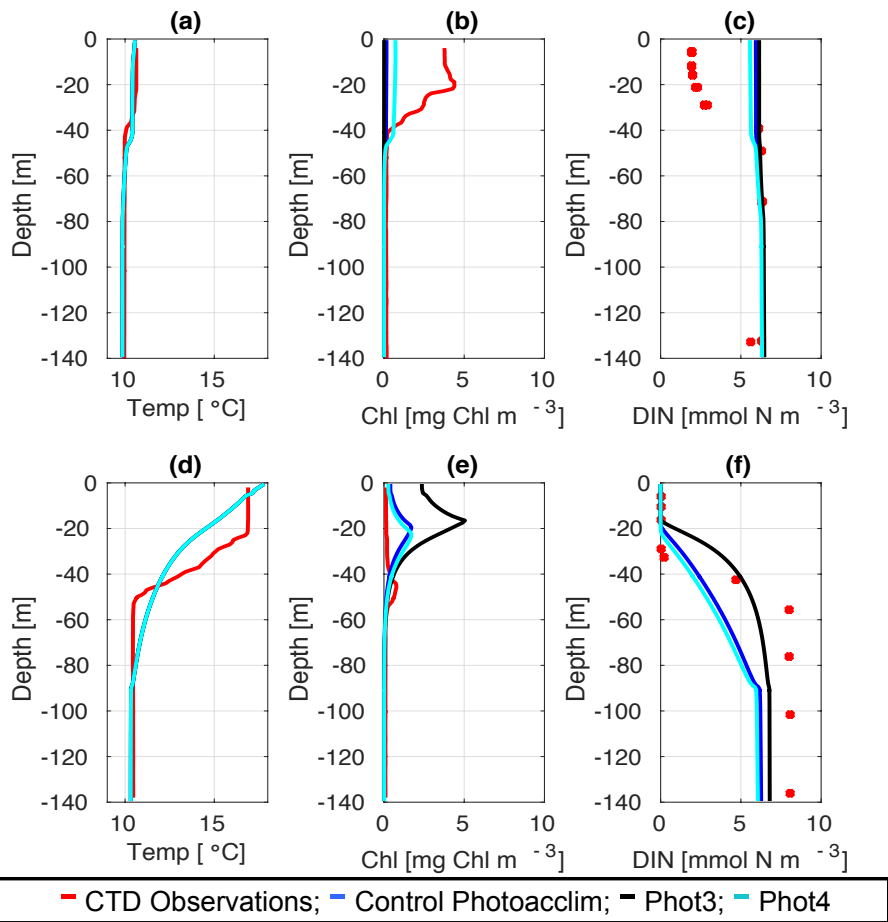


Figure 4.23: CTD observations from the SSB programme (red line) including data for: springtime (20/04/2015) (a) temperature, (b) chlorophyll-*a*, and (c) DIN; for summertime (24/07/2015) for (d) temperature, (e) chlorophyll-*a*, and (f) DIN along the S2P3-Photoacclim (blue line), Phot 3 ($Q_m = 0.2$; black line), and Phot 4 ($Q_m = 0.6$; cyan line).

Lower values of Q_m ($= 0.4 \text{ mg N (mg C)}^{-1}$) produces lower values in the profiles of P_{\max}^{chl} and E_k , increasing a mismatch with observations in comparison to the Control Photoacclim experiment. While a value of $Q_m = 0.6 \text{ mg N (mg C)}^{-1}$ increases the value of the physiological profiles.

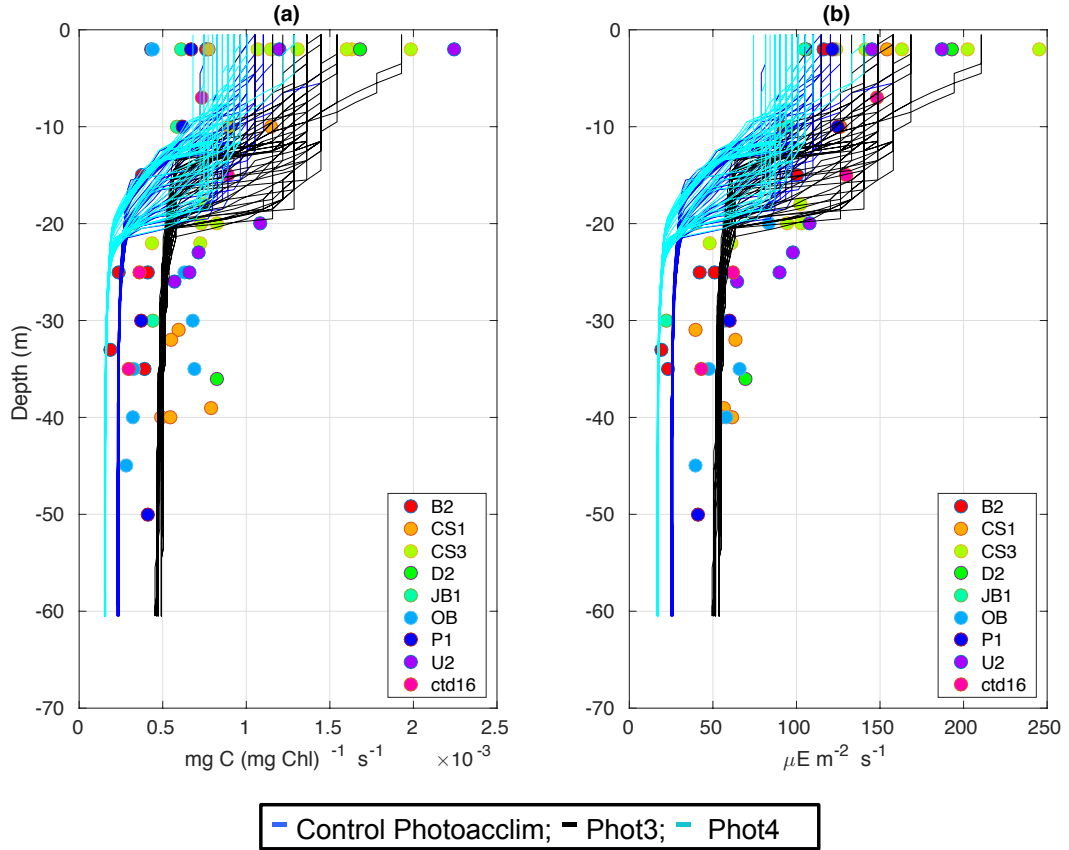


Figure 4.24: Observations from the cruises CD173 and JR98 in different locations of the Celtic Sea, including Control Photoacclim (blue lines), Phot 3 ($Q_m = 0.2$; black lines), and Phot 4 ($Q_m = 0.6$; cyan lines) for: (a) chlorophyll-a specific maximum light-saturated photosynthesis rate (P_{\max}^{Chl}) and (b) light saturation parameter (E_k). The data from the model was plotted for the same days that the observations were collected.

The experiments Phot5 and Phot6 test the sensitivity of the S2P3-Photoacclim to changes in θ_{\max}^{N} , ranging from 0.15 to 0.45 mg Chl (mg N) $^{-1}$, respectively (Table 4.4). This parameter produces changes in the dynamics of the ecosystem in terms of the timing and magnitude of the spring phytoplankton bloom (Figure 4.25), being able to delay it by 33 days (year 2014) and by 41 days (year 2015) when $\theta_{\max}^{\text{N}} = 0.15$ mg Chl (mg N) $^{-1}$ and, on the other hand, producing earlier spring phytoplankton blooms than the Control Photoacclim experiment by 11 days (year 2014) and 15 days (year 2015) when $\theta_{\max}^{\text{N}} = 0.45$ mg Chl (mg N) $^{-1}$ as shown in Table 4.11. The S2P3-Photoacclim model is, on average, the most sensitive to changes of the θ_{\max}^{N} parameter in terms of the timing and magnitude of the

spring phytoplankton bloom.

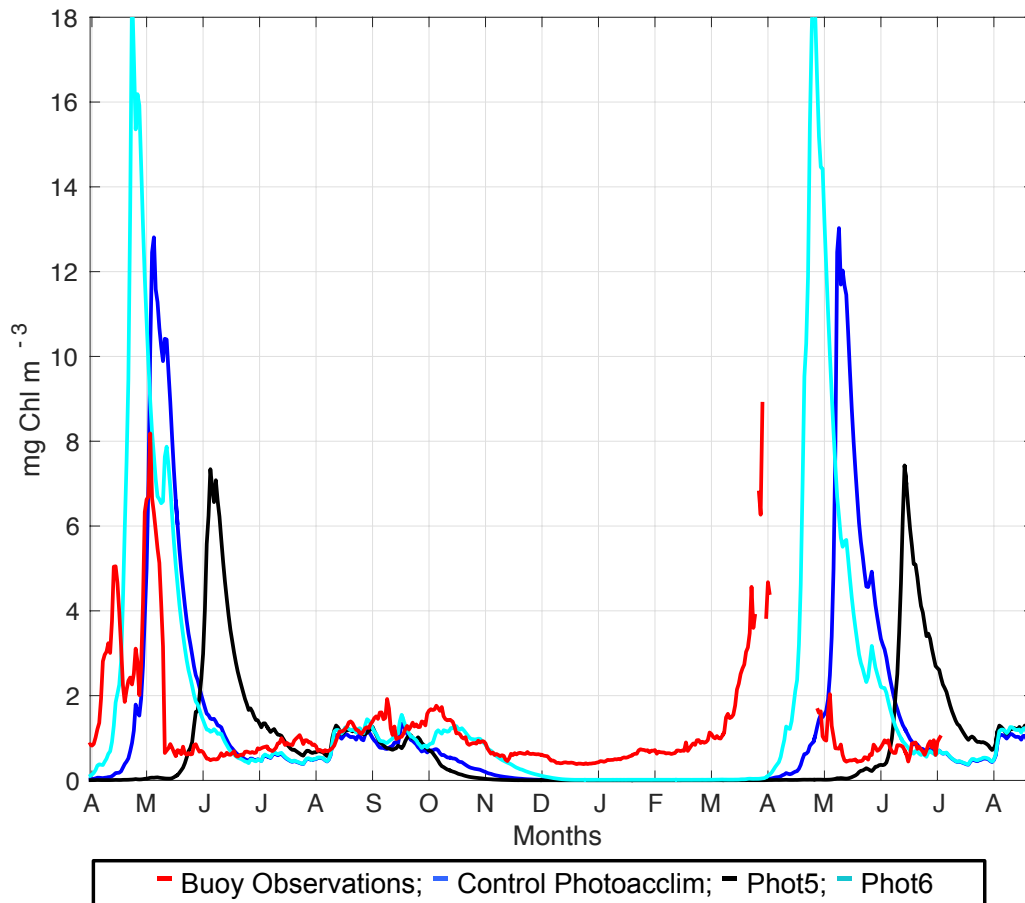


Figure 4.25: SSB buoy observations (red line) from the start of April 2014 to end of June 2015 compared to the Control Photoacclim (blue line), Phot 5 ($\theta_{\max}^N = 0.15$; black line), and Phot 6 ($\theta_{\max}^N = 0.45$; cyan line) shown from start of April 2014 to the end of August 2015 for surface chlorophyll-*a*.

In the comparison to CTD observations, the spring phytoplankton bloom has not yet started in the Phot5 ($\theta_{\max}^N = 0.15$) experiment, therefore, there are low values of surface chlorophyll-*a* (Figure 4.26b). During summer, an SCM can be observed for Phot5 ($\theta_{\max}^N = 0.15$) and Phot6 ($\theta_{\max}^N = 0.45$; Figure 4.26e), with Phot6 experiment showing a very similar SCM than in the Control Photoacclim experiment.

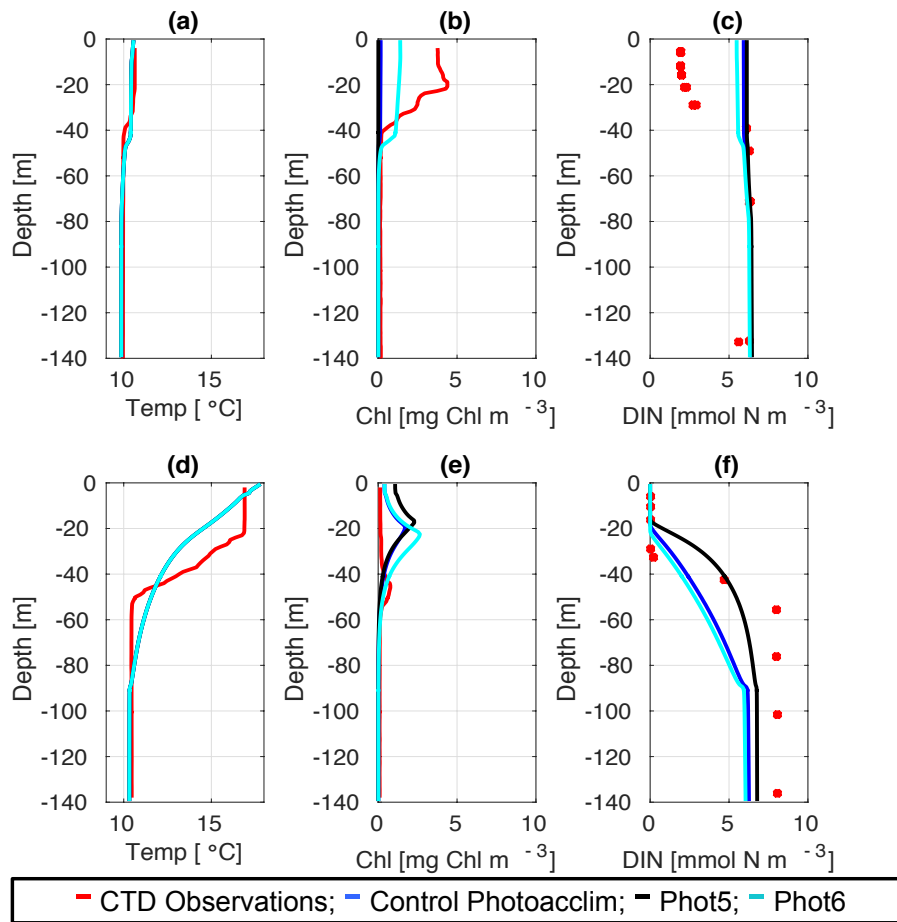


Figure 4.26: CTD observations from the SSB programme (red line) including data for: springtime (20/04/2015) (a) temperature, (b) chlorophyll-*a*, and (c) DIN; for summer-time (24/07/2015) for (d) temperature, (e) chlorophyll-*a*, and (f) DIN along the S2P3-Photoacclim (blue line), Phot 5 ($\theta_{\max}^N = 0.15$; black line), and Phot 6 ($\theta_{\max}^N = 0.45$; cyan line).

Finally, θ_{\max}^N produces changes in the physiological variables shown in Figure 4.27, with lower profile values for the Phot6 experiment through the water column in comparison to the Control Photoacclim experiment, but higher values than in the Control Photoacclim experiment when decreasing θ_{\max}^N to $0.15 \text{ mg Chl (mg N)}^{-1}$ (Phot5 experiment).

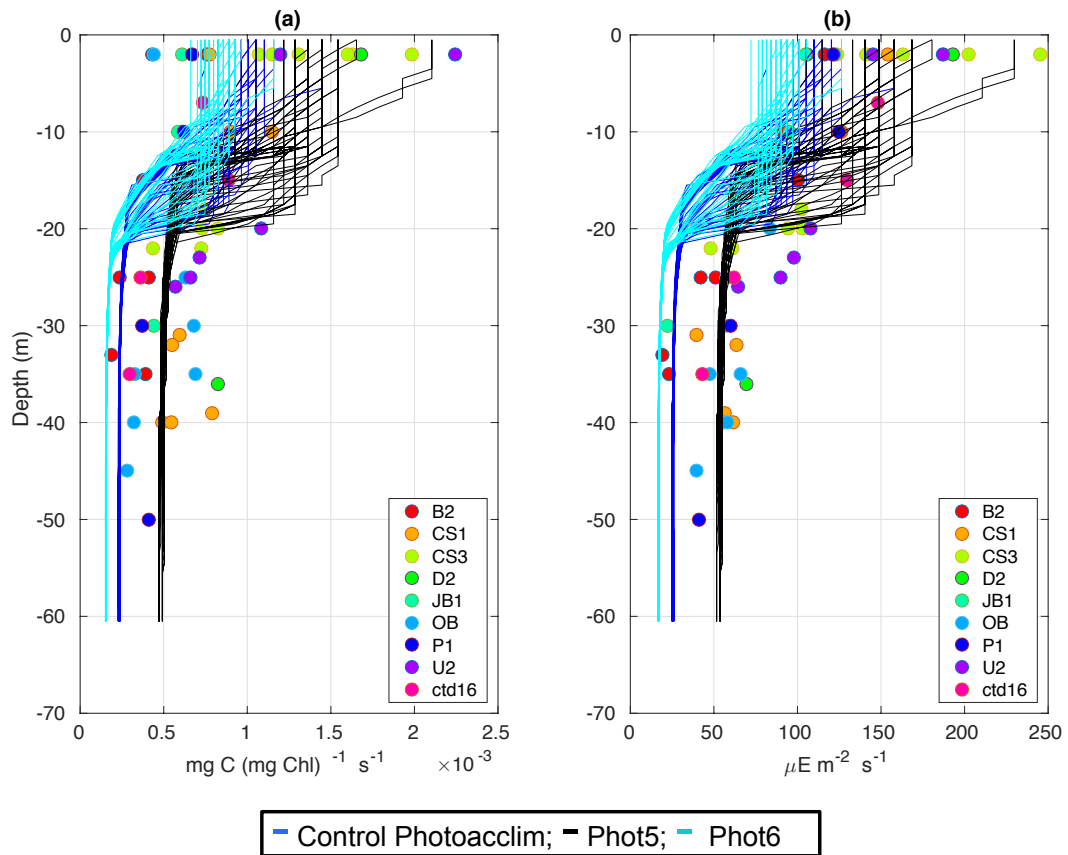


Figure 4.27: Observations from the cruises CD173 and JR98 in different locations of the Celtic Sea, including Control Photoacclim (blue lines), Phot 5 ($\theta_{\max}^{\text{N}} = 0.15$; black lines), and Phot 6 ($\theta_{\max}^{\text{N}} = 0.45$; cyan lines) for: (a) chlorophyll-a specific maximum light-saturated photosynthesis rate (P_{\max}^{Chl}) and (b) light saturation parameter (E_k). The data from the model was plotted for the same days that the observations were collected.

Respiration rates in the S2P3-Photoacclim were also analysed, ranging from 0.01 d^{-1} (Phot7) to 0.03 d^{-1} (Phot8), showing that the model is less sensitive to changes in respiration rates in terms of the timing and magnitude of the spring phytoplankton bloom (Figure 4.28; Table 4.11). Moreover, small differences are observed between these experiments and the Control Photoacclim experiment in terms of the magnitude of the SCM during summer (Figure 4.29e).

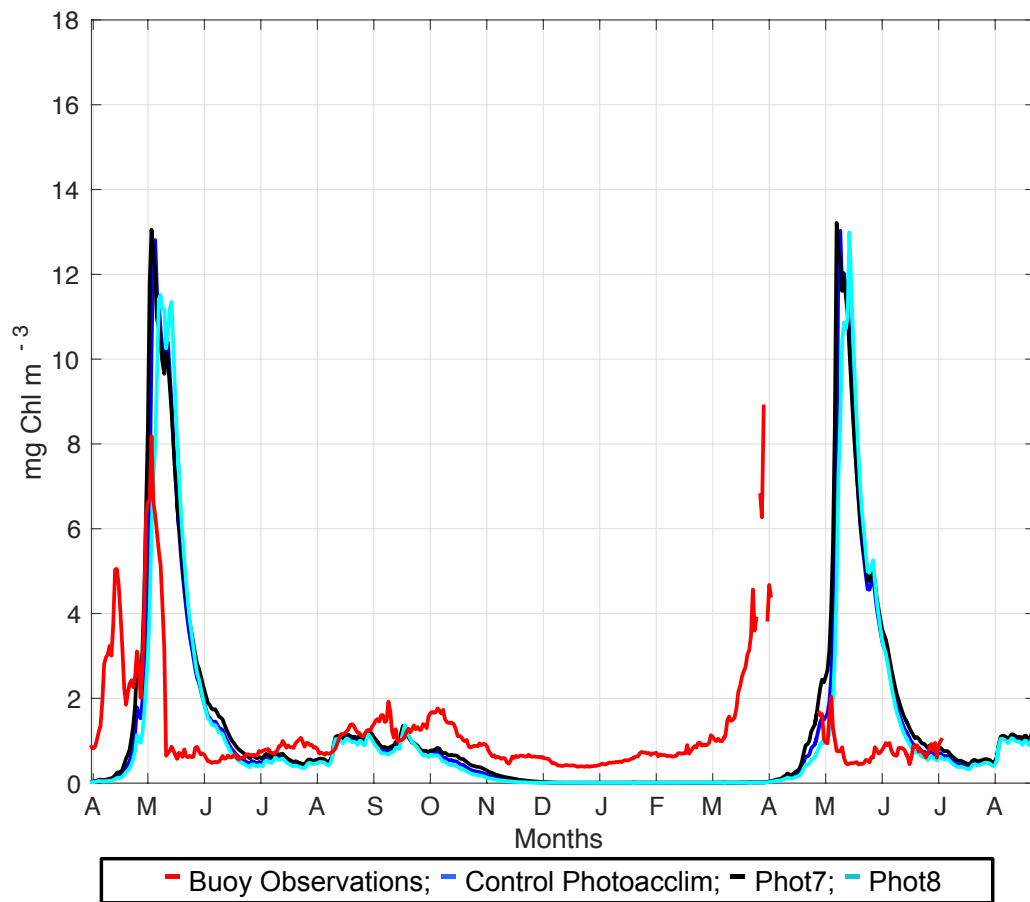


Figure 4.28: SSB buoy observations (red line) from the start of April 2014 to end of June 2015 compared to the Control Photoacclim (blue line), Phot 7 ($R_C = R_{chl} = R_n = 0.01$; black line), and Phot8 ($R_C = R_{chl} = R_n = 0.03$; cyan line) shown from start of April 2014 to the end of August 2015 for surface chlorophyll-*a*.

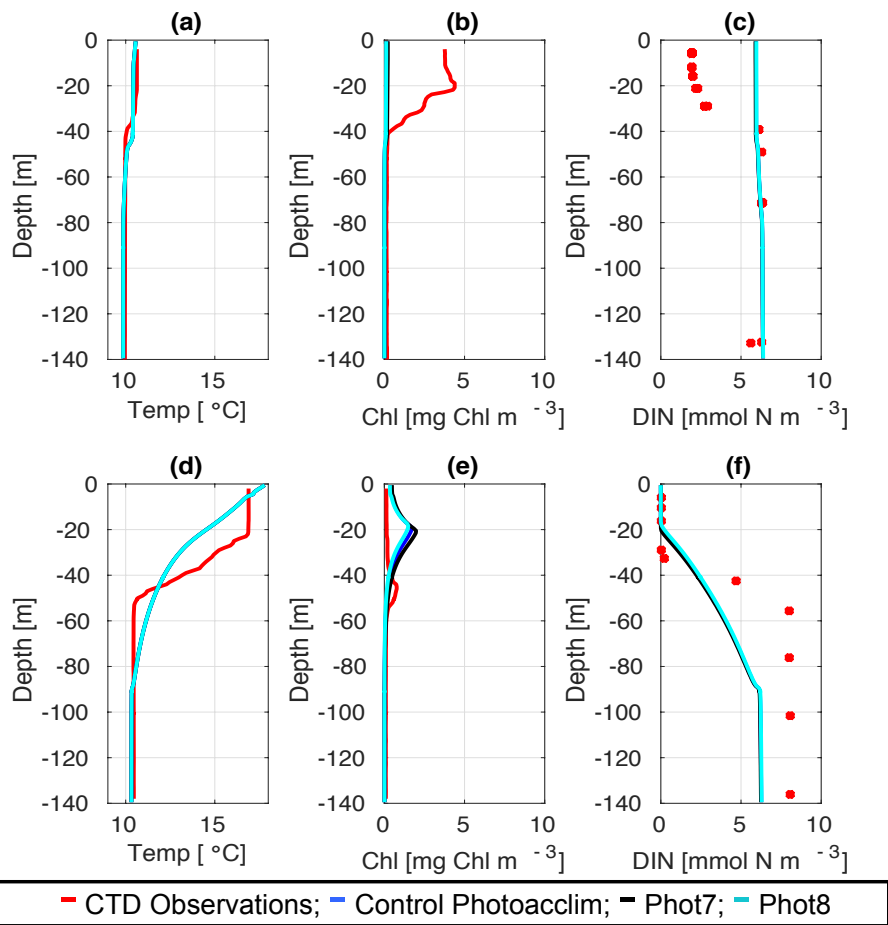


Figure 4.29: CTD observations from the SSB programme (red line) including data for: springtime (20/04/2015) (a) temperature, (b) chlorophyll-*a*, and (c) DIN; for summer-time (24/07/2015) for (d) temperature, (e) chlorophyll-*a*, and (f) DIN along the S2P3-Photoacclim (blue line), Phot 7 ($R_C = R_{chl} = R_n = 0.01$; black line), and Phot8 ($R_C = R_{chl} = R_n = 0.03$; cyan line).

Finally, changes in the respiration rates show small differences for the Phot7 and Phot8 experiments in terms of P_{max}^{Chl} and E_k (Figure 4.30), changing values only at the surface (top 20 m of the water column).

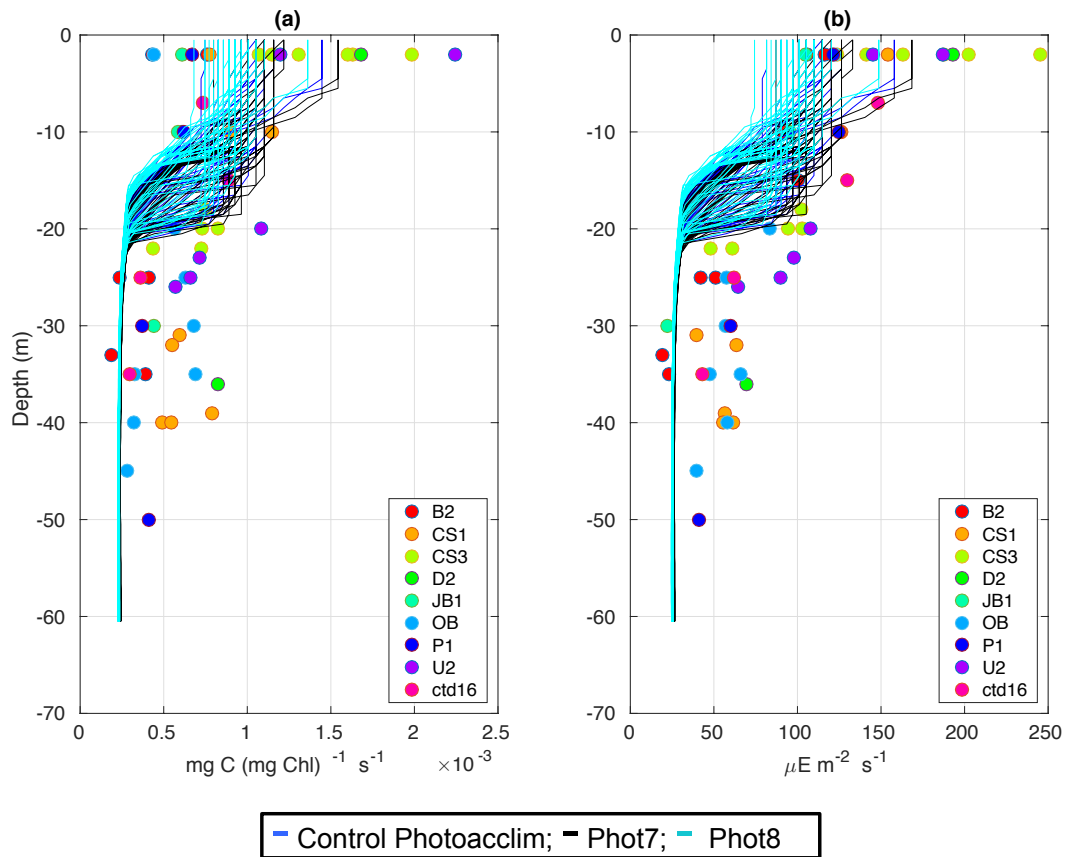


Figure 4.30: Observations from the cruises CD173 and JR98 in different locations of the Celtic Sea, including Control Photoacclim (blue lines), Phot 7 ($R_C = R_{\text{chl}} = R_n = 0.01$; black line), and Phot8 ($R_C = R_{\text{chl}} = R_n = 0.03$; cyan line) for: (a) chlorophyll-a specific maximum light-saturated photosynthesis rate (P_{\max}^{Chl}) and (b) light saturation parameter (E_k). The data from the model was plotted for the same days that the observations were collected.

Experiments	Years	Timing spring phytoplankton bloom (date)	Magnitude spring phytoplankton bloom (mg Chl m ⁻³)
Phot1 ($P_{\max}^C \downarrow$)	2014	26 th May	306.9
	2015	12 th June	273.6
Phot2 ($P_{\max}^C \uparrow$)	2014	18 th April	245.9
	2015	25 th April	292.9
Phot3 ($Q_m \downarrow$)	2014	28 th May	410.3
	2015	15 th June	376.1
Phot4 ($Q_m \uparrow$)	2014	18 th April	200.4
	2015	25 th April	219.2
Phot5 ($\theta_{\max}^N \downarrow$)	2014	28 th May	118.2
	2015	16 th June	118.4
Phot6 ($\theta_{\max}^N \uparrow$)	2014	14 th April	497.3
	2015	21 st April	496.2
Phot7 ($R_c = R_{\text{chl}} = R_n \downarrow$)	2014	24 th April	266.2
	2015	3 rd May	286.8
Phot8 ($R_c = R_{\text{chl}} = R_n \uparrow$)	2014	29 th April	197.5
	2015	12 th May	230.9
Control Photoacclim	2014	25 th April	224.1
	2015	6 th May	261.9

Table 4.10: List of the experiments run for the S2P3-Photoacclim model including the year of observations, and timing and magnitude of the spring phytoplankton bloom.

Experiments	Years	Difference timing spring phytoplankton bloom (days)	Difference magnitude spring phytoplankton bloom (mg Chl m ⁻³)
Phot1 ($P_{\max}^C \downarrow$)	2014	-31	-82.8
	2015	-37	-11.7
Phot2 ($P_{\max}^C \uparrow$)	2014	7	-21.8
	2015	11	-31
Phot3 ($Q_m \downarrow$)	2014	-33	-186.2
	2015	-40	-114.2
Phot4 ($Q_m \uparrow$)	2014	7	23.7
	2015	11	42.7
Phot5 ($\theta_{\max}^N \downarrow$)	2014	-33	105.9
	2015	-41	143.5
Phot6 ($\theta_{\max}^N \uparrow$)	2014	11	-273.2
	2015	15	-234.3
Phot7 ($R_c = R_{chl} = R_n \downarrow$)	2014	1	-42.1
	2015	3	-24.9
Phot8 ($R_c = R_{chl} = R_n \uparrow$)	2014	-4	26.6
	2015	-6	31

Table 4.11: List of the experiments run for the S2P3-Photoacclim model including the year of observations, and differences in the timing and magnitude of the spring phytoplankton bloom (differences given by the Control Photoacclim minus each experiment). Orange colour represents the largest difference in terms of the timing of the spring phytoplankton bloom between the Control Photoacclim and a given experiment; the red colour represents the largest difference in terms of the magnitude of the spring phytoplankton bloom between the Control Photoacclim and a given experiment.

4.4.2.3 S2P3 v8.0

Finally, a sensitivity analysis was performed for the S2P3 v8.0 model, by changing nine different parameters, which were included in the analysis of the S2P3-Photoacclim and the S2P3-NPZ models. A total of 18 experiments were analysed in comparison to the observations, including characteristics of the ecosystem dynamics such as the timing and magnitude of the spring phytoplankton bloom, and the total annual zooplankton biomass (Table 4.12), which enabled to quantify which parameter produces the most changes in this model and which one produces the least (Table 4.13).

Because the number of figures plotted for this sensitivity analysis was large, they are shown in the Appendix section of this work, except for the experiments NPZPhot 1, 2, 9, 10, 11, and 12 that showed results closest to observations (Figures 4.31 - 4.39).

Differences in sensitivity experiments for the S2P3 v8.0 model could be compared with those of the S2P3-NPZ and the S2P3-Photoacclim models. As expected, for the physiological parameters analysed in this model (P_{\max}^C , Q_m , θ_{\max}^N , and respiration rates) similar changes in behaviour were observed for the ecosystem dynamics in comparison to the sensitivity analysis of those parameters in the S2P3-Photoacclim model. The physiological variables have similar responses in the S2P3 v8.0 model (Figures A7, A10, and A13) and the ones studied in the S2P3-Photoacclim model (Figures 4.21, 4.24, 4.27, and 4.30).

The default values of each parameter are different to the ones found in the S2P3-NPZ and S2P3-Photoacclim models, but these were changed by -50% and +50% as in former sensitivity analyses. The first experiments NPZPhot1 and NPZPhot2 test the P_{\max}^C parameter, showing that the model is less sensitive to these changes in terms of the timing and magnitude of the spring phytoplankton bloom than in the S2P3-Photoacclim model (Tables 4.11, 4.13), possibly due to the inclusion of zooplankton in the S2P3 v8.0 model, accounting to be more important for these spring characteristics than photo-acclimation. Additionally, no changes in the magnitude of the spring zooplankton bloom could be observed (Figure 4.31b); a delayed bloom is observed for the NPZPhot1 experiment, which agrees with the later phytoplankton blooms as shown in Figure 4.31a. The largest differences caused by the changes in P_{\max}^C occur during spring, with Figure 4.31b,c showing the spring phytoplankton bloom in the NPZPhot1 and NPZPhot2 experiments. No changes can be observed

during summer in comparison to the Control NPZPhot experiment (Figure 4.32e,f).

The analysis of Q_m show some differences regarding the sensitivity study performed for that parameter in the S2P3-Photoacclim model. When $Q_m = 0.225 \text{ mg Chl (mg N)}^{-1}$ (NPZPhot3 experiment), a delayed spring bloom occurs for phytoplankton and zooplankton but the magnitude of the spring phytoplankton bloom is higher than in the Control NPZPhot experiment (Figure A5). These differences between a delayed bloom produced by NPZPhot3 can be observed in the profile of chlorophyll-*a* during spring, where no spring bloom can be observed by that date (Figure A6b); on the other hand, NPZPhot4 shows the same timing than in the Control NPZPhot experiment, with higher concentrations of surface chlorophyll-*a*.

The S2P3-Photoacclim model was the most sensitive to changes in the θ_{\max}^N parameter in terms of the timing and magnitude of the spring phytoplankton bloom (Table 4.11). Similarly this parameter was, on average, the one to produce the most changes in the timing of the spring phytoplankton bloom for the S2P3 v8.0 model. The NPZPhot5 and NPZPhot6 experiments produced changes not only in the timing but in the magnitude of the spring phytoplankton bloom (Figure A8), with less productive and delayed spring blooms when θ_{\max}^N was lower ($0.075 \text{ mg Chl (mg N)}^{-1}$). The spring zooplankton bloom coincide with the timing of the phytoplankton blooms. Additionally, Figure A9 shows that the largest differences between the Control NPZPhot and these experiments occur during spring, with a delayed bloom in the NPZPhot5 and a large spring bloom for the NPZPhot6.

Finally, for the last set of physiological parameters considered in the S2P3 v8.0 model, respiration rates were analysed. Sensible changes in terms of the timing and magnitude of the spring blooms could be produced (Figure A11), with earlier blooms when the respiration rates are lower (NPZPhot7) and delayed blooms by ~ 15 days when the respiration rates are higher (NPZPhot8). Similar to all the experiments shown in the S2P3 v8.0 model, differences with the Control NPZPhot experiment can only be observed during spring (Figure A12), with a marked SML for the NPZPhot7 experiment (Figure A12b) and similar values of surface chlorophyll-*a* than in the Control NPZPhot experiment; on the other hand, the NPZPhot8 experiment showed that the spring phytoplankton bloom has not yet started in comparison to CTD observations.

The experiments NPZPhot9 and NPZPhot10 analyse the γ_1 parameter, ranging from 0.05 to 0.15 (Table 4.5), respectively. Small differences are observed in terms of the timing and magnitude of the spring phytoplankton bloom (Figure 4.34a), showing lower values of surface chlorophyll-*a* during spring than the Control NPZPhot experiment (Figure 4.35b). Moreover, the model did not show a strong sensitivity to changes in γ_1 in terms of physiological variables (Figure 4.36). On average, the S2P3 v8.0 model is the least sensitive to changes in γ_1 in terms of the timing and magnitude of the spring phytoplankton bloom and the total annual zooplankton biomass than any of the other parameters analysed (Table 4.13).

The NPZPhot11 and NPZPhot12 experiments show larger differences in the timing of the spring phytoplankton bloom than in the analysis of γ_2 in the S2P3-NPZ model. The zooplankton biomass differences coincide with the phytoplankton differences between each experiment, but the predator-prey coupling is not as strong as the one shown in Figure 4.11b. Differences in the surface chlorophyll-*a* can be observed in comparison to the Control NPZPhot experiment (Figures 4.37a, 4.38b). Additionally, Figure 4.39 showed differences in the shallower layers of the water column for P_{\max}^{chl} and E_k .

The predator-prey coupling did not seem to be as strong as shown in the S2P3-NPZ model, in the case of the experiments NPZPhot13 and NPZPhot14, secondary blooms are not observed in Run5 ($\lambda = 0.375$) and Run 6 ($\lambda = 1.125$; Figure 4.11). The λ parameter generated differences in the timing of the spring phytoplankton bloom in comparison to the Control NPZPhot experiment. The NPZPhot13 was run with $\lambda=0.1$ (mmol N m^{-3})⁻¹, showing more productive spring blooms than the Control NPZPhot experiment (Figure A14a) with lower peak spring bloom but longer duration and, therefore, delaying the spring zooplankton bloom (Figure A14b). Moreover, during spring the NPZPhot14 show that the spring bloom has not started yet (Figure A15b), while the NPZPhot13 show similar values of surface chlorophyll to the Control NPZPhot. Additionally, changes in λ produce slight differences during summer in the SCM (Figure A15e) and DIN concentrations (Figure A15f). On the other hand, physiological variables also change with λ , with higher values of P_{\max}^{chl} and E_k when λ is lower.

The NPZPhot15 and NPZPhot16 experiments show that the S2P3 v8.0 model is, on average, the most sensitive to changes in R_m in terms of the magnitude of the spring phytoplankton bloom (Table 4.13). The effects that R_m has in the model dynamics are very similar to the ones found in the case of experiments that change λ (NPZPhot13, NPZPhot14). Lower values in the maximum ingestion rate of phytoplankton can produce earlier and larger spring phytoplankton blooms (Figure A17a) compared to the Control NPZPhot experiment. On the other hand, a higher value of R_m shows a delayed spring bloom (Figure A18b) compared to the CTD observations and the Control NPZPhot experiment. Additionally, lower values of R_m produces higher values on P_{\max}^{chl} and E_k , with larger differences in the shallower depths.

Finally, zooplankton mortality produced differences in the timing of the spring bloom, with delays of 30 days (year 2014) and 35 days (year 2015) for the NPZPhot17 experiment ($m = 0.01$; Figure A20a), affecting the timing and magnitude of the spring zooplankton bloom (Figure A20b). Differences in the timing and magnitude of the spring phytoplankton bloom are small between the Control NPZPhot and the NPZPhot18 ($m = 0.03$) experiments, but larger differences can be observed in terms of zooplankton biomass for both experiments. Zooplankton mortality affects the S2P3 v8.0 model the most in terms of total annual zooplankton biomass. On the other hand, because the spring bloom is delayed when m is lower, low values of surface chlorophyll- a are observed during spring (Figure A21b); during summer there are no large differences between chlorophyll- a and DIN profiles (Figure A21e,f). Finally, the largest differences between physiological variables (Figure A22) are given by zooplankton mortality, changing the vertical profiles in the shallower levels of the water column by, for example, increasing P_{\max}^{C} and E_k when m is higher.

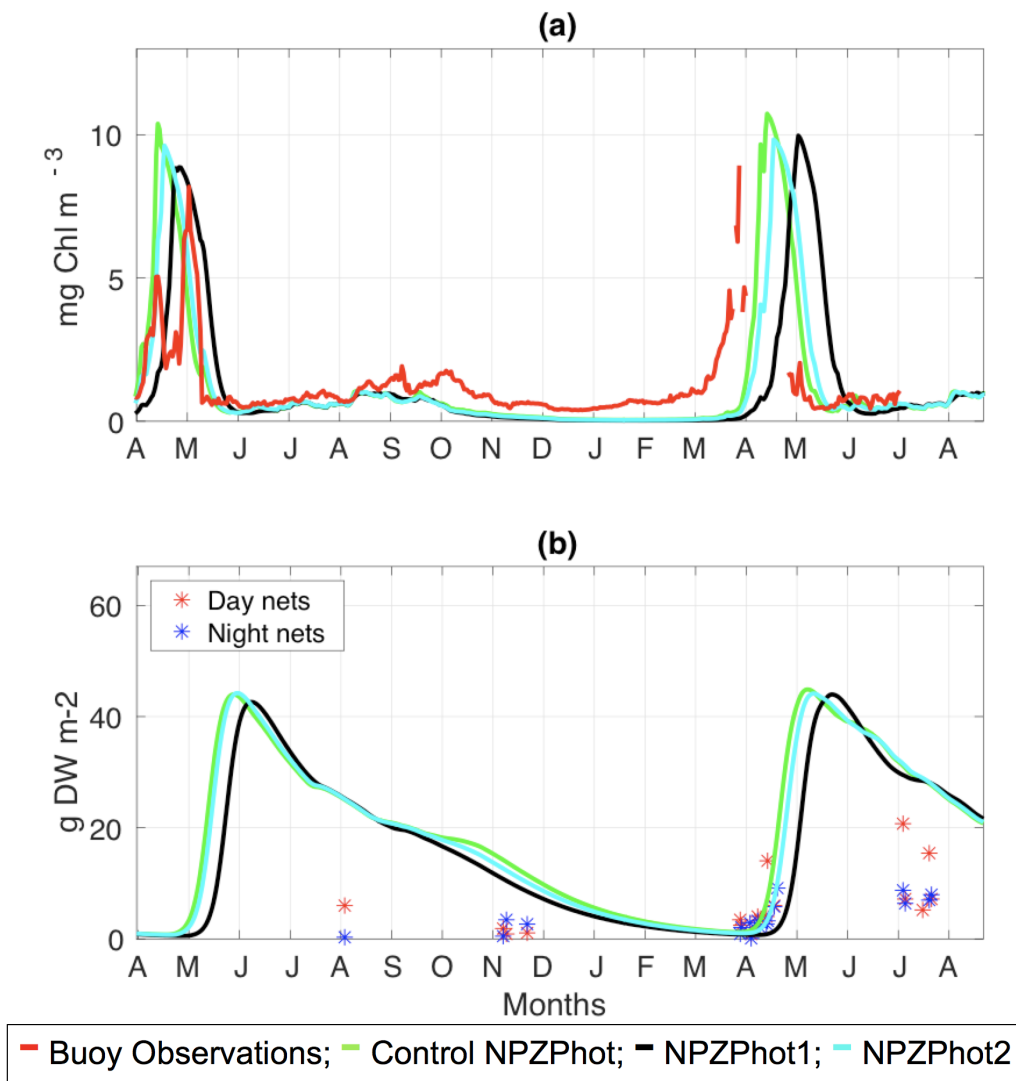


Figure 4.31: SSB buoy observations (red line) from the start of April 2014 to end of June 2015 compared to the Control NPZPhot (green line), NPZPhot 1 ($P_{\text{max}}^{\text{C}} = 1.75$; black line), and NPZPhot 2 ($P_{\text{max}}^{\text{C}} = 5.25$; cyan line) shown from start of April 2014 to the end of August 2015 for (a) surface chlorophyll-*a* and (b) zooplankton biomass.

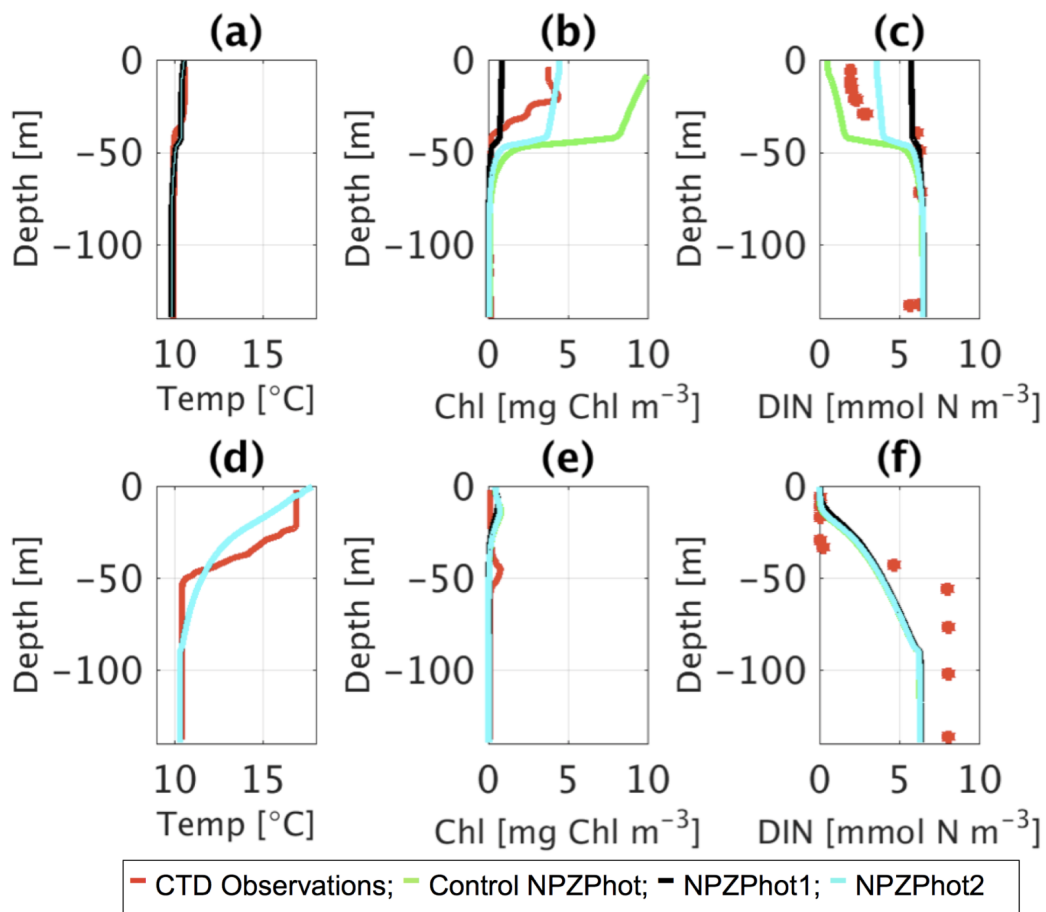


Figure 4.32: CTD observations from the SSB programme (red line) including data for: springtime (20/04/2015) (a) temperature, (b) chlorophyll-*a*, and (c) DIN; for summertime (24/07/2015) for (d) temperature, (e) chlorophyll-*a*, and (f) DIN along the Control NPZPhot (green line), NPZPhot 1 ($P_{\max}^C = 1.75$; black line), and NPZPhot 2 ($P_{\max}^C = 5.25$; cyan line).

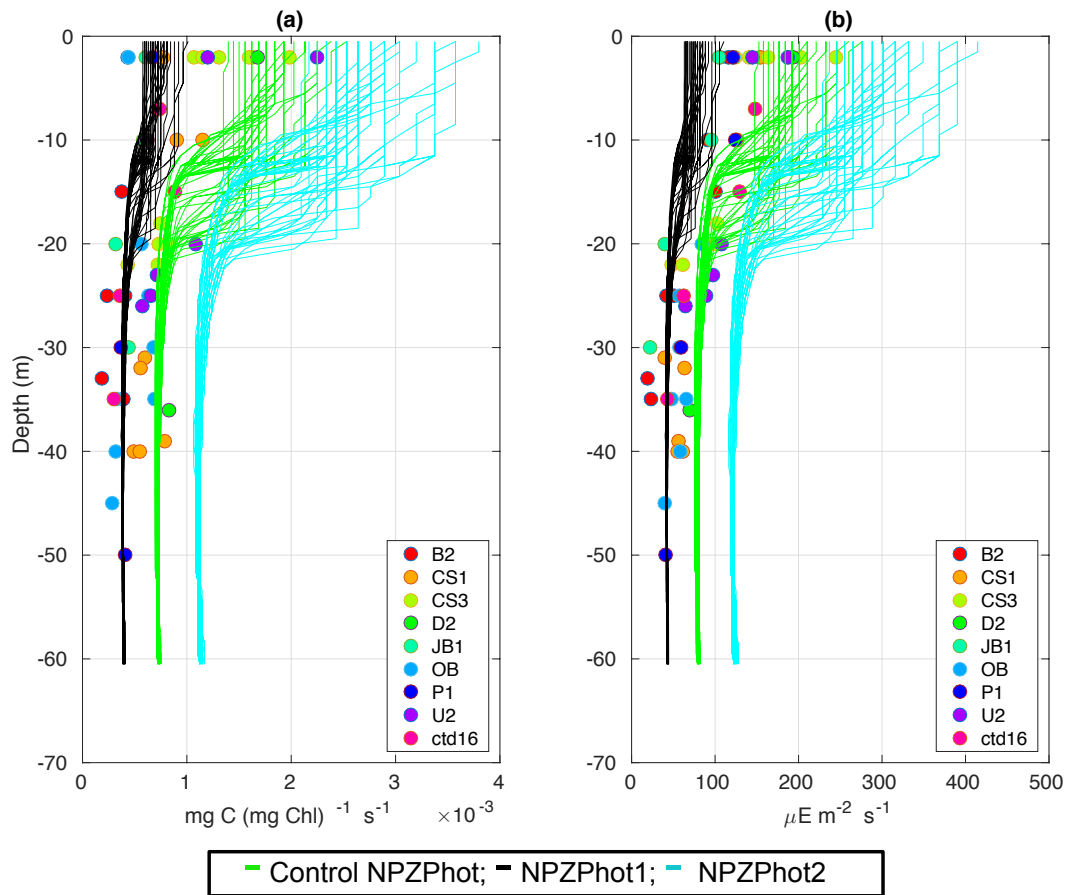


Figure 4.33: Observations from the cruises CD173 and JR98 in different locations of the Celtic Sea, including Control NPZPhot (green lines), NPZPhot 1 ($P_{\max}^C = 1.75$; black lines), and NPZPhot 2 ($P_{\max}^C = 5.25$; cyan lines) for: (a) chlorophyll-*a* specific maximum light-saturated photosynthesis rate (P_{\max}^{Chl}) and (b) light saturation parameter (E_k). The data from the model was plotted for the same days that the observations were collected.

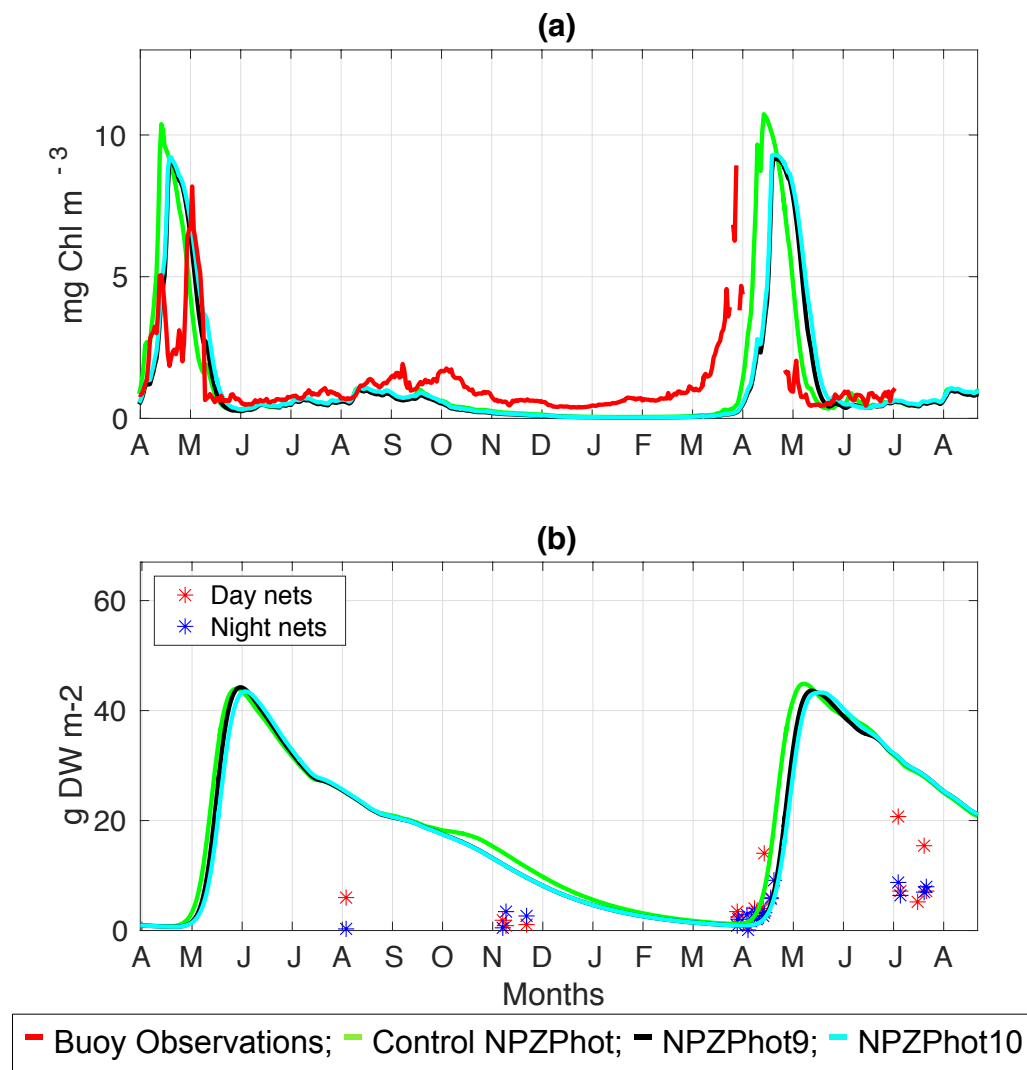


Figure 4.34: SSB buoy observations (red line) from the start of April 2014 to end of June 2015 compared to the Control NPZPhot (green line), NPZPhot 9 ($\gamma_1 = 0.05$; black line), and NPZPhot 10 ($\gamma_1 = 0.15$; cyan line) shown from start of April 2014 to the end of August 2015 for (a) surface chlorophyll-*a* and (b) zooplankton biomass.

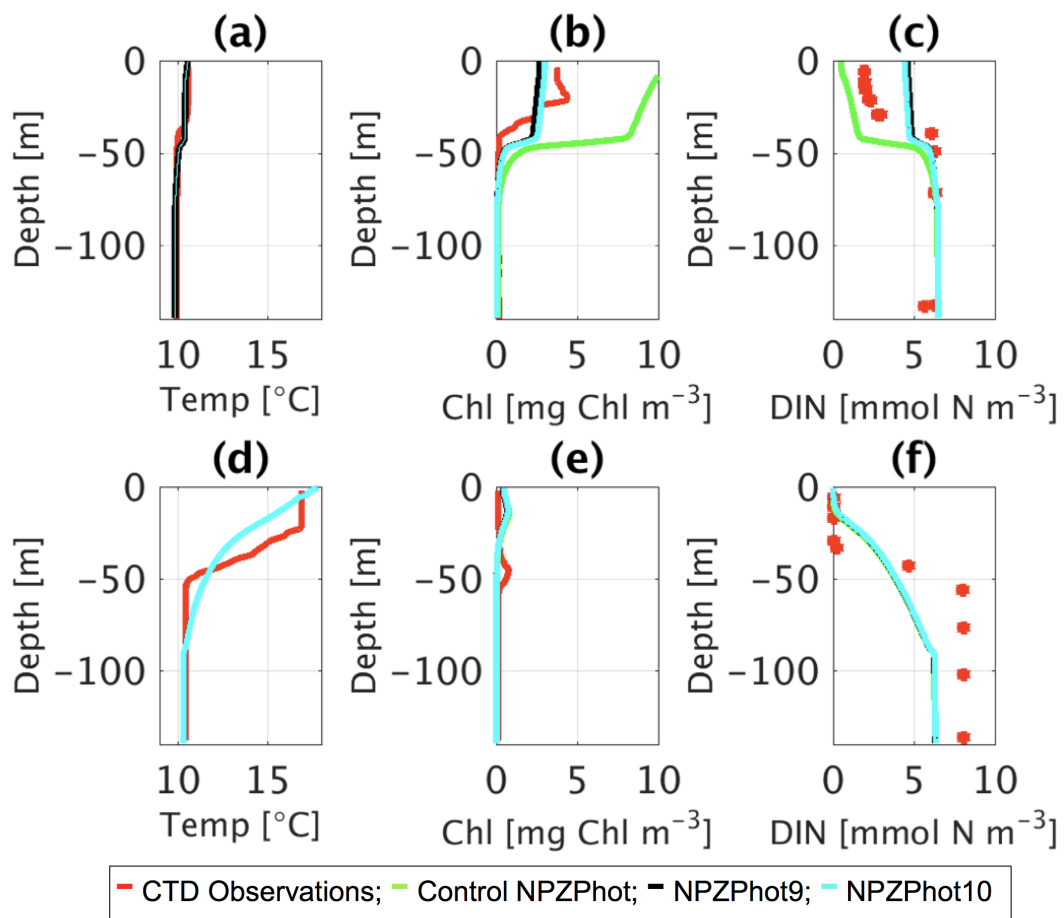


Figure 4.35: CTD observations from the SSB programme (red line) including data for: springtime (20/04/2015) (a) temperature, (b) chlorophyll-*a*, and (c) DIN; for summertime (24/07/2015) for (d) temperature, (e) chlorophyll-*a*, and (f) DIN along the Control NPZPhot (green line), NPZPhot 9 ($\gamma_1 = 0.05$; black line), and NPZPhot 10 ($\gamma_1 = 0.15$; cyan line).

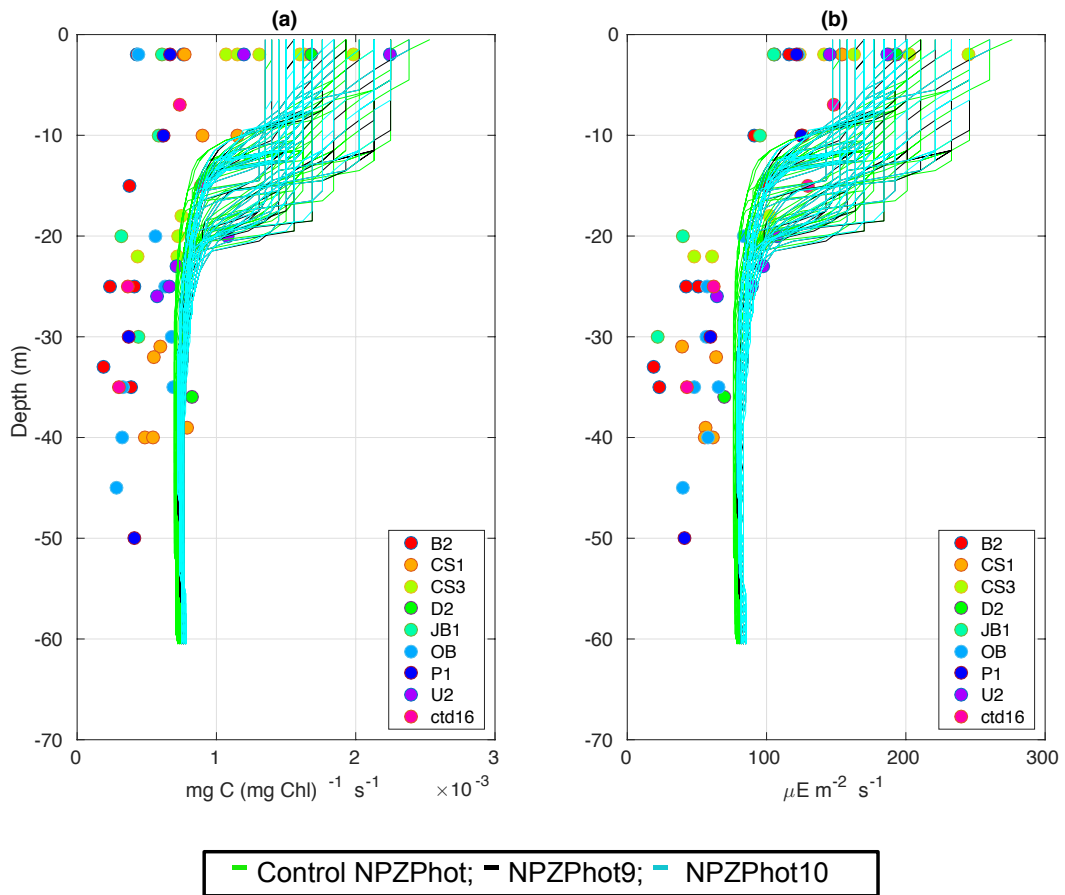


Figure 4.36: Observations from the cruises CD173 and JR98 in different locations of the Celtic Sea, including Control NPZPhot (green lines), NPZPhot 9 ($\gamma_1 = 0.05$; black lines), and NPZPhot 10 ($\gamma_1 = 0.15$; cyan lines) for: (a) chlorophyll-*a* specific maximum light-saturated photosynthesis rate (P_{\max}^{Chl}) and (b) light saturation parameter (E_k). The data from the model was plotted for the same days that the observations were collected.

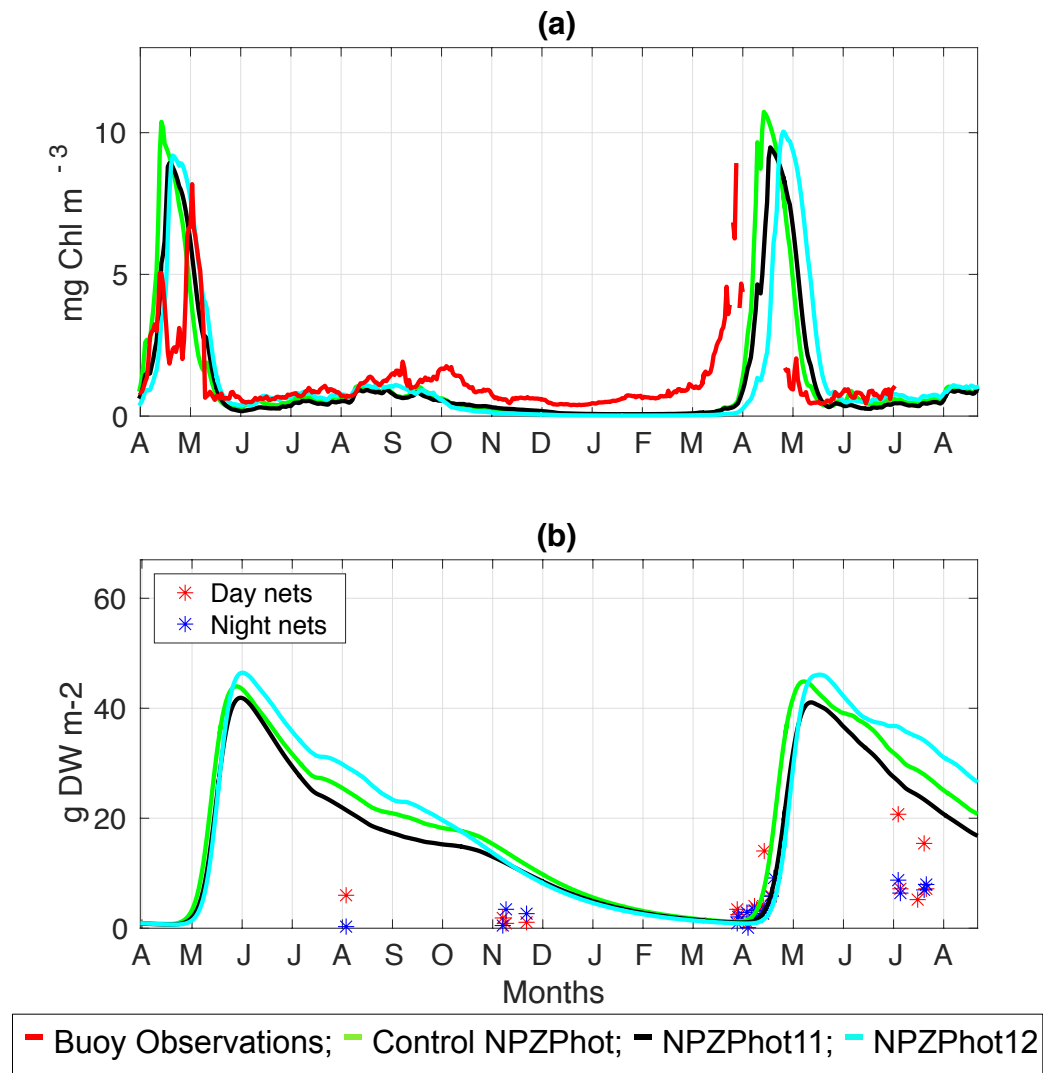


Figure 4.37: SSB buoy observations (red line) from the start of April 2014 to end of June 2015 compared to the Control NPZPhot (green line), NPZPhot 11 ($\gamma_2 = 0.2$; black line), and NPZPhot 12 ($\gamma_2 = 0.6$; cyan line) shown from start of April 2014 to the end of August 2015 for (a) surface chlorophyll-*a* and (b) zooplankton biomass.

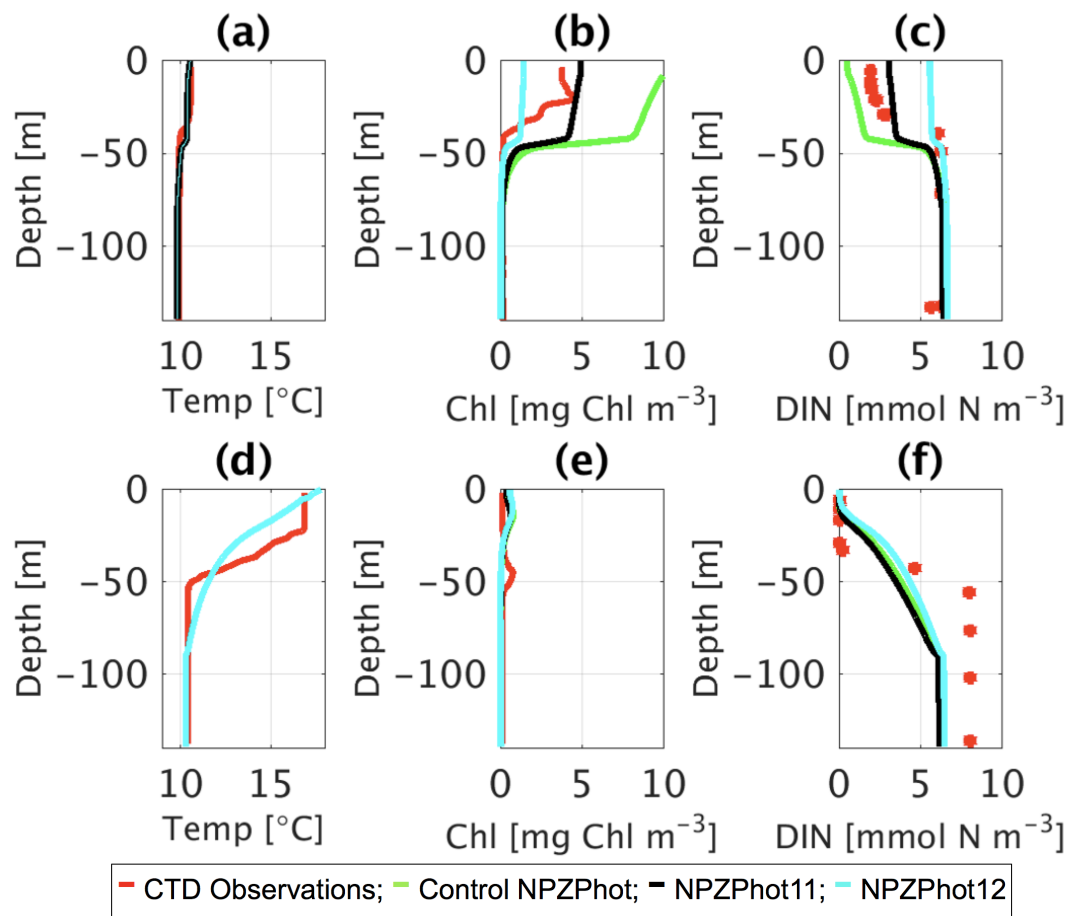


Figure 4.38: CTD observations from the SSB programme (red line) including data for: springtime (20/04/2015) (a) temperature, (b) chlorophyll-*a*, and (c) DIN; for summertime (24/07/2015) for (d) temperature, (e) chlorophyll-*a*, and (f) DIN along the Control NPZPhot (green line), NPZPhot 11 ($\gamma_2 = 0.2$; black line), and NPZPhot 12 ($\gamma_2 = 0.6$; cyan line).

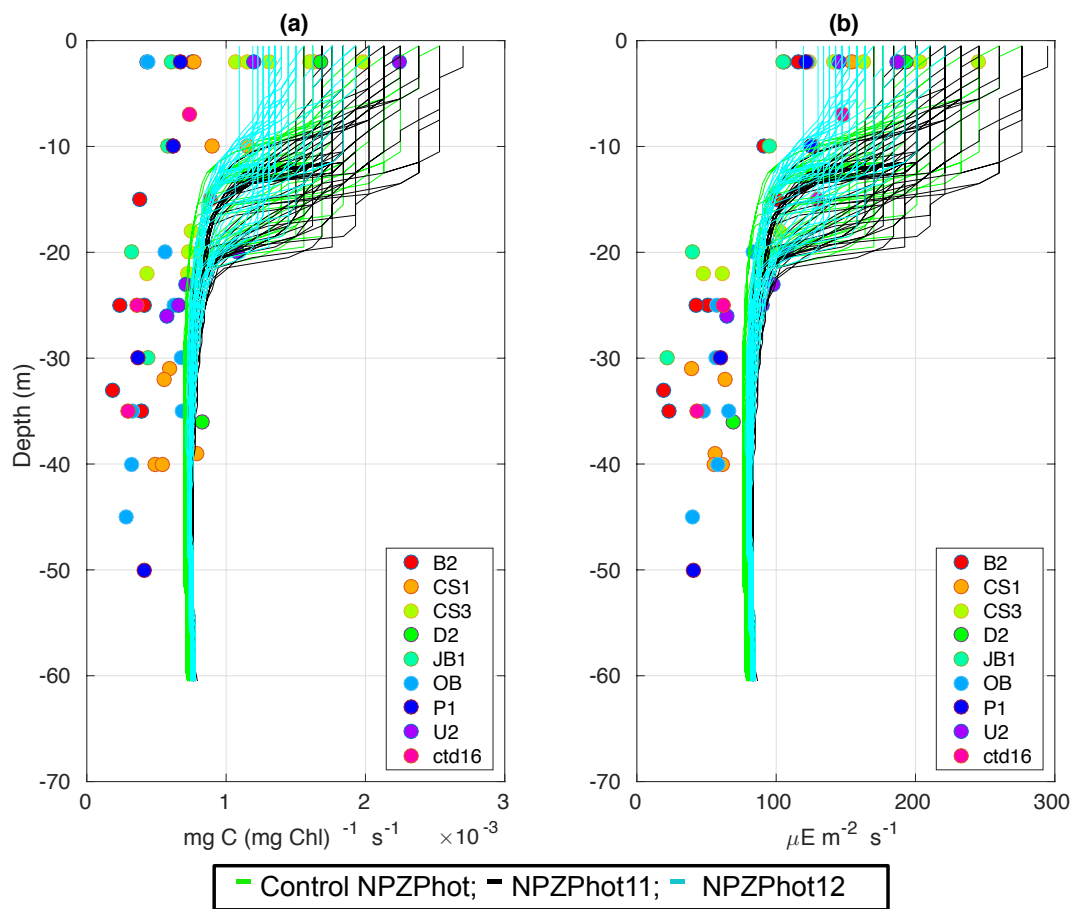


Figure 4.39: Observations from the cruises CD173 and JR98 in different locations of the Celtic Sea, including Control NPZPhot (green lines), NPZPhot 11 ($\gamma_2 = 0.2$; black lines), and NPZPhot 12 ($\gamma_2 = 0.6$; cyan lines) for: (a) chlorophyll-*a* specific maximum light-saturated photosynthesis rate (P_{\max}^{Chl}) and (b) light saturation parameter (E_k). The data from the model was plotted for the same days that the observations were collected.

Experiments	Years	Timing spring phytoplankton bloom (date)	Magnitude spring phytoplankton bloom (mg Chl m ⁻³)	Total annual zooplankton biomass (g DW m ⁻²)
NPZPhot1 ($P_{\max}^C \downarrow$)	2014	14 th April	88.4	5656
	2015	25 th April	208.7	5362
NPZPhot2 ($P_{\max}^C \uparrow$)	2014	4 th April	114.9	6003
	2015	12 th April	176.7	5906
NPZPhot3 ($Q_m \downarrow$)	2014	2 nd May	156.1	3658
	2015	13 th May	236.2	3884
NPZPhot4 ($Q_m \uparrow$)	2014	4 th April	118.7	6334
	2015	9 th April	118	6389
NPZPhot5 ($\theta_{\max}^N \downarrow$)	2014	19 th May	103.5	3055
	2015	21 st May	103.1	3514
NPZPhot6 ($\theta_{\max}^N \uparrow$)	2014	25 th March	110.2	6733
	2015	27 th March	211.5	6797
NPZPhot7 ($R_C = R_{chl} = R_n \downarrow$)	2014	31 st March	36.4	6432
	2015	6 th April	106.1	6410
NPZPhot8 ($R_C = R_{chl} = R_n \uparrow$)	2014	18 th April	126.6	5515
	2015	27 th April	256.6	5173
NPZPhot9 ($\gamma_1 \downarrow$)	2014	9 th April	93.3	5941
	2015	15 th April	163	5804
NPZPhot10 ($\gamma_1 \uparrow$)	2014	8 th April	113.7	5869
	2015	14 th April	192.6	5724
NPZPhot11 ($\gamma_2 \downarrow$)	2014	5 th April	93.4	5268
	2015	11 th April	153.4	5235
NPZPhot12 ($\gamma_2 \uparrow$)	2014	11 th April	113.6	6613
	2015	21 st April	201.5	6392
NPZPhot13 ($\lambda \downarrow$)	2014	29 th March	282.8	6834
	2015	3 rd April	349.7	6807
NPZPhot14 ($\lambda \uparrow$)	2014	14 th April	61.4	5296
	2015	25 th April	159.7	4997
NPZPhot15 ($R_m \downarrow$)	2014	29 th March	292.5	6840
	2015	3 rd April	359.2	6812
NPZPhot16 ($R_m \uparrow$)	2014	14 th April	61.4	5283
	2015	25 th April	159.5	4992
NPZPhot17 ($m \downarrow$)	2014	3 rd May	238	8362
	2015	14 th May	203.5	8369
NPZPhot18 ($m \uparrow$)	2014	31 st March	104.4	4311
	2015	6 th April	134.5	4368
Control NPZPhot	2014	3 rd April	137.7	6110
	2015	9 th April	172.6	6094

Table 4.12: List of the experiments run for the S2P3 v8.0 model including the year of observations, timing and magnitude of the spring phytoplankton bloom, and total annual zooplankton biomass values.

Experiments	Years	Difference timing spring phytoplankton bloom (days)	Difference magnitude spring phytoplankton bloom (mg Chl m ⁻³)	Difference total annual zooplankton biomass (g DW m ⁻²)
NPZPhot1 ($P_{\max}^C \downarrow$)	2014 2015	-11 -16	49.3 -36.1	454 732
NPZPhot2 ($P_{\max}^C \uparrow$)	2014 2015	-1 -3	22.8 -4.1	107 188
NPZPhot3 ($Q_m \downarrow$)	2014 2015	-29 -34	-18.4 -63.6	2452 2210
NPZPhot4 ($Q_m \uparrow$)	2014 2015	-1 0	19 54.6	-224 -295
NPZPhot5 ($\theta_{\max}^N \downarrow$)	2014 2015	-46 -42	34.2 69.5	3055 2580
NPZPhot6 ($\theta_{\max}^N \uparrow$)	2014 2015	9 13	27.5 -38.9	-623 -703
NPZPhot7 ($R_C = R_{chl} = R_n \downarrow$)	2014 2015	3 3	101.3 66.5	-322 -316
NPZPhot8 ($R_C = R_{chl} = R_n \uparrow$)	2014 2015	-15 -18	11.1 -84	595 921
NPZPhot9 ($\gamma_1 \downarrow$)	2014 2015	-6 -6	44.4 9.6	169 290
NPZPhot10 ($\gamma_1 \uparrow$)	2014 2015	-5 -5	24 -20	241 370
NPZPhot11 ($\gamma_2 \downarrow$)	2014 2015	-2 -2	44.3 19.2	842 859
NPZPhot12 ($\gamma_2 \uparrow$)	2014 2015	-8 -12	24.1 -28.9	-503 -298
NPZPhot13 ($\lambda \downarrow$)	2014 2015	5 6	-145.1 -177.1	-724 -713
NPZPhot14 ($\lambda \uparrow$)	2014 2015	-11 -16	76.3 12.9	814 1097
NPZPhot15 ($R_m \downarrow$)	2014 2015	5 6	-154.8 -186.6	-730 -718
NPZPhot16 ($R_m \uparrow$)	2014 2015	-11 -16	76.3 13.1	827 1102
NPZPhot17 ($m \downarrow$)	2014 2015	-30 -35	-100.3 -30.9	-2252 -2275
NPZPhot18 ($m \uparrow$)	2014 2015	3 3	33.3 38.1	1799 1726

Table 4.13: List of the experiments run for the S2P3 v8.0 model including the year of observations, differences in the timing and magnitude of the spring phytoplankton bloom, and differences in the total annual zooplankton biomass values (differences given by the Control NPZPhot minus each experiment). Orange colour represents the largest difference in terms of the timing of the spring phytoplankton bloom between the Control NPZPhot and a given experiment; the red colour represents the largest difference in terms of the magnitude of the spring phytoplankton bloom between the Control NPZPhot and a given experiment; and the grey colour represents the largest difference in terms of the total annual zooplankton biomass between the Control NPZPhot and a given experiment.

4.5 Discussion

4.5.1 Calibrating models: a validation

The calibration of each model developed in this work was done on a trial-and-error basis where numerous parameter combinations were tested in order to find the most accurate version of each model in comparison to *in situ* observations. Calibrating models is a complex task, involving expertise, time, and computing resources.

Figure 4.6a shows differences in the timing and magnitude of the spring phytoplankton bloom between the optimised/calibrated versions of S2P3-NPZ, S2P3-Photoacclim, and S2P3 v8.0 models. As these features are a key focus of this work, this highlights the importance of introducing more realistic representations of biology and physics into the model, given that the S2P3 v8.0 model shows fewer quantitative differences with observations in comparison to the other two models developed. This important features were discussed in Chapter 3, suggesting that differences found in comparison to observations were significant to consider further development of the model complexity and this also represented a weakness of the S2P3 v7.0 model. However, it is important to note that there are remaining differences between the newly developed models and observations because each of these models are representing the CCS location with different limitations. For example, the S2P3-Photoacclim and S2P3 v8.0 models consider the metabolic rates for nitrogen remineralisation (R_N), chlorophyll degradation (R_{chl}), and maintenance respiration rate (R_C) as equal; and the S2P3-Photoacclim model does not consider a realistic grazing. Furthermore, despite the S2P3-NPZ and S2P3 v8.0 considering zooplankton, these models do not take into account seasonal variability of zooplankton biomass composition, and the S2P3-NPZ model does not consider photo-acclimation of phytoplankton.

The models were tuned using parameter ranges based on published data (Table 4.2). The true ranges for each NPZ and physiological parameter might mismatch those suggested in the literature, because many of those observations come from laboratory experiments performed under controlled conditions or from models that might include different assumptions, turbulent closure schemes, and dimensionality in a particular ecosystem (Geider et al., 1998; Franks et al., 1986). This may explain why not all the parameter values shown in Table 4.6 for the Control NPZ, Control Photoacclim, and for the Control NPZPhot

experiments are within the ranges suggested by other studies (Table 4.2). Furthermore, values referred in Table 4.2 were also obtained from different locations, which might differ in the characteristics of the CCS location in terms of the zooplankton and phytoplankton biomass compositions, advective fluxes, and assumptions from the models used.

Ward et al. (2010) stated that models are often underdetermined by data due to insufficient observations. For this study approximately two years of phytoplankton biomass data were available for the CCS location, while in the case of the zooplankton biomass observations those were collected only during certain days per year allowing only a discrete representation of the seasonal cycle of zooplankton, and finally, profiles of physiological data were only collected during summertime of the years 2003 and 2005; but each model could potentially be calibrated for over 51 years if longer time-series of observations existed. Mismatch between the calibrated models and observations is also driven by water column processes including advection and diffusion that were not considered in these 1-D models, but affects the real water column where the observations were taken. For example, advective fluxes during the time that the observations were sampled could be producing differences in DIN in the water column through horizontal entrainment, increasing the phytoplankton new PP (Tweddle et al., 2013). Horizontal advection could also influence the turbulent mixing, by contributing more nutrients into the thermocline, being able to support enhanced PP and increasing the typical estimates of annual PP rates (Tweddle et al., 2013).

It is important to note that the S2P3-Photoacclim model shows the largest differences in terms of surface chlorophyll-*a* in the timing of the spring phytoplankton bloom (Figure 4.6a), while the S2P3-NPZ model showed a better agreement with observations. It is well-known that annual cycles of mixing and grazing regulate the timing and magnitude of the spring bloom (Fasham et al., 1990; Frost, 1987; Evans & Parslow, 1985; Ryther & Hulburt, 1960), with the pre-bloom structure of zooplankton being important for the initiation of the bloom (Zhao et al., 2013). For example, if zooplankton are able to increase their biomass fast enough to keep pace with the phytoplankton growth, then the bloom may be delayed. On the other hand, a later phytoplankton bloom may lead to increased grazing pressure (Marra et al., 1995), as zooplankton have had longer time to reproduce, thus limiting the magnitude of the spring bloom. Consequently, the effect of

zooplankton on the timing of the spring bloom and the fact that the S2P3-NPZ model has a larger number of parameters available to be constrained (Table 4.3) in comparison to the S2P3-Photoacclim model (Table 4.4), it makes easier to minimise differences with observations. Finally, a more sophisticated model (S2P3 v8.0), explicitly accounts for zooplankton biomass and for the dynamics of internal quotas of phytoplanktonic cells, with phytoplankton biomass being in carbon, nitrogen, and chlorophyll currencies, allowing the decoupling of nutrient uptake from carbon fixation (Ayata et al., 2013; Bernard, 2011; Mairet et al., 2011; Bougaran et al., 2010; Flynn, 2008; Klausmeier et al., 2004). The S2P3 v8.0 model showed the best agreement with observations in comparison to the other models developed in this work, having a good representation of phytoplankton dynamics at the CCS location.

Greater complexity allowed the S2P3 v8.0 model to resolve a more diverse range of biogeochemical dynamics, which could be applicable at different sites of the shelf sea. Including additional parameters in models can add more unconstrained degrees of freedom (Ward et al., 2010), but also allows for more parameter combinations and, therefore, more flexibility to constrain S2P3 v8.0 in order to reproduce observations as seen in Figure 4.6a. S2P3 v8.0 also allows comparisons with zooplankton biomass data (Figure 4.6b) and physiological observations (Figure 4.8), permitting more accuracy and confidence to calibrate it and a better representation of the physical-biological processes of the CCS location. However, it is important to note that the addition of new parameters in any model needs to be balanced against any increase in uncertainty associated with those extra parameters. Additionally, despite having more sophisticated formulations of the ecosystem, S2P3 v8.0 continues to be a 1-D model, allowing multiple experiments to be run at the same time with relatively low computational cost.

4.5.2 Sensitivity analysis: dynamic responses to model parameterisations

The field of marine biogeochemical modelling has progressed through the development of both simple and complex models, ranging from models that include implicit representation of the marine biota (Najjar et al., 1992; Bacastow & Maier-Reimer, 1990), to ones that have a more detailed representation of phytoplankton functional groups (LeQuéré et al., 2005). In any case, sensitivity studies are important tools to improve the accuracy of shelf

sea models (Chen et al., 2013), but developing these analyses has to be done carefully in order to identify which processes are responsible for the observed model behaviour (Ward et al., 2013). In this work, the same methodology was used in each model to perform the sensitivity analysis, so that the parameters which have the largest effect in each model could be found. A direct comparison was done in terms of model attributes considering: the timing and magnitude of the spring phytoplankton bloom, and the total annual zooplankton biomass, providing better insights on the effects that each parameter produce in the behaviour of each model.

Table 4.13 shows the differences between the model attributes calculated between each experiment and the Control NPZPhot, showing that S2P3 v8.0 is strongly influenced by NPZ parameters, with the maximum ingestion rate of phytoplankton (R_m) and zooplankton mortality rate (m) having the largest effect in the magnitude of the spring phytoplankton bloom and in the total annual zooplankton biomass. It is well known that zooplankton are key players in the biogeochemical cycling of carbon and nutrients in marine ecosystems (Beaugrand & Kirby, 2010, Beaugrand et al., 2010), influencing the export of organic matter to the deep ocean (Juul-Pedersen et al., 2010; González et al., 2009). In the S2P3-NPZ model, changes of the parameters λ (Figure 4.13), R_m (Figure 4.15), and m (Figure 4.17) can lead to the collapse of zooplankton populations, a consequence that was not observed for the sensitivity analysis of those parameters in the S2P3 v8.0 model. According to Levin & Lubchenco (2008), small perturbations in biological systems can be magnified through nonlinear relationships, a behaviour that may be a characteristic feature of ecosystem models (Anderson et al., 2010). Additionally, grazing responses comprise the dominant losses for phytoplankton in the ocean (Banse, 1994), influencing plankton stocks and primary production (Franks et al., 1986). However, the ecological stoichiometry added into the S2P3 v8.0 was also demonstrated to have an important effect in the model dynamics, responding to the changes of λ , R_m , and m to a smaller extent than in the S2P3-NPZ model.

Photoacclimation has an important influence on the timing of the spring phytoplankton bloom (Table 4.13), with θ_{\max}^N affecting the S2P3 v8.0 model the most in terms of this model attribute. Ayata et al. (2013) demonstrated that taking into account photoacclimation and variable stoichiometry of phytoplankton growth in marine ecosystem models, produce qualitative and quantitative differences in phytoplankton dynamics. Moreover,

these quota formulations in S2P3 v8.0 were compared to the available dataset of physiological observations (Hickman et al., 2012; Hickman et al., 2009; Moore et al., 2006). It is interesting to note that the sensitivity analysis of NPZ parameters produced differences in the physiological variables P_{\max}^{chl} and E_k , specially at the surface, suggesting that the predator-prey interactions are relevant for phytoplankton physiology, presumably through feedbacks whereby zooplankton mediated nutrient cycling. The results shown in this chapter and the validation of the S2P3 v8.0 using observational data suggest that simultaneously fitting of zooplankton biomass and phytoplankton photo-acclimation can constrain better the timing and magnitude of the spring phytoplankton bloom than in the S2P3 v7.0, S2P3-NPZ, and S2P3-Photoacclim models. Consequently, it is suggested that further analysis is performed about the seasonal cycle of phytoplankton and PP by using the S2P3 v8.0 model.

4.5.3 Concluding remarks

This study presents a comprehensive analysis of each model developed in this work, demonstrating that the combination of an NPZ framework and the photo-acclimation of phytoplankton in one model produces a better representation of the ecosystem based on the comparison to observations. This combined framework offers a novel and innovative improvement to the S2P3 model, for application to the CCS location and more broadly within shelf sea systems. The development of the S2P3 v8.0 model provides a better fit to observations in comparison to the S2P3 v7.0 (Chapter 3, Figure 3.5), S2P3-NPZ, and S2P3-Photoacclim models. Improved confidence in the S2P3 v8.0 model thus suggest improved insights in studies about the effects of meteorology on PP, and phytoplankton dynamics would be possible. Open questions from Chapter 3 will be revisited in Chapter 5 with this novel model.

Appropriate parameterisations to represent shelf seas is a subject that should be further supported by fieldwork campaigns and future work should aim to include additional datasets with longer time-series. For this study, constraining the seasonal cycle of the phytoplankton physiology is not possible due to the lack of physiological observations during other periods of the year, furthermore, phytoplankton and zooplankton biomass datasets

only include the years 2014 and 2015 but longer time-series would help to improve the model calibration. Many model parameters quantities are poorly constrained observationally mainly due to the fact that model state variables are highly integrated pools, which are affected by biotic and abiotic factors in the environment, making them difficult to be determined by *in situ* measurements. For this study, is not possible to constrain the seasonal cycle of the phytoplankton physiology because physiological observations only includes summertime.

In future works, a parameter optimisation algorithm should be considered to optimise the calibration of the S2P3 v8.0 model by doing it automatically through different statistical techniques (e.g. least squares, linear or non-linear regression, maximum likelihood, etc), as opposite as done in this work with a trial-and-error methodology in order to understand how the dynamics of each model changed with different parameter values. Automatic parameter optimisation of the model would allow in future research to find the best agreement between the model and observations in other regions of the shelf sea without running dozens of experiments, maybe proving to be a useful tool for the model parameterisation. However, in order to use an automatic parameter calibration, it is relevant to know how the model behaves in different locations under different parameter values, which involves information that is likely to not be represented by the statistical tools based on the analysis of residuals. Consequently, it is suggested that a combination of trial-and-error and automatic parameter optimisation can also be applied.

The tuning and sensitivity analysis performed in this chapter allows a better understanding of the ecosystem dynamics represented in the model and how it is influenced by each parameter. This is a necessary step showing that the model is providing a realistic representation of the shelf sea. By considering the timing and magnitude of the spring phytoplankton bloom, and the total annual zooplankton biomass as features to be calculated, a quantitative and clearer comparison between each model could be developed. Finally, the model calibration will never be in perfect agreement with all the observations, particularly in this case, where only one type of phytoplankton and zooplankton were considered. Thus responses must represent some typical or average dynamics and cannot represent any effects of competition between types. Additionally no stages of zooplankton growth were taken into account, which might affect the predator-prey interactions (Fennel, 2001).

Overall, this chapter has shown that the S2P3 v8.0 model is able to reasonably represent the integrated behaviour of the mixture of species that inhabit the NW European Shelf Sea.

Chapter 5

Inter-annual variability of primary production due to wind and cloud effects using a simple 1-D NPZ model with photo-acclimation

5.1 Abstract

The newly developed S2P3 v8.0 model is used to reassess the meteorological impact on the inter-annual variability of PP at the CCS location. The model is run from 1965 - 2015 and forced by different meteorological components including wind speed, cloud coverage, air temperature, and relative humidity. Targeted experiments were performed with different meteorological setups and parameter values, providing new insights into the model dynamics and responses of phytoplankton productivity to the influence of meteorology. Based on these experiments, it was found that cloud coverage has the largest effect on the inter-annual variability of NPP, due to the inclusion of photo-acclimation in the model that allows variability of NPP due to changes in irradiance, and daily variability of clouds has an associated direct influence on this light availability. Additionally, wind speed affects the timing of the spring phytoplankton bloom by delaying it when the daily variability of wind is high during early spring and extreme events (e.g. storms) are present. Further experiments developed with an analysis of different model parameters show the robustness of these results.

5.2 Introduction

Temperate shelf seas are important regions due to their high productivity relative to the deep ocean. These ecosystems are strongly constrained by their hydrodynamics and local atmospheric conditions (Lacroix & Nival, 1998). In order to understand how these regions may change in future it is necessary to study the existing inter-annual variability of phytoplankton forcing and how this is controlled by these local atmospheric conditions.

Spring months provide the largest contribution to annual phytoplankton production as this is when the spring bloom happens, therefore, in most temperate shelf seas the initiation of the spring phytoplankton bloom marks the start of the seasonal production cycle (Tian et al., 2011). The timing of the spring phytoplankton bloom is also important for the development of zooplankton (Rey et al., 1987), fish stocks (Platt et al., 2003), and the continental shelf pump, therefore understanding the role of the environmental conditions that affect the spring phytoplankton bloom has wider implications.

The inter-annual variability of the spring phytoplankton bloom is determined by the balance between available light, clouds, winds (Townsend et al., 1994), and also by the availability of inorganic nutrients, and phytoplankton biomass losses associated with respiration, grazing, and sedimentation (Platt et al., 1991; Smetacek & Passow, 1990). Additionally, during summer months, short-term wind events can determine the physical structure of the surface layer and thermocline (Ridderinkhof, 1992), altering the SCM and generating entrainment of inorganic nutrients into the surface layer (Yin et al., 1995). Finally, during winter months, wind-driven turbulence and decreasing water temperatures break down the thermal stratification. Altogether, differences in the year-to-year production during the different periods of the seasonal cycle of phytoplankton will affect the inter-annual variability of the annual phytoplankton production.

Several 1D simple physical and biological coupled models have been applied in different situations and have proved to be a good tool to study the ecosystem dynamics in relation to hydrodynamic constraints (Marsh et al., 2015; Sharples et al., 2006; Lacroix & Nival, 1998; Tusseau et al., 1997; Lacroix & Nival, 1996; Fasham et al., 1990).

This chapter aims to reassess the analysis performed in Chapter 3 by using the newly developed S2P3 v8.0 model (see Chapter 4) to investigate the relationship between phytoplankton production at the CCS location and local meteorological components. This will be achieved by running experiments developed with different meteorological forcing and different parameter values to compare and to quantify the importance of meteorological variables in terms of NPP variability.

The S2P3 v8.0 model will also be answer the hypothesis that changing the model structure by adding a realistic grazing impact on phytoplankton and photo-acclimation can generate different feedbacks between meteorology and inter-annual variability of PP. Moreover, the S2P3 v8.0 is expected to produce more confident answers about the direct and indirect controls of meteorology on PP and how they operate for the CCS location.

5.3 Methods

5.3.1 Model set up, meteorological forcing, and experiments

The S2P3 v8.0 model used in this chapter is forced by daily meteorological observations including wind speed, cloud coverage, air temperature, and relative humidity from 1960 to 2015, with the first five years considered as the spin-up period of the model and, therefore, neglected in the analysis of the results. Meteorological forcing is described in Chapter 2, section 2.3 and will not be described again in this section. The S2P3 v8.0 model set up for the CCS location correspond to the one described in Chapter 2, section 2.4.

A series of experiments were developed to reassess the effect of meteorology on inter-annual variability of PP. These experiments correspond to those described in Chapter 3, section 3.3.1.2, i.e. Control-based experiments. Table 3.1 is shown again in this chapter (Table 5.1) to summarise the experiment setups, including a Control experiment, and Wind-only, Cloud-only, Temperature-only, and Humidity-only experiments. Additionally, the parameter values listed in Table 5.2 are the same for each control-based experiment and they correspond to the values found for the calibrated version of the S2P3 v8.0 model (see Chapter 4, section 4.3.3.3 for more information).

5.3.2 Robustness and parameterisations

A new series of experiments was developed to assess the robustness of the results found with the control-based experiments described in section 5.3.1. Each control-based experiment was re-run with different parameter values. In this case, only three parameters were changed to investigate how the results for each experiment (described in Table 5.1) are sensitive to the model parameterisation.

The three parameters changed were: the maximum value of the phytoplankton chlorophyll : phytoplankton nitrogen ratio (θ_{\max}^N), the maximum ingestion rate of phytoplankton (R_m), and the zooplankton mortality rate (m). The choice of these parameters was based on the results found in Chapter 4, which demonstrated that the S2P3 v8.0 model is most sensitive to changes in these parameters in terms of the timing and magnitude of the spring phytoplankton bloom and total annual zooplankton biomass (see Chapter 4, Table 4.12).

Because the model is sensitive to these parameters, they were only changed from their calibrated value (Table 5.2) by -10% and +10% with each experiment described in Table 5.1 run with two different values at the extremes of this range.

Table 5.3 shows new experiments developed in this section with different parameter values. These experiments have the same set up as in the control-based experiments listed in Table 5.1. For example, the Control 1 to Control 6 experiments are forced with climatological meteorology as in the Control experiment (Table 5.1), but with different parameter values. The same procedure is applied to the rest of the experiments showed in Table 5.3.

5.3.3 Statistical analysis

Statistical analyses were performed in this chapter, including Pearson correlations and RMSD calculations as described in Chapter 3, section 3.3.3.

In this chapter, RMSD calculations are used to measure the difference between the total annual NPP, total spring NPP, total summer NPP, total autumn + winter NPP, and timing of the spring phytoplankton bloom between the Control experiments and each control-based experiments described in sections 5.3.1 and 5.3.2.

Standard deviations (STD) were calculated for the wind speed and cloud coverage time-series to quantify the amount of variation or dispersion of those sets of data values. STD bounds of $\pm 1 \times \text{STD}$ (68% of observations inside that range) and $\pm 2 \times \text{STD}$ (95% of observations inside that range) were calculated from the mean of wind speed and cloudiness during the 51 years (1965 - 2015) in order to represent a limit used to define and quantify extreme meteorological events driven by wind and cloudiness. Therefore, values of wind speed higher than $2 \times \text{STD}$ are assumed to represent storms.

$$STD = \sqrt{\frac{1}{N-1} \sum_{i=1}^N (x_i - \bar{x})^2},$$

where N is the number of observations of the time-series, $x_i = \{x_1, x_2, \dots, x_N\}$ are the

observed values of the time-series, and \bar{x} is the mean values of those observations.

Run name	Wind speed	Cloud coverage	Air temperature	Relative Humidity
Default	Observed	Observed	Observed	Observed
Control	Climatology	Climatology	Climatology	Climatology
Wind-only	Observed	Climatology	Climatology	Climatology
Cloud-only	Climatology	Observed	Climatology	Climatology
Temperature-only	Climatology	Climatology	Observed	Climatology
Humidity-only	Climatology	Climatology	Climatology	Observed

Table 5.1: List of the control-based experiments developed for the S2P3 v8.0 and corresponding meteorological forcing.

Parameters	Units	Values
P_{\max}^C	d^{-1}	3.5
Q_m	$mg\ N\ (mg\ C)^{-1}$	0.45
θ_{\max}^N	$mg\ Chl\ (mg\ N)^{-1}$	0.15
$R_C = R_{chl} = R_n$	d^{-1}	0.02
γ_1	dimensionless	0.1
γ_2	dimensionless	0.4
λ	$(mmol\ N\ m^{-3})^{-1}$	0.2
R_m	d^{-1}	3.5
m	d^{-1}	0.02

Table 5.2: List of parameters previously investigated within Chapter 4 with corresponding units and values used for the Control experiment, Wind-only, Cloud-only, Temperature-only, and Humidity-only experiments.

Name of experiments					Parameter values
Control 1	Wind-only 1	Cloud-only 1	Temperature-only 1	Humidity-only 1	$\theta_{\max}^N = 0.135$
Control 2	Wind-only 2	Cloud-only 2	Temperature-only 2	Humidity-only 2	$\theta_{\max}^N = 0.165$
Control 3	Wind-only 3	Cloud-only 3	Temperature-only 3	Humidity-only 3	$R_m = 3.15$
Control 4	Wind-only 4	Cloud-only 4	Temperature-only 4	Humidity-only 4	$R_m = 3.85$
Control 5	Wind-only 5	Cloud-only 5	Temperature-only 5	Humidity-only 5	$m = 0.018$
Control 6	Wind-only 6	Cloud-only 6	Temperature-only 6	Humidity-only 6	$m = 0.022$

Table 5.3: List of experiment names and parameter values developed for the S2P3 v8.0 model. See meteorological forcing of each experiment in Table 5.1.

5.4 Results

This section is divided into five subsections that outline the results found. To assess the main hypothesis of this chapter, the first subsection introduces the dynamics of the S2P3 v8.0 model. The second subsection investigates the effects of each meteorological variable on inter-annual variability of PP using results from the control and control-based experiments. The third subsection shows the effects of meteorology per season during the year. The fourth subsection shows the seasonal and inter-annual variability of control and control-based experiments with different parameterisations to address the robustness of the results found in the first and second subsections. Finally, the fifth subsection investigates the mechanisms through which wind speed and cloud coverage influence the annual and seasonal NPP.

5.4.1 Insights into the S2P3 v8.0 model

This section provides a general overview of the dynamics of the full S2P3 v8.0 model, by showing daily time-series from 1965 to 2015 for the calibrated version of this model (Figure 5.1). Figure 5.1a shows the start of thermal stratification during early spring with observable inter-annual variability in the extent of stratification. Once the water column is stratified, the spring phytoplankton bloom can be observed (Figure 5.1b), followed by the start of the spring zooplankton bloom (Figure 5.1c). As phytoplankton grows, DIN concentrations in the surface start to deplete reaching a minimum value during spring and summer months, and increasing when thermal stratification breaks down during winter months (Figure 5.1d). Finally, NPP time-series show seasonal and inter-annual phytoplankton dynamics (Figure 5.1e).

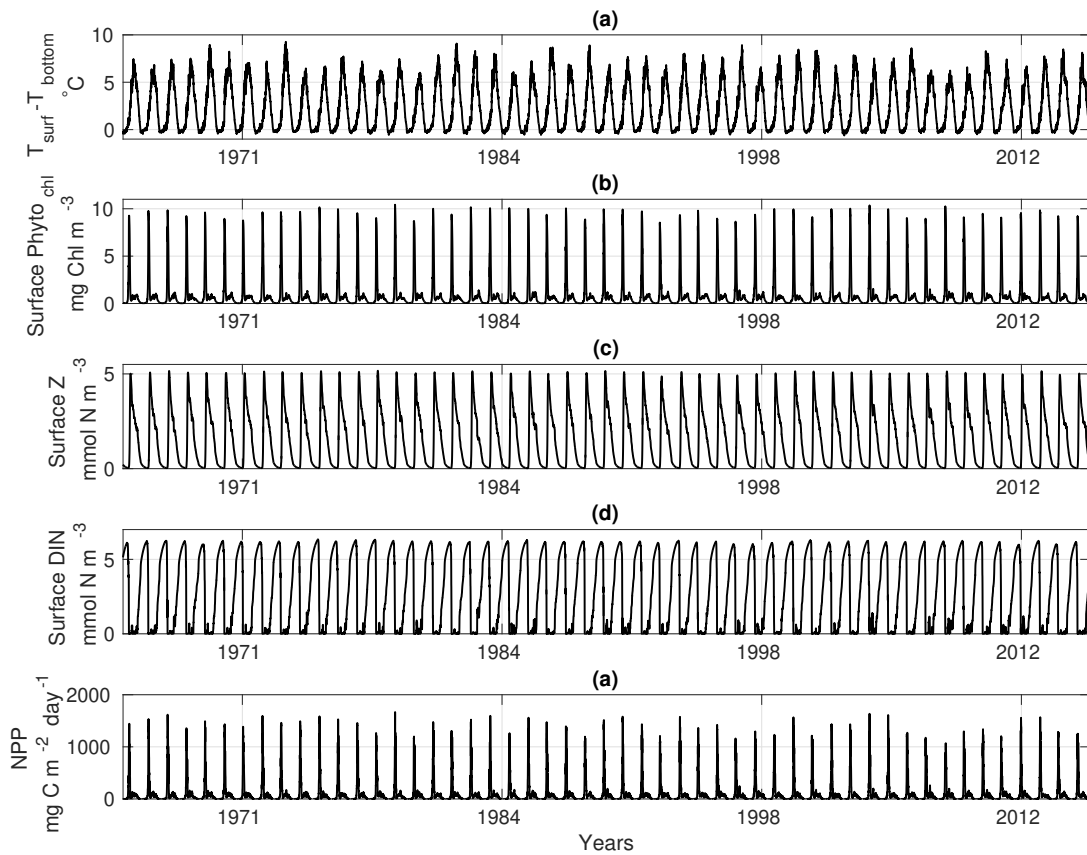


Figure 5.1: Daily time-series from 1965 to 2015 for the calibrated version of the S2P3 v8.0 model (default experiment), including: (a) surface temperature minus bottom temperature ($^{\circ}\text{C}$), (b) surface chlorophyll-a (mg Chl m^{-3}), (c) surface zooplankton biomass (mmol N m^{-3}), (d) surface DIN (mmol N m^{-3}), and (e) NPP ($\text{mg C m}^{-2} \text{day}^{-1}$).

Figure 5.2 shows contour plots of the S2P3 v8.0 model output, showing daily profiles of temperature (Figure 5.2a), phytoplankton chlorophyll-a (Figure 5.2b), zooplankton biomass (Figure 5.2c), phytoplankton chlorophyll : phytoplankton carbon ratio (Figure 5.2d), and DIN (Figure 5.2e) for the years 2014 and 2015 which correspond to the observation period of the SSB programme. Figure 5.2 allows a more detailed overview of the model dynamics, with yellow colours representing high values of each variable and blue colours representing the lowest values. Water column temperature increases from April of each year, reaching a maximum value at the surface during summer months. At the same time, the spring phytoplankton bloom can be observed during April, reaching $\sim 10 \text{ mg Chl}$

m^{-3} . Additionally, the spring zooplankton bloom can be observed approximately a month after the spring phytoplankton bloom is developed, with zooplankton being able to grow during summer months and decreasing until a minimum value during winter due to a low ingestion of phytoplankton (as phytoplankton biomass will also be low in winter) and, therefore, decreasing zooplankton growth. A fraction of the dead zooplankton, depending on the value of γ_2 (see Chapter 2, eq. 2.44), will go back directly to the DIN pool and the rest will go to sediments or higher trophic levels. These spring blooms also mark the start of DIN depletion at the surface, a state that lasts until the end of summer. Finally, the phytoplankton chlorophyll : phytoplankton carbon ratio shows the highest values during winter months when irradiance levels are low and it increases towards spring, and then decreases until the end of summer due to the lower concentrations of chlorophyll in the cell to avoid internal damage due to high irradiance during this period, highlighting the photo-acclimation process of the S2P3 v8.0 model.

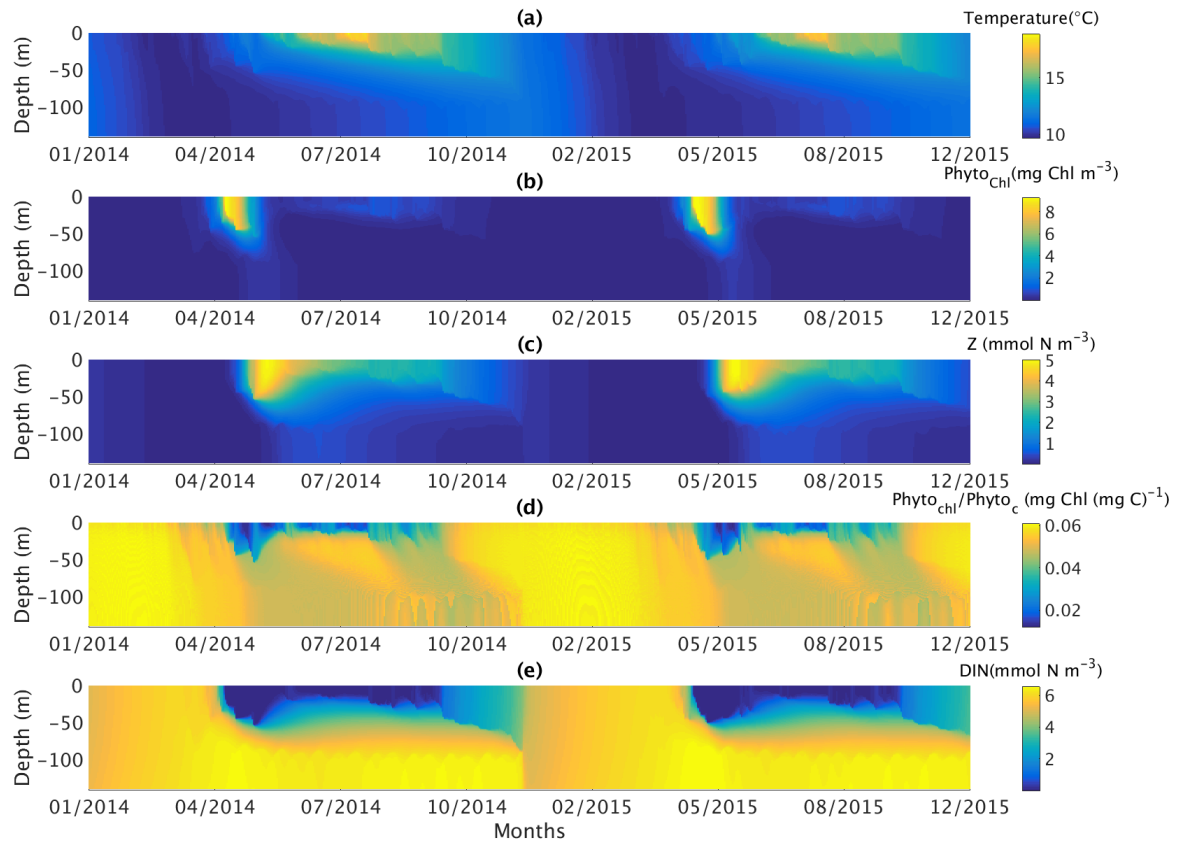


Figure 5.2: Contoured daily vertical profiles for the start of 2014 to the end of 2015 for the calibrated version of the S2P3 v8.0 model (default experiment) including: (a) temperature ($^{\circ}\text{C}$), (b) phytoplankton chlorophyll-a (mg Chl m^{-3}), (c) zooplankton biomass (mmol N m^{-3}), (d) phytoplankton chlorophyll : phytoplankton carbon ratio ($\text{mg Chl (mg C)}^{-1}$), and (e) DIN (mmol N m^{-3}).

5.4.2 Meteorological effects on inter-annual variability of primary production

The control experiment and each control-based experiment developed in this chapter are compared to each meteorological variable in terms of the total annual NPP as shown in Figure 5.3. A statistical analysis shows no significant correlation between the total annual NPP of the wind-only experiment and the total annual average wind speed ($r^2 = 0.07$, $p > 0.05$; Figure 5.3a). Additionally, significant correlations are observed between the total annual NPP of the cloud-only experiment and the total annual average cloud coverage

($r^2 = -0.193$, $p < 0.05$; Figure 5.3b), the total annual NPP of the temperature-only experiment and the total annual average air temperature ($r^2 = -0.257$, $p < 0.05$; Figure 5.3c), and the total annual NPP of the humidity-only experiment and the total annual average relative humidity ($r^2 = -0.2$, $p < 0.05$; Figure 5.3d). However, the significant correlations found are weak, showing that the effects of these meteorological variables (including wind) can have an effect in total annual NPP that is not well represented with a Pearson correlation due to non-linear responses of phytoplankton PP to the changes in the weather conditions, which can also differ in the timescale of the variability in weather components and phytoplankton responses.

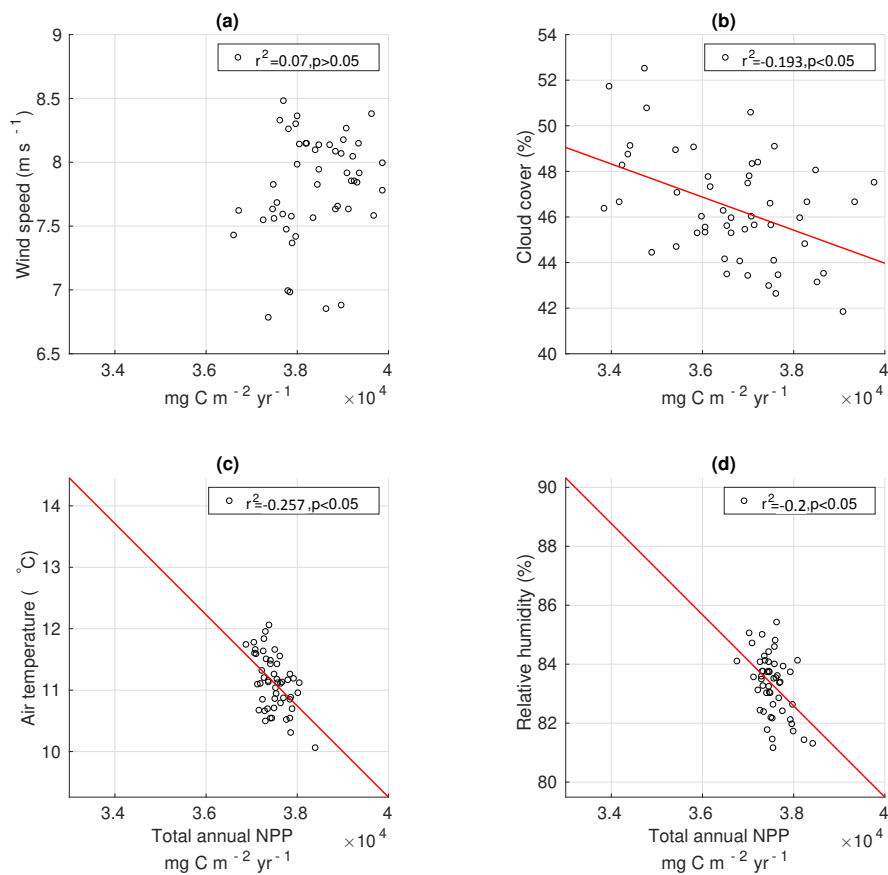


Figure 5.3: Scatter plots calculated from 1965 to 2015. Red line represents the significant regression line of the relationships between the total annual NPP ($\text{mg C m}^{-2} \text{yr}^{-1}$) and (a) total annual average wind, (b) total annual average cloud coverage, (c) total annual average air temperature, and (d) total annual average relative humidity.

Figure 5.4a shows the total annual NPP ($\text{mg C m}^{-2} \text{ yr}^{-1}$) from 1965 to 2015 between the wind-only experiment minus the control experiment (black lines), the cloud-only experiment minus the control experiment (red lines), the temperature-only experiment minus the control experiment (blue lines), and the humidity-only experiment minus the control experiment (cyan lines). The differences between the cloud-only experiment and the control experiment show that $> 80\%$ of the values of total annual NPP difference are less than zero. Moreover, $> 90\%$ of the differences in total annual NPP difference between the wind-only experiment and the control experiment are greater than zero.

Figure 5.4b shows RMSD calculations of total annual NPP for the four control-based experiments relative to the control experiment, with the largest value of RMSD found in the case of the cloud-only experiment ($1664.5 \text{ mg C m}^{-2} \text{ yr}^{-1}$), followed by the wind-only experiment ($1196.5 \text{ mg C m}^{-2} \text{ yr}^{-1}$), temperature-only experiment ($302.9 \text{ mg C m}^{-2} \text{ yr}^{-1}$), and the lowest RMSD value was given by the humidity-only experiment ($302.8 \text{ mg C m}^{-2} \text{ yr}^{-1}$). This suggests that the largest difference in total annual NPP between the control experiment and the control-based experiments is driven by the inter-annual variability of cloud coverage. The RMSD also shows strong inter-annual variability (Figure 5.4c) in the cloud-only experiment but this is always higher in each 5 year period than the other control-based experiments except for the periods 1965 - 1970 and 1990 - 1995 where the highest values of the RMSD were found in the wind-only experiment.

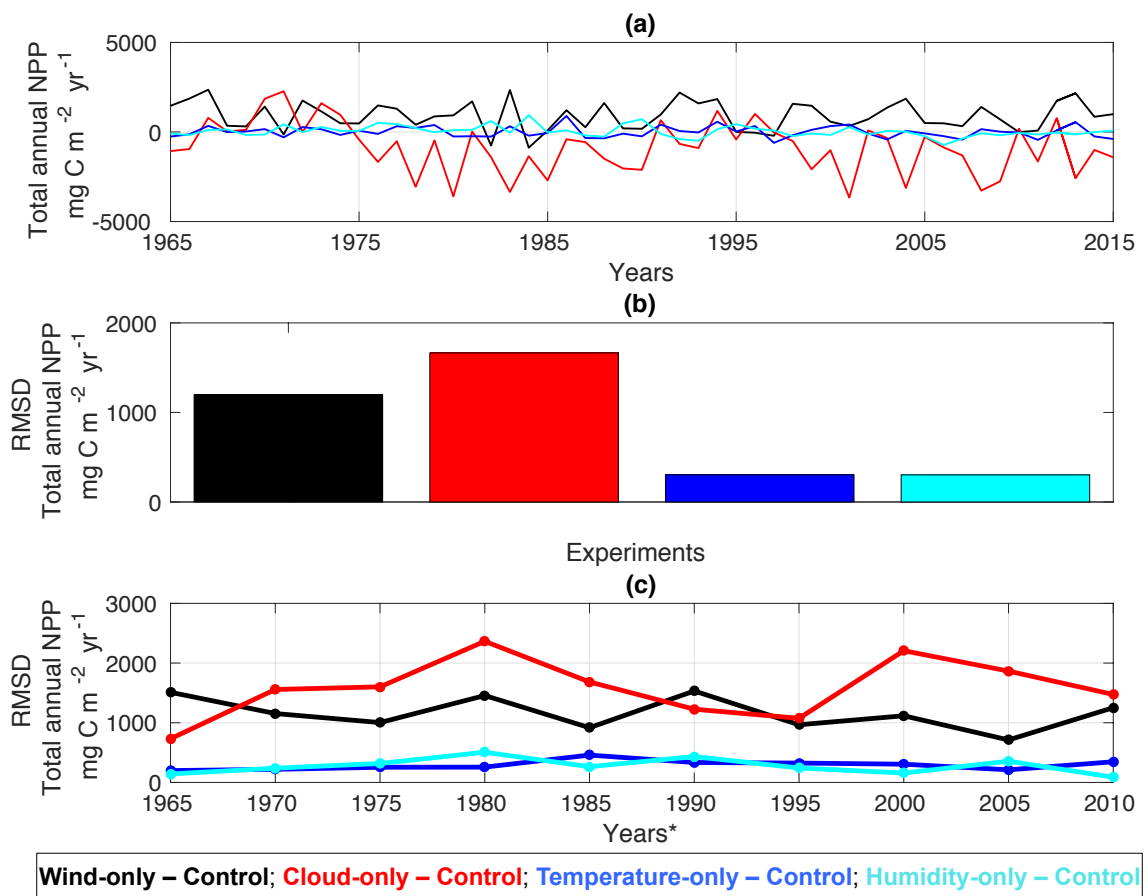


Figure 5.4: Differences relative to the control experiment of the wind-only experiment (represented in black), cloud-only experiment (represented in red), temperature-only experiment (represented in blue), and humidity-only experiment (represented in cyan) over the period 1965 - 2015 for (a) total annual NPP ($\text{mg C m}^{-2} \text{ yr}^{-1}$), (b) RMSD of total annual NPP ($\text{mg C m}^{-2} \text{ yr}^{-1}$), and (c) RMSD of total annual NPP ($\text{mg C m}^{-2} \text{ yr}^{-1}$), where years with a star (\star) in the x-label represent a mean value of the RMSD every five years starting from 1965.

Another feature of interest for this study is the timing of the spring phytoplankton bloom. Figure 5.5a shows the difference between each control-based experiment and the control experiment in terms of this feature. Large differences can be observed for the wind-only experiment (black line), with $\sim 39\%$ of the differences in spring phytoplankton bloom start times are less than zero, i.e. 20 years show earlier spring blooms for the wind-only experiment than in the control experiment. The cloud-only, temperature-only, and humidity-only experiments show less variability during the years 1965 to 2015 than the wind-only exper-

iment. These differences are quantified with an RMSD (Figure 5.5b), showing that wind speed has the largest effect on the timing of the spring phytoplankton bloom, followed by cloud-only and the temperature-only experiments, and the lowest RMSD value was given by the humidity-only experiment.

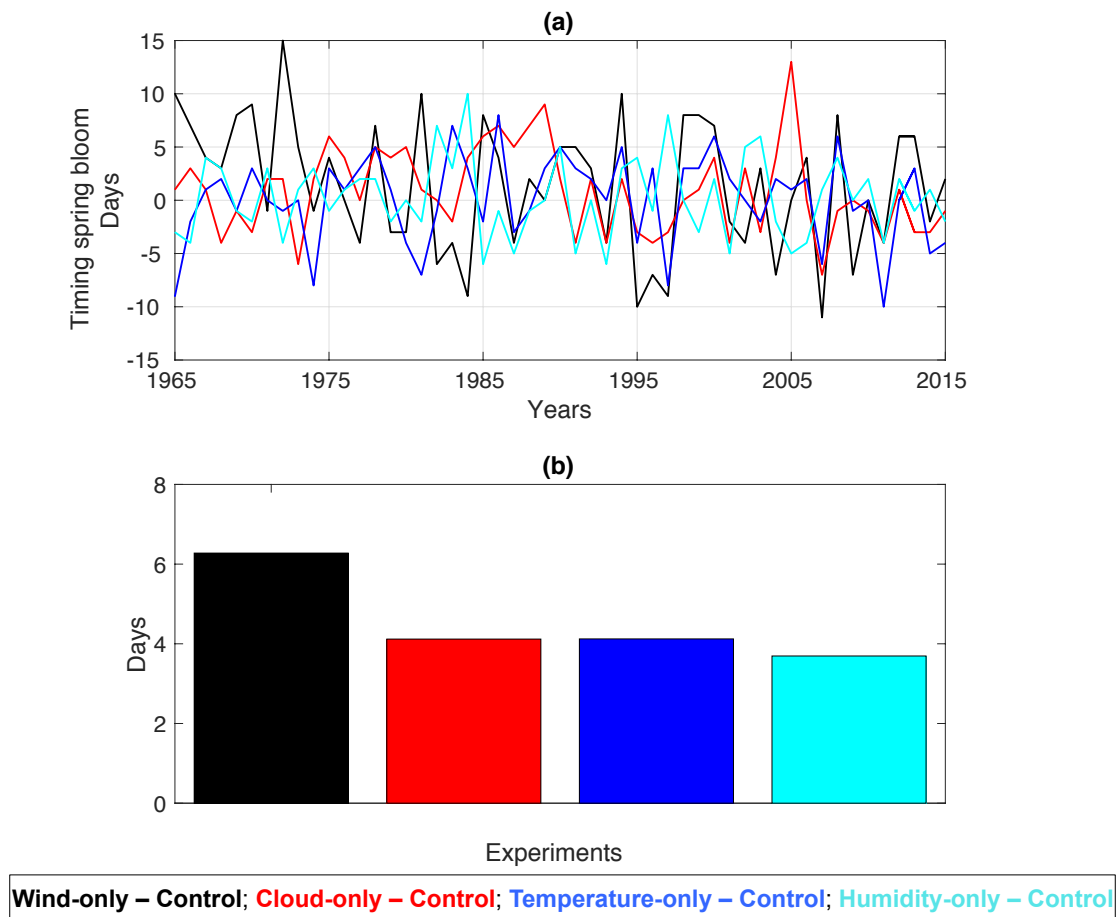


Figure 5.5: Differences relative to the control experiment of the wind-only experiment (represented in black), cloud-only experiment (represented in red), temperature-only experiment (represented in blue), and humidity-only experiment (represented in cyan) over the period 1965 - 2015 for (a) the timing of the spring phytoplankton bloom, and (b) an RMSD for the timing of the spring phytoplankton bloom.

One of the main differences between the S2P3 v7.0 and the S2P3 v8.0 models is that cloud cover instead of wind speed is the meteorological variable with the most influence on the inter-annual variability of NPP over 1965-2015. This difference might be caused by

the addition of photo-acclimation in the S2P3 v8.0, as phytoplankton growth will change in response to variability in irradiance, with cloud cover being one of the meteorological variables that directly affects the amount of light available for phytoplankton, whereas wind speed will influence the inter-annual variability of NPP due to changes in the mixing of the water column. Analysing the differences between the S2P3 v7.0 and S2P3 v8.0 model in terms of the response of phytoplankton growth to irradiance is relevant to understand the effects of photo-acclimation in the newly developed model. Figure 5.6 shows a comparison between daily surface PAR (W m^{-2}) and daily NPP ($\text{mg C m}^{-2} \text{ day}^{-1}$) over the course of the year (the colour indicates the day of the year) from the period of 1965-2015 for (a) S2P3 v7.0 model, and (b) S2P3 v8.0 model. It can be observed that the relationship between phytoplankton growth and irradiance at the surface of the water column is different in each model, with significant differences during autumn and early winter months (red dots), with the S2P3 v7.0 model showing larger variability in terms of NPP between 50 - 200 (W m^{-2}) of surface PAR, while in the S2P3 v8.0 model, the majority of NPP is maintained between approximately between 0 - 100 $\text{mg C m}^{-2} \text{ day}^{-1}$, possibly because phytoplankton growth is more strongly related to light variability in the S2P3 v8.0 model. The S2P3 v7.0 model's winter production might be primarily driven by nutrient availability subject to wind speed and mixing processes in the water column. Furthermore, large differences between each model can be observed during days 150 - 200 (green dots), with lower values of NPP (and less variability) in the S2P3 v8.0 model than in the S2P3 v7.0 model, possibly indicating the importance of zooplankton grazing in this period, when zooplankton usually starts to grow. Future work may which to focus on improving the understanding of the direct mechanisms of photo-acclimation and zooplankton on the results found in Figure 5.4. However, it is clear that the addition of these processes is relevant as it more accurately models the response of phytoplankton growth to their physical environment.

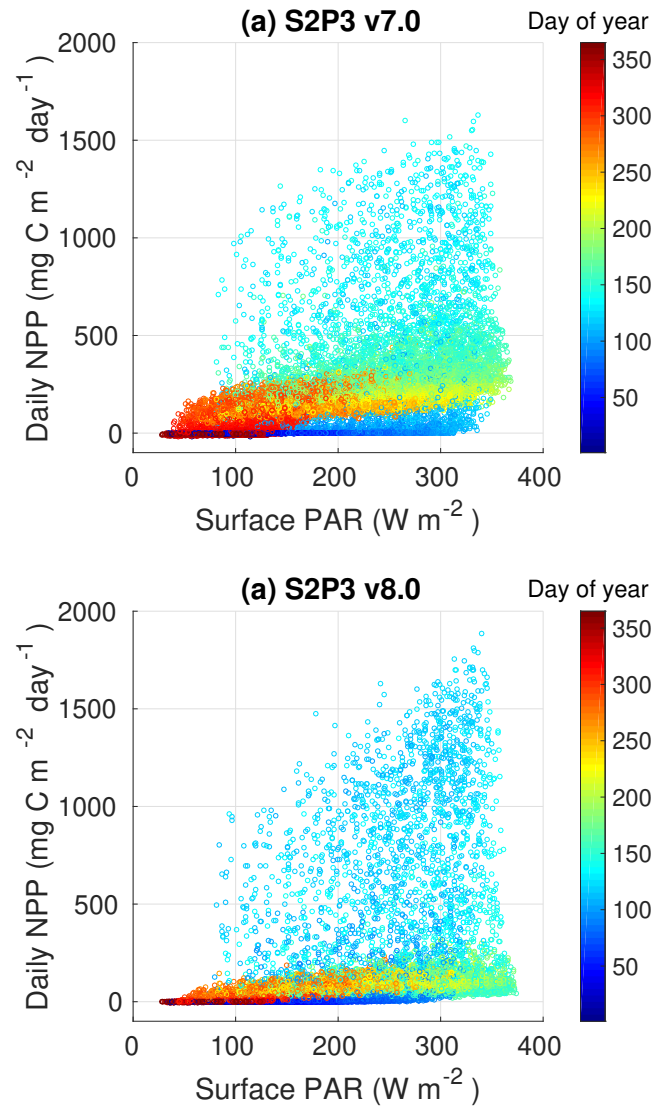


Figure 5.6: Daily surface PAR versus daily NPP for 1965-2015 for the (a) S2P3 v7.0 model, and (b) S2P3 v8.0 model. Colorbar represents the day of the year, from day 0 to 365.

5.4.3 Seasonal variability of primary production

Seasonal variability is also analysed, by focusing on three periods during the year: spring NPP, which is considered to start with the spring phytoplankton bloom as defined in Chapter 3 and ends when surface chlorophyll-a is less than $1.5 \text{ mg Chl m}^{-3}$. The same assumption as done in Chapter 3 it is considered here: the onset of the spring phytoplankton bloom is linked to the development of thermal stratification. Furthermore, the

meteorological experiments developed for Chapter 3 and Chapter 5 involve changes in thermal stratification due to the different forcing applied through the experiments, contrary to Chapter 4, where a direct comparison to surface chlorophyll was used as a proxy to calculate the timing of the spring bloom. Therefore, in order to explore the hypothesis of this chapter, the start of the spring bloom is considered to start once a stratified layer is settled. Additionally, summer periods are considered to start when the spring phytoplankton bloom finishes and end when stratification breaks down (i.e. when surface temperature minus bottom temperature $< 0.5\text{ }^{\circ}\text{C}$). Finally, autumn and winter months are defined as from the end of the summer until the start of the spring phytoplankton bloom in the next year.

Figure 5.7a shows the spring period in terms of the differences between each control-based experiment and the control experiment for total spring NPP ($\text{mg C m}^{-2}\text{ yr}^{-1}$), total summer NPP (Figure 5.7b; $\text{mg C m}^{-2}\text{ yr}^{-1}$), and total autumn + winter NPP (Figure 5.7c; $\text{mg C m}^{-2}\text{ yr}^{-1}$). These differences were quantified for each experiment and period of the year through an RMSD analysis (Figure 5.7d), showing that during the spring period (blue bars), wind speed has the largest effect in terms of NPP ($2783\text{ mg C m}^{-2}\text{ yr}^{-1}$), followed by cloud coverage ($1580\text{ mg C m}^{-2}\text{ yr}^{-1}$), air temperature ($818\text{ mg C m}^{-2}\text{ yr}^{-1}$), and the lowest differences were found for relative humidity ($758\text{ mg C m}^{-2}\text{ yr}^{-1}$). Additionally, similar results were found and quantified with an RMSD analysis for the summer period (blue bars), with wind speed having the largest effect on summer production ($1611\text{ mg C m}^{-2}\text{ yr}^{-1}$), followed by cloud coverage ($705\text{ mg C m}^{-2}\text{ yr}^{-1}$), air temperature ($335\text{ mg C m}^{-2}\text{ yr}^{-1}$), and relative humidity ($269\text{ mg C m}^{-2}\text{ yr}^{-1}$). Moreover, the autumn and winter periods (yellow bars) show that wind speed also has the largest effect on the inter-annual variability of NPP over that period of the year ($1833\text{ mg C m}^{-2}\text{ yr}^{-1}$), followed by relative humidity ($1077\text{ mg C m}^{-2}\text{ yr}^{-1}$), air temperature ($989\text{ mg C m}^{-2}\text{ yr}^{-1}$), and the lowest RMSD value was found for cloud coverage ($729\text{ mg C m}^{-2}\text{ yr}^{-1}$).

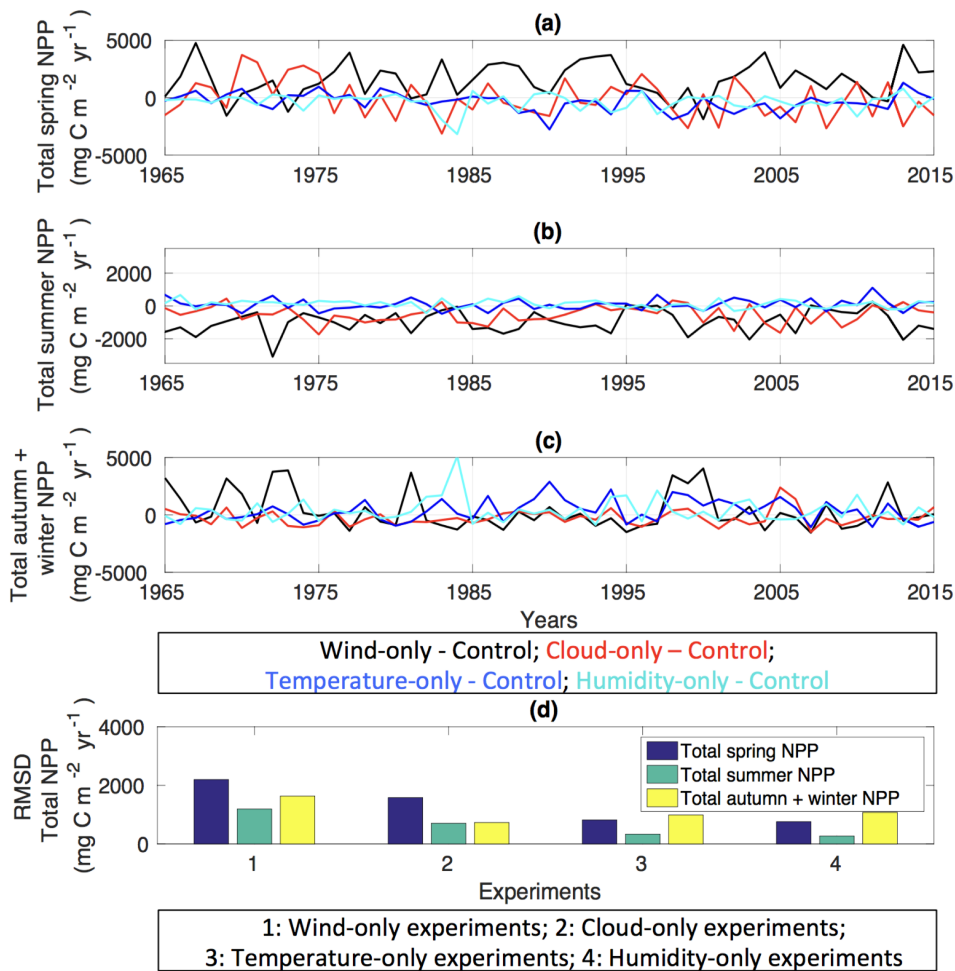


Figure 5.7: Differences relative to the control experiment of the wind-only experiment (represented in black), cloud-only experiment (represented in red), temperature-only experiment (represented in blue), and humidity-only experiment (represented in cyan) over the period 1965 - 2015 for (a) total spring NPP ($\text{mg C m}^{-2} \text{ yr}^{-1}$), (b) total summer NPP ($\text{mg C m}^{-2} \text{ yr}^{-1}$), (c) total autumn + winter NPP ($\text{mg C m}^{-2} \text{ yr}^{-1}$), and (d) an RMSD for the total spring NPP (blue colour), total summer NPP (green colour), and total autumn + winter NPP (yellow colour).

5.4.4 Parameterisation: a validation for robustness

In Chapter 4 it was demonstrated that certain parameter values can have large effects on the model dynamics. In this section, different experiments were developed to assess the robustness of the results found in this chapter. Table 5.3 shows each experiment used to address this validation.

Figure 5.8 shows the difference of total annual NPP ($\text{mg C m}^{-2} \text{ yr}^{-1}$) between each control-based experiment and the control experiment when $\theta_{\text{max}}^{\text{N}} = 0.135 \text{ mg Chl (mg N)}^{-1}$ (black lines) and $\theta_{\text{max}}^{\text{N}} = 0.165 \text{ mg Chl (mg N)}^{-1}$ (red lines) for the wind-only experiment (Figure 5.8a), cloud-only experiment (Figure 5.8a), temperature-only experiment (Figure 5.8c), and humidity-only experiment (Figure 5.8d). It can be observed that Figure 5.8 shows a similar structure of the annual NPP in all the experiments compared, with the cloud-only experiment showing the greatest inter-annual variability over the period 1965 to 2015.

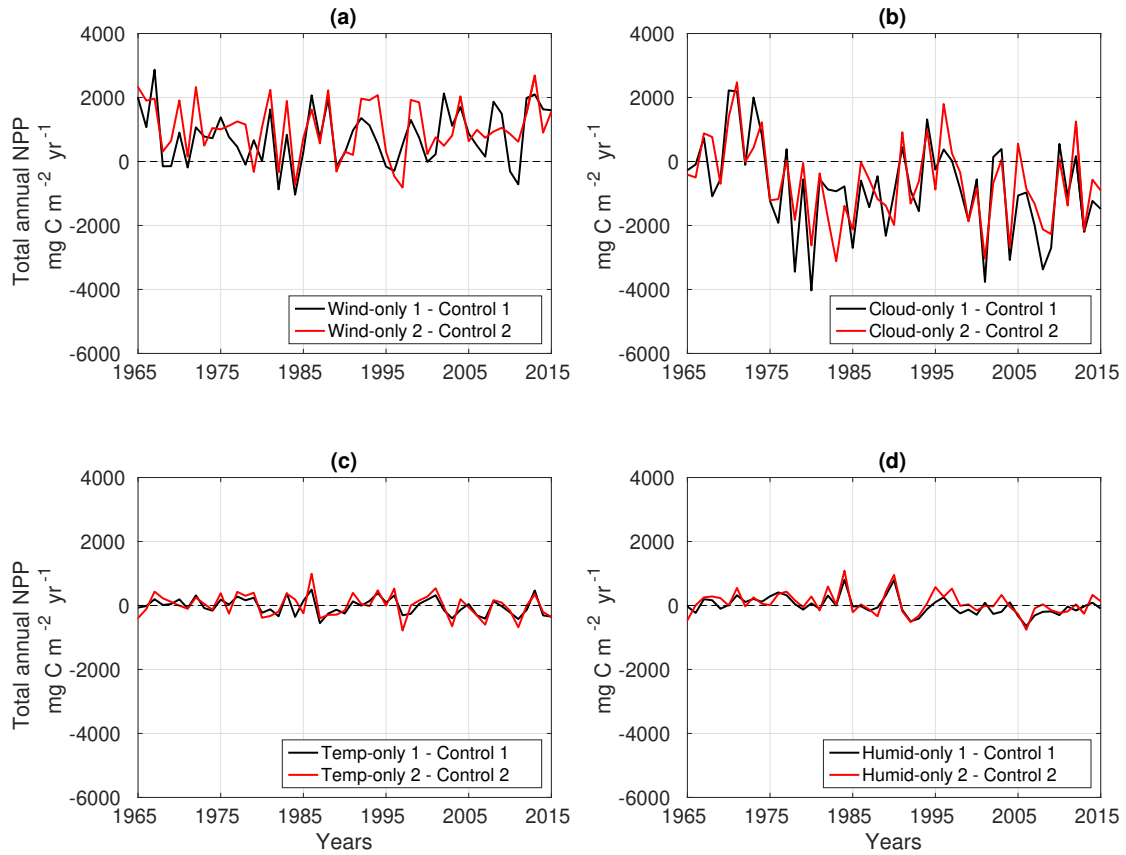


Figure 5.8: Differences of total annual NPP ($\text{mg C m}^{-2} \text{ yr}^{-1}$) from 1965 - 2015 relative to the control 1 ($\theta_{\max}^N \downarrow$) and control 2 ($\theta_{\max}^N \uparrow$) experiments and the (a) wind-only 1 - 2 experiments (black and red colours, respectively) (b) cloud-only 1 - 2 experiments (black and red colours, respectively), (c) temperature-only 1 - 2 experiments (black and red colours, respectively), and (d) humidity-only 1 - 2 experiments (black and red colours, respectively).

The same procedure as shown in Figure 5.8 is performed in Figure 5.9, but with the control-based experiments and control experiments that consider the parameter values of $R_m = 3.15 \text{ d}^{-1}$ (black lines) and $R_m = 3.85 \text{ d}^{-1}$ (red lines). Similar results in terms of total annual NPP are shown between each experiment, showing fewer differences than the ones observed in Figure 5.8 when changing θ_{\max}^N .

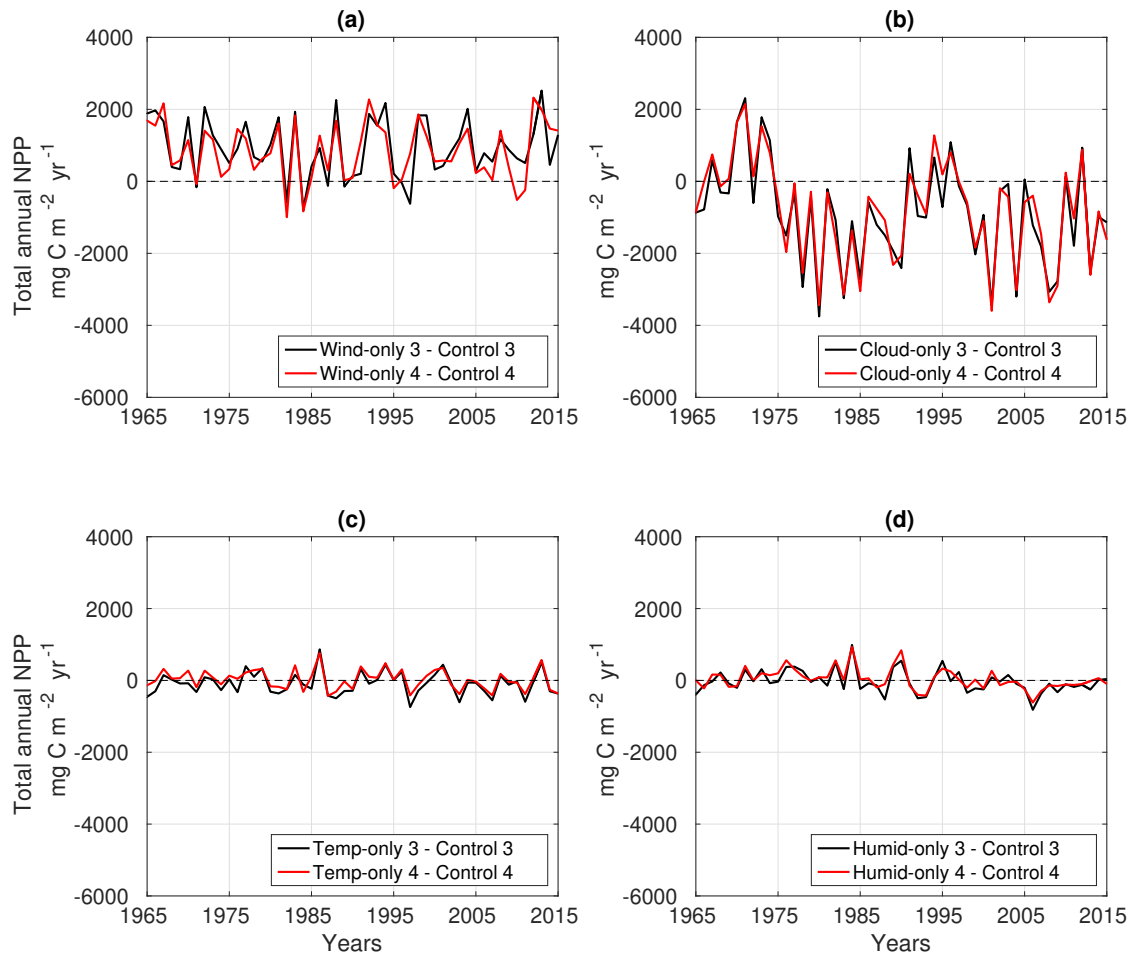


Figure 5.9: Differences of total annual NPP ($\text{mg C m}^{-2} \text{yr}^{-1}$) from 1965 - 2015 relative to the control 3 ($R_m \downarrow$) and control 4 ($R_m \uparrow$) experiments and (a) wind-only 3 - 4 experiments (black and red colours, respectively) (b) cloud-only 3 - 4 experiments (black and red colours, respectively), (c) temperature-only 3 - 4 experiments (black and red colours, respectively), and (d) humidity-only 3 - 4 experiments (black and red colours, respectively).

The experiments in Figure 5.10 show the last comparison for the control-based experiments and the control experiments in terms of the total annual NPP ($\text{mg C m}^{-2} \text{yr}^{-1}$) when varying the zooplankton mortality from $m = 0.018 \text{ d}^{-1}$ (black lines) to $m = 0.022 \text{ d}^{-1}$ (red lines). Small differences can be observed in each experiment with different values of zooplankton mortality, but the structure of annual production is very similar to the ones in Figures 5.8 and 5.9.

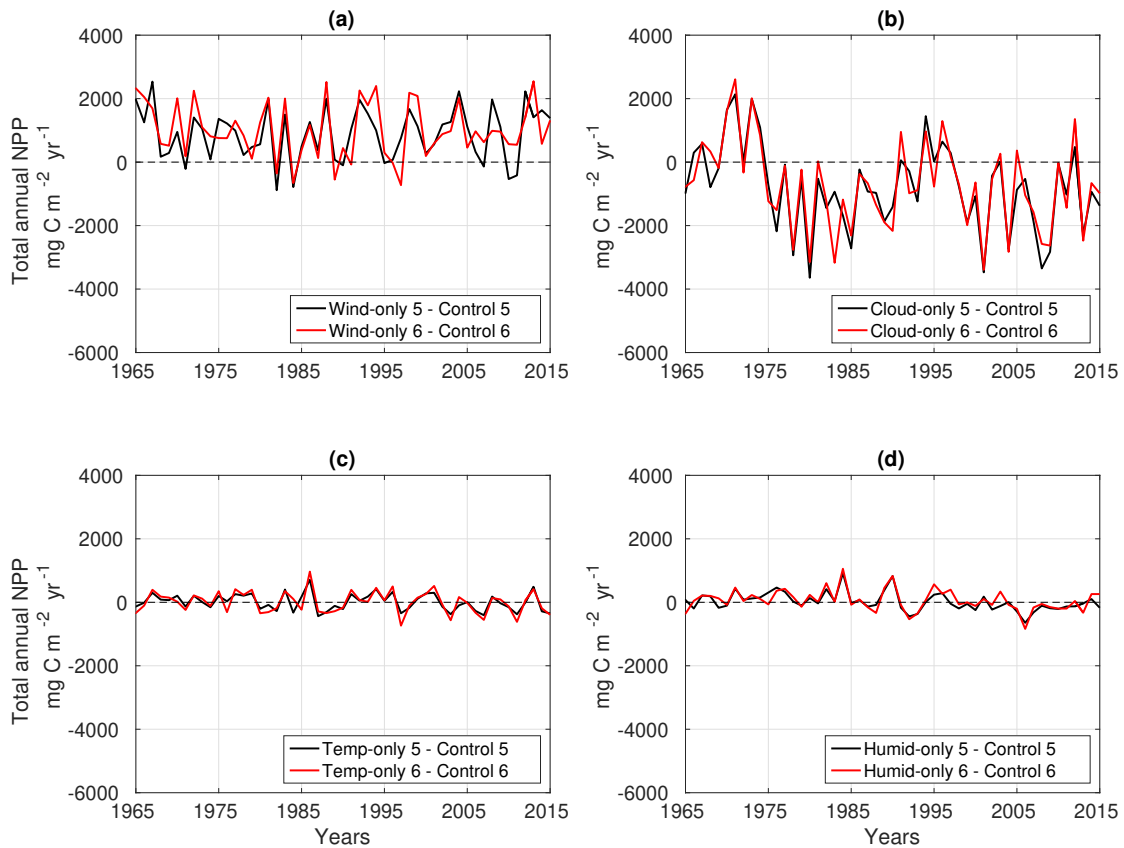


Figure 5.10: Differences of total annual NPP ($\text{mg C m}^{-2} \text{ yr}^{-1}$) from 1965 - 2015 relative to the control 5 ($\text{m} \downarrow$) and control 6 ($\text{m} \uparrow$) experiments and (a) wind-only 5 - 6 experiments (black and red colours, respectively) (b) cloud-only 5 - 6 experiments (black and red colours, respectively), (c) temperature-only 5 - 6 experiments (black and red colours, respectively), and (d) humidity-only 5 - 6 experiments (black and red colours, respectively).

Figure 5.11 quantifies and summarises the differences between each control-based experiment and control experiment when $\theta_{\text{max}}^{\text{N}}$, R_{m} , and m are changed, including an RMSD analysis for the total annual NPP (Figure 5.11a), showing that cloud coverage produces the largest RMSD values in all the experiments, demonstrating that the results found in section 5.4.2 are robust within the range of parameter values chosen and the annual variability of NPP is mainly driven by cloud coverage, followed by wind speed, air temperature, and relative humidity. These results are compared to the ones found in section 5.4.3, demonstrating the robustness of the results found with the S2P3 v8.0 model within the range

of variability in those parameters which have the strongest effect on model dynamics. On the other hand, the spring, summer, and autumn + winter periods of the year were also calculated for these experiments, not showing the inter-annual pattern observed in Figure 5.11a, with small differences between each experiment during each season.

Additional experiments were run by varying θ_{\max}^N by -5% and +5% to investigate the sensitivity of the model to the results found for the annual phytoplankton production and during each season (spring, summer, and autumn + winter). These results are shown in the appendix section, with Figure A23 showing that the results are robust within the chosen parameter ranges for the total annual NPP (Figure A23a); similar results are found in the control-based experiments during the different seasons than in Figure 5.11b,c,d, showing the strong variability driven annually mainly by cloud is not obvious in each season.

Further experiments were also conducted for the R_m and m parameters, varying from -20% to +20% (Figure A24), and from -30% to +30% (Figure A25). Results were shown to be robust within the new ranges of the parameters in terms of the total annual NPP (Figures A24a, A25a), while, on the other hand, the spring and summer periods were shown to be sensitive to the variation of these parameters under the ranges chosen. Moreover, autumn + winter periods show robust results for the range of the parameters in these experiments.

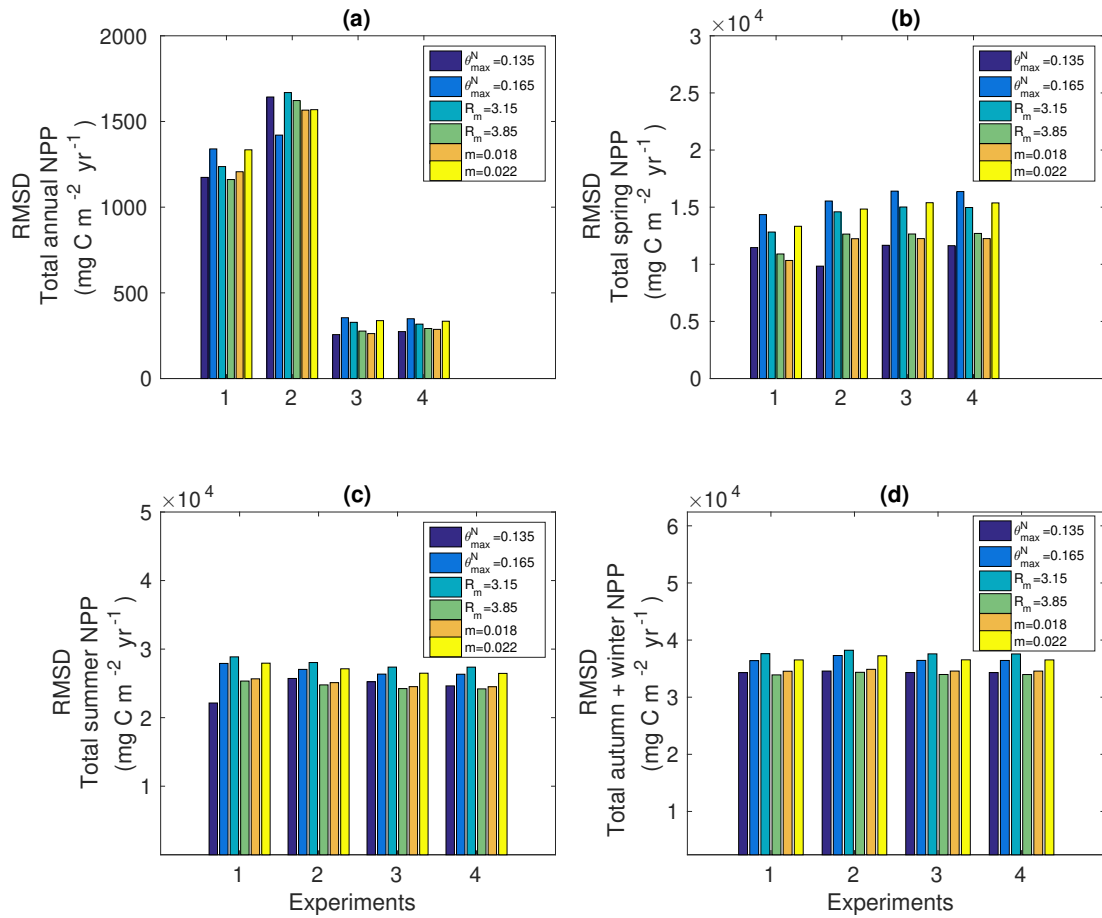


Figure 5.11: RMSD calculations from the year 1965 to the year 2015 for the control-based experiments with $\theta_{max}^N = 0.135$ (blue bars), $\theta_{max}^N = 0.165$ (light blue bars), $R_m = 3.15$ (turquoise bars), $R_m = 3.85$ (green bars), $m = 0.018$ (orange bars), and $m = 0.022$ (yellow bars) for the wind-only 1 - 6 experiments, cloud-only 1 - 6 experiments, temperature-only 1 - 6 experiments, and humidity-only 1 - 6 experiments in terms of (a) total annual NPP (mg C m⁻² yr⁻¹), (b) total spring NPP (mg C m⁻² yr⁻¹), (c) total summer NPP (mg C m⁻² yr⁻¹), and (d) total autumn + winter NPP (mg C m⁻² yr⁻¹).

5.4.5 A deeper look into wind and cloud inter-annual variability and their direct mechanisms of influence on primary production

Given the results found in previous sections, a deeper analysis was performed for wind speed and cloud coverage to understand the direct mechanisms that affect inter-annual variability of NPP.

In wind-only experiment results shown in Figure 5.4a, a few years always had lower total annual NPP than the control experiment, these years included: 1982, 1984, and 1997. Another three years were chosen to be compared, including the years 1983, 1994, and 2013, which are some of the years that show the largest values of total annual NPP. These six years were chosen to be compared due to their opposite behaviour found in the wind-only experiment in contrast to the control experiment's total annual NPP: the years 1982, 1984, and 1997 are the only years that show a negative value for the total annual NPP difference with the control experiment (Figure 5.4a), meaning that during those years, wind speed produced less annual NPP than in the control experiment; the years 1983, 1994, and 2013 exhibit large positive differences of total annual NPP between the wind-only and control experiments, meaning that wind speed produced more annual NPP than in the control experiment. The results found in Figure 5.4 shows that the contrasting values of total annual NPP during the chosen years could give deeper insights about how wind speed is affecting phytoplankton annual cycle. Figure 5.12 presents these years in terms of daily NPP, showing that the years with a negative difference in the total annual NPP (black lines) have earlier spring phytoplankton blooms than the years showing the largest positive difference of total annual NPP (blue lines). This suggests that wind speed is directly affecting the timing of the spring phytoplankton bloom, with a positive significant correlation found between the timing of spring bloom and the total annual NPP for the wind-only experiment during 1965-2015 ($r^2 = 0.23$, $p < 0.05$; Figure 5.13), demonstrating that the later the spring bloom, the more annual production will be in a given year. However, this significant correlation is weak and explain only 23% of the variability of total annual NPP due to changes in the timing of the spring bloom, suggesting that other processes might be relevant such as the magnitude of the spring bloom and summer growth (see Figure 5.12). Table 5.4 shows the chosen years, JD for the timing of the spring phytoplankton bloom, and the total annual NPP.

Years	JD timing of spring phytoplankton bloom	Total annual NPP ($\text{g C m}^{-2} \text{ yr}^{-1}$)
1982	102	36.7
1983	104	39.8
1984	99	36.6
1994	118	39.3
1997	99	37.2
2013	114	39.6

Table 5.4: List of the chosen years to analyse wind speed effects on inter-annual variability of NPP, including the JD for the timing of the spring phytoplankton bloom, and total annual NPP.

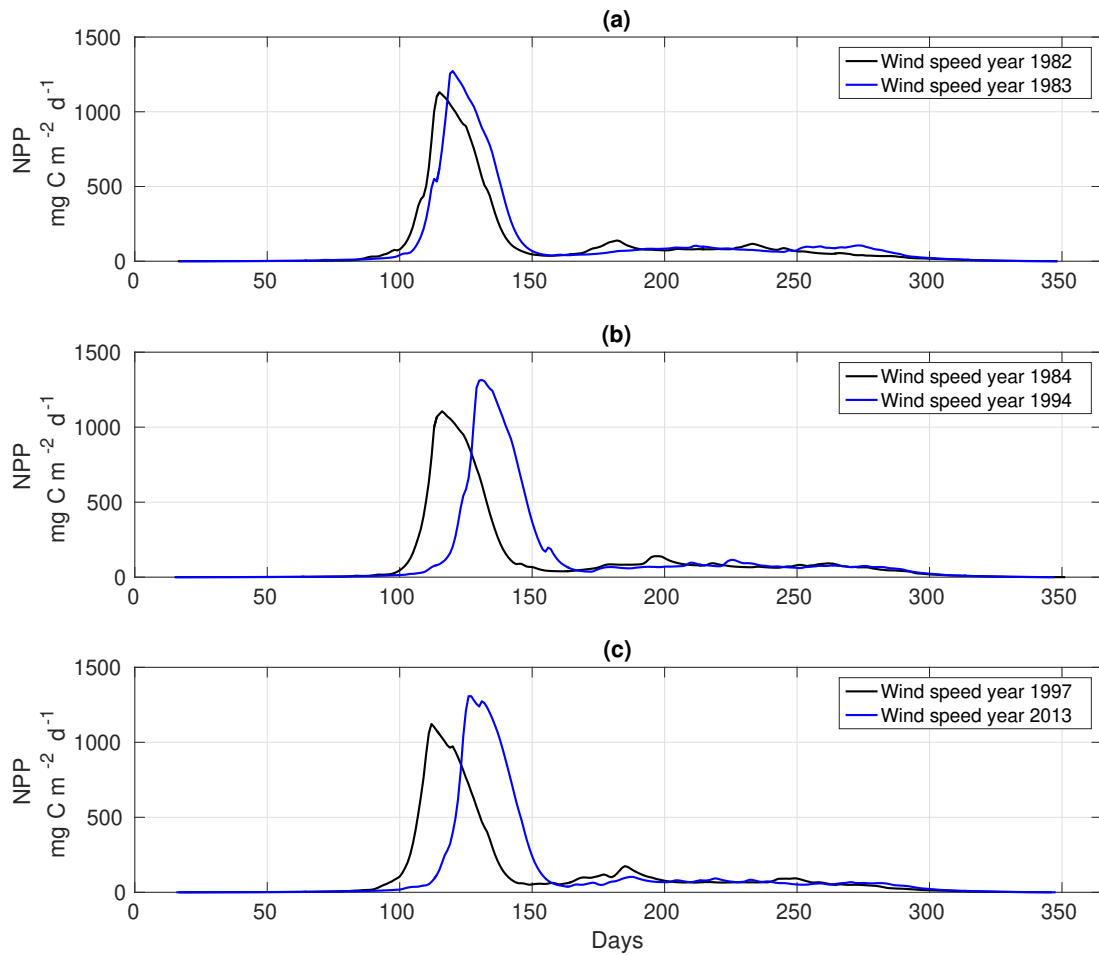


Figure 5.12: Comparison of daily time-series of NPP ($\text{mg C m}^{-2} \text{ day}^{-1}$) for the wind-only experiment for (a) year 1982 (black line) and year 1983 (blue line), (b) year 1984 (black line) and year 1994 (blue line), and (c) year 1997 (black line) and year 2013 (blue line).

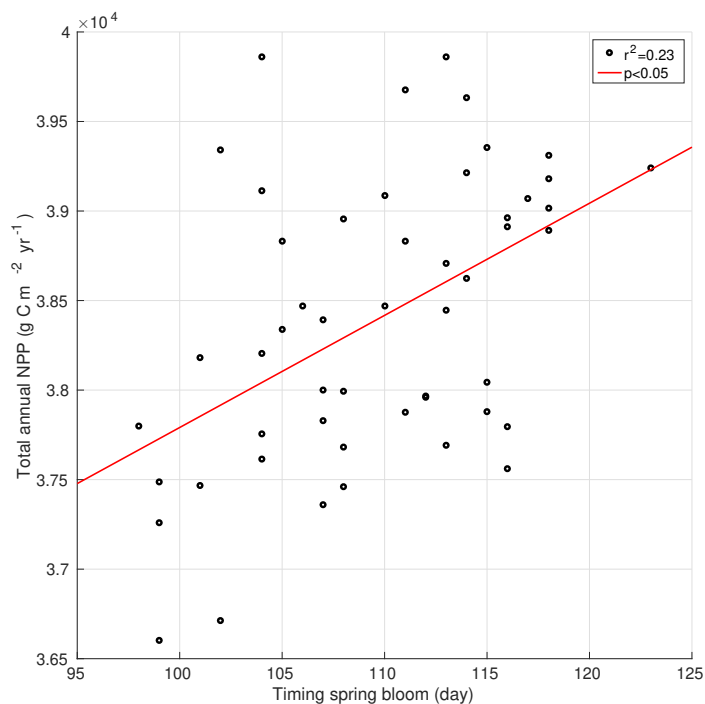


Figure 5.13: Scatter plot calculated from 1965 to 2015. Red line represents the significant regression line of the relationships between the timing of the spring bloom (days) and the total annual NPP ($\text{g C m}^{-2} \text{ yr}^{-1}$) for the wind-only experiment.

To understand the direct mechanism that wind speed has on the timing of the spring phytoplankton bloom between different years, a closer overview to wind speed time-series are considered in Figure 5.14, beginning ten days before the earliest spring phytoplankton bloom starts, i.e. year 1982 for Figure 5.14a, year 1984 for Figure 5.14b, and year 1997 for Figure 5.14c (black lines). The time-series finishes one day after the start of the spring phytoplankton bloom for the years 1983, 1994, and 2013 (blue lines). Additionally, the vertical black lines show the day that the spring phytoplankton bloom starts for each year; the horizontal blue- and red-dashed lines represent $\pm 1 \times \text{STD}$ and $\pm 2 \times \text{STD}$ from the mean of the wind speed time-series, respectively, calculated from 1965 - 2015 so they are the same in each plot. Storms are defined based on values of wind speed being higher than $\pm 2 \times \text{STD}$ (i.e. 15.3 m s^{-1}), corresponding to a total of 721 events (storms) during the 1965-2015 period according to this definition (Figure 5.16). It is possible to observe that in the years when the spring phytoplankton bloom is earlier, wind speed tends to be higher in the ten days prior to the spring bloom start. The STD for these ten days in each year were

calculated and showed that for Figure 5.14a, the year 1982 shows less variability of wind speed with an $STD=2.933$, while the year 1983 has an $STD=3.089$. On the other hand, the years 1984 and 1994 show an $STD= 3.836$ and $STD=2.856$, showing larger variability of wind speed before the spring bloom in the year 1984, but during the year 1994 there are storms observed during the ten days prior to the spring bloom of the year 1984, suggesting that, on average, higher values of wind speed, even though they have less variability, are enough to delay the spring bloom. Finally, the years 1997 and 2013 show an $STD=3.583$ and $STD=4.463$, respectively.

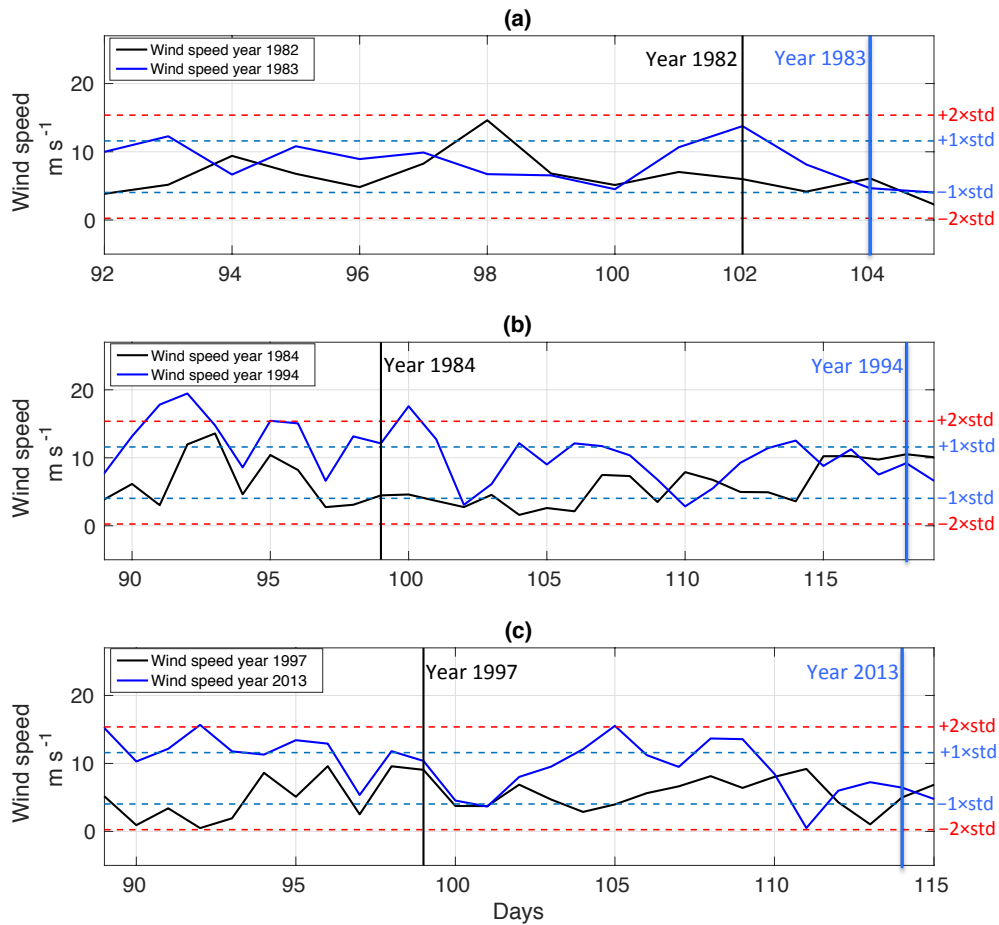


Figure 5.14: Comparison of daily time-series of wind speed (m s^{-1}) for (a) year 1982 (black line) and year 1983 (blue line), (b) year 1984 (black line) and year 1994 (blue line), and (c) year 1997 (black line) and year 2013 (blue line). Vertical lines represent the start of the spring phytoplankton bloom for each corresponding year, horizontal blue-dashed lines represent $\pm 1 \times \text{STD}$, and horizontal red-dashed lines represent $\pm 2 \times \text{STD}$.

Figure 5.12 shows that when the spring phytoplankton blooms are later, they reach higher peaks. However, there are no significant correlations found between the timing of the spring bloom and the spring daily NPP for the wind-only experiment ($r^2 = -0.03$, $p > 0.05$). To understand why earlier spring phytoplankton blooms lead to less annual production, depth profiles of temperature and DIN were analysed. Figure 5.15 shows the same years chosen to study wind speed in this section, showing ten days averaged vertical profiles of temperature and DIN prior to the start of the spring phytoplankton bloom for each re-

spective year. Figure 5.15a,b shows that the vertical profiles of temperature and DIN are very similar between the years 1982 and 1983 because they only have two days difference in terms of the timing of the spring phytoplankton bloom (Table 5.4). On the other hand, differences are visible when the differences in the start of the spring phytoplankton bloom are larger in between years. Figure 5.15c shows that during the year 1994 a deeper SML can develop, allowing phytoplankton to deplete more nutrients due to the larger standing stocks of DIN in the SML where phytoplankton can grow (Figure 5.15d). The same process can be observed for the years 1997 and 2013 (Figure 5.15e,f).

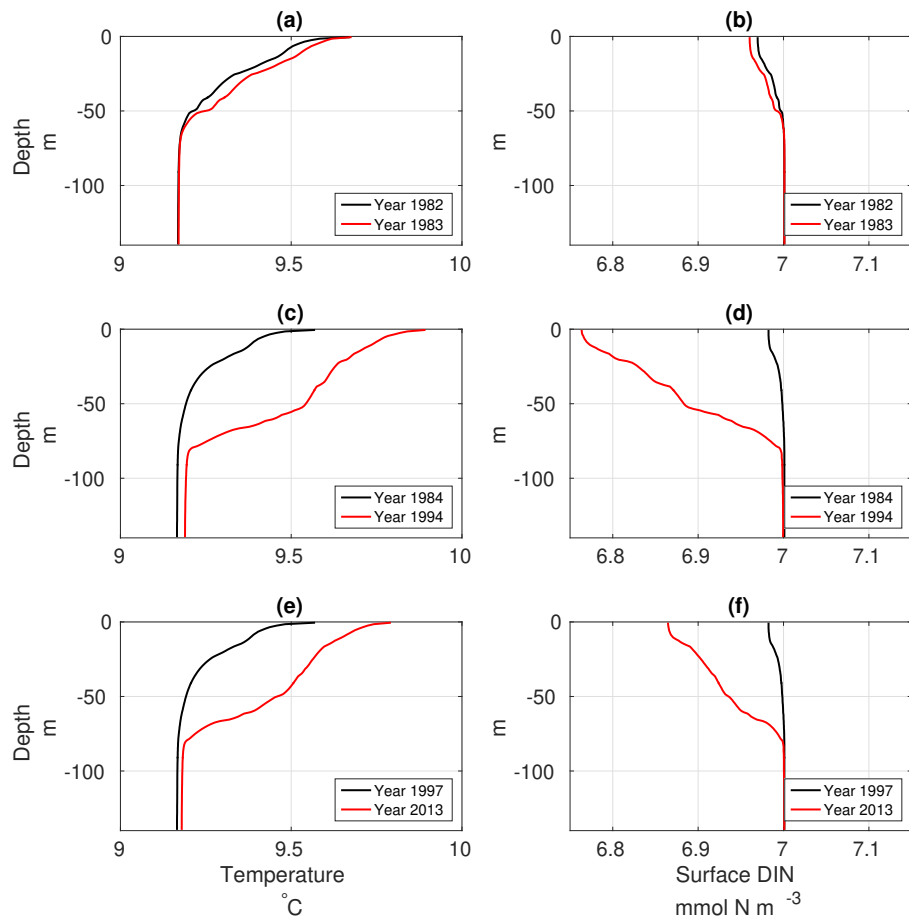


Figure 5.15: Ten days averaged vertical profiles prior to the start of the spring phytoplankton bloom for temperature including: (a) year 1982 (black line) and year 1983 (red line), (c) year 1984 (black line) and year 1994 (red line), and (e) year 1997 (black line) and year 2013 (red line); and for DIN including: (b) year 1982 (black line) and year 1983 (red line), (d) year 1984 (black line) and year 1994 (red line), and (f) year 1997 (black line) and year 2013 (red line).

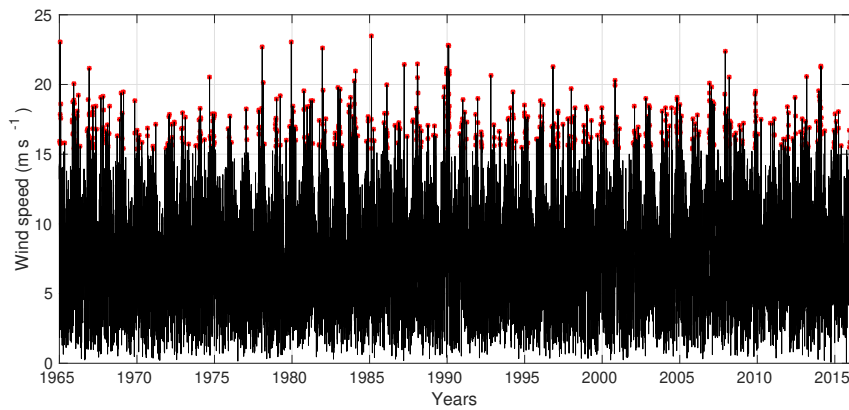


Figure 5.16: Daily wind speed time-series from 1965-2015 (black line) as a forcing of the model. Red dots represent the day when storms events occur (wind speed is higher than 15.3 m s^{-1}).

The impact of cloud coverage was also analysed in this section. The years 1971, 1996, and 2012 were chosen based on the inter-annual variability of total annual NPP, showing that those years show the largest positive difference between the cloud-only experiment and the control experiment. On the other hand, the years 1980, 2001, and 2013 show the greatest negative differences between the cloud-only experiment and the control experiment in terms of the total annual NPP.

Figure 5.17 presents the years chosen to analyse the direct mechanism that cloudiness has to affect annual phytoplankton production, showing that the affect of cloud cover over NPP in comparison to wind speed produces more noticeable changes in a daily basis, showing different spikes in the years 1980, 2001, and 2013, proving that the inclusion of photo-acclimation makes phytoplankton production more sensitive to changes in irradiance and cloud cover have a direct effect on how much irradiance phytoplankton will obtain, while wind speed changes NPP through mixing processes in the water column. Figure 5.17 also shows small differences are observed in terms of the timing of the spring phytoplankton bloom and no significant correlations were found between the start of the spring bloom and the total annual NPP for the cloud-only experiment ($r^2 = 0.02$, $p > 0.05$). The largest differences that cloud cover produces in the annual phytoplankton production seem to related to daily variations in the NPP during the spring bloom and summer growth periods.

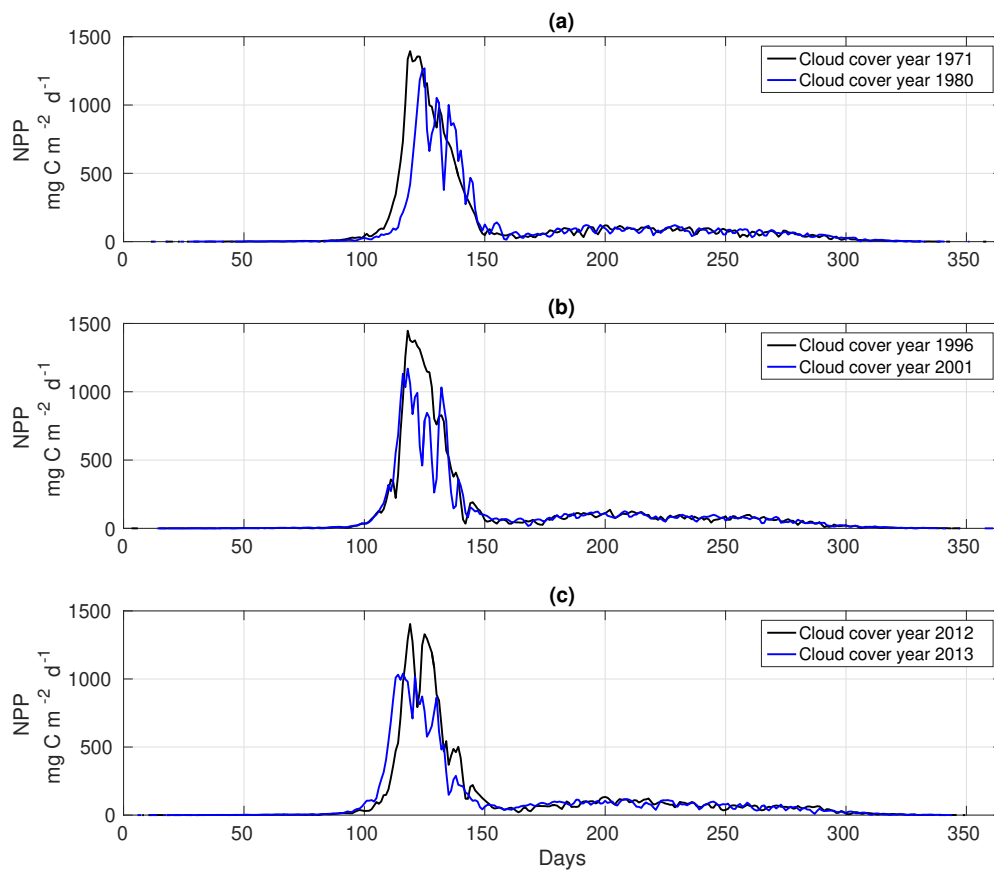


Figure 5.17: Comparison of daily time-series of NPP ($\text{mg C m}^{-2} \text{day}^{-1}$) for the cloud-only experiment for (a) year 1971 (black line) and year 1980 (blue line), (b) year 1996 (black line) and year 2001 (blue line), and (c) year 2012 (black line) and year 2013 (blue line).

Similar to the wind speed analysis, cloud coverage was also closely analysed during the ten-day prior to the spring bloom of the years 1971, 2001, 2013 (represented with vertical black lines in Figure 5.18). In this case, the spring bloom period was also shown until day 150.

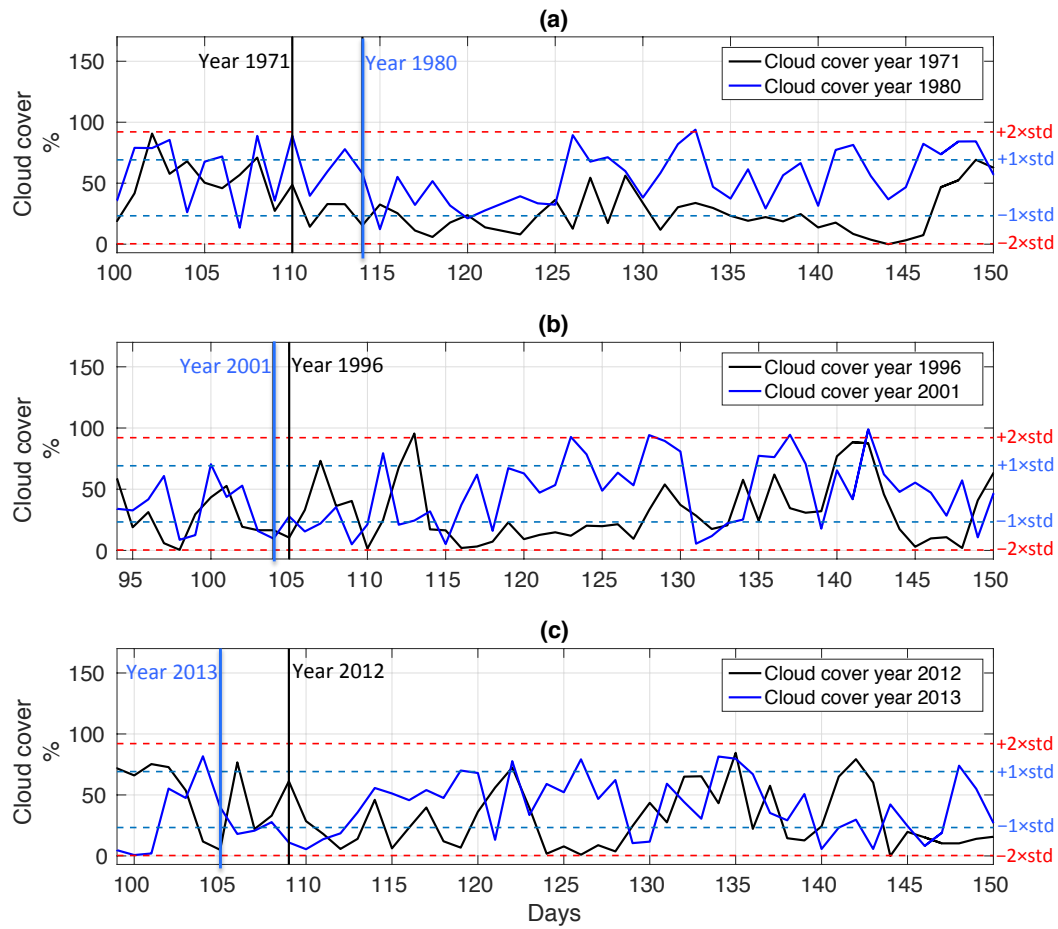


Figure 5.18: Comparison of daily time-series of cloud coverage (%) for (a) year 1971 (black line) and year 1980 (blue line), (b) year 1996 (black line) and year 2001 (blue line), and (c) year 2012 (black line) and year 2013 (blue line). Vertical lines represent the start of the spring phytoplankton bloom for each corresponding year, horizontal blue-dashed lines represent $\pm 1 \times \text{STD}$, and horizontal red-dashed lines represent $\pm 2 \times \text{STD}$.

Figure 5.19 shows a close-up of Figure 5.18 for the spring phytoplankton bloom period. A comparison between the daily cloud coverage and daily NPP is observed for (a) year 1980, (b) year 2001, and (c) year 2013. During those three years, it is possible to observe an inverse relationship between the daily variations of cloudiness and daily phytoplankton production, i.e. when cloud cover increases in a given day, then NPP diminishes during that day. However, correlations do not show to be significant between cloud coverage and NPP during those years in spring (figure not shown): 1980 ($r^2=0.006$, $p > 0.05$), 2001 ($r^2=0.003$,

$p > 0.05$), 2013 ($r^2=0.002$, $p > 0.05$). This inverse relationship can only be observed when the daily variability of cloudiness is big enough ($> 40\%$) from one day to another.

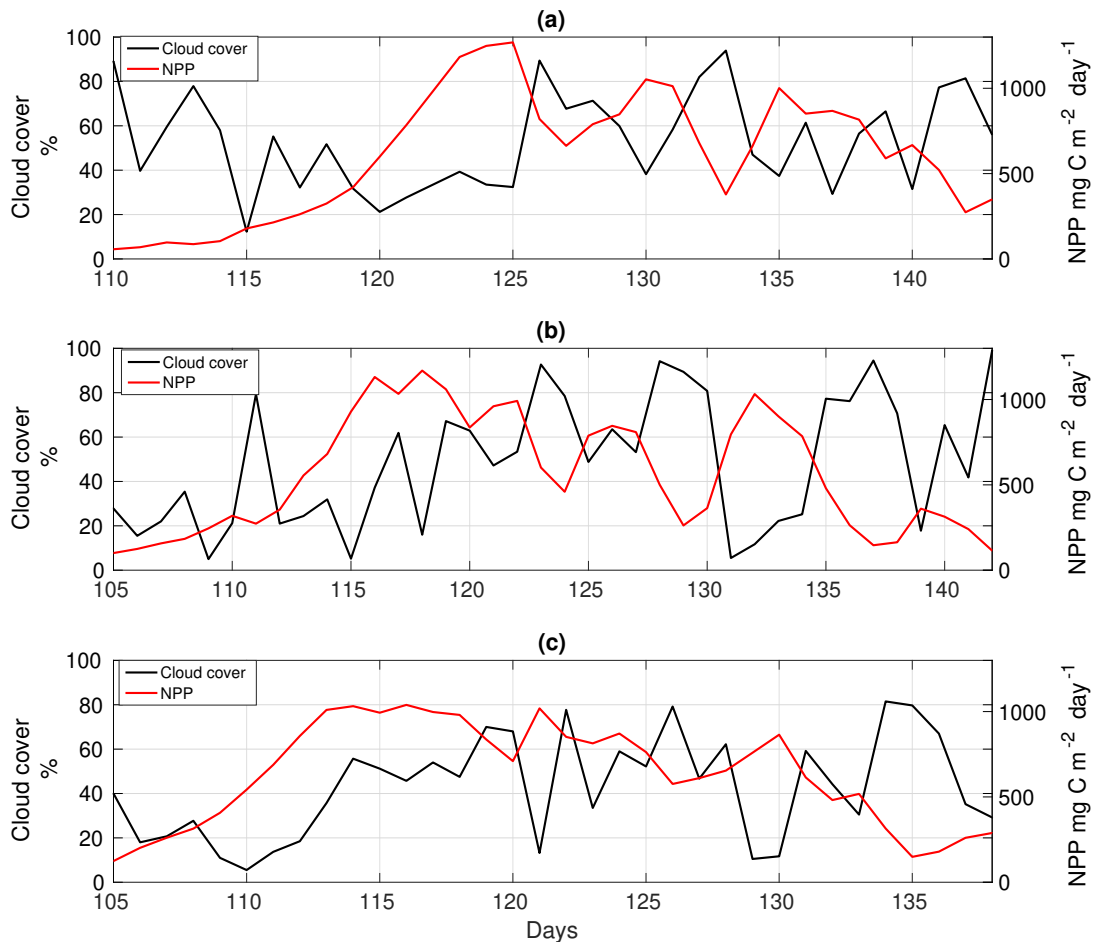


Figure 5.19: Daily time-series for NPP ($\text{mg C m}^{-2} \text{ day}^{-1}$; red lines) and cloud coverage (%) (black lines) from the start of the spring phytoplankton bloom to the day 150 of (a) the year 1980, (b) year 2001, (c) year 2013.

Further analysis was performed to analyse the effects of cloud coverage on daily variability of NPP during summer months (from day 150 to day 250) for the years 1980, 2001, and 2013. Figure 5.20 shows similar results to the ones observed during the spring phytoplankton bloom, with an inverse relationship between the daily variations of cloudiness and daily phytoplankton production. Furthermore, during the summer period, correlations are negative and significant for each year studied (Figure 5.21), explaining up to 44% (year

1980) of the summer variability due to changes in cloud cover, contrary to the correlations found during spring months.

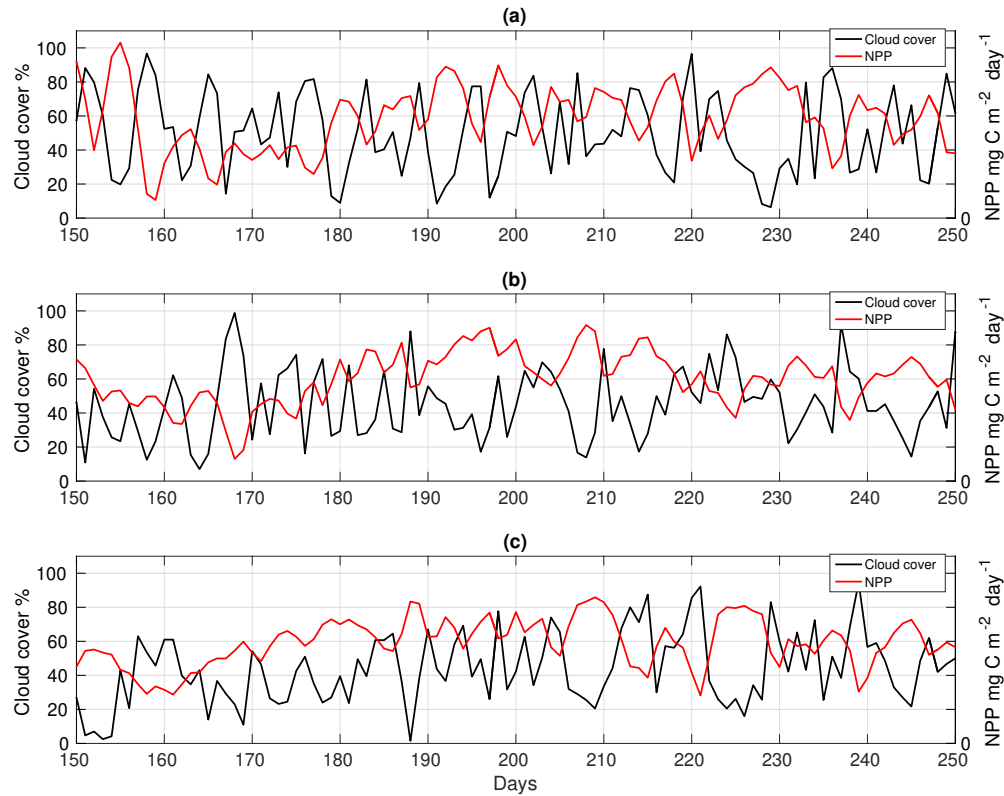


Figure 5.20: Daily time-series for NPP ($\text{mg C m}^{-2} \text{ day}^{-1}$; red lines) and cloud coverage (%) (black lines) during summer from the day 150 to the day 250 of (a) the year 1980, (b) year 2001, (c) year 2013.

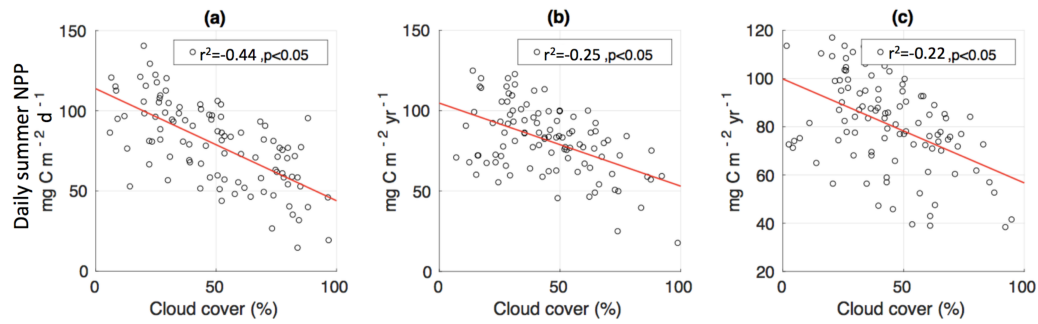


Figure 5.21: Scatter plots calculated between cloud coverage (%) and total NPP ($\text{mg C m}^{-2} \text{ day}^{-1}$) during summer from the day 150 to the day 250 of (a) the year 1980, (b) year 2001, (c) year 2013. Red line represents the significant regression line of the relationships between the daily summer NPP and cloud coverage.

5.5 Discussion

The results present the ecosystem behaviour of the S2P3 v8.0 model (Figures 5.1, 5.2), demonstrating that the newly developed model can reproduce the expected planktonic behaviour of a temperate shelf sea as shown in Chapter 4 (section 4.4.1.3), through qualitative and quantitative comparison of the model to the observations of the CCS location.

This section analyses the meteorological controls on PP; the robustness of the results found through an analysis of parameters values; and finally, concluding remarks for this chapter are stated.

5.5.1 Direct and indirect controls of wind speed and cloud coverage on phytoplankton production variability

It is interesting to compare the results obtained with the S2P3 v7.0 model in Chapter 3 (Marsh et al., 2015; Sharples et al., 2006) and the results obtained in this chapter with the S2P3 v8.0 model because of the differences found between each model analysis. For example, Figure 5.3 shows that cloud coverage, air temperature, and relative humidity are significant and negatively correlated to the total annual NPP, while, on the other hand, wind speed does not show significant correlations with the phytoplankton annual production. In contrast, Figure A2 shows that with the S2P3 v7.0 model there were no significant correlations found between the total annual NPP and any of the meteorological variables. This implies a significant difference in the model dynamics due to the incorporation of zooplankton as a state variable and the influence it has on the phytoplankton dynamics (Irigoiien et al., 2005; Cushing, 1990) and also due to the addition of photo-acclimation. While in the simplest model used in Chapter 3, meteorology was not correlated to phytoplankton annual NPP, Figure 5.3 demonstrates that the influence that clouds, air temperature, and relative humidity have on phytoplankton growth become more important, possibly related to the photo-acclimation process that directly relate to how the algal cells are adapting to changes in irradiance (Moore et al., 2006; MacIntyre et al., 2002; Falkowski & LaRoche, 1991), suggesting that cloud coverage, air temperature, and relative humidity, have a direct influence on the available light for phytoplankton to photosynthesise and an indirect impact through turbulent fluxes, changing the water column stability.

Additional to the comparison between total annual NPP and each meteorological variable, Figure 5.4 shows different results to the ones found in Chapter 3. The S2P3 v8.0 model has demonstrated that cloud coverage may have the largest impact on the inter-annual variability of phytoplankton production. The importance of wind speed for the phytoplankton annual production found in Chapter 3 is diminished in the newly developed model for inter-annual variability of the annual NPP. However, wind speed still has the largest influence in another important feature: the timing of the spring phytoplankton bloom (Figure 5.5). The effects of wind speed on the inter-annual variability of the timing of the spring phytoplankton bloom is related to the vertical mixing of the water column induced by wind (Follows & Dutkiewicz, 2001), directly affecting the development of thermal stratification (Townsend et al., 1994) by adding vertical turbulence and destabilising the water column, and, therefore, affecting the start of the spring phytoplankton bloom (Simpson & Sharples, 2012; Riley, 1942). It is interesting to note that the response of total annual NPP variability is not significantly correlated with annual wind speed (Figure 5.3), suggesting that the effects of wind speed on inter-annual variability of phytoplankton growth are driven by non-linear responses of phytoplankton, as wind speed will directly affect the water column mixing, which will produce different responses such as changes in the DIN availability, mixing of phytoplankton and zooplankton, and it will also have an impact in tidal mixing. Altogether, it will result in a change of phytoplankton growth, which is not possible to observe in Figure 5.3a as this process will be indirectly affected by wind speed at shorter timescales than annual variability.

The influence of wind speed on the timing of the spring phytoplankton bloom is shown in Figure 5.12, also demonstrating that earlier blooms are significantly correlated to lower annual phytoplankton production ($r^2=0.23$, $p < 0.05$). However, despite this correlation being significant, it only explains 23% of the inter-annual variability of NPP due to the timing of the spring bloom, suggesting that there are other processes during the year can be influencing the annual NPP and that possibly explains the 77% of remaining variability that does not correspond to the timing of the spring bloom, but it could also be due to the magnitude/length of the spring bloom or summer growth. Moreover, for the case of the default, wind-only, and cloud-only experiments, there are significant correlations found between the total spring NPP and the total annual NPP, showing $r^2=0.15$ ($p <$

0.05), $r^2=0.2$ ($p < 0.05$), and $r^2=0.75$ ($p < 0.05$), respectively. It is interesting to note that the timing and magnitude of the spring bloom accounts for 40% of the inter-annual variability of NPP in the wind-only experiment, while on the cloud-only experiment, 75% of this variability is accounted only by the magnitude of the spring bloom, demonstrating that because of photo-acclimation, NPP variability is more sensitive to changes in irradiance directly driven by cloud cover changes. During years where the spring phytoplankton bloom occurs later, a deeper thermocline can be set in comparison to years with earlier spring phytoplankton blooms due to higher levels of irradiance reached by that point and due to longer day length. These later blooms allow a deeper SML and more strongly established thermocline (Figure 5.15), enhancing the availability of inorganic nutrients for phytoplankton to deplete (Rumyantseva et al., 2015; Rippeth et al., 2009) and, therefore, allowing them to grow more (Rippeth, 2005) than in the years with earlier blooms observed.

Prior to the onset of the spring bloom, phytoplankton are especially sensitive to weather perturbations (Lacroix & Nival, 1998). In this study, it is shown that later spring phytoplankton blooms are driven by large variability and extreme events (e.g. storms; Figure 5.16) during the days prior to the initiation of the spring phytoplankton bloom (Figure 5.14). Towards spring, the increase in irradiance will create a warm surface layer (Sharples et al., 2006) that will not be able to be dissipated by tidal stirring (Kobayashi et al., 2006) but the stratification can be delayed by wind speed daily variability and when storms are present during the early spring days (Williams et al., 2013). These results also demonstrate that the inconclusive findings about the initiation of the spring phytoplankton bloom due to wind stress presented in Chapter 3, section 3.5.3 (Figure 3.12) are now resolved with the use of the S2P3 v8.0 model because daily variability of wind speed is taken into account in these experiments, contrary to the knockout-wind experiment developed in Chapter 3 where wind speed was smoothed to only represent seasonal variability of wind, losing daily variability. Another important reason for the difference in the results obtained is that the inclusion of zooplankton in the model is making S2P3 v8.0 to have a different response to wind speed, because mixing and grazing regulate the timing and magnitude of the spring bloom (Fasham et al., 1990; Frost, 1987; Evans & Parslow, 1985; Ryther & Hulburt, 1960), therefore, the mixing driven by wind speed will not only affect the stratification of the water column, but the concentrations of inorganic nutrients available for phytoplankton growth which will be directly linked to the grazing pressure due to zooplankton,

furthermore, phytoplankton and zooplankton will also be mixed in the water column; while in the S2P3 v7.0 the grazing effect was not affected by wind speed, but only had a direct dependency on phytoplankton biomass. This results in later spring phytoplankton blooms when wind speed variability is larger, contrary to the results obtained for the knockout-wind experiment in Chapter 3, because the daily variability of wind speed included in the wind-only experiment will change the turbulence mixing of the water column, contrary to the knockout-wind experiment which does not include this variability. Therefore, more mixing in the water column driven by wind will affect the onset of thermal stratification which will produce later spring blooms. Another important feature from the S2P3 v8.0 model that should be taken into account when analysing the timing of the spring phytoplankton bloom is the improvement from a fixed grazing rate into a seasonally varying dynamic zooplankton component (see Chapter 4).

The question about the direct influences of meteorological variables on the inter-annual variability of annual phytoplankton production remains, leading to a seasonal analysis. Figure 5.7 shows the different periods during the year including spring, summer, and autumn + winter. It is important to notice that wind speed has the largest influence on the inter-annual variability of spring, summer, and autumn + winter phytoplankton production. These findings are supported by the effect that wind speed is demonstrated to have on the timing and magnitude of the spring phytoplankton bloom, the timing being a crucial feature that will also modify the annual phytoplankton production. Additionally, during summer months, wind speed variability might induce nutrient inputs from deeper layers into the bottom of the thermocline, especially during spring tides periods (Sharples et al., 2001). Due to the addition of photo-acclimation, phytoplankton can be more sensitive to changes in light and nutrient availability and this might lead to larger inter-annual variability of the SCM (Cullen et al., 2015), driven by wind pulses during summer periods (Williams et al., 2013). On the other hand, relative humidity was shown to have the largest influence on the autumn + winter months (Figure 5.7d), presumably because of the influence that this meteorological variable has on the latent heat flux and the long-wave heat flux, changing the water column temperature and, therefore, surface buoyancy and water column stability, producing shallow and short-term stratification affecting phytoplankton production.

Cloud coverage is another important meteorological component that drives inter-annual variability of phytoplankton production. Figure 5.17 shows that clouds can also affect the timing of the spring phytoplankton bloom due to the increasing radiation during spring that is directly modulated by cloud cover (Townsend et al., 1994). Despite the influence that clouds have on light, their effects on the start of the spring phytoplankton bloom within the model are not as important as the ones driven by vertical mixing of the water column due to wind speed (Figure 5.5). The largest difference driven by clouds is during spring (Figure 5.18), when cloud cover is to be inversely correlated to phytoplankton NPP, i.e. large daily variations in cloud coverage produce a large daily variation in phytoplankton production. The reduction of light due to a high percentage of clouds on a given day will inhibit phytoplankton growth during that day, showing that photo-acclimation will make phytoplankton more sensitive to large daily variations of light. Moreover, Figure 5.7d showed that cloud coverage has the largest effect on summer production after wind speed. The same mechanism that affects inter-annual variability of NPP during spring months can be observed during summer months due to cloud variability.

Cloud coverage inter-annual and daily variability have a strong effect on the spring phytoplankton bloom and summer production. Despite wind speed being shown to be the meteorological component that affects NPP the most during spring and summer periods, on average, clouds are responsible for a larger variability of annual phytoplankton PP (Figure 5.4).

5.5.2 Parameterisation: robustness of the meteorological effects on phytoplankton production variability

The control and control-based experiments developed with different parameter values show that the results found in this chapter are robust within reasonable ranges of parameter variability: the inter-annual variability of annual phytoplankton production is always most influenced by clouds (Figure 5.11a). However, these large differences can not be observed for the each season of the year (Figure 5.11b,c,d), suggesting that the processes that are driven by clouds that produce inter-annual variability of total NPP have a different timescale, rather than seasonally. Therefore, daily variability of cloud cover could be producing responses of phytoplankton growth at similar timescales as shown in Figures

5.18, 5.19.

5.5.3 Concluding remarks

This study presents a quantitative analysis of the effects of meteorology on the inter-annual variability of phytoplankton production in a version of the S2P3 model with more biological fidelity, showing different results to the ones found in Chapter 3 where the control and control-based experiments were analysed. This demonstrates the extent of the effects that inclusion of zooplankton and photo-acclimation have when modelling shelf sea ecosystems. Using a more realistic and complex model has given more confidence to the results found based on quantitative and qualitative comparisons with observations for the CCS location and Celtic Sea (see Chapter 4), revealing cloud cover as one of the most important meteorological components for long-term phytoplankton variability. However, the influence that wind speed has on the inter-annual variability of PP during spring and summer cannot be neglected due to its importance, driving vertical mixing of the water column, nutrient inputs for deeper layers, and inhibition of thermal stratification.

Chapters 4 and 5 have demonstrated that the S2P3 v8.0 model is able to reasonably represent the integrated behaviour of phytoplankton and how they react to environmental conditions as planktonic communities. In future works, this model can be set for different locations of the NW European shelf sea, although care should be taken when doing the parameterisation and calibrating for a new region, because it has been demonstrated that even though the results in this chapter showed to be robust within reasonable parameter ranges, a poorly constrained model can affect the outcome of the results as shown in Chapter 4.

Chapter 6

Synthesis

6.1 Synthesis and discussion from this work

Temperate shelf seas are important for many human activities (Holt et al., 2017) and the correct development and management of these ecosystems will depend on the understanding of the resident organisms and their ecosystem functions (Sharples et al., 2013), as well as the environmental drivers that affect plankton communities.

Phytoplankton are at the base of the trophic chain in the ocean (Vargas et al., 2006), therefore, inter-annual variability in their growth affects many other organisms at higher trophic levels. Some of those organisms are directly influenced by phytoplankton, such as zooplankton (Irigoiien et al., 2005). Zooplankton play a central role in the biogeochemical cycles of the ocean and in the energy transfer to fish and carbon transfer to the benthos (Giering et al., 2018; Marquis et al., 2011). In consequence, variations in the seasonal cycle of phytoplankton will have a large impact on the entire shelf sea ecosystem.

Both complex and simple ecosystem models have been used to study shelf seas and the ecosystem dynamics (Marsh et al., 2015; Edwards et al., 2012; Holt et al., 2012; Yool et al., 2011; Sharples & Holligan, 2006; Sharples et al., 2006; Fasham et al., 1990), but a clear consensus about the direct and indirect roles of meteorology on long-term phytoplankton productivity has not been reached. This work aimed to improve our knowledge regarding the meteorological impacts on inter-annual variability of phytoplankton PP using a 1-D physical and biological coupled model.

In Chapter 3, the S2P3 v7.0 model was used to estimate the effects of four meteorological

variables on the inter-annual variability of phytoplankton NPP over the past five decades. It was found that wind speed provides a larger impact on the inter-annual variability of PP at the CCS location in the NW European shelf sea. Inconclusive results about the direct impact that wind has on the seasonal cycle of phytoplankton and a mismatch between the model and buoy observations during the years 2014 - 2015 from the SSB programme, led to further model development.

Chapter 4 presented three new models developed from S2P3 v7.0, adding an NPZ framework (S2P3-NPZ), photo-acclimation of phytoplankton (S2P3-Photoacclim), and a model that included both processes in one (S2P3 v8.0). These models aimed to better represent ecosystem dynamics based on a comparison to zooplankton biomass and physiological rate observations. Table 6.1 shows the quantified differences between the four models used in this work. It is clear that, on average, the least productive model corresponds to the S2P3 v8.0 model, followed by the S2P3-NPZ, S2P3 v7.0, and S2P3-Photoacclim. This shows the impact and complexity that the predator-prey relationship has in the model dynamics, with the addition of zooplankton grazing as one of the main losses of phytoplankton (Franks et al., 1986). On the other hand, the S2P3 v7.0 model shows, on average, more total annual NPP than the S2P3-NPZ model, suggesting that the influence of a constant grazing rate is not as strong in comparison to the one provided by the zooplankton grazing (NPZ framework), because the predator-prey relationship can not be entirely represented in the S2P3 v7.0 model, with the S2P3-NPZ showing a correlation between the phytoplankton and zooplankton biomass: when phytoplankton biomass is low, zooplankton biomass is also low; but when phytoplankton reaches a maximum, zooplankton biomass starts increasing; on the other hand, when zooplankton biomass reaches a maximum, phytoplankton biomass reaches a minimum value. This process is not possible to be observed in the S2P3 v7.0 model, where the sinusoidal behaviour set for the grazing starts as soon as phytoplankton biomass starts increasing. Additionally, S2P3-Photoacclim showed, on average, to have the highest total annual NPP, demonstrating that the phenotypic responses of phytoplankton to changes in the environment and the addition of variable stoichiometric ratios of C:N:Chl, allows for more efficient phytoplankton, which all use the available resources to grow.

The same methodology was used to calculate the total spring NPP and the total summer NPP for each model (Table 6.1), in both Chapters 3 and 5. It is shown that for

the S2P3 v7.0 model, on average, 69.2% of the annual phytoplankton production occurs during the spring phytoplankton bloom. On the other hand, for the S2P3-NPZ model, on average, only 37.8% of the annual production occurs during spring months, showing that the predator-prey relationship has a strong influence on the magnitude of the spring phytoplankton bloom every year. Additionally, the S2P3-Photoacclim model shows a very strong spring phytoplankton bloom, corresponding to $\sim 90\%$ of the total annual NPP. Finally, for the S2P3 v8.0 model, only 67.4% of the annual production corresponds to the spring bloom period. It is important to note that different definitions for the start of the spring phytoplankton bloom were calculated, with the results shown here given by the definition of settled stratification (i.e. surface temperature minus bottom temperature $> 0.5^\circ\text{C}$ for at least ten consecutive days; Simpson & Sharples, 2012). This definition shows a strong, positive, and significant correlation between the timing of the spring bloom defined directly by a threshold of surface chlorophyll (Henson et al., 2009; Siegel et al., 2002) over $1.5 \text{ mg Chl m}^{-3}$ ($r^2 = 0.63$, $p < 0.05$) and 2 mg Chl m^{-3} ($r^2 = 0.52$, $p < 0.05$). Furthermore, the results for each model (Table 6.1) do not show to be strongly sensitive to the different definitions of the timing of the spring bloom calculated in this work, with a range of $\sim 2\%$ difference in terms of the total spring NPP : total annual NPP. Consequently, despite the many different quantitative definitions of the timing of the spring bloom in the literature, including specific thresholds or rates of increase in phytoplankton concentration or chlorophyll biomass (see also White et al., 2009; Greve et al., 2005), the two definitions tested in this work, have demonstrated that differences in the results are negligible.

The large differences shown and quantified between each model might (see Chapter 4, section 4.4.1.3), show that adding photo-acclimation and zooplankton in the S2P3 v7.0 model, have quantitative differences in terms of the timing of the spring bloom, and the total spring NPP (Table 4.7). The differences between the S2P3-NPZ, S2P3-Photoacclim, and S2P3 v8.0 model can account for the importance of the processes added as it can change the dynamics of the model. Moreover, Chapter 4 demonstrated, through a sensitivity analysis, that a correct parameterisation of the models is relevant for the results, and that the inclusion of observations of zooplankton biomass and physiological rates of phytoplankton allowed to constrain each model not only based in phytoplankton biomass (surface chlorophyll) and DIN profiles (CTD observations). Furthermore, the S2P3 v8.0 resulted in different answers to the questions posed with regard to meteorological forcing

as shown in Chapter 5, showing that clouds have the largest impact on the inter-annual variability of the NPP, contrary to the findings from Chapter 3, which showed that wind speed is the main driver controlling inter-annual variability of NPP. The results differ between the S2P3 v7.0 and the S2P3 v8.0 model, but in Chapter 5 it was also shown that wind speed affects the most during spring and summer seasons. This implies that the overall effects of zooplankton grazing and photo-acclimation provide more realistic insights about the ecosystem dynamics of the CCS location and their impact is enough to produce differences in the results found with the S2P3 v7.0 model.

Model	Characteristic	Mean	Maximum	Minimum	STD
S2P3 v7.0	Total spring NPP ($g C m^{-2} yr^{-1}$)	39.6	54.7	33.5	5.8
	Total summer NPP ($g C m^{-2} yr^{-1}$)	17.2	22.9	56.9	5.1
	Total annual NPP ($g C m^{-2} yr^{-1}$)	57.1	61.1	53.1	1.8
S2P3-NPZ	Total spring NPP ($g C m^{-2} yr^{-1}$)	21.1	49.3	7.2	9.8
	Total summer NPP ($g C m^{-2} yr^{-1}$)	28.2	39.7	6.8	7.7
	Total annual NPP ($g C m^{-2} yr^{-1}$)	55.7	60.0	52.7	1.5
S2P3-Photoacclim	Total spring NPP ($g C m^{-2} yr^{-1}$)	35.6	40.7	25.7	4.8
	Total summer NPP ($g C m^{-2} yr^{-1}$)	3.8	11.4	0.6	4.2
	Total annual NPP ($g C m^{-2} yr^{-1}$)	39.4	42.4	37.0	1.7
S2P3 v8.0	Total spring NPP ($g C m^{-2} yr^{-1}$)	25.5	39.5	14.5	3.7
	Total summer NPP ($g C m^{-2} yr^{-1}$)	10.3	12.9	6.8	1.1
	Total annual NPP ($g C m^{-2} yr^{-1}$)	37.8	47.8	33.4	2.2

Table 6.1: Comparison between the S2P3 v7.0, S2P3-NPZ, S2P3-Photoacclim, and S2P3 v8.0 models in terms of the total spring NPP, total summer NPP, and total annual NPP calculated from 1965 to 2015, including the mean, maximum, minimum, and STD values.

6.2 Wider implications and model considerations

6.2.1 Modelling different regions of the ocean

Further applications of the newly developed S2P3 v8.0 model can be assessed in different locations of the NW European shelf sea. Sharples et al. (2006) used the S2P3 v7.0 model in other regions of the NW European Shelf Sea to understand the effects of the spring-neap tidal cycle on the spring phytoplankton bloom. On the other hand, Marsh et al. (2015) used the same S2P3 v7.0 model in the NW European shelf, the western English Channel, and the East China and Yellow Seas regions. Therefore, the S2P3 v8.0 model could be applied to other regions apart from the CCS location as in this work.

To apply the S2P3 v8.0 model to different coastal regions of the global ocean, it would be important to consider that in certain regions that have strong influence of riverine inputs or in high-latitude shelf seas where the sea-ice interaction is the predominant factor controlling the ecosystem dynamics of the area, there will be differences between the model representation of those regions and observations. The model is able to identify regions where other horizontal processes might have a large influence on the shelf sea dynamics (Marsh et al., 2015). For example, regions of the shelf sea that are strongly influenced by riverine inputs, can be expected to have lower salinity in the surface waters or there could also be changes in salinity (and density profiles) due to water coming from the open ocean specially near the shelf edge; and therefore, this would lead to changes in stratification, phytoplankton productivity, and alterations in light attenuation by non-algal particles and dissolved organic matter (Smyth et al., 2010; Groom et al., 2009).

6.2.2 Model development: can higher vertical resolution provide better insights about shelf sea dynamics?

The highest vertical resolution used in this work was 1m. The user can set the number of vertical levels in the model to change the vertical resolution, which consequently will also change the timestep (see CFL condition, Chapter 2, section 2.1.2). For example, in this work the number of vertical levels was of 140 to achieve 1m vertical resolution as the total depth considered 140m. However, attempts to run experiments at even higher vertical resolutions (e.g. 0.5m, considering 280 vertical levels), produced instabilities in the model

because the CFL condition could not be met for this case. It was shown that different vertical resolutions in the S2P3 v7.0 model produced differences in the biological processes of the model, varying the total annual NPP (see Chapter 2, Figure 2.12), contrary to what Sharples (1999) stated in the first version of this model. Therefore, vertical resolution considerations are important to realistically represent different shelf sea processes. For the S2P3 v8.0 model, the highest vertical resolution achieved was 1m as in the S2P3 v7.0 model.

Increasing model vertical resolution also increases the model running cost. Many modellers have to compromise between the computational cost and model realism (Øie Kvile et al., 2018), especially when modelling long-term experiments. However, for marine ecologists, predicting realistic vertical turbulent mixing and horizontal distribution of the thermocline can have a large impact on the biological processes that are influenced by these physical components (Hickman et al., 2009). Inaccurate predictions of such processes can occur due to the limited knowledge of mixing processes, vertical density gradients, or poorly constrained model parameterisations. Moreover, turbulent processes play a crucial role in ecosystem modelling as the physical part of the model is dependant on turbulent mixing (e.g. processes such as shelf sea water circulation, surface temperature, air-sea heat fluxes, etc), and how this is resolved in the model is based on the specification of boundary conditions and, to a large extent, based on which type of turbulence model is used. Therefore, it is suggested that turbulence closure schemes need to be carefully chosen and additional manipulation of the turbulent diffusivity within vertical density gradients should be considered to account for the effects of non-resolved processes (Canuto et al., 2001) and to represent the mechanisms by which stratification suppresses turbulence and mixing. Improvements in this field could allow simple models to run at higher vertical resolutions, which could be accounted for in future improvements of the S2P3 v8.0 model and further model development to perform experiments in different shelf seas of the ocean at a higher vertical resolution to have a better representation of the shelf sea ecosystem dynamics at a relatively low computational cost relative to 2-D and 3-D models.

6.2.3 Model physics constraining biology

Another feature of the S2P3 v8.0 model to focus on is the physical part of the model because the biological structure is largely dependent on the physical structure, which, ul-

timately, can limit the validation and calibration of the model in terms of the biological components. Throughout Chapter 4, the model temperature structure appears to be in poor agreement with the CTD observations from the UK SSB data for summer months (24/07/2015; see Figure 4.7d). The model appears continuously stratified to approximately 70 m, whereas CTD data indicate a mixed layer with a strong thermocline around 50 m. The thermocline is the transition region between the nutrient-poor, well-lit surface layer and the darker, nutrient-rich deeper water (Young et al., 2004), which plays an important role in determining the biological properties of the water column. Therefore, this results in differences between each model developed in Chapter 4 and the CTD observations in terms of chlorophyll, showing differences in the depth at which the SCM is developed, being in each model always shallower than the observations, reaching a maximum of chlorophyll around 20m depth, while CTD data shows that the SCM is reached at ~ 45 m depth (Figure 4.7e). Based on the results obtained by Rippeth et al. (2005), it is suggested that the mixing driven by the spring-neap tidal cycle and wind derived energy could be influencing the differences between the thermocline and SCM of the models and the CTD, through turbulence generated by thermocline processes that the models can not completely represent maybe due to a coarse vertical resolution. Furthermore, these differences in the chlorophyll profile will also affect the vertical structure of DIN (Figure 4.7f), showing a marked nitracline in the CTD observations ranging from 30-50m, while in each model developed, the DIN profile shows a larger range in depth of a weak nitracline (varying from approximately 20m to 70m depth) which is related to the temperature vertical profiles that the models are simulating. Therefore, it can be concluded that the models were able to predict the gross features of the observed temperature field in comparison to the CTD data, but they were unable to adequately resolve the strong vertical temperature gradients. Similar to the results found by Young et al. (2004) in the Celtic Sea using a 3-D model, where it is suggested that these differences can be subject to an insufficient vertical resolution, a factor which is limited by available computer power.

6.2.4 Validate and support modelling results with *in situ* observations and remote sensing

Chapter 4 demonstrated that observations of zooplankton biomass (Giering et al., 2018) and physiological rates of phytoplankton (Hickman et al., 2012; Hickman et al., 2009) were

relevant for the model development, including a better calibration and assuring higher confidence in the results found in Chapter 5. This validation, using both zooplankton biomass and physiological rates of phytoplankton observations are rarely found in the literature, providing novel work to the marine biogeochemistry modelling field of shelf seas. Moreover, the zooplankton biomass observations were available for the CCS location, while the physiological observations were taken at different locations of the shelf sea, which allowed comparisons with the models for the seasonally-stratified locations near the CCS, neglecting observations that belong to the Irish Sea (vertically mixed region) and near to the shelf edge (CS2 and N1 locations) as they do not represent a good proxy to compare the models for two reasons: the CCS location is characterised for being a seasonally stratified region; and the S2P3 models do not consider advection, which becomes a relevant process in the shelf edge. Therefore, it is important to fund and support further research cruises in shelf seas to calculate and acquire more observations, which will help the model to improve the calibration process and provide better model parameterisations. However, quantifying the relative contributions of different driving forces and photosynthetic rates are not straightforward. Moreover, collecting data with high spatial and temporal resolution to test scientific hypotheses requires long-term logistic preparations and many cruises depend on the local weather conditions to successfully acquire samples. Nevertheless, despite the costs associated to research vessels, the benefits that they provide through direct and accurate observations for a wide array of oceanographic parameters, and via autonomous vehicles, is relevant for model validation in order to enable a better understanding of shelf sea ecosystems and predictions about how they will change. Finally, laboratory experiments to calculate zooplankton biomass and photosynthetic rates as explained in Chapter 4 (sections 4.3.1.1 and 4.3.1.2, respectively), requires multiple considerations, additional use of many software, and, in many cases, calibration and normalisation of the results found.

A limitation of the measurements made by research vessels is that they are not synoptic, i.e. the data are not sampled simultaneously at different locations (Simpson & Sharples, 2012) to resolve the highly dynamic nature of biogeochemical phenomena. Therefore, another approach that could be considered to collect more observations to validate and calibrate numerical models rely on remote sensing. Since the 1970s, the remote sensing of ocean properties has become increasingly valuable supplement for direct observations via water

reflectance observations, a synoptic view of algal blooms, phytoplankton community structure, PP, sediment plumes, oil spills, benthic habitats, and linkages between biology and the physical/chemical environment (Frouin et al., 2019; Platt et al., 2008). However, it is important to underline that remote sensing also has its own limitations, for example, in the case of visible and infra-red sensors to measure sea surface temperature (SST), it is compromised by cloud cover as it is only possible to be used in cloud-free conditions; furthermore, in shelf sea regions the presence of suspended sediments and coloured dissolved organic matter supplied to coastal waters mainly via rivers can complicate the accurate determination of chlorophyll (Simpson & Sharples, 2012). Consequently, many efforts have been done to overcome these limitations. For example, in 2002, the Moderate-resolution Imaging Spectroradiometer (MODIS) sensor was launched on NASA's Aqua satellite platform with a capacity to detect phytoplankton chlorophyll fluorescence for assessing phytoplankton physiological status (Minnett, 2001). Behrenfeld et al. (2009) used satellite sensors to detect natural fluorescence from surface chlorophyll to provide information on phytoplankton physiology, such as nutrient stress. Furthermore, the Marine Primary Production: Model Parameters from Space (MAPPS) project of the European Space Agency (ESA) aims to assemble a global database of photosynthesis - irradiance parameters to study basin-scale variability in the photo-physiological response of marine phytoplankton (Bouman et al., 2018). Open-access and continuous observations at high temporal resolution (i.e. long-time series) from this project could be used to further analyse the S2P3 v8.0 model and improve numerical parameterisations, which has been shown to define the model dynamics (see Chapter 4). Finally, another project to improve remote sensing involves the Plankton, Aerosol, Cloud and ocean Ecosystem (PACE; <https://pace.gsfc.nasa.gov>) mission as part of the NASA Earth-observing satellite mission to continue and advance in observations of global ocean colour, biogeochemistry, and ecology, as well as carbon cycle, aerosols and clouds (Werdell, 2019).

6.2.5 Wider implications about shelf sea modelling: marine policies

Managing, and predicting shelf sea ecosystems and their short- and long-term integrated impacts on the global ocean requires reliable numerical models. Modelling the CCS location with a simple 1-D model that includes an NPZ framework and stoichiometric varying ratios of Chl:C:N (i.e. photo-acclimation) have been demonstrated to be a useful tool to

further understand the interactions of plankton communities, vertical processes, and the effects of meteorology on phytoplankton production.

Wider implications of this work could provide better insights into the future quality, health, and sustainability of the UK shelf seas, due to the improved understanding of the complex interactions that the environment has on planktonic communities (Hardman-Mountford et al., 2005). Therefore, models such as S2P3 v8.0, can provide practical feedbacks about long-term predictions of possible environmental responses to changes in physical forcing. This will be an important tool if the model provides answers about the biological and physical interactions within the shelf sea and the consequences of these interactions on the functioning of the whole coastal system, including its sensitivity to environmental changes. The implications can involve improvements in predicting the shelf sea behaviour to weather and climate changes, and provide insights to the implications of human activities such as fisheries (Perry et al., 2005) and fish stocks in the shelf sea (Sims, 2006). Shelf seas and coastal waters provide about 90% of global fish catches (Pauly et al., 2002), with variability of fish stocks and fish distributions being linked to physical perturbations on phytoplankton production (Tenore et al., 1995; Ware & Thomson, 1991). For example, in the Celtic Sea it has been found that in the seabed banks around the CCS location there is a large fishing activity during the stratified period between April and August suggested to be due to an increase in PP modulated by the spring-neap tidal cycle that allows large supplies of nutrients into the photic zone, and due greater concentrations of zooplankton within the region influenced by the seabed banks and elevated PP (Sharples et al., 2013). Using the S2P3 v8.0 model to analyse the CCS location and the impact that the spring-neap tidal cycle and inter-annual variability of PP will have on the fishing activity of the region is not only relevant to allow a reassessment of the marine policies of the UK (Rogers & Greenaway, 2005), but also understanding the links between oceanographic processes and fishing activity is necessary for the creation of marine protected areas and marine renewable energy installations (Sharples et al., 2013).

Shelf seas and coastal marine environments are exceptionally vulnerable to climate change; their dynamics and ecosystems are coupled systems that are highly constrained by external forcing from atmospheric, oceanic, and terrestrial factors (Holt et al., 2010). Studies involving satellite radiometer data (Gomez-Gesteira et al., 2008) and long-term monitoring

time-series (Hughes et al., 2010; van Leussen et al., 1996) have shown evidence for the warming of the NW European shelf over the past decades. Over the next century, the temperature increase is the most noticeable and robust impact of climate change on the NW European shelf. Many studies have used regional models to understand the effects of climate change in the shelf sea ecosystem. Particularly in the NW European shelf sea, models have been applied based on climate model projections (Wakelin et al., 2012; Holt et al., 2012; Holt et al., 2010), facing challenges to resolve the small-scale dynamics of the shelf sea in comparison to global models (Groger et al., 2013). To assess the impacts of climate change, many global socio-economic scenarios are being developed by the Intergovernmental Panel on Climate Change (IPCC) to provide climate scenarios that take into account estimates of possible magnitudes of greenhouse gas emissions that are responsible for much of the climate change (Flint & Flint, 2012). These scenarios are used as boundary conditions for Global Climate Models (GCMs) that provide us with insight into how human behaviour in the future may influence changes in climate. However, despite GCMs being used to estimate climate future projects, their horizontal and vertical resolution are usually too coarse (e.g. one grid-cell size on the order of $2.5^\circ \times 2.5^\circ$, i.e. $\sim 275 \times 275 \text{ km}^2$) to accurately capture shelf sea regional topography (1 - 100 km), therefore, a method used to solve this issue is to do a spatial interpolation, statistical downscaling, or dynamical downscale of a GCM projection by using its outputs to drive a regional shelf seas model (Tinker et al., 2016). Downscaling is the process of transferring the climate information from a climate model with coarse spatial and fine temporal scales to the fine scale required by models that address effects of climate. Dynamical downscaling is computationally expensive for processing multi-decadal simulations from GCMs, while statistical downscaling considers less computational resources (Flint & Flint, 2012). Therefore, analysing future climate projections with the S2P3 v8.0 model is suggested here as novelty work for the CCS location and other temperate shelf sea locations (e.g. North Sea, English Channel, East China and Yellow Seas, etc) to understand how the planktonic communities are going to be affected by climate change, for which it would be necessary to choose a GCM projection for a selected location and downscale it using one of the methods mentioned above depending on the questions that are to be assessed. Projections for future changes in climate have shown to be uncertain because of the dependency on scenarios of future anthropogenic and natural forcing that are also uncertain; an incomplete understanding and imprecise models of the climate system and, finally because of the existence of inter-

nal climate variability (Collins et al., 2013). Therefore, it is important to improve model understanding and acquiring observations to validate and build more realistic models. The local weather of the NW European shelf sea is also a matter of discussion and taking into account these changes can better predict how the plankton communities will behave in future, with many different studies concluding that the impacts of global rising temperatures will produce a larger increase of sea temperature in shelf seas than the open-ocean (Tinker et al., 2016; Groger et al., 2013; Holt et al., 2010). The difference in temperature increase between shelf and open-ocean based in model simulations occurs because shelf seas are shallower than the winter mixed layer depths of the open-ocean (Holt et al., 2010).

6.3 Concluding remarks

This thesis provides a thorough investigation into the effects of meteorology and inter-annual variability of NPP, including differences during each seasonal period (spring, summer, autumn + winter) due to inter-annual and daily variability in wind speed, cloud coverage, air temperature, and relative humidity. Understanding the consequences of these meteorological drivers on phytoplankton PP can help in the response to the effects that climate change and its linked alterations to seasonal weather conditions will produce in the marine planktonic communities of shelf seas (Costello et al., 2006). Additionally, this work have demonstrated that the structure, validation, and parameterisation of a model are important features for the hypotheses to be tested due to the different answers that can be obtained based on those model features.

Appendix

Tidal constituents	u-component	v-component
M_2	0.355	0.192
S_2	0.138	0.074
N_2	0.068	0.037

Table A.1: Three main tidal constituents (M_2 , S_2 , and N_2) in the CCS location calculated using POLCOMS model and used to force the S2P3 model along with meteorological forcing, including a spring-neap tidal cycle using the two components (u,v) of every tidal constituent [ms^{-1}].

Months	Wind control-based experiment	Cloud control-based experiment	Temperature control-based experiment	Humid control-based experiment
April	0.1613*	0.1659*	0.1254*	0.0011
April + May	0.0891*	0.0656	0.0734	0.0085
April + May + June	0.0847*	0.0509	0.0581	0.0122

Table A.2: Values of correlations (r-squared) between the total annual net PP ($gCm^{-2}yr^{-1}$) and total net PP ($gCm^{-2}day^{-1}$) averaged monthly during April, April + May, April + May + June over the period of 1965-2015 using different control-based experiments for every correlation. Other periods during the year were omitted in this table because no significant correlations were found. Values of r-squared with a star (\star) represent the experiments that show significant correlation during that months ($p < 0.05$).

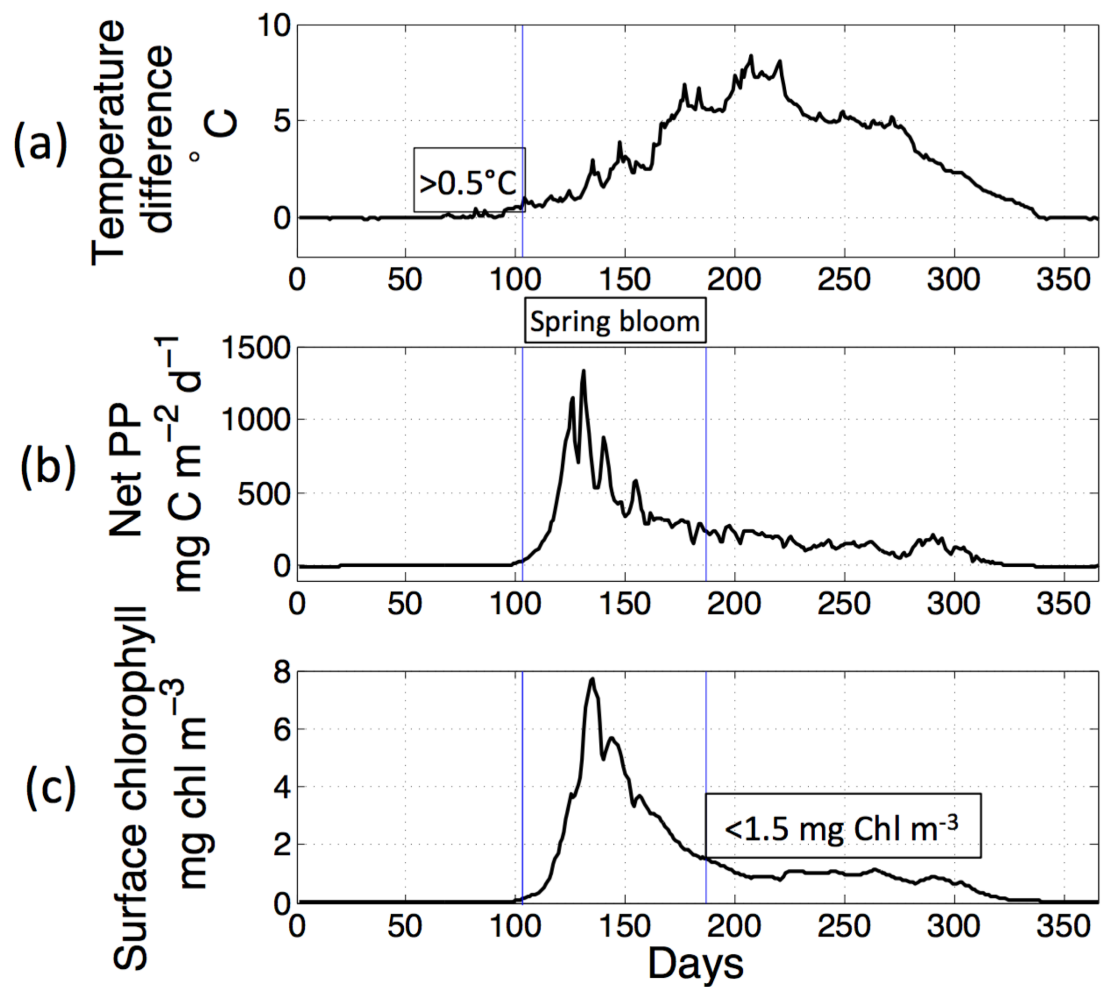


Figure A1: (a) Temperature difference (surface temperature minus bottom temperature, °C). When temperature difference is more than 0.5 °C for at least ten days, it defines the start of the spring phytoplankton bloom. The vertical blue line represent the day when this criteria is met, (b) Daily NPP showing the spring phytoplankton bloom (between the days marked by the blue vertical lines), (c) Surface chlorophyll-*a* showing the end of the spring phytoplankton bloom when it is less than 1.5 mg C m⁻³. These plots show the year 1965 from the default experiment, as an example.

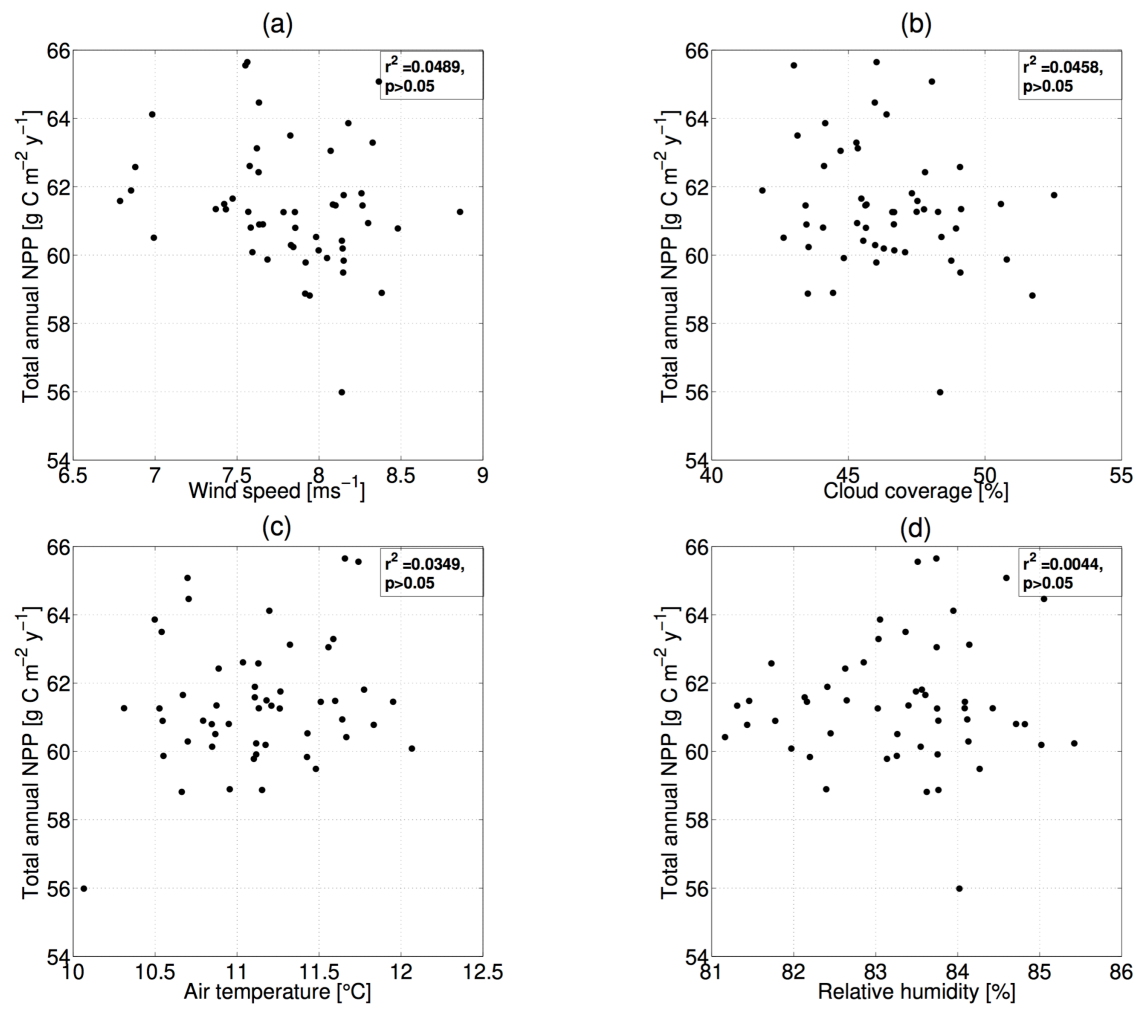


Figure A2: Scatter plots calculated for the period 1965 and 2015. Correlations represented between the total annual NPP and (a) wind speed, (b) cloud coverage, (c) air temperature, and (d) relative humidity.

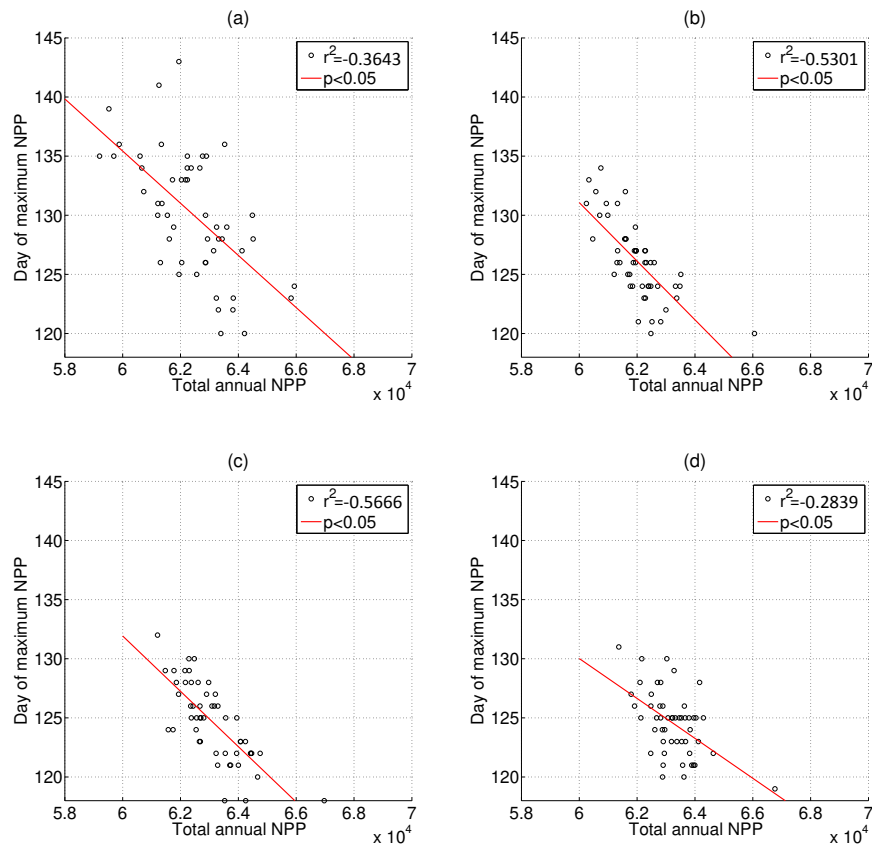


Figure A3: Scatter plots calculated for the period 1965 and 2015. Red line represents the regression line of the correlations between the day of maximum NPP (days) and total annual NPP ($\text{mg C m}^{-2} \text{ yr}^{-1}$) for (a) wind-only experiment, (b) cloud-only experiment, (c) temperature-only experiment, and (d) humid-only experiment.

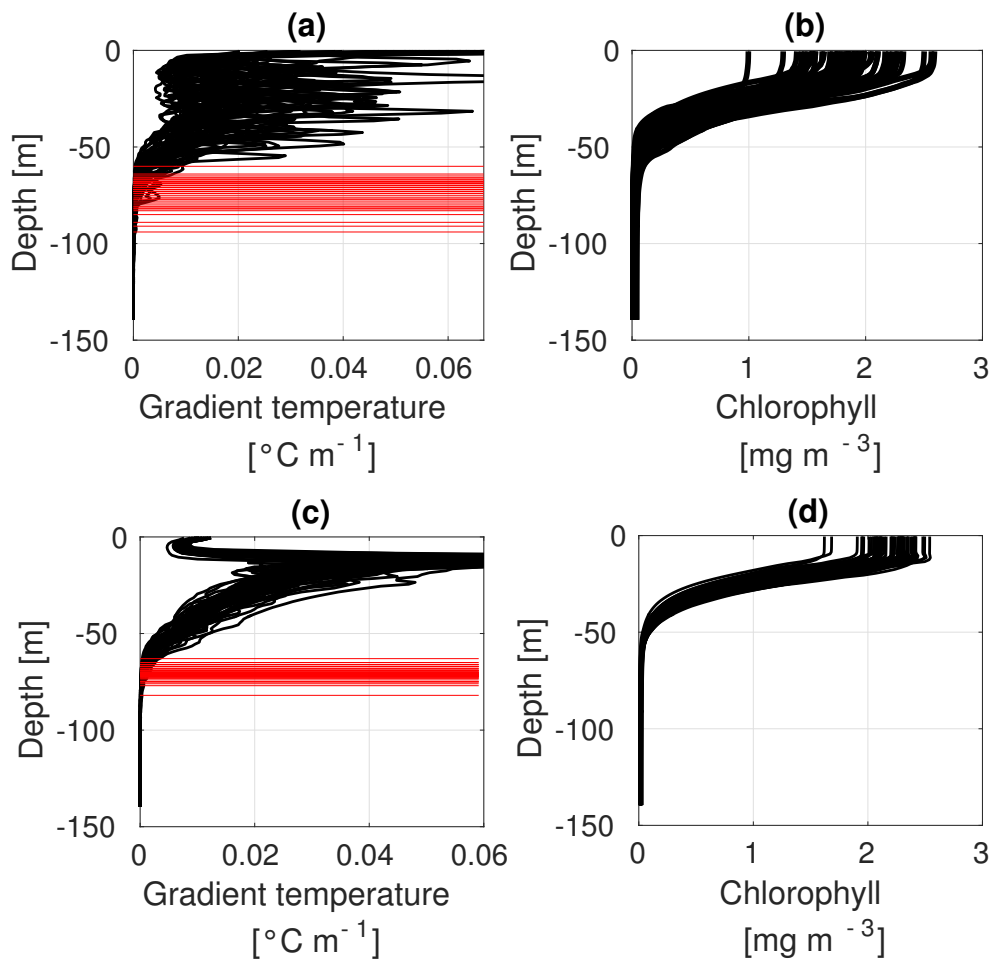


Figure A4: Plot of vertical profiles of temperature averaged ($^{\circ}\text{C}$) over spring period from daily profiles and gradient profiles of temperature ($^{\circ}\text{C m}^{-1}$) calculated during 1965 - 2015. (a) mean gradient profiles of temperature over spring for the default experiment. Red lines represent the surface BML calculated when the gradient = 0, (b) mean profiles of chlorophyll-*a* (mg m^{-3}) over spring for the default experiment, (c) mean gradient profiles of temperature over spring for the knockout-wind experiment. Red lines represent the surface BML calculated when the gradient = 0, (d) mean profiles of chlorophyll-*a* (mg m^{-3}) over spring for the knockout-wind experiment.

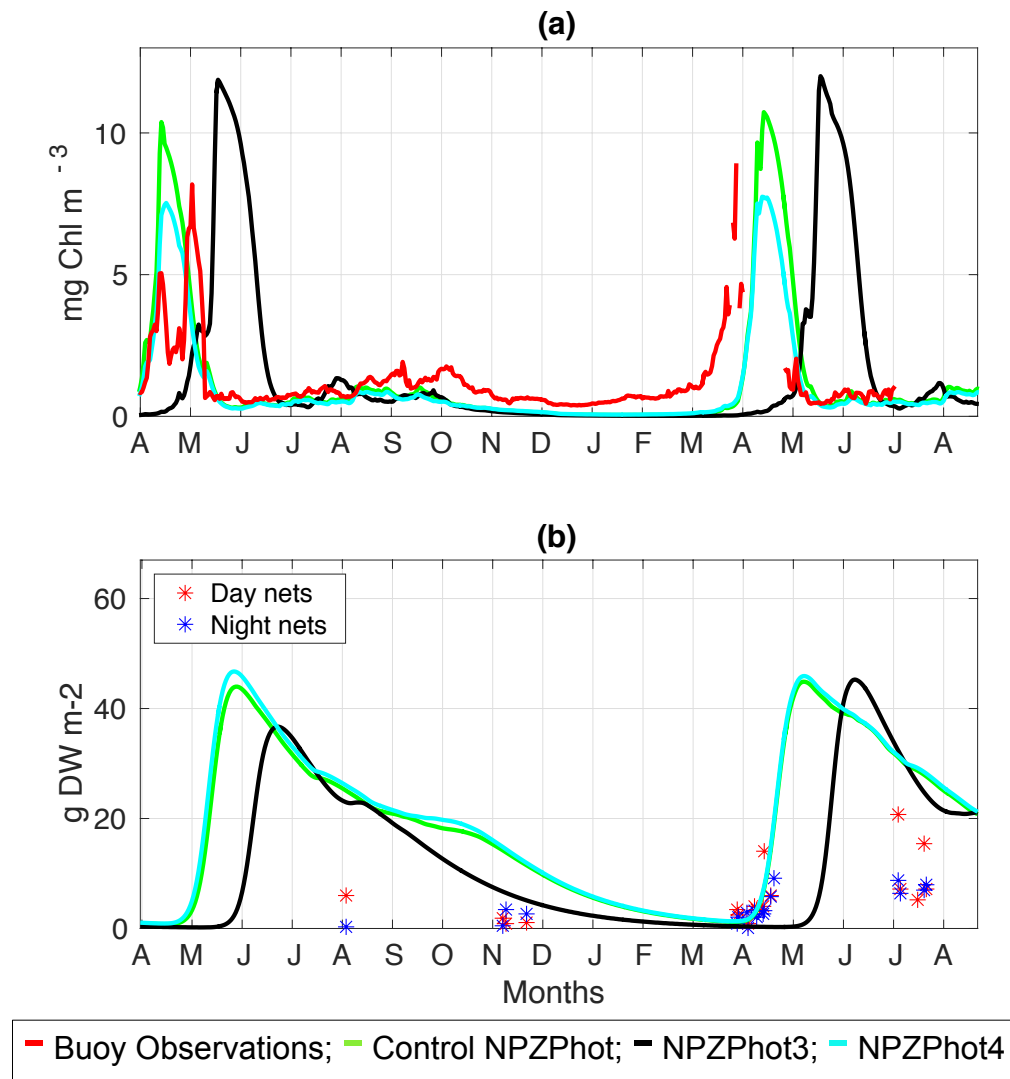


Figure A5: SSB buoy observations (red line) from the start of April 2014 to end of June 2015 compared to the Control NPZPhot (green line), NPZPhot 3 ($Q_m = 0.225$; black line), and NPZPhot 4 ($Q_m = 0.675$; cyan line) shown from start of April 2014 to the end of August 2015 for (a) surface chlorophyll-*a* and (b) zooplankton biomass.

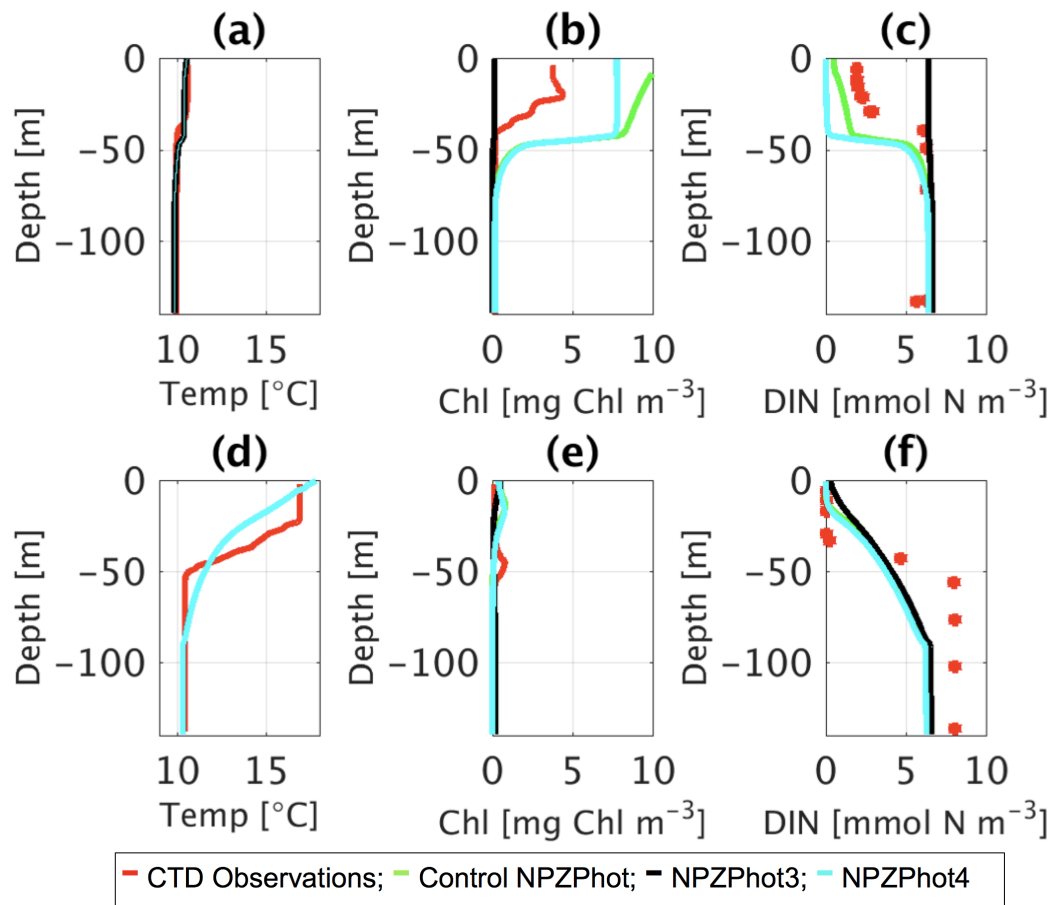


Figure A6: CTD observations from the SSB programme (red line) including data for: springtime (20/04/2015) (a) temperature, (b) chlorophyll-*a*, and (c) DIN; for summertime (24/07/2015) for (d) temperature, (e) chlorophyll-*a*, and (f) DIN along the Control NPZPhot (green line), NPZPhot 3 ($Q_m = 0.225$; black line), and NPZPhot 4 ($Q_m = 0.675$; cyan line).

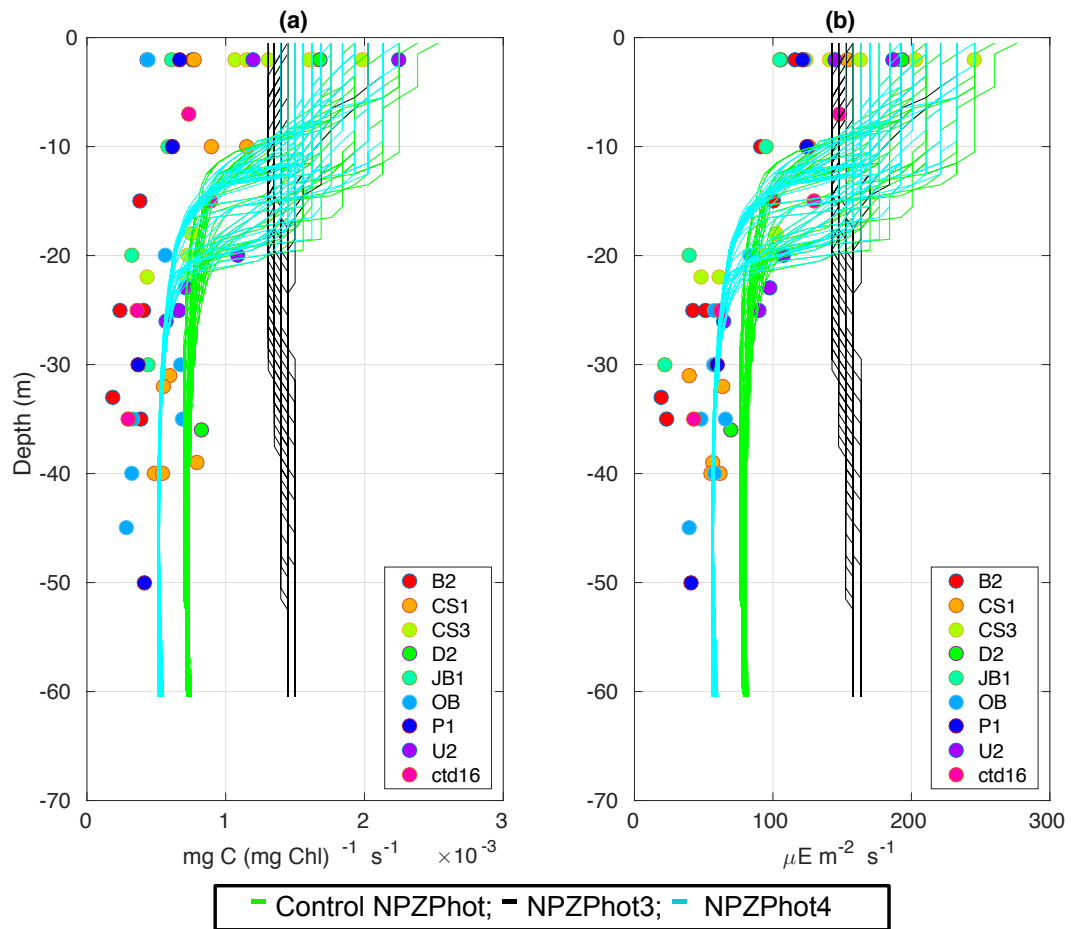


Figure A7: Observations from the cruises CD173 and JR98 in different locations of the Celtic Sea, including Control NPZPhot (green lines), NPZPhot 3 ($Q_m = 0.225$; black lines), and NPZPhot 4 ($Q_m = 0.675$; cyan lines) for: (a) chlorophyll-*a* specific maximum light-saturated photosynthesis rate (P_{\max}^{Chl}) and (b) light saturation parameter (E_k). The data from the model was plotted for the same days that the observations were collected.

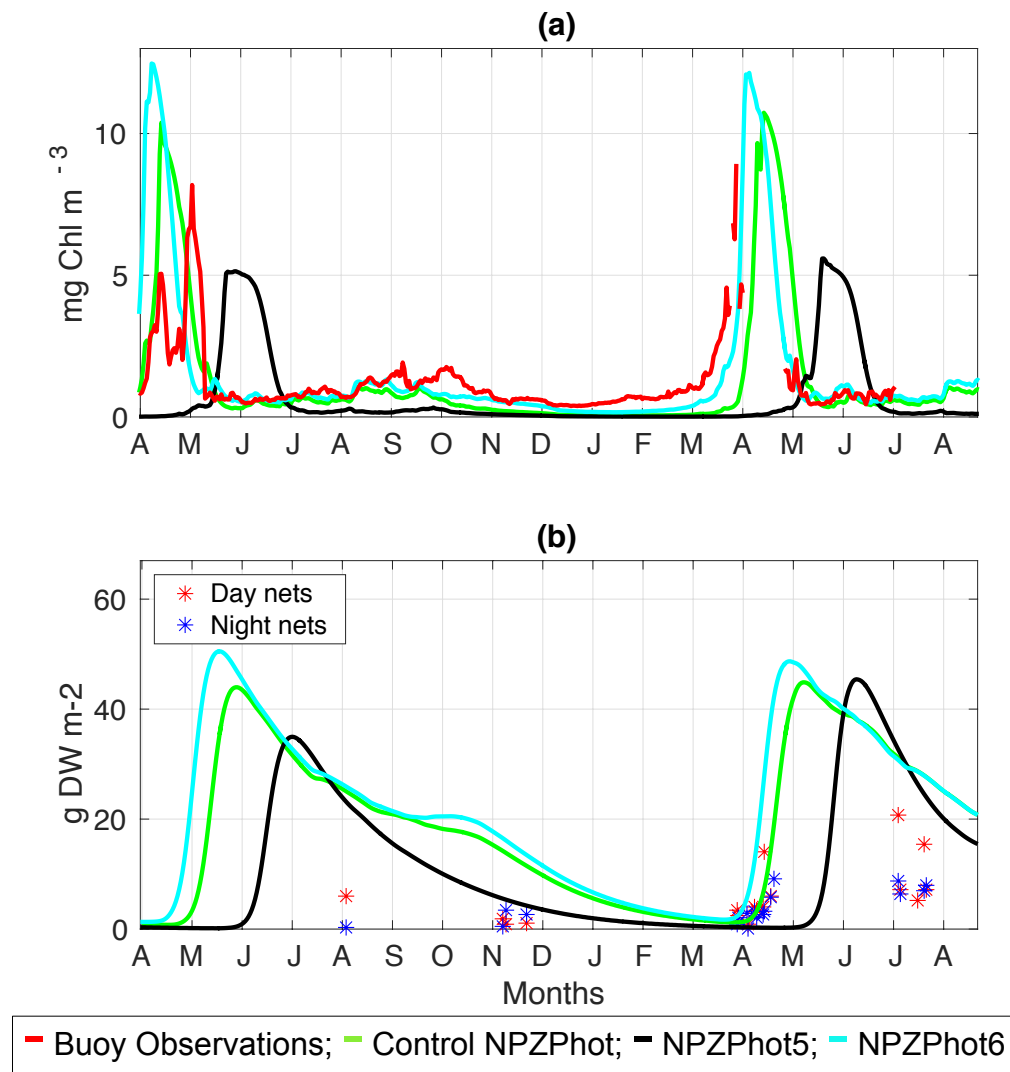


Figure A8: SSB buoy observations (red line) from the start of April 2014 to end of June 2015 compared to the Control NPZPhot (green line), NPZPhot 5 ($\theta_{\max}^N = 0.075$; black line), and NPZPhot 6 ($\theta_{\max}^N = 0.225$; cyan line) shown from start of April 2014 to the end of August 2015 for (a) surface chlorophyll-*a* and (b) zooplankton biomass.

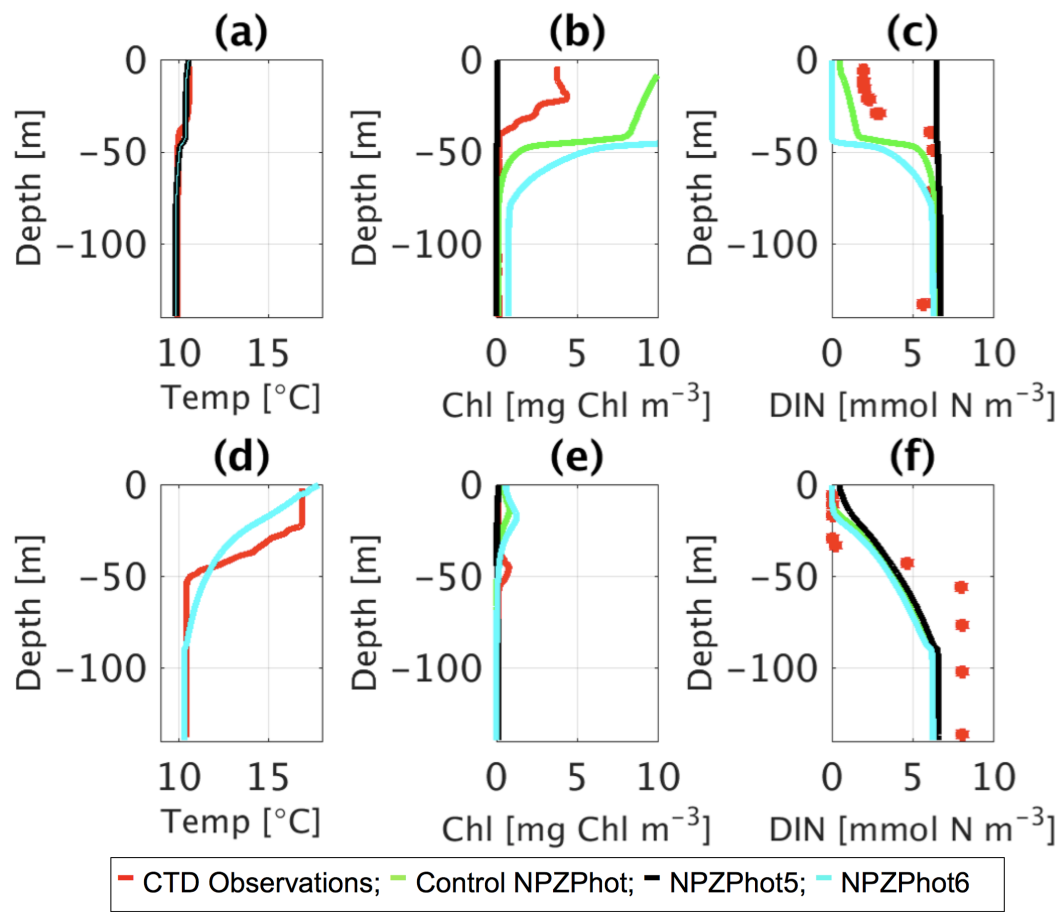


Figure A9: CTD observations from the SSB programme (red line) including data for: springtime (20/04/2015) (a) temperature, (b) chlorophyll-*a*, and (c) DIN; for summer-time (24/07/2015) for (d) temperature, (e) chlorophyll-*a*, and (f) DIN along the Control NPZPhot (green line), NPZPhot 5 ($\theta_{\max}^N = 0.075$; black line), and NPZPhot 6 ($\theta_{\max}^N = 0.225$; cyan line).

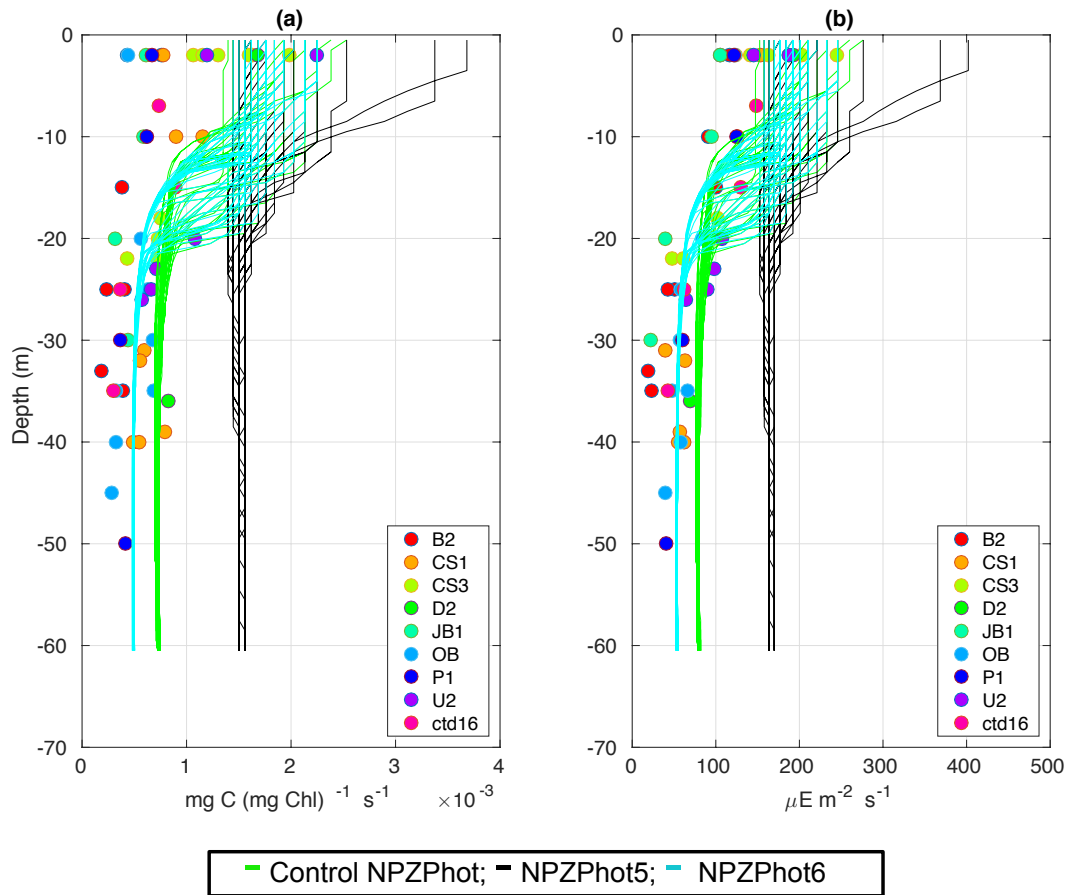


Figure A10: Observations from the cruises CD173 and JR98 in different locations of the Celtic Sea, including Control NPZPhot (green lines), NPZPhot 5 ($\theta_{\max}^N = 0.075$; black lines), and NPZPhot 6 ($\theta_{\max}^N = 0.225$; cyan lines) for: (a) chlorophyll-*a* specific maximum light-saturated photosynthesis rate (P_{\max}^{Chl}) and (b) light saturation parameter (E_k). The data from the model was plotted for the same days that the observations were collected.

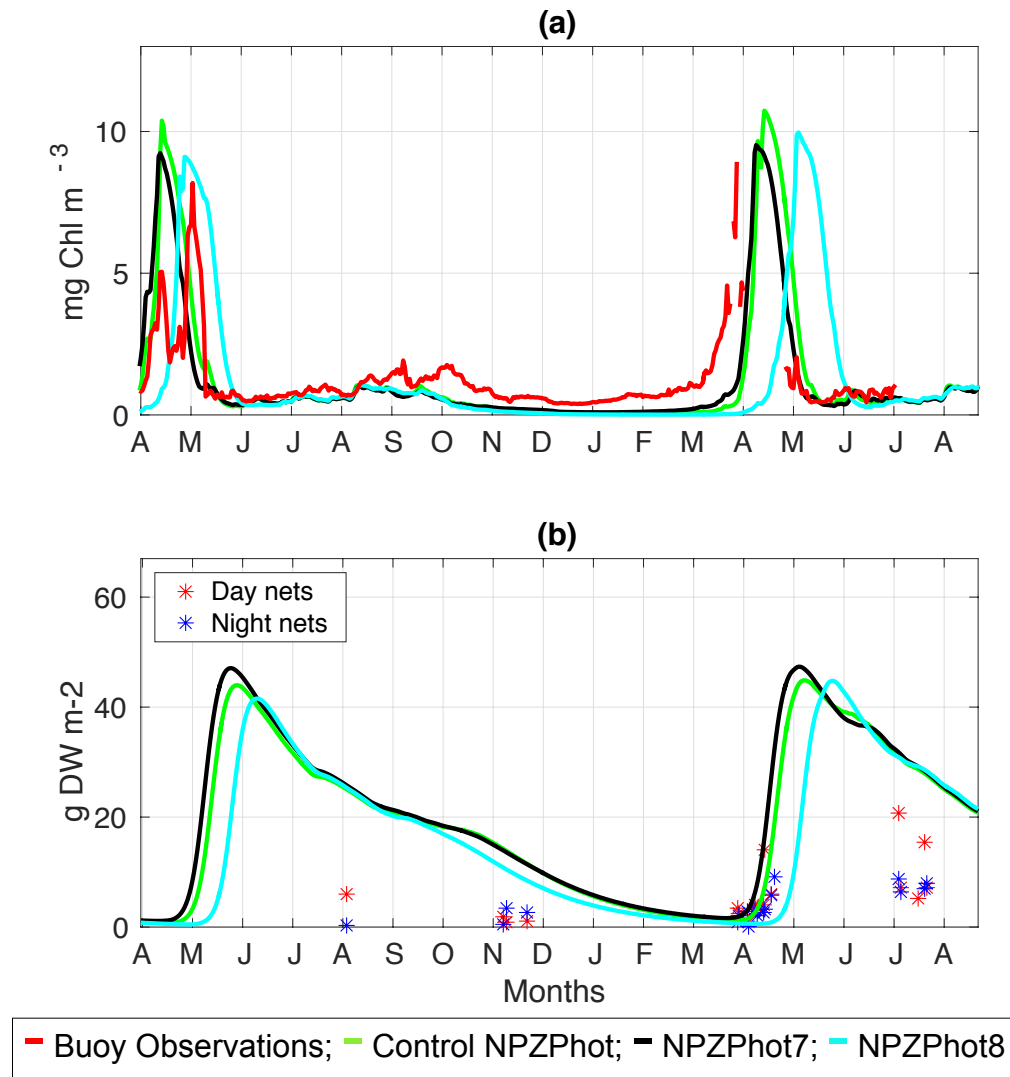


Figure A11: SSB buoy observations (red line) from the start of April 2014 to end of June 2015 compared to the Control NPZPhot (green line), NPZPhot 7 ($R_C = R_{chl} = R_n = 0.01$; black line), and NPZPhot 8 ($R_C = R_{chl} = R_n = 0.03$; cyan line) shown from start of April 2014 to the end of August 2015 for (a) surface chlorophyll-*a* and (b) zooplankton biomass.

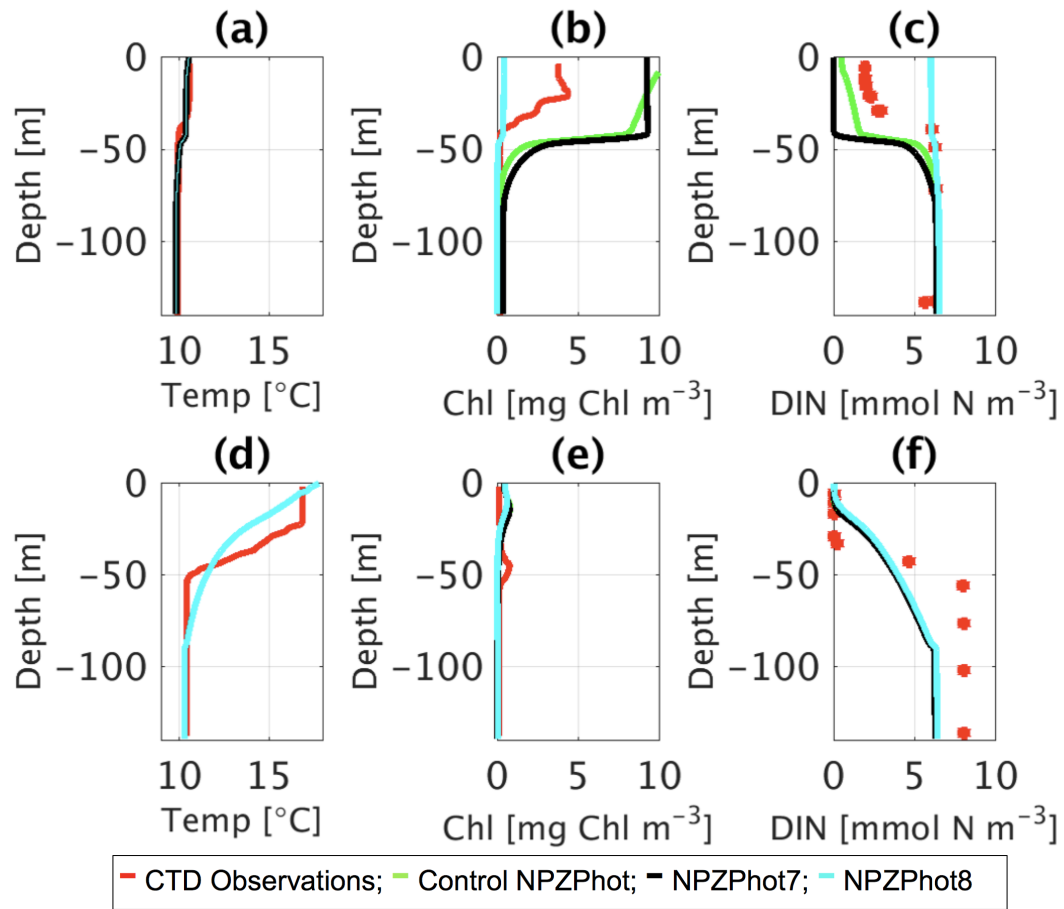


Figure A12: CTD observations from the SSB programme (red line) including data for: springtime (20/04/2015) (a) temperature, (b) chlorophyll-*a*, and (c) DIN; for summer-time (24/07/2015) for (d) temperature, (e) chlorophyll-*a*, and (f) DIN along the Control NPZPhot (green line), NPZPhot 7 ($R_C = R_{chl} = R_n = 0.01$; black line), and NPZPhot 8 ($R_C = R_{chl} = R_n = 0.03$; cyan line).

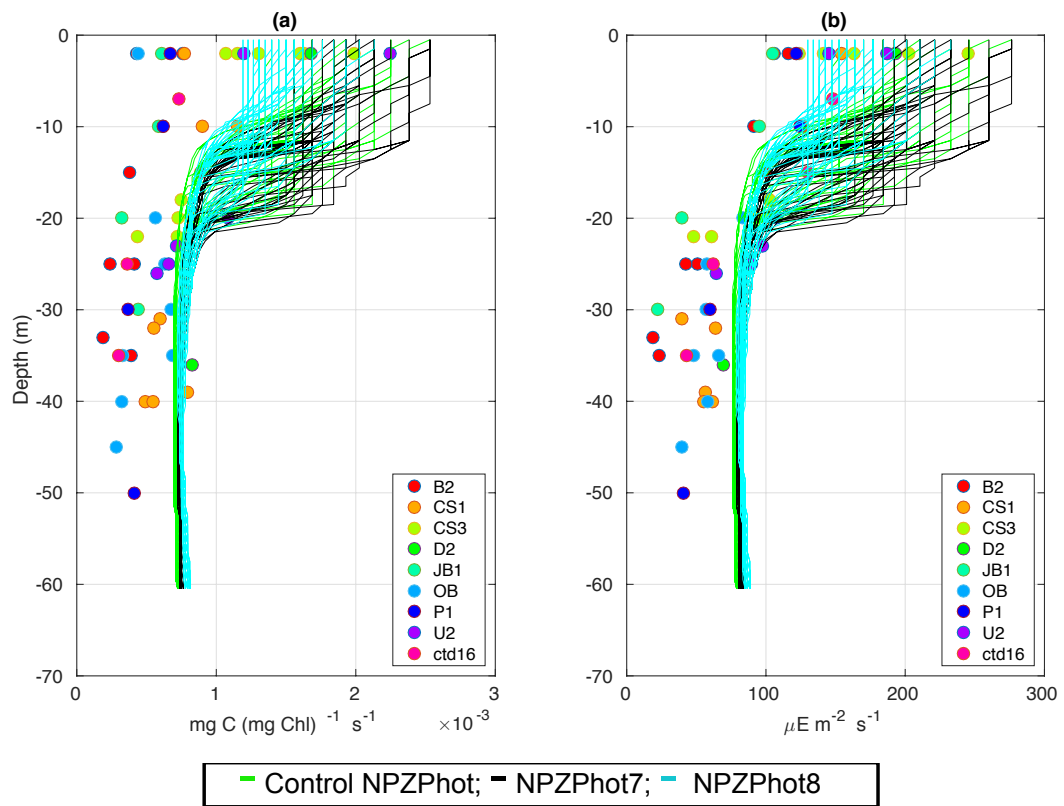


Figure A13: Observations from the cruises CD173 and JR98 in different locations of the Celtic Sea, including Control NPZPhot (green lines), NPZPhot 7 ($R_C = R_{\text{chl}} = R_n = 0.01$; black lines), and NPZPhot 8 ($R_C = R_{\text{chl}} = R_n = 0.03$; cyan lines) for: (a) chlorophyll-*a* specific maximum light-saturated photosynthesis rate (P_{\max}^{Chl}) and (b) light saturation parameter (E_k). The data from the model was plotted for the same days that the observations were collected.

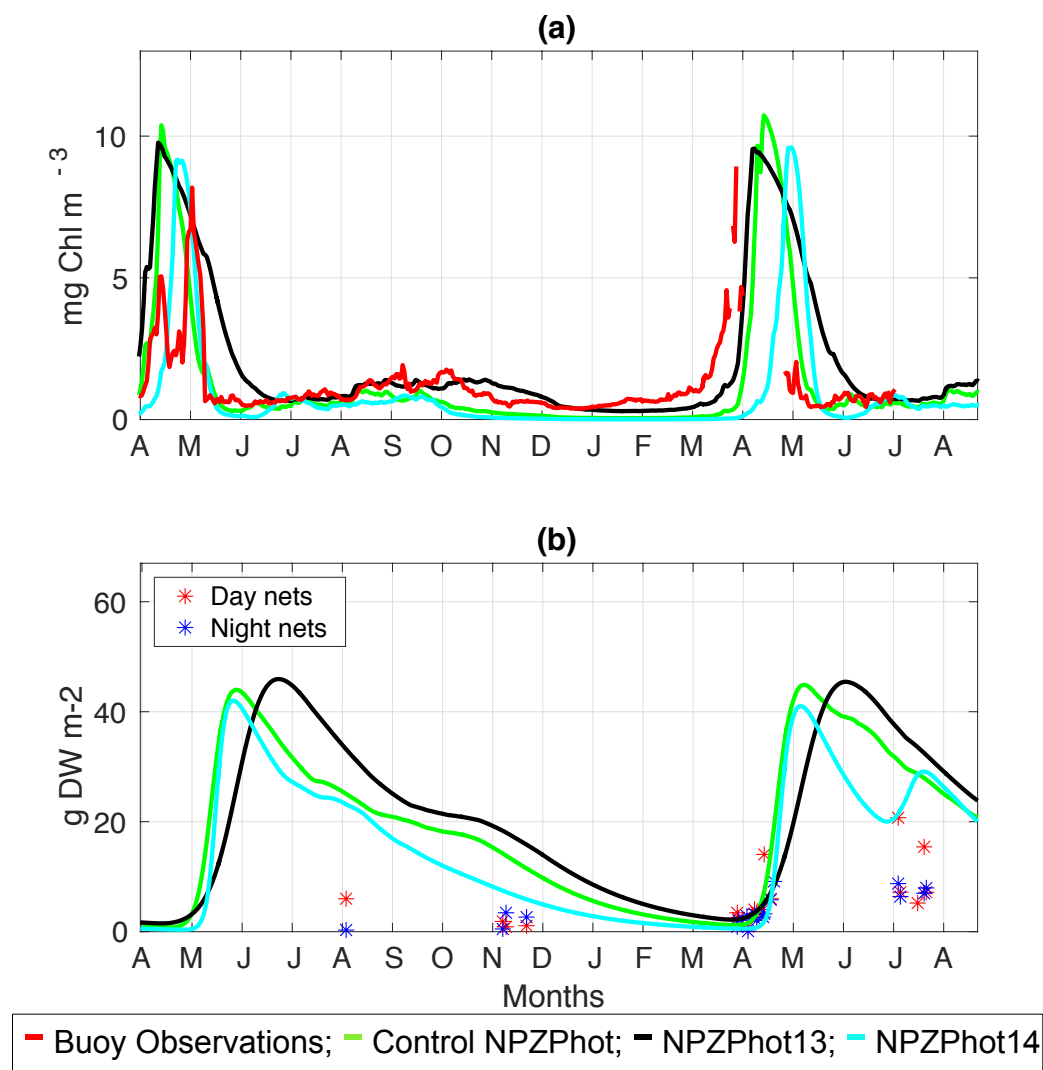


Figure A14: SSB buoy observations (red line) from the start of April 2014 to end of June 2015 compared to the Control NPZPhot (green line), NPZPhot 13 ($\lambda = 0.1$; black line), and NPZPhot 14 ($\lambda = 0.3$; cyan line) shown from start of April 2014 to the end of August 2015 for (a) surface chlorophyll-*a* and (b) zooplankton biomass.

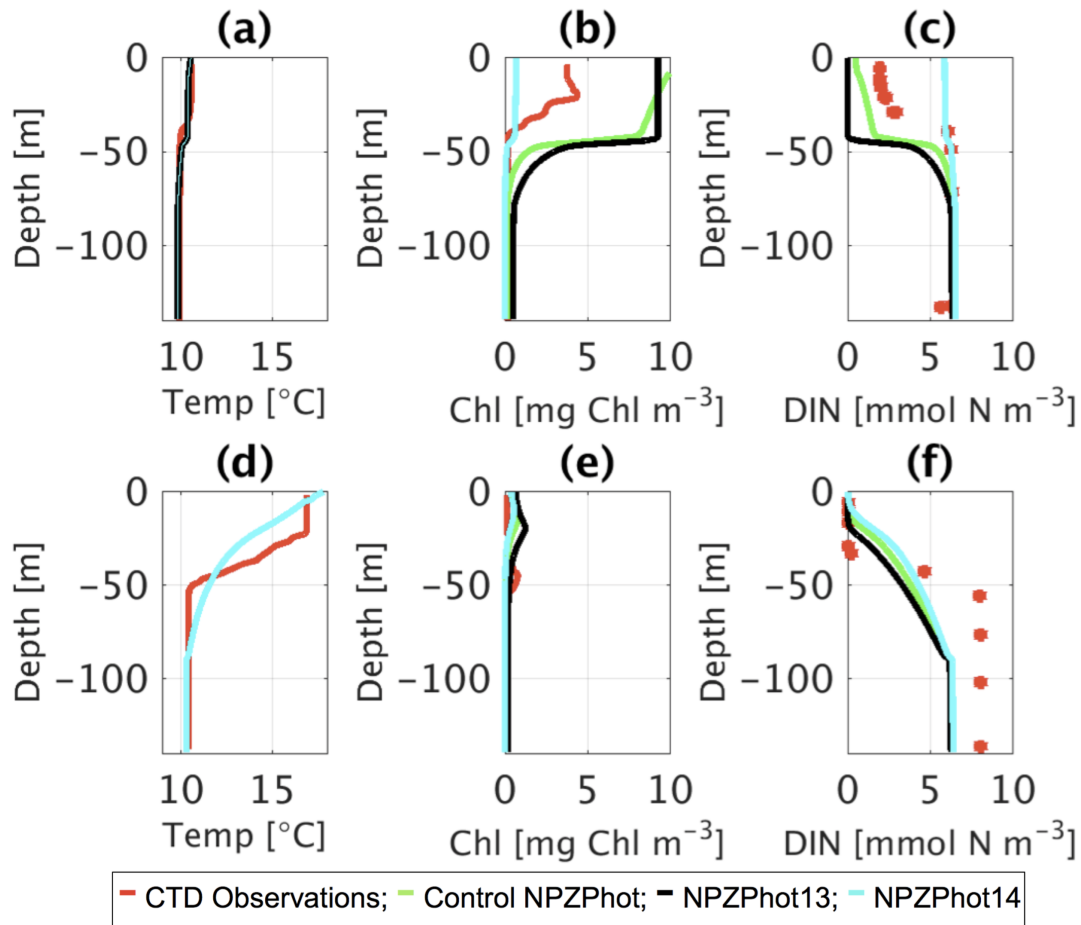


Figure A15: CTD observations from the SSB programme (red line) including data for: springtime (20/04/2015) (a) temperature, (b) chlorophyll-*a*, and (c) DIN; for summertime (24/07/2015) for (d) temperature, (e) chlorophyll-*a*, and (f) DIN along the Control NPZPhot (green line), NPZPhot 13 ($\lambda = 0.1$; black line), and NPZPhot 14 ($\lambda = 0.3$; cyan line).

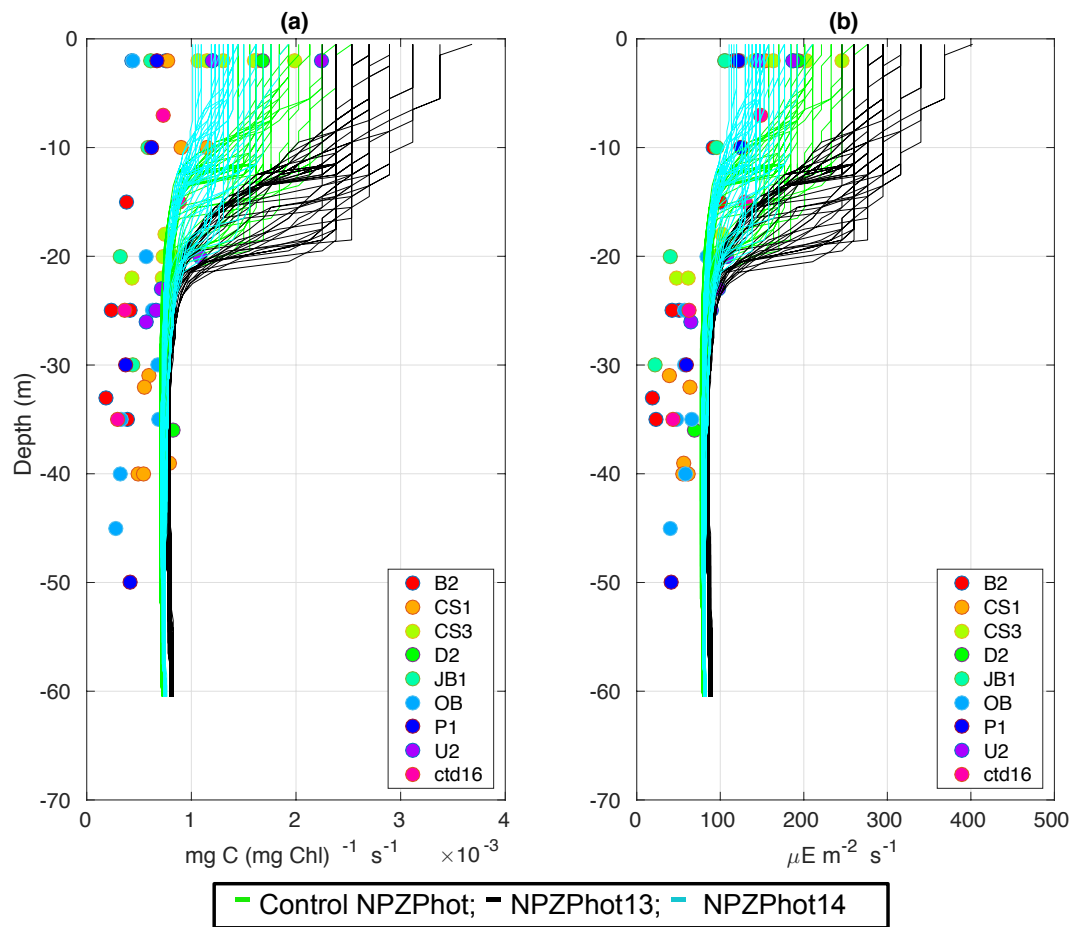


Figure A16: Observations from the cruises CD173 and JR98 in different locations of the Celtic Sea, including Control NPZPhot (green lines), NPZPhot 13 ($\lambda = 0.1$; black lines), and NPZPhot 14 ($\lambda = 0.3$; cyan lines) for: (a) chlorophyll-*a* specific maximum light-saturated photosynthesis rate (P_{\max}^{Chl}) and (b) light saturation parameter (E_k). The data from the model was plotted for the same days that the observations were collected.

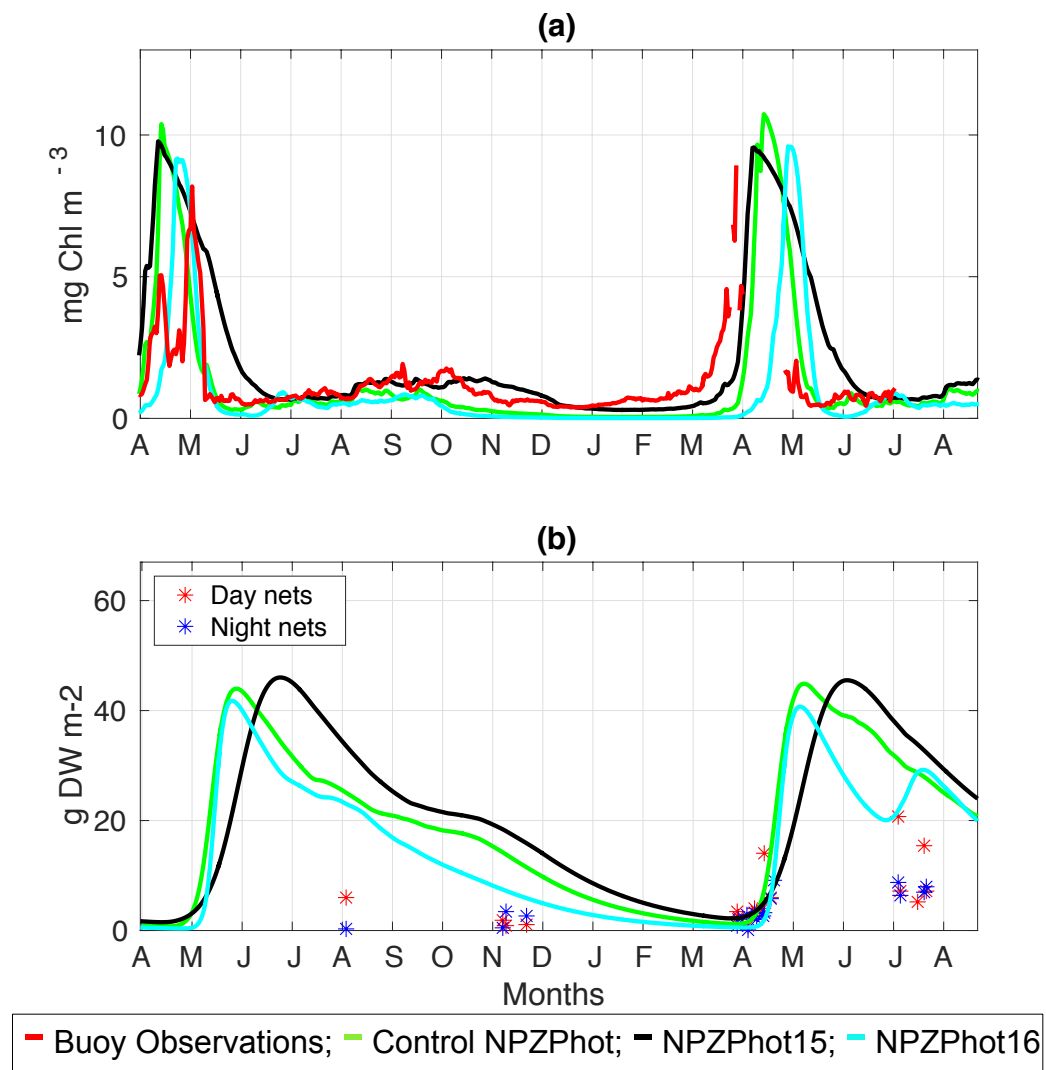


Figure A17: SSB buoy observations (red line) from the start of April 2014 to end of June 2015 compared to the Control NPZPhot (green line), NPZPhot 15 ($R_m = 1.75$; black line), and NPZPhot 16 ($R_m = 5.25$; cyan line) shown from start of April 2014 to the end of August 2015 for (a) surface chlorophyll-*a* and (b) zooplankton biomass.

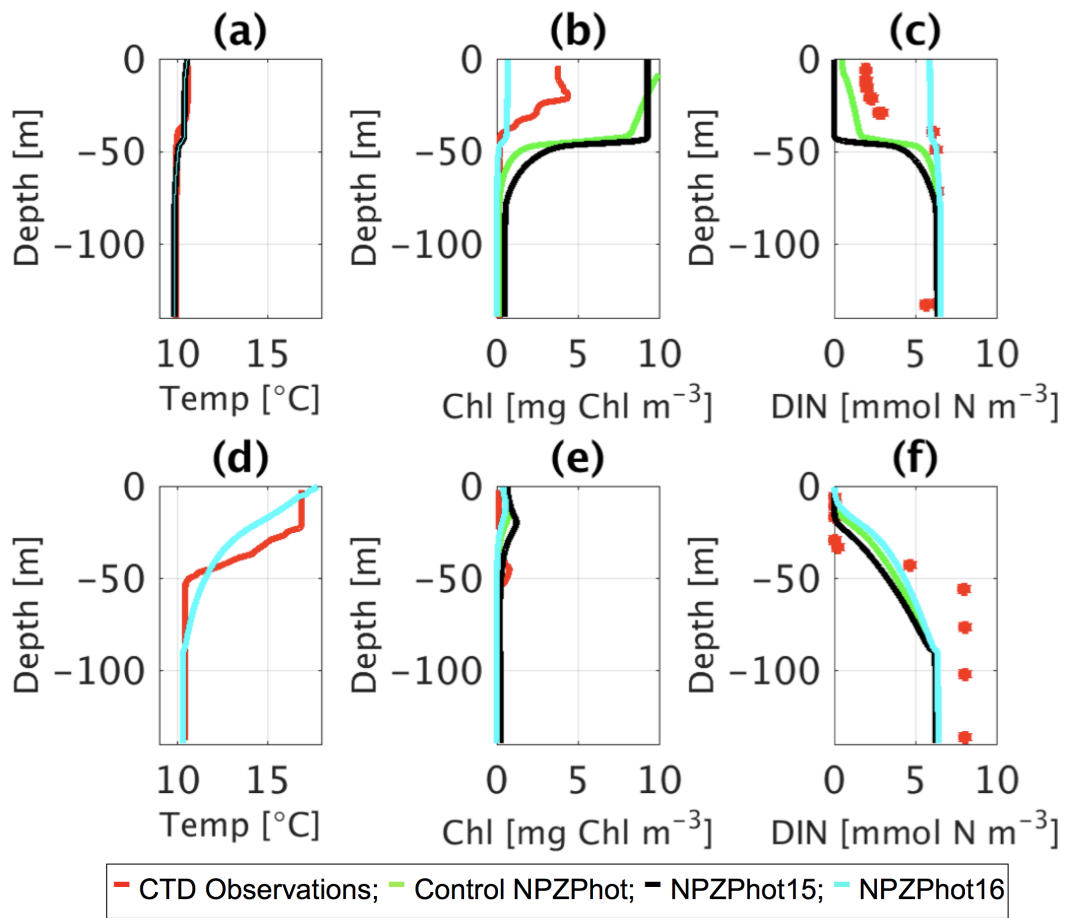


Figure A18: CTD observations from the SSB programme (red line) including data for: springtime (20/04/2015) (a) temperature, (b) chlorophyll-*a*, and (c) DIN; for summertime (24/07/2015) for (d) temperature, (e) chlorophyll-*a*, and (f) DIN along the Control NPZPhot (green line), NPZPhot 15 ($R_m = 1.75$; black line), and NPZPhot 16 ($R_m = 5.25$; cyan line).

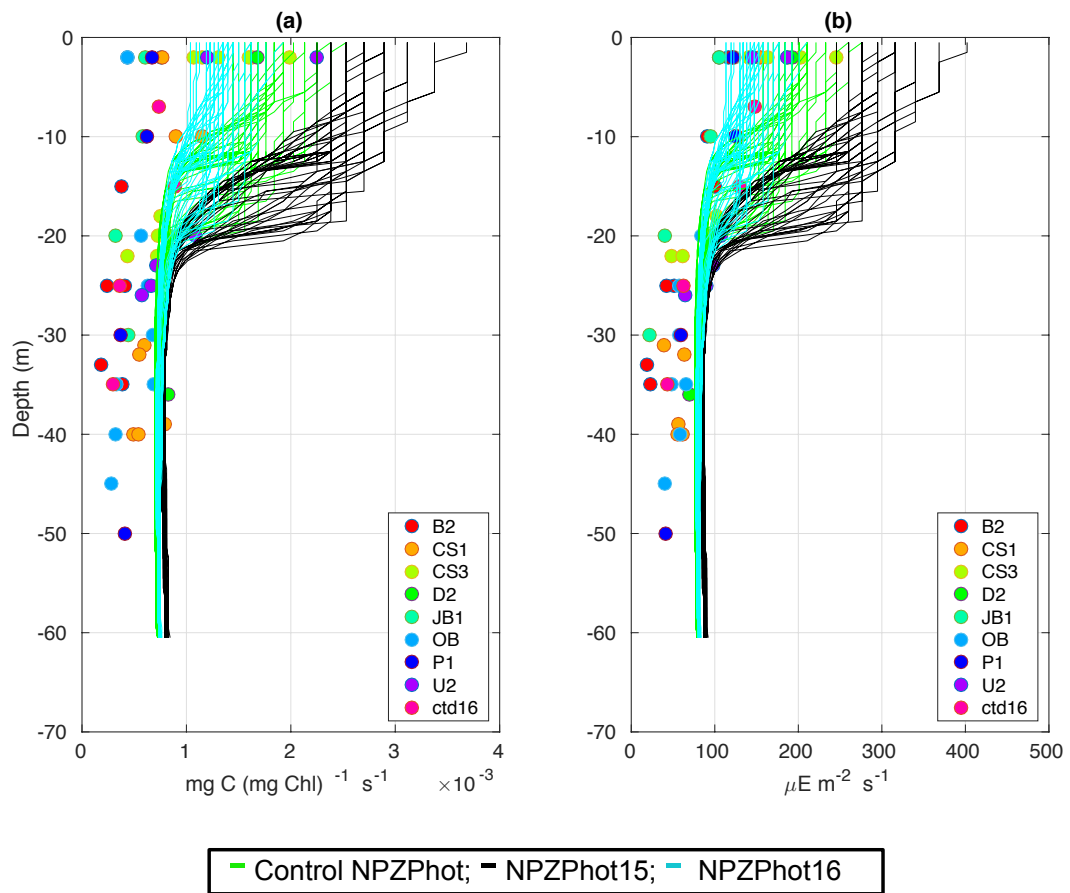


Figure A19: Observations from the cruises CD173 and JR98 in different locations of the Celtic Sea, including Control NPZPhot (green lines), NPZPhot 15 ($R_m = 1.75$; black lines), and NPZPhot 16 ($R_m = 5.25$; cyan lines) for: (a) chlorophyll-*a* specific maximum light-saturated photosynthesis rate (P_{\max}^{Chl}) and (b) light saturation parameter (E_k). The data from the model was plotted for the same days that the observations were collected.

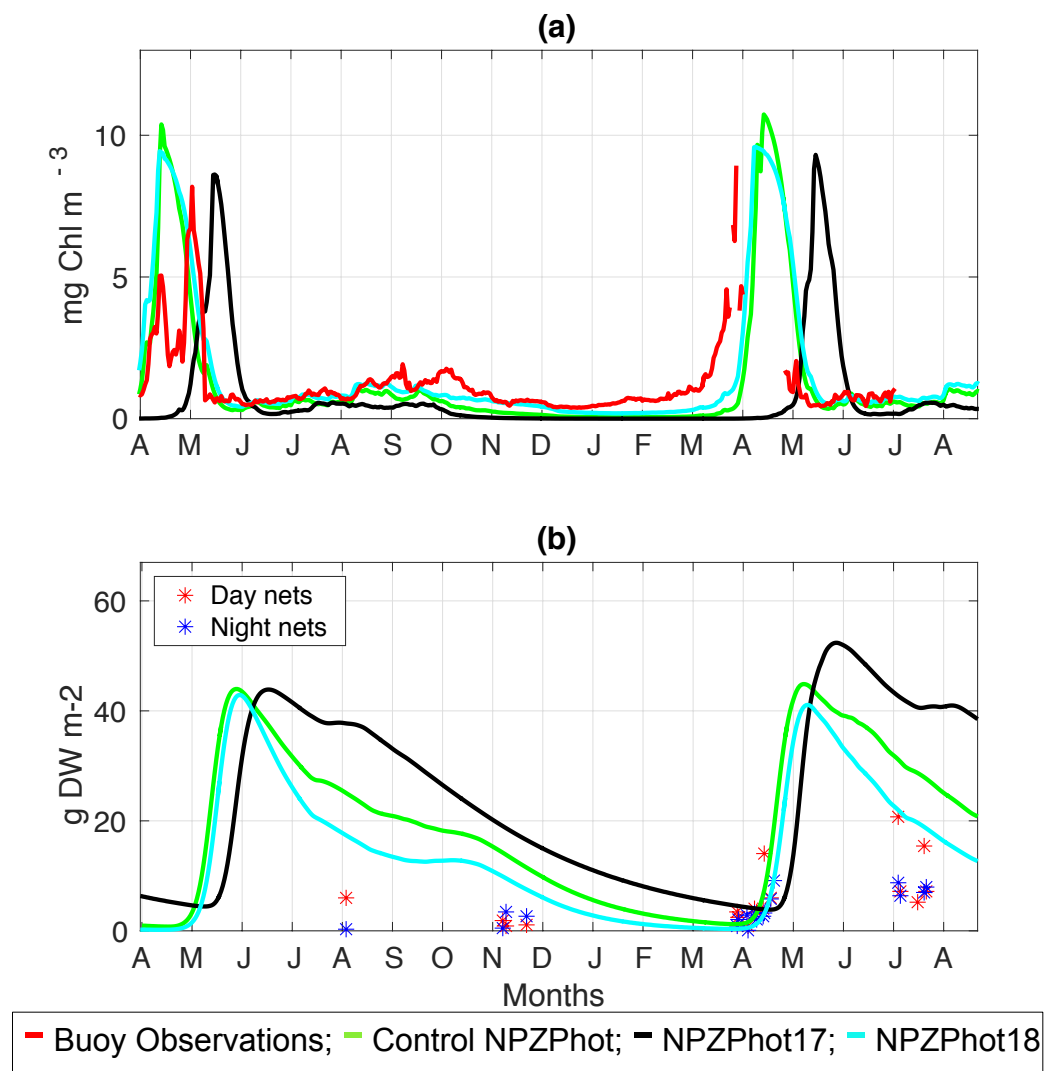


Figure A20: SSB buoy observations (red line) from the start of April 2014 to end of June 2015 compared to the Control NPZPhot (green line), NPZPhot 17 ($m = 0.01$; black line), and NPZPhot 18 ($m = 0.03$; cyan line) shown from start of April 2014 to the end of August 2015 for (a) surface chlorophyll-*a* and (b) zooplankton biomass.

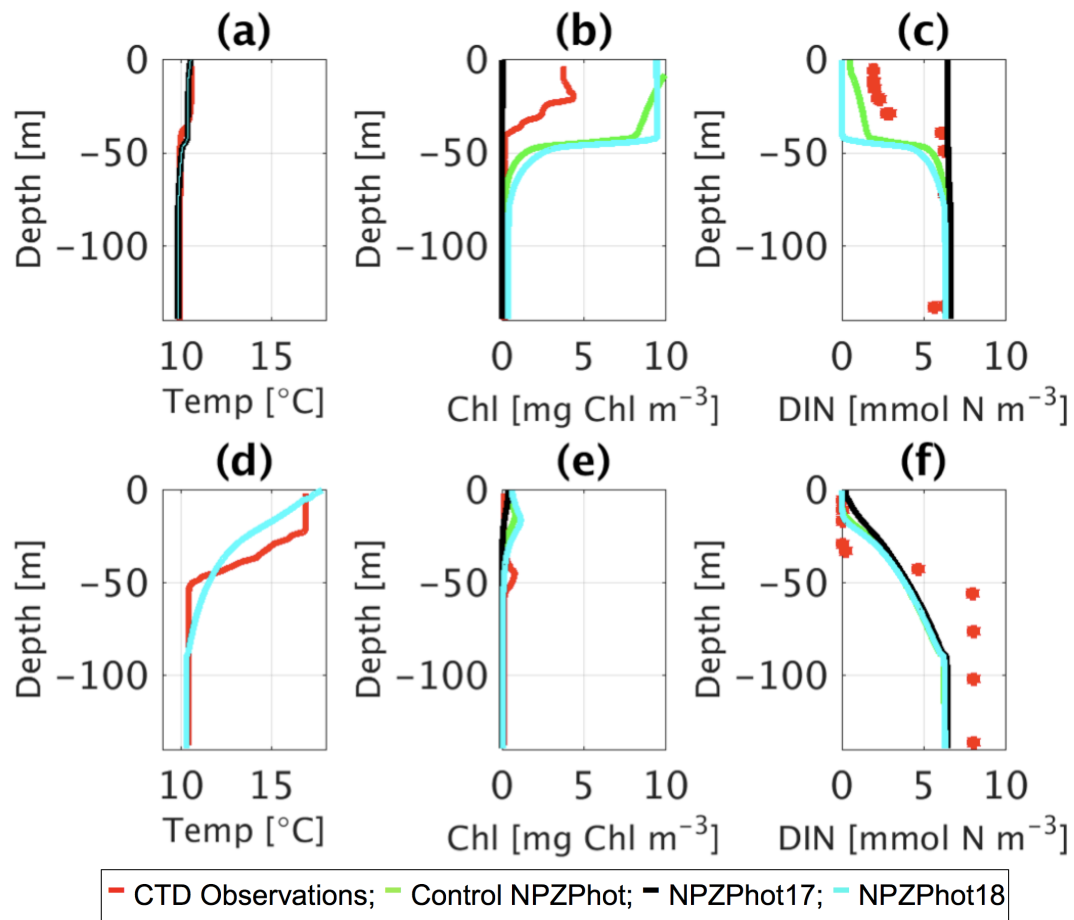


Figure A21: CTD observations from the SSB programme (red line) including data for: springtime (20/04/2015) (a) temperature, (b) chlorophyll-*a*, and (c) DIN; for summertime (24/07/2015) for (d) temperature, (e) chlorophyll-*a*, and (f) DIN along the Control NPZPhot (green line), NPZPhot 17 ($m = 0.01$; black line), and NPZPhot 18 ($m = 0.03$; cyan line).

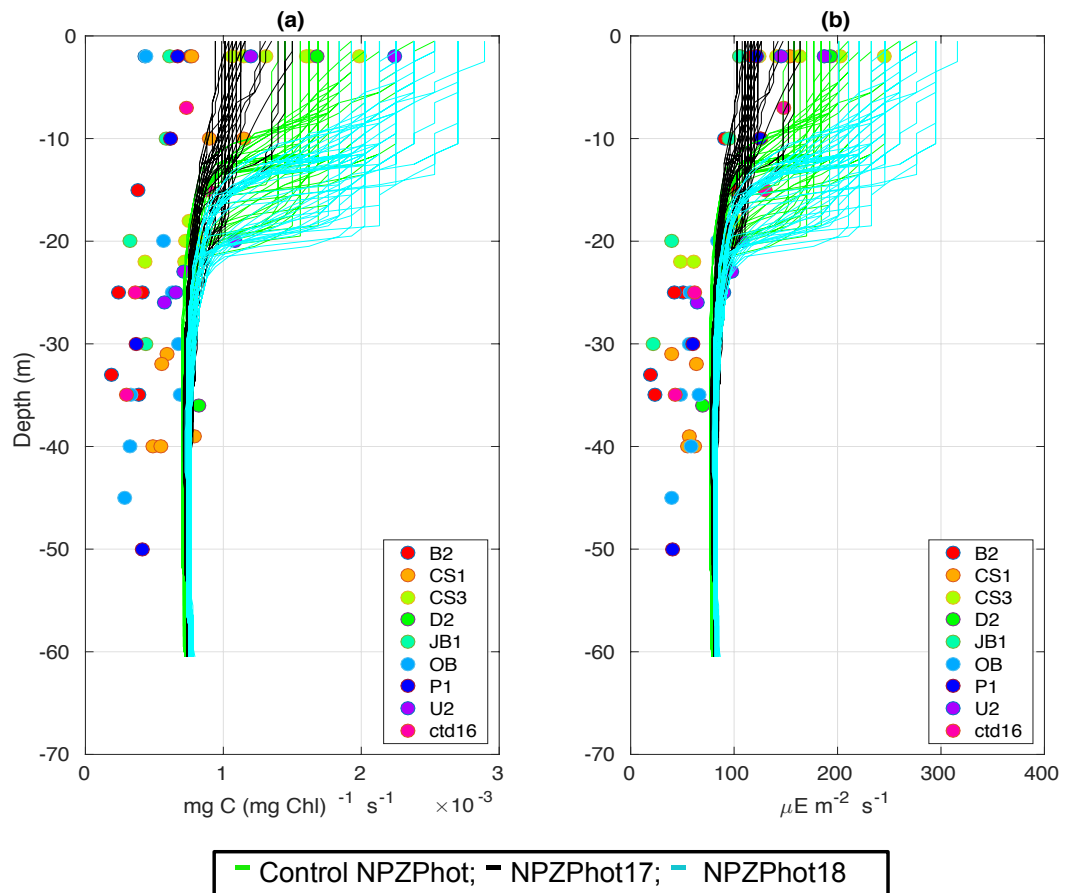


Figure A22: Observations from the cruises CD173 and JR98 in different locations of the Celtic Sea, including Control NPZPhot (green lines), NPZPhot 17 ($m = 0.01$; black lines), and NPZPhot 18 ($m = 0.03$; cyan lines) for: (a) chlorophyll-*a* specific maximum light-saturated photosynthesis rate (P_{\max}^{Chl}) and (b) light saturation parameter (E_k). The data from the model was plotted for the same days that the observations were collected.

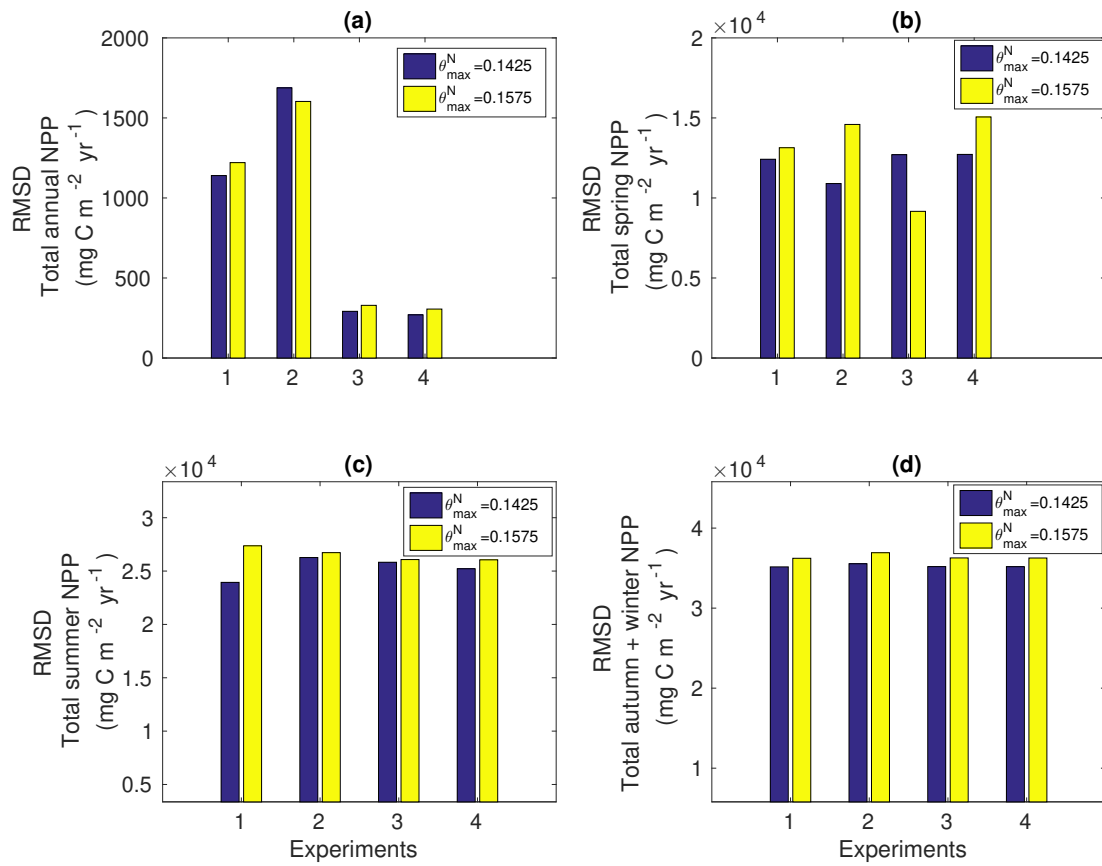


Figure A23: RMSD calculations from the year 1965 to the year 2015 for the control-based experiments with $\theta_{\max}^N = 0.1425$ (blue bars) and $\theta_{\max}^N = 0.1575$ (yellow bars) of (a) total annual NPP ($\text{mg C m}^{-2} \text{ yr}^{-1}$), (b) total spring NPP ($\text{mg C m}^{-2} \text{ yr}^{-1}$), (c) total summer NPP ($\text{mg C m}^{-2} \text{ yr}^{-1}$), and (d) total autumn + winter NPP ($\text{mg C m}^{-2} \text{ yr}^{-1}$).

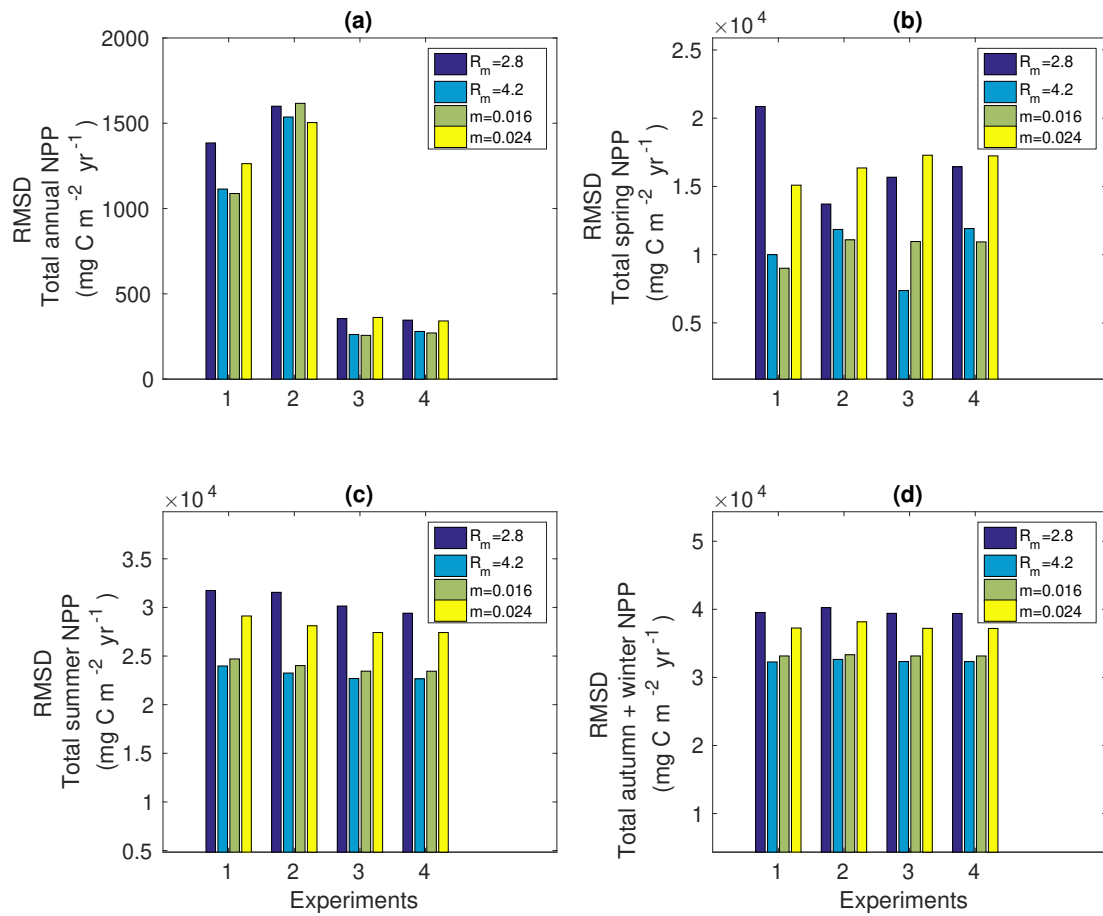


Figure A24: RMSD calculations from the year 1965 to the year 2015 for the control-based experiments with $R_m = 2.8$ (blue bars), $R_m = 4.2$ (turquoise bars), $m = 0.016$ (green bars), and $m = 0.024$ (yellow bars) of (a) total annual NPP ($\text{mg C m}^{-2} \text{ yr}^{-1}$), (b) total spring NPP ($\text{mg C m}^{-2} \text{ yr}^{-1}$), (c) total summer NPP ($\text{mg C m}^{-2} \text{ yr}^{-1}$), and (d) total autumn + winter NPP ($\text{mg C m}^{-2} \text{ yr}^{-1}$).

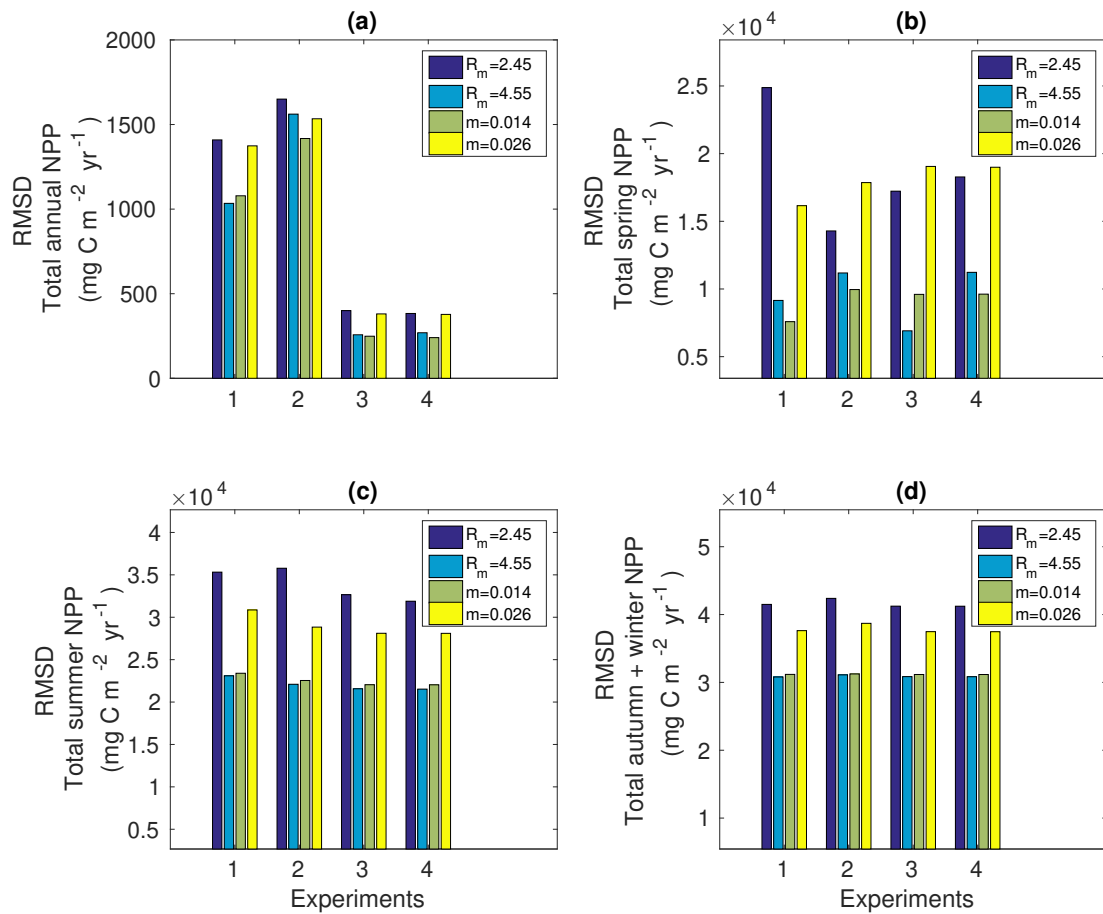


Figure A25: RMSD calculations from the year 1965 to the year 2015 for the control-based experiments with $R_m = 2.45$ (blue bars), $R_m = 4.55$ (turquoise bars), $m = 0.014$ (green bars), and $m = 0.026$ (yellow bars) of (a) total annual NPP ($\text{mg C m}^{-2} \text{ yr}^{-1}$), (b) total spring NPP ($\text{mg C m}^{-2} \text{ yr}^{-1}$), (c) total summer NPP ($\text{mg C m}^{-2} \text{ yr}^{-1}$), and (d) total autumn + winter NPP ($\text{mg C m}^{-2} \text{ yr}^{-1}$).

List of references

Anderson, T. R. (2005), Plankton functional type modelling: running before we can walk?, *Journal of Plankton Research*, 27(11), 1073-1081, <https://doi.org/10.1093/plankt/fbi076>.

Anderson, T. R., Gentleman, W. C., and B. Sinha (2010), Influence of grazing formulations on the emergent properties of a complex ecosystem model in a global ocean general circulation model, *Progress in Oceanography*, 87(1-4), 201-213.

Artioli, Y., Blackford, J. C., Butenschon, M., Holt, J. T., and S. L. Wakelin (2012), The carbonate system in the North Sea: Sensitivity and model validation, *Journal of Marine Systems*, 102-104(0), 1-13.

Ayata, S. D., Lévy, M., Aumont, O., Sciandra, A., Sainte-Marie, J., Tagliabue, A., and O. Bernard (2013), Phytoplankton growth formulation in marine ecosystem models: Should we take into account photo-acclimation and variable stoichiometry in oligotrophic areas?, *Journal of Marine Systems*, 125, 29-40, <https://doi.org/10.1016/j.jmarsys.2012.12.010>.

Bacastow, R. and E. Maier-Reimer (1990), Ocean-circulation model of the carbon cycle, *Climate Dynamics*, 4, 95-125.

Banse, K. (1994), Grazing and zooplankton production as key controls of phytoplankton production in the open ocean, *Oceanography*, 7, 13-20.

Barlow, R., M. Kyewalyanga, H. Sessions, M. van den Berg, and T. Morris (2008), Phyto-

plankton pigments, functional types, and absorption properties in the Delagoa and Natal Bights of the Agulhas ecosystem, *Estuarine, Coastal and Shelf Science*, 80, 201–211.

Barton, A., M. Lozier, and R. Williams (2014). Physical controls of variability in North Atlantic phytoplankton communities. *Limnology and Oceanography*, 60(1), 181–197.

Beaugrand, G. and R. R. Kirby (2010), Climate, plankton and cod, *Global Change Biology*, 16, 1268–1280.

Beaugrand, G., Edwards, M., and L. Legendre (2010), Marine biodiversity, ecosystem functioning, and carbon cycles, *Proceedings of the National Academy of Sciences of the United States of America*, 107, 10120–10124.

Behrenfeld, M. J. (2010), Abandoning Sverdrup’s critical depth hypothesis on phytoplankton blooms, *Ecology*, 91(4), 977– 989.

Behrenfeld, M. J., and E. S. Boss (2014), Resurrecting the ecological underpinnings of ocean plankton blooms, *Annual Review of Marine Science*, 6, 167– 194.

Behrenfeld, M. J., and E. S. Boss (2018), Student’s tutorial on bloom hypotheses in the context of phytoplankton annual cycles, *Global Change Biology*, 24, 55 - 77, <https://doi.org/10.1111/gcb.13858>.

Behrenfeld, M., and P. Falkowski (1997), Photosynthetic rates derived from satellite-based chlorophyll concentration, *Limnology and Oceanography*, 42(1), 1–20.

Behrenfeld, M. J., Doney, S. C., Lima, I., Boss, E. S., and D. A. Siegel (2013), Annual cycles of ecological disturbance and recovery underlying the subarctic Atlantic spring plankton bloom, *Global Biogeochemical Cycles*, 27, 526 - 540, <https://doi.org/10.1002/gbc.20050>.

Behrenfeld, M. J., Westberry, T. K., Boss, E. S., O’Malley, R. T., Siegel, D. A., Wiggert, J. D., Franz, B. A., McClain, C. R., Feldman, G. C., Doney, S. C., Moore, J. K.,

- Dall'Olmo, G., Milligan, A. J., Lima, I., and N. Mahowald (2009), Satellite-detected fluorescence reveals global physiology of ocean phytoplankton, *Biogeosciences*, 6, 779 - 794, <https://www.biogeosciences.net/6/779/2009/>.
- Bernard, O. (2011), Hurdles and challenges for modelling and control of microalgae for CO₂ mitigation and biofuel production, *Journal of Process Control*, 21, 1378-1389.
- Bougaran, G., Bernard, O., and A. Sciandra (2010), Modeling continuous cultures of microalgae colimited by nitrogen and phosphorus, *Journal of Theoretical Biology*, 265, 443-454.
- Bouman, H. A., Platt, T., Doblin, M., Figueiras, F. G., Gudmundsson, K., Gudfinnsson, H. G., Huang, B., Hickman, A., Hiscock, M., Jackson, T., Lutz, V. A., Melin, F., Rey, F., Pepin, P., Segura, V., Tilstone, G. H., Van Dongen-Vogels, V. and S. Sathyendranath (2018), Photosynthesis-irradiance parameters of marine phytoplankton: synthesis of a global data set, *Earth System Science Data*, 10, 251 - 266, <https://doi.org/10.5194/essd-10-251-2018>.
- Bowers, D., and J. Simpson (1987), Mean position of tidal fronts in European Shelf Seas, *Continental Shelf Research*, 7(1), 35-44, [https://doi.org/10.1016/0278-4343\(87\)90062-8](https://doi.org/10.1016/0278-4343(87)90062-8).
- Bozec, Y., H. Thomas, K. Elkalay, and H. de Baar (2005), The continental shelf pump for CO₂ in the North Sea - evidence from summer observation, *Marine Chemistry*, 93(2-4), 131-147, <https://doi.org/10.1016/j.marchem.2004.07.006>.
- Calbet, A. (2008), The trophic roles of microzooplankton in marine systems. *ICES Journal of Marine Science*, 65(3), 325-331, <https://doi.org/10.1093/icesjms/fsn013>.
- Canuto, V., A. Howard, Y. Cheng, and M. Dubovikov (2001), Ocean turbulence. Part I: One-point closure model - Momentum and heat vertical diffusivities, *Journal of Physical Oceanography*, 31(6), 1413-1426, [https://doi.org/10.1175/1520-0485\(2001\)031<1413:OTPIOP>2.0.CO;2](https://doi.org/10.1175/1520-0485(2001)031<1413:OTPIOP>2.0.CO;2).

Canuto, V. A., and M. Dubovikov (1996), A dynamical model for turbulence. I. General formalism, *Physics of Fluids*, 8, 571, <https://doi.org/10.1063/1.868842>.

Carr, M., et al. (2006), A comparison of global estimates of marine primary production from ocean color, *Deep-Sea Research Part II-Topical Studies in Oceanography*, 53(5-7), 741-770, <https://doi.org/10.1016/j.dsr2.2006.01.028>.

Checkley, D. M. (1980), The egg production of a marine planktonic copepod in relation to its food supply: laboratory studies, *Limnology and Oceanography*, 25, 430-466.

Chen, C., H. Liu, and R. Beardsley (2003), An unstructured grid, finite-volume, three-dimensional, primitive equations ocean model: Application to coastal ocean and estuaries, *Journal of Atmospheric and Oceanic Technology*, 20(1), 159-186, [https://doi.org/10.1175/1520-0426\(2003\)020<0159:AUGFVT>2.0.co;2](https://doi.org/10.1175/1520-0426(2003)020<0159:AUGFVT>2.0.co;2).

Chen, F., Shapiro, G., and R. Thain (2013), Sensitivity of Sea Surface Temperature Simulation by an Ocean Model to the Resolution of the Meteorological Forcing, *International Scholarly Research Notices Oceanography*, Volume 2013, Article ID 215715, 12, <http://dx.doi.org/10.5402/2013/215715>.

Chen, B., Zheng, L., Bangqin, H., Song, S., and H. Liu (2013), Seasonal and spatial comparisons of phytoplankton growth and mortality rates due to microzooplankton grazing in the northern South China Sea, *Biogeosciences*, 10, 2775 - 2785.

Cloern, J. E., C. Grenz, and L. Videgar-Lucas (1995), An empirical model of the phytoplankton chlorophyll:carbon ratio - The conversion factor between productivity and growth rate, *Limnology and Oceanography*, 40(7), 1313 - 1321, <https://doi.org/10.4319/lo.1995.40.7.1313>.

Cloern, J. E., S. Q. Foster, and A. E. Kleckner (2014), Phytoplankton primary production in the world's estuarine-coastal ecosystem, *Biogeosciences* 11, 2477-2501.

Colebrook, J. (1979), Continuous plankton records: Seasonal cycles of phytoplankton and copepods in the North-Atlantic ocean and the North-Sea, *Marine Biology*, 51(1), 23-32.

Collins, M., Knutti, R., Arblaster, J., Dufresne, J. L., Fichefet, T., Friedlingstein, P., Gao, X., Gutowski, W. J., Johns, T., Krinner, G., Shongwe, M., Tebaldi, C., Weaver, A. J., and M. Wehner (2013), Long-term Climate Change: Projections, Commitments and Irreversibility. In: *Climate Change 2013: The Physical Science Basis. Contribution of Working Group I to the Fifth Assessment Report of the Intergovernmental Panel on Climate Change* [Stocker, T. F., D. Qin, G. K. Plattner, M. Tignor, S. K. Allen, J. Boschung, A. Nauels, Y. Xia, V. Bex and P. M. Midgley (eds.)], Cambridge University Press, Cambridge, United Kingdom and New York, NY, USA.

Cosper, E. (1982), Influence of light intensity on diel variations in rates of growth, respiration and organic release of a marine diatom: comparison of diurnally constant and fluctuating light, *Journal of Plankton Research*, 4, 705-724.

Costello, J. H., Sullivan, B. K. and D. J. Gifford (2006), A physical-biological interaction underlying variable phenological responses to climate change by coastal zooplankton, *Journal of Plankton Research*, 28(11), 1099 - 1105, <https://doi.org/10.1093/plankt/fb1042>.

Cullen, J. (1982), The Deep Chlorophyll Maximum - Comparing vertical profiles of Chlorophyll-a, *Canadian Journal of Fisheries and Aquatic Sciences*, 39(5), 791-803, <https://doi.org/10.1139/f82-108>.

Cullen, J., C. Carlson, and S. Giovannoni (2015), Subsurface Chlorophyll Maximum Layers: Enduring Enigma or Mystery Solved?, *Annual Review of Marine Science*, Vol 7, 7, 207-239, <https://doi.org/10.1146/annurev-marine-010213-135111>.

Cushing, D. H. (1990), Plankton production and year-class strength in fish populations: an update of the match/mismatch hypothesis, *Advances in Marine Biology*, 26, 250-293.

Davis, C., C. Mahaffey, G. Wolff, and J. Sharples (2014), A storm in a shelf sea: Variation

in phosphorus distribution and organic matter stoichiometry, *Geophysical Research Letters*, 41(23), 8452-8459, <https://doi.org/10.1002/2014GL061949>.

Droop, M. R. (1983), 25 years of algal growth kinetics, *Botanica Marina*, 26, 99-112.

Durbin, E. G., Campbell, R. G., Casas, M. C., Ohman, M. D., Niehoff, B., Runge, J., and M. Wagner (2003) Interannual variation in phytoplankton blooms and zooplankton productivity and abundance in the Gulf of Maine during winter, *Marine Ecology Progress Series*, 254.

Dutkiewicz, S., Hickman, A. E., Jahn, O., Gregg, W. W., Mouw, C. B., and M. J. Follows (2015), Capturing optically important constituents and properties in a marine biogeochemical and ecosystem model, *Biogeosciences*, 12, 4447-4481, <https://doi.org/10.5194/bg-12-4447-2015>.

Edwards, K., R. Barciela, and M. Butenschom (2012), Validation of the NEMO-ERSEM operational ecosystem model for the North West European Continental Shelf, *Ocean Science*, 8(6), 983-1000, <https://doi.org/10.5194/os-8-983-2012>.

Elliott, A., and T. Clarke (1991), Seasonal stratification in the Northwest european shelf seas, *Continental Shelf Research*, 11(5), 467-492.

Eppley, R. W. (1972), Temperature and phytoplankton growth in the sea, *Fishery Bulletin*, 70(4), 1063-1085.

Evans, G. T. and J. S. Parslow (1985), A model of annual plankton cycles, *Journal of Marine Biology and Oceanography*, 3, 327-347.

Everett, J. D., Baird, M. E., Buchanan, P., Bulman, C., Davies, C., Downie, R., Griffiths, C., Heneghan, R., Kloser, R. J., Laiolo, L., Lara-Lopez, A., Lozano-Montes, H., Matear, R. J., McEnnulty, F., Robson, B., Rochester, W., Skerratt, J., Smith, J. A., Strzelecki, J., Suthers, I. M., Swadling, K. M., van Ruth, P., and A. J. Richardson (2017), Modeling what we sample and sampling what we model: challenges for zooplankton model assessment,

Frontiers in Marine Science, 4, <https://doi.org/10.3389/fmars.2017.00077>.

Falkowski P. G. (1980), Light-Shade Adaptation in Marine Phytoplankton, In: Falkowski P. G. (eds) Primary Productivity in the Sea, Environmental Science Research, 19, Springer, Boston, MA.

Falkowski, P. G. (1992), Molecular ecology of phytoplankton photo-synthesis, In Falkowski, P. G. & Woodhead, A. D., Primary Productivity and Biogeochemical Cycles in the Sea, Plenum Press, New York, pp. 47 - 68.

Falkowski, P. G., Dubinsky, Z., and K. Wyman (1985), Growth-irradiance relationships in phytoplankton, *Limnology and Oceanography*, 30, 311-321.

Falkowski, P. G. and J. LaRoche (1991), Acclimation to spectral irradiance in algae, *Journal of Phycology*, 27, 8-14.

Falkowski, P. G., and J. A. Raven (1997), *Aquatic Photosynthesis*, Blackwell Science, UK.

Fasham, M. J. R., Holligan, P. M., and P. R. Pugh (1983), The spatial and temporal development of the spring phytoplankton bloom in the Celtic Sea, *Progress in Oceanography*, 12(1), 87 - 145, [https://doi.org/10.1016/0079-6611\(83\)90007-1](https://doi.org/10.1016/0079-6611(83)90007-1).

Fasham M. J. R., Ducklow, H. W., and S. M. McKelvie (1990), A nitrogen-based model of plankton dynamics in the oceanic mixed layer, *Journal of Marine Research*, 48, 591-639.

Fennel, W. (2001), Modeling of copepods with links to circulation models, *Journal of Plankton Research*, 23(11), 1217 - 1232, <https://doi.org/10.1093/plankt/23.11.1217>.

Fernand, L., K. Weston, T. Morris, N. Greenwood, J. Brown, and T. Jickells (2013), The contribution of the deep chlorophyll maximum to primary production in a seasonally stratified shelf sea, the North Sea, *Biogeochemistry*, 113(1-3), 153-166, <https://doi.org/10.1007/s10533-013-9831-7>.

Field, C., M. Behrenfeld, J. Randerson, and P. Falkowski (1998), Primary production of

the biosphere: Integrating terrestrial and oceanic components, *Science*, 281(5374), 237-240.

Fleming, V., and S. Kaitala (2006), Phytoplankton Spring Bloom Intensity Index for the Baltic Sea Estimated for the years 1992 to 2004, *Hydrobiologia*, 554, 57 - 65.

Flint, L. E. and A. L. Flint (2012), Downscaling future climate scenarios to fine scales for hydrologic and ecological modeling and analysis, *Ecological Process*, 1, <https://doi.org/10.1186/2192-1709-1-2>.

Flynn, K. J. (2008), The importance of the form of the quota curve and control of non-limiting nutrient transport in phytoplankton models, *Journal of Plankton Research*, 30(4), 423-438.

Follows, M. and S. Dutkiewicz (2001), Meteorological modulation of the North Atlantic spring bloom, *Deep Sea Research Part II: Topical Studies in Oceanography*, 49(1-3), 321-344.

Follows, M., Dutkiewicz, S., Grant, S., and S. W. Chisholm (2007), Emergent biogeography of microbial communities in a model ocean, *Science*, 315(5820), 1843-6.

Franks, P. J. S., Wroblewski, J. S., and Frierl, G. R. (1986), Behavior of a simple plankton model with food-level acclimation by herbivores, *Marine Biology*, 91, 121-129.

Franks, P. J. S. (2002), NPZ models of plankton dynamics: their construction, coupling to physics, and application, *Journal of Oceanography*, 58, 379-387.

Friedland, K. D., Leaf, R. T., Kane, J., Tommasi, D., Asch, R. G., Rebuck, N., Ji, R., Large, S. I., Stock, C., and V. S. Saba (2015), Spring bloom dynamics and zooplankton biomass response on the US Northeast Continental Shelf, *Continental Shelf Research*, 102, 47 - 61, <https://doi.org/10.1016/j.csr.2015.04.005>.

Frouin, R. J., Franz, B. A., Ibrahim, A., Knobelspiesse, K., Ahmad, Z., Cairns, B., Chowdhary, J., Dierssen, H. M., Tan, J., Dubovik, O., Huang, X., Davis, A. B., Kalashnikova,

O., Thompson, D. R., Remer, L. A., Boss, E., Coddington, O., Deschamps, P., Gao, B., Gross, L., Hasekamp, O., Omar, A., Pelletier, B., Ramon, D., Steinmetz, F., and P. Zhai (2019), Atmospheric Correction of Satellite Ocean-Color Imagery During the PACE Era, *Frontiers in Earth Science*, 7, 145.

Frost, B. W. (1972), Effects of size and concentration of food particles on the feeding behavior of the marine planktonic copepod *Calanus pacificus*, *Limnology and Oceanography*, 17, 805-815.

Frost, B.W. (1987), Grazing control of phytoplankton stock in the open subarctic Pacific Ocean: a model assessing the role of mesozooplankton, particularly the large calanoid copepods *Neocalanus* spp, *Marine Ecology Progress Series*, 39, 49-68.

Garside, C., and J. Garside (1993), The f-ratio on 20°W during the North-Atlantic bloom experiment, *Deep-Sea Research Part II - Topical Studies in Oceanography*, 40(1-2), 75-90.

Geider, R. J. (1987), Light and temperature dependence of the carbon to chlorophyll a ratio in microalgae and cyanobacteria: implications for physiology and growth of phytoplankton, *New Phytologist*, 106, 1 - 34.

Geider, R. J. (1992), Respiration: Taxation without representation, In: Falkowski P.G., Woodhead A.D., Vivirito K. (eds), *Primary Productivity and Biogeochemical Cycles in the Sea*, Environmental Science Research, 43, Springer, Boston, MA.

Geider, R. J. (1993), Quantitative phytoplankton ecophysiology: implications for primary production and phytoplankton growth, *ICES Marine Science Symposia*, 197: 52-62.

Geider, R. J., and H. L. MacIntyre (1996), A dynamic model of photoadaptation in phytoplankton, *Limnology and Oceanography*, 41(1), 1-15.

Geider, R. J., MacIntyre, H. L., and T. M. Kana (1997), A dynamic model of phytoplankton growth and acclimation: Responses of the balanced growth rate and chlorophyll a:carbon ration to light, nutrient-limitation and temperature, *Marine Ecology Progress*

Series, 148, 187-200.

Geider, R. J., MacIntyre, H. L., and T. M. Kana (1998), A dynamic regulatory model of phytoplanktonic acclimation to light, nutrients, and temperature, *Limnology and Oceanography*, 43(4), 679-694.

Giering, S. L. C, et al. (2018), Seasonal variation of zooplankton community structure and trophic position in the Celtic Sea: A stable isotope and biovolume spectrum approach, *Progress in Oceanography*, <https://doi.org/10.1016/j.pocean.2018.03.012>.

Gill, A. E. (1982), *Atmosphere-Ocean Dynamics*, International Geophysics Series, 30, Academic Press, London.

Goffart, A., Hecq, J. H., and L. Legendre (2015), Drivers of the winter-spring phytoplankton bloom in a pristine NW Mediterranean site, the Bay of Calvi (Corsica): A long-term study (1979-2011), *Progress in Oceanography*, 137, 121-139, <https://doi.org/10.1016/j.pocean.2015.05.027>.

Gomez-Gesteira, M., deCastro, M., Alvarez, I., and J. L. Gomez-Gesteira (2008), Coastal sea surface temperature warming trend along the continental part of the Atlantic Arc (1985 - 2005), *Journal of Geophysical Research*, 113.

González, H. E., Daneri, G., Iriarte, J. L., Yannicelli, B., Menschel, E., Barria, C., Pantoja, S., and L. Lizzáraga (2009), Carbon fluxes within the epipelagic zone of the Humboldt Current system of Chile: the significance of euphausiids and diatoms as key functional groups for the biological pump, *Progress in Oceanography*, 83, 217-227.

Gorsky, G., Ohman, M. D., Picheral, M., Gasparini, S., Stemmann, L., Romagnan, J. B., Cawood, A., Pesant, S., Garcia-Comas, C., and F. Prejger (2010), Digital zooplankton image analysis using the ZooScan integrated system, *Journal of Plankton Research*, 32, 285-303, <http://dx.doi.org/10.1093/plankt/fbp124>.

Greve, W., Prinage, S., Zidowitz, H., Nast, J., and F. Reiners (2005), On the phenology

of North Sea ichthyoplankton, *ICES Journal of Marine Science*, 62, 1216 - 1223.

Groger, M., Maier-Reimer, E., Mikolajewicz, U., Moll, A., and D. Sein (2013), NW European shelf under climate warming: implications for open ocean; shelf exchange, primary production, and carbon absorption, *Biogeosciences*, 10, 3767 - 3792.

Groom, S., Martinez-Vicente, V., Fishwick, J., Tilstone, G., Moore, G., Smyth, T., and D. Harbour (2009), The Western English Channel Observatory: optical characteristics of station L4, *Journal of Marine Systems*, 77, 278 - 295, 2009.

Hardman-Mountford, N. J., Allen, J. I., Frost, M. T., Hawkins, S. J., Kendall, M. A., Mieszkowska, N., Richardson, K., A., and P. J. Somerfield (2005), Diagnostic monitoring of a changing environment: An alternative UK perspective, *Marine Pollution Bulletin*, 50(12), 1463 - 1471, <https://doi.org/10.1016/j.marpolbul.2005.06.022>.

Heath, M. R. and D. J. Beare (2008), New primary production in northwest European shelf seas, 1960-2003, *Marine Ecology Progress Series*, 363, 183-203, <https://doi.org/10.3354/meps07460>.

Henson, S., J. Dunne, and J. Sarmiento (2009), Decadal variability in North Atlantic phytoplankton blooms, *Journal of Geophysical Research-Oceans*, 114, <https://doi.org/10.1029/2008JC005139>.

Hickman, A., Holligan, M., Moore, C. M., Sharples, J., Krivtsov, V., and M. R. Palmer (2009), Distribution and chromatic adaptation of phytoplankton within a shelf sea thermocline, *Limnology and Oceanography*, 54(2), 525-536.

Hickman, A., C. Moore, J. Sharples, M. Lucas, G. Tilstone, V. Krivtsov, and P. Holligan (2012), Primary production and nitrate uptake within the seasonal thermocline of a stratified shelf sea, *Marine Ecology Progress Series*, 463, 39-57.

Hlaili, A. S., Niquil, N., and L. Legendre (2014), Planktonic food webs revisited: Reanalysis of results from the linear inverse approach, *Progress in Oceanography*, 120, 216 - 229,

<https://doi.org/10.1016/j.pocean.2013.09.003>.

Holligan, P. M. et al. (1984a), Vertical distribution and partitioning of organic carbon in mixed, frontal and stratified waters of the English Channel, *Marine Ecology Progress Series*, 14, 111 - 127.

Holligan, P. M., Williams, P. J. L., Purdie, D., and R. P. Harris (1984b), Photosynthesis, respiration and nitrogen supply of plankton populations in stratified, frontal and tidally mixed shelf waters, *Marine Ecology Progress Series*, 17, 201 - 213.

Holling, C. S. (1959), Some characteristics of simple types of predation and parasitism, *The Canadian Entomologist*, 7.

Holt, J., Butenschon, M., Wakelin, S. L., Artioli, Y., and J. I. Allen (2012), Oceanic controls on the primary production of the northwest European continental shelf: model experiments under recent past conditions and a potential future scenario, *Biogeosciences*, 9, 97 - 117.

Holt, J., and R. Proctor (2008), The seasonal circulation and volume transport on the northwest European continental shelf: A fine-resolution model study, *Journal of Geophysical Research-Oceans*, 113(C6), <https://doi.org/10.1029/2006JC004034>.

Holt, J., S. Wakelin, and J. Huthnance (2009), Down-welling circulation of the northwest European continental shelf: A driving mechanism for the continental shelf carbon pump, *Geophysical Research Letters*, 36, <https://doi.org/10.1029/2009GL038997>.

Holt, J., Wakelin, S., Lowe, J., and J. Tinker (2010), The potential impacts of climate change on the hydrography of the northwest European continental shelf, *Progress in Oceanography*, 86, 361 - 379.

Holt, J., Butenschon, M., Wakelin, S. L., Artioli, Y., and J. I. Allen (2012), Oceanic controls on the primary production of the northwest European continental shelf: model experiments under recent past conditions and a potential future scenario, *Biogeosciences*,

9, 97-117, <https://doi.org/10.5194/bg-9-97-2012>.

Holt, J., et al. (2017), Prospects for improving the representation of coastal and shelf seas in global ocean models, *Geoscientific Model Development*, 10(1), 499-523, <https://doi.org/10.5194/gmd-10-499-2017>.

Hu, S., Chen, C., Ji, R., Townsend, D., Tian, R., Beardsley, R., and C. Davis (2011), Effects of Surface Forcing on Interannual Variability of the Fall Phytoplankton Bloom in the Gulf of Maine Revealed Using a Process-Oriented Model, *Marine Ecology Progress Series*, 427.

Hughes, S., Holliday, N., Beszczynska-Moeller, A., and I. Yashayaev (2010), ICES Report on Ocean Climate 2009.

Hull et al. (2017), Shelf Sea Biogeochemistry - CaNDyFLoSS SmartBuoy, Cefas, UK, V1, <https://doi.org/10.14466/CefasDataHub.37>.

Humphreys, M. and C. M. Moore (2015), Cruise Report (Shelf Sea Biogeochemistry): RRS Discovery Cruise DY033, 11 July - 3 August 2015, University of Southampton, (181 pp).

Hyde, K., J. O'Reilly, and C. Oviatt (2007), Validation of SeaWiFS chlorophyll a in Massachusetts Bay, *Continental Shelf Research*, 27(12), 1677-1691, <https://doi.org/10.1016/j.csr.2007.02.002>.

Hydes, D. J., Gowen, R. J., Holliday, N., Shammon, T., and D. Mills (2004), External and internal control of winter concentrations of nutrients (N, P and Si) in north-west European shelf seas, *Estuarine Coastal and Shelf Science*, 59, 151 - 161.

Irigoiien, X., Huisman, J. and R. P. Harris (2004), Global biodiversity patterns of marine phytoplankton and zooplankton, *Nature*, 429, 863-867.

Irigoiien, X., Flynn, K. J., and R. P. Harris (2005), Phytoplankton blooms: a 'loop-hole' in microzooplankton grazing impact?, *Journal of Plankton Research*, 27(4), 313-321,

<https://doi.org/10.1093/plankt/fbi011>.

Jassby, A. D. and T. Platt (1976), Mathematical formulation of the relationship between photosynthesis and light for phytoplankton, *Limnology and Oceanography*, 21, 540-547.

Joint, I., and A. Pomroy (1993), Phytoplankton biomass and production in the Southern North Sea, *Marine Ecology Progress Series*, 99(1-2), 169-182, <https://doi.org/10.3354/meps099169>.

Joint, I., and S. Groom (2000), Estimation of phytoplankton production from space: current status and future potential of satellite remote sensing, *Journal of Experimental Marine Biology and Ecology*, 250(1-2), 233-255, [https://doi.org/10.1016/S0022-0981\(00\)00199-4](https://doi.org/10.1016/S0022-0981(00)00199-4).

Joint, I., Owens, N., Pomroy, A., and A. Pomeroy (1986), Seasonal production of photosynthetic picoplankton and nanoplankton in the Celtic Sea, *Marine Ecology Progress Series*, 28(3), 251 - 258.

Joint, I., Wollast, R., Chou, L., Batten, S., Elskens, M., Edwards, E., Hirst, A., Burkill, P., Groom, S., Gibb, S., Miller, A., Hydes, D., Dehairs, F., Antia, A., Barlow, R., Rees, A., Pomroy, A., Brockmann, U., Cummings, D., Lampitt, R., Loijens, M., Mantoura, F., Miller, P., Raabe, T., Alvarez-Salgado, X., Stelfox, C., and J. Woolfenden (2001), Pelagic production at the Celtic Sea shelf break, *Deep Sea Research Part II: Topical Studies in Oceanography*, 48(14 - 15), 3049 - 3081, [https://doi.org/10.1016/S0967-0645\(01\)00032-7](https://doi.org/10.1016/S0967-0645(01)00032-7).

Juul-Pedersen, T., Michel, C., and M. Gosselin (2010), Sinking export of particular to organic material from the euphotic zone in the eastern Beaufort Sea, *Marine Ecology Progress Series*, 410, 55-70.

Kanda, J., D. A. Ziemann, L. D. Conquest and P. K. Bienfang (1989), Light-dependency of nitrate uptake by phytoplankton over the spring bloom in Auke Bay, Alaska, *Marine Biology*, 103, 563-569, <https://doi.org/10.1007/BF00399589>.

- Kasai, H., H. Saito, A. Yoshimori, and S. Taguchi (1997), Variability in timing and magnitude of spring bloom in the Oyashio region, the western subarctic Pacific off Hokkaido, Japan, *Fisheries Oceanography*, 6(2), 118-129, <https://doi.org/10.1046/j.1365-2419.1997.00034.x>.
- Kirk, J.T.O. (1994), *Light and Photosynthesis in Aquatic Ecosystems*, Cambridge University Press, Cambridge.
- Kiørboe, T., Tiselius, P., Mitchell-Innes, B., Hansen, J. L. S., Visser, A. W., and X. Mari (1998), Intensive aggregate formation with low vertical flux during an upwelling-induced diatom bloom, *Limnology and Oceanography*, 43(1), 104-116.
- Knight, P. J., and M. J. Howarth (1999), The flow through the north channel of the Irish Sea, *Continental Shelf Research*, 19(5), 693 - 716, [https://doi.org/10.1016/S0278-4343\(98\)00110-1](https://doi.org/10.1016/S0278-4343(98)00110-1).
- Klausmeier, C., Litchman, E., and S. Levin (2004), Phytoplankton growth and stoichiometry under multiple nutrient limitation, *Limnology and Oceanography*, 49, 1463-1470.
- Kobayashi, S., J. Simpson, T. Fujiwara, and K. Horsburgh (2006), Tidal stirring and its impact on water column stability and property distributions in a semi-enclosed shelf sea (Seto Inland Sea, Japan), *Continental Shelf Research*, 26(11), 1295-1306, <https://doi.org/10.1016/j.csr.2006.04.006>.
- Koeve, W. (2001), Wintertime nutrients in the North Atlantic - New approaches and implications for estimates of seasonal new production, *Marine Chemistry*, 74, 245 - 260, <http://oceanrep.geomar.de/8513/>.
- Lacroix, G. and P. Nival (1996), Modelling the interannual variability of the primary production in Mediterranean waters, *Progress in Belgian Oceanographic Research*, Royal Academy of Belgium, Brussels, 119 - 122.

- Lacroix, G. and P. Nival (1998), Influence of meteorological variability on primary production dynamics in the Ligurian Sea (NW Mediterranean Sea) with a 1D hydrodynamic/biological model, *Journal of Marine Systems*, 16(1 - 2), 23 - 50, [https://doi.org/10.1016/S0924-7963\(97\)00098-5](https://doi.org/10.1016/S0924-7963(97)00098-5).
- Langdon, C. (1988), On the causes of interspecific differences in the growth-irradiance relationship for phytoplankton. A comparative study of the growth-irradiance relationship of three marine phytoplankton species: *Skeletonema costatum*, *Olisthodiscus luteus* and *Gonyaulax tamarensis*, *Journal of Plankton Research*, 10, 1291-1312.
- Lee, D. B., Song, H. Y., Park, C. and K. H. Choi (2012), Copepod feeding in a coastal area of active tidal mixing: diel and monthly variations of grazing impacts on phytoplankton biomass, *Marine Ecology*, 33, 88-105, <https://doi.org/10.1111/j.1439-0485.2011.00453.x>.
- Legendre, L. and R. B. Rivkin (2002), Fluxes of carbon in the upper ocean: regulation by food-web control nodes, *Marine Ecology Progress Series*, 242, 95-109.
- Le Quéré, C., Harrison, S. P., Prentice, I. C., Buitenhuis, E. T., Aumont, O., Bopp, L., Claustre, H., Cotrim da Cunha, L., Geider, R., Giraud, X., Klaas, C., Kohfeld, K. E., Legendre, L., Manizza, M., Platt, T., Rivkin, R. B., Sathyendranath, S., Uitz, J., Watson, A. J. and D. Wolf-Gladrow (2005), Ecosystem dynamics based on plankton functional types for global ocean biogeochemistry models, *Global Change Biology*, 11, 2016-2040.
- Levin, S. A. and J. Lubchenco (2008), Resilience, robustness, and marine ecosystem-based management, *BioScience*, 58, 27-32.
- Lewis, M. R. and J. C. Smith (1983), A small volume, short-incubation-time method for measurement of photosynthesis as a function of incident irradiance, *Marine Ecology Progress Series*, 13, 99-102.
- Lilliefors, H. W. (1967), On the Kolmogorov-Smirnov Test for Normality with Mean and Variance Unknown. *Journal of American Statistical Association*, 62(318), 99-402,

<http://dx.doi.org/10.2307/2283970>.

Liu, K., L. Atkinson, R. Quiñones, and L. Talaue-McManus (2010), Biogeochemistry of continental margins in a global context, Carbon and Nutrient Fluxes in Continental Margins, 3-24, The IGBP Series. Springer, Berlin, Heidelberg.

Loder, J. W., and T. Platt (1985), Physical controls on phytoplankton production at tidal fronts, paper presented at Proceedings of the 19th European Marine Biology Symposium, Cambridge University Press.

Longhurst, A. (1995), Seasonal cycles of pelagic production and consumption, Progress in Oceanography, 36(2), 77 - 167, [https://doi.org/10.1016/0079-6611\(95\)00015-1](https://doi.org/10.1016/0079-6611(95)00015-1).

Longhurst, A., S. Sathyendranath, T. Platt, and C. Caverhill (1995), An estimate of global primary production in the ocean from satellite radiometer data, Journal of Plankton Research, 17(6), 1245-1271, <https://doi.org/10.1093/plankt/17.6.1245>.

Lotka A. J. (1932), The growth of mixed populations: Two species competing for a common food supply, Journal of the Washington Academy of Sciences, 22(16), 461 - 469.

MacIntyre, H. L., Kanna, T. M., Anning, T., and R. Geider (2002), Photoacclimation of photosynthesis irradiance response curves and photosynthetic pigments in microalgae and cyanobacteria, Journal of Phycology, 38, 17-38.

Mairet, F., Bernard, O., Masci, P., Lacour, T. and A. Sciandra (2011), Modelling neutral lipid production by the microalga *Isochrysis aff. galbana* under nitrogen limitation, Biore-source Technology, 102, 142-149.

Marañón, E., Cermeño, P., and V. Pérez (2005), Continuity in the photosynthetic production of dissolved organic carbon from eutrophic to oligotrophic waters, Marine Ecology Progress Series, 299(7), 7-17.

Margalef, R. (1968), Perspectives in ecological theory, Limnology and Oceanography, 14(2),

313-315, <https://doi.org/10.4319/lo.1969.14.2.0313>.

Marquis, E., Niquil, N., Vezina, A. F., Petitgas, P., and C. Dupuy (2011), Influence of planktonic foodweb structure on a system's capacity to support pelagic production: an inverse analysis approach. *ICES Journal of Marine Science*, 68, 803 - 812, <http://dx.doi.org/10.1093/icesjms/fsr027>.

Marra, J., Langdon, C., and C. A. Knudson (1995), Primary production, water column changes, and the demise of a *Phaeocystis* bloom at the Marine Light-Mixed Layers site (59°N, 21°W) in the northeast Atlantic Ocean, *Journal of Geophysical Research*, 100, 6633 - 6643.

Marsh, R., A. Hickman, and J. Sharples (2015), S2P3-R (v1.0): a framework for efficient regional modelling of physical and biological structures and processes in shelf seas, *Geoscientific Model Development*, 8(10), 3163-3178, <https://doi.org/10.5194/gmd-8-3163-2015>.

McAllister, C. D. (1970), Zooplankton rations, phytoplankton mortality and the estimation of marine production, in: *Marine food chains*, Ed. by J. H. Steele, Berkley: University of California Press, 419-457.

Melin, F., G. Zibordi, and J. Berthon (2007), Assessment of satellite ocean color products at a coastal site, *Remote Sensing of Environment*, 110(2), 192-215, <https://doi.org/10.1016/j.rse.2007.02.026>.

Mellor, G., and T. Yamada (1982), Development of a turbulence closure-model for geophysical fluid problems, *Reviews of Geophysics*, 20(4), 851-875, <https://doi.org/10.1029/RG020i004p00851>.

Mills, D. K., Laane, R. W. P. M., Rees, J. M., Rutgers van der Loeff, M., Suylen, J. M., Pearce, D. J., Sivyer, D. B., Heins, C., Platt, K., and M. Rawlinson (2003), *Smartbuoy: A marine environmental monitoring buoy with a difference*, Editor(s): H. Dahlin, N. C. Flemming, K. Nittis, S. E. Petersson, Elsevier Oceanography Series, Elsevier, 69, 311-316, [https://doi.org/10.1016/S0422-9894\(03\)80050-8](https://doi.org/10.1016/S0422-9894(03)80050-8).

- Minnett, P. (2013), Satellite Remote Sensing of Sea Surface Temperatures, Reference Module in Earth Systems and Environmental Sciences, 10.1016/B978-0-12-409548-9.04340-2.
- Moore, C., D. Suggett, A. Hickman, Y. Kim, J. Tweddle, J. Sharples, R. Geider, and P. Holligan (2006), Phytoplankton photoacclimation and photoadaptation in response to environmental gradients in a shelf sea, *Limnology and Oceanography*, 51(2), 936-949.
- Moore, C., D. Suggett, P. Holligan, J. Sharples, E. Abraham, M. Lucas, T. Rippeth, N. Fisher, J. Simpson, and D. Hydes (2003), Physical controls on phytoplankton physiology and production at a shelf sea front: a fast repetition-rate fluorometer based field study, *Marine Ecology Progress Series*, 259, 29-45, <https://doi.org/10.3354/meps259029>.
- Moore, J. K., Doney, S. C., Kleypas, J. A., Glover, D. M., and I. Y. Fung (2001), An intermediate complexity marine ecosystem model for the global domain, *Deep Sea Research Part II: Topical Studies in Oceanography*, 49(1-3), 403-462, [https://doi.org/10.1016/S0967-0645\(01\)00108-4](https://doi.org/10.1016/S0967-0645(01)00108-4).
- Muller-Karger, F. E., Varela, R., Thunell, R., Luerssen, R., Hu, C. and J. J. Walsh (2005), The importance of continental margins in the global carbon cycle, 32, *Geophysical Research Letters*, <https://doi.org/10.1029/2004GL021346>.
- Mullin, M. M., Stewart, E. F., and Fuglister, F. J. (1975), Ingestion by planktonic grazers as a function of concentration of food, *Limnol. Oceanogr.*, 20, 259-262.
- Najjar, R. G., Sarmiento, J. L., and J. R. Toggweiler (1992), Downward transport and fate of organic matter in the ocean: simulations with a general circulation model, *Global Biogeochemical Cycles*, 6(1), 45-76.
- Øie Kville, K., Romagnoni, G., Dagestad, K., Langangen, Ø. and T. Kristiansen (2018), Sensitivity of modelled North Sea cod larvae transport to vertical behaviour, ocean model resolution and interannual variation in ocean dynamics, *ICES Journal of Marine Science*, 75(7), 2413 - 2424, <https://doi.org/10.1093/icesjms/fsy039>.

- Palmer, J. R. and I. J. Totterdell (2001), Production and export in a global ocean ecosystem model, *Deep-Sea Research*, 48, 1169–1198.
- Pauly, D., Christensen, V., Guenette, S. et al. (2002), Towards sustainability in world fisheries, *Nature*, 418, 689 - 695, <https://doi.org/10.1038/nature01017>.
- Penning De Vries, F. W. T., Brunsting, A. H. M. and H. H. Van Laar (1974), Products, requirements and efficiency of biosynthesis a quantitative approach, *Journal of Theoretical Biology*, 45(2), 339-377.
- Pedrós-Alió, C. (2006), Marine microbial diversity: can it be determined?, *Trends in Microbiology*, 14(6), 257-263, <https://doi.org/10.1016/j.tim.2006.04.007>.
- Perry, A. L., Low, P. J., Ellis, J. R., and J. D. Reynolds (2005), Climate Change and Distribution Shifts in Marine Fishes, *Science*, 308(5730), 1912 - 1915, <https://doi.org/10.1126/science.1111322>.
- Peterson, W. T., and J. E. Keister (2003), Interannual variability in copepod community composition at a coastal station in the northern California Current: a multivariate approach, *Deep Sea Research Part II: Topical Studies in Oceanography*, 50(14-16), 2499-2517, [https://doi.org/10.1016/S0967-0645\(03\)00130-9](https://doi.org/10.1016/S0967-0645(03)00130-9).
- Pingree, R., P. Holligan, and G. Mardell (1978), Effects of vertical stability on phytoplankton distributions in summer or Northwest European Shelf, *Deep-Sea Research*, 25(11), 1011-&, [https://doi.org/10.1016/0146-6291\(78\)90584-2](https://doi.org/10.1016/0146-6291(78)90584-2).
- Pingree, R., P. Holligan, G. Mardell, and R. Head (1976), Influence of physical stability on spring, summer and autumn phytoplankton blooms in Celtic Sea, *Journal of the Marine Biological Association of the United Kingdom*, 56(4), 845-873.
- Pingree, R. D., P. R. Pugh, P. M. Holligan, and G. R. Forster (1975), Summer phytoplankton blooms and red tides along tidal fronts in the approaches to the English Channel,

Nature, 258(5537), 672-677.

Pingree, R. D., and D. K. Griffiths (1978), Tidal fronts on the shelf seas around the British Isles, *Journal of Geophysical Research: Oceans*, 83(C9), 4615-4622, <https://doi.org/10.1029/JC083iC09p04615>.

Platt, T. C., Bird, D. F., and S. Sathyendranath (1991), Critical depth and marine production, *Proceedings of the Royal Society*, 246(1317), <https://doi.org/10.1098/rspb.1991.0146>.

Platt, T., Sathyendranath, S., Forget, M., Caverhill, C., Bouman, H. Devred, E., and S. Son (2008), Operational estimation of primary production at large geographical scales, *Remote Sensing of Environment*, 112, 3437 - 3448.

Platt, T., Fuentes-Yaco, C., and K. T. Frank (2003), Spring algal bloom and larval fish survival, *Nature*, 423, 398-399.

Poulton, A. (2015), Cruise Report (Shelf Sea Biogeochemistry): RRS Discovery Cruise DY029, 1-30 April 2015, NOC Southampton, (174 pp).

Prestidge, M., and A. Taylor (1995), A modelling investigation of the distribution of stratification and phytoplankton abundance in the Irish Sea, *Journal of Plankton Research*, 17(7), 1397-1420.

Raymont, J. E. G. (1980), *Plankton and productivity in the oceans*, New York: Pergamon Press, 2.

Redfield, A. C., B. H. Ketchum, and F. A. Richards (1963), The influence of organisms on the composition of sea-water, in: Hill, M.N. (Ed.) *The composition of seawater: Comparative and descriptive oceanography*, *The sea: ideas and observations on progress in the study of the seas*, 2, 26-77.

Rey, F., Skjoldal H. R., and D. Slagstad (1987), Primary production in relation to climatic

changes in the Barents Sea. In: Loeng H, editor. The effect of oceanographic conditions on distribution and population dynamics of commercial fish stocks in the Barents Sea, Proceedings of the 3rd Soviet-Norwegian symposium, 1986, 26-28, Murmansk.

Richardson, K., Nielsen, T., Pedersen, F., Heilmann, J., Lokkegaard, B., and H. Kaas (1998), Spatial heterogeneity in the structure of the planktonic food web in the North Sea, Marine Ecology Progress Series, 168, 197 - 211.

Richardson, K., and F. Pedersen (1998), Estimation of new production in the North Sea: consequences for temporal and spatial variability of phytoplankton, Ices Journal of Marine Science, 55(4), 574-580, <https://doi.org/10.1006/jmsc.1998.0402>.

Ridderinkhof, H. (1992), On the effects of variability in meteorological forcing on the vertical structure of a stratified watercolumn, Continental Shelf Research, 12(1), 25 - 36, [https://doi.org/10.1016/0278-4343\(92\)90004-4](https://doi.org/10.1016/0278-4343(92)90004-4).

Riley, G. A. (1942), The relationship of vertical turbulence and spring diatom flowerings, Journal of Marine Research, 5(1), 66-87.

Riley, G. A. (1946), Factors controlling phytoplankton populations on Georges Bank, Journal of Marine Research, 6, 54-71.

Rippeth, T. (2005), Mixing in seasonally stratified shelf seas: a shifting paradigm, Philosophical Transactions of The Royal Society A Mathematical Physical and Engineering Sciences, 363(1837), 2837-2854, <https://doi.org/10.1098/rsta.2005.1662>.

Rippeth, T. P., Palmer, M. R., Simpson, J. H., Fisher, N. R., and J. Sharples (2005), Thermocline mixing in summer stratified continental shelf seas, Geophysical Research Letters, 32.

Rippeth, T., P. Wiles, M. Palmer, J. Sharples, and J. Tweddle (2009), The diapycnal nutrient flux and shear-induced diapycnal mixing in the seasonally stratified western Irish Sea, Continental Shelf Research, 29(13), 1580-1587, <https://doi.org/10.1016/j.csr.2009>.

04.009.

Rogers, S. I. and B. Greenaway (2005), A UK perspective on the development of marine ecosystem indicators, *Marine Pollution Bulletin*, 50(1), 9 - 19, <https://doi.org/10.1016/j.marpolbul.2004.10.028>.

Rumyantseva, A., N. Lucas, T. Rippeth, A. Martin, S. Painter, T. Boyd, and S. Henson (2015), Ocean nutrient pathways associated with the passage of a storm, *Global Biogeochemical Cycles*, 29(8), 1179-1189, <https://doi.org/10.1002/2015GB005097>.

Ryther, J. H., and E. M. Hulburt (1960), On winter mixing and the vertical distribution of phytoplankton, *Limnology and Oceanography*, 5(3), 337 - 338, <https://doi.org/10.4319/10.1960.5.3.0337>.

Sarmiento, J. L. and N. Gruber (2006), *Ocean Biogeochemical Dynamics*, Princeton, Woodstock: Princeton University Press.

Sarmiento, J. L., Slater, R. D., Fasham, M. J. R., Ducklow, H. W., Toggweiler, J. R., and G. T. Evans (1993), A seasonal three dimensional ecosystem model of nitrogen cycling in the North Atlantic euphotic zone, *Global Biogeochemical Cycles*, 7, 417-450.

Sharples, J. (1999), Investigating the seasonal vertical structure of phytoplankton in shelf seas, *Progress in Oceanography*, 3-38.

Sharples, J. (2008), Potential impacts of the spring-neap tidal cycle on shelf sea primary production, *Journal of Plankton Research*, 30(2), 183-197, <https://doi.org/10.1093/plankt/fbm088>.

Sharples, J., Ellis, J. R., Nolan, G., and B. E. Scott (2013), Fishing and the oceanography of a stratified shelf sea, *Progress in Oceanography*, 117, 130 - 139, <https://doi.org/10.1016/j.pocean.2013.06.014>.

Sharples, J., and P. Tett (1994), Modeling the effect of physical variability on the midwater

- chlorophyll maximum, *Journal of Marine Research*, 52(2), 219-238, <https://doi.org/10.1357/0022240943077109>.
- Sharples, J., and P. M. Holligan (2006), Interdisciplinary studies in the Celtic Seas, in *The Sea*, edited by H. U. Press, pp. 1003-1031.
- Sharples, J., O. Ross, B. Scott, S. Greenstreet, and H. Fraser (2006), Inter-annual variability in the timing of stratification and the spring bloom in the North-western North Sea, *Continental Shelf Research*, 26(6), 733-751, <https://doi.org/10.1016/j.csr.2006.01.011>.
- Sharples, J., C. Moore, T. Rippeth, P. Holligan, D. Hydes, N. Fisher, and J. Simpson (2001), Phytoplankton distribution and survival in the thermocline, *Limnology and Oceanography*, 46(3), 486-496.
- Shchepetkin, A., and J. McWilliams (2005), The regional oceanic modeling system (ROMS): a split-explicit, free-surface, topography-following-coordinate oceanic model, *Ocean Modelling*, 9(4), 347-404, <https://doi.org/10.1016/j.ocemod.2004.08.002>.
- Shi, J., Y. Liu, X. Mao, X. Guo, H. Wei, and H. Gao (2017). Interannual variation of spring phytoplankton bloom and response to turbulent energy generated by atmospheric forcing in the central Southern Yellow Sea of China: Satellite observations and numerical model study. *Continental Shelf Research*, 143, 257-270.
- Siegel, D. A. and Doney, S. C. and J. A. Yoder (2002), The North Atlantic Spring Phytoplankton Bloom and Sverdrup's Critical Depth Hypothesis, 296, 730 - 733.
- Sigler, M. F., Stabeno, P. J., Eisner, L. B., Napp, J. M., and F. J. Mueter (2014), Spring and fall phytoplankton blooms in a productive subarctic ecosystem, the eastern Bering Sea, during 1995–2011, *Deep Sea Research Part II: Topical Studies in Oceanography*, 109, 71-83, <https://doi.org/10.1016/j.dsr2.2013.12.007>.
- Simpson, J. H., Crisp, D. J. and C. Hearn (1981), *The Shelf-Sea Fronts: Implications of*

Their Existence and Behaviour, *Philosophical Transactions of the Royal Society of London, Series A, Mathematical and Physical Sciences*, 302(1472), 531-46, <http://www.jstor.org/stable/37036>.

Simpson, J. H. (1997), Physical processes in the ROFI regime, *Journal of Marine Systems*, 12(1-4), 3-15, [https://doi.org/10.1016/S0924-7963\(96\)00085-1](https://doi.org/10.1016/S0924-7963(96)00085-1).

Simpson, J. H. (1998), The Celtic Seas, In: *The Sea*, 11, 659 - 582, Edited by Robinson, A.R. and Brink, K.H, John Wiley & Son.

Simpson, J. H. and D. G. Bowers (1981), Models of stratification and frontal movement in shelf seas, *Deep Sea Research Part A, Oceanographic Research Papers*, 28(7), 727 - 738, [https://doi.org/10.1016/0198-0149\(81\)90132-1](https://doi.org/10.1016/0198-0149(81)90132-1).

Simpson, J. H. and D. G. Bowers (1990), Data Bank Oceanography: testing models of the seasonal heat cycle in shelf seas, *Physics of Shallow Seas*, H. Wang, J. Wang and H. Dai. Beijing: China Ocean Press, 291 - 304.

Simpson, J. H., and J. Hunter (1974), Fronts in Irish Sea, *Nature*, 250(5465), 404-406, <https://doi.org/10.1038/250404a0>.

Simpson, J. H., and D. Bowers (1984), The role of tidal stirring in controlling the seasonal heat cycle in shelf seas, *Annales Geophysicae*, 2(4), 411-416.

Simpson, J. H., and J. Sharples (2012), Introduction to the physical and biological oceanography of shelf seas, xxiv, 424 p., 416 p. of col. plates pp., Cambridge University Press, Cambridge ; New York.

Sims, D. (2006), Impacts of Climate Change on Fish in Marine Climate Change Impacts Annual Report Card 2006 (Eds. Buckley, P. J., Dye, S. R. and J. M. Baxter), Online Summary Reports, MCCIP, Lowestoft, <http://www.mccip.org.uk/>.

Six, K. D. and E. Maier-Reimer (1996), Effects of plankton dynamics on seasonal carbon

fluxes in an ocean general circulation model, *Global Biogeochemical Cycles*, 10, 559–583.

Smetacek, V. and U. Passow (1990), Spring bloom initiation and Sverdrup's critical-depth model, *Limnology and Oceanography*, 35(1), 228 - 234, <https://doi.org/10.4319/lo.1990.35.1.0228>.

Smith, M. J., D. P. Tittensor, V. Lyutsarev, and E. Murphy (2015), Inferred support for disturbance-recovery hypothesis of North Atlantic phytoplankton blooms, *Journal of Geophysical Research: Oceans*, 120, 7067-7090, <https://doi.org/10.1002/2015JC011080>.

Smyth, T. J., Fishwick, J. R., Al-Moosawi, L., Cummings, D. G., Harris, C., Kitidis, V., Rees, A., Martinez-Vicente, V., and E. M. S. Woodward (2010), A broad spatio-temporal view of the Western English Channel observatory, *Journal of Plankton Research*, 32, 585 - 601, <https://doi.org/10.1093/plankt/fbp128>.

Sommer, U., Adrian, R., De Senerpont Domis, L., Elser, J. J., Gaedke, U., Ibelings, B., Jeppesen, E., Lurling, M., Molinero, J. C., Mooij, W. M., van Donk, E., and M. Winder (2012), Beyond the Plankton Ecology Group (PEG) Model: Mechanisms Driving Plankton Succession, *Annual Review of Ecology, Evolution, and Systematics*, 43(1), 429 - 448.

Steele, J. H. (1974), *The structure of marine ecosystems*, Harvard University Press, Cambridge, Massachusetts.

Steele, J. H., and C. S. Yentsch (1960), The vertical distribution of chlorophyll, *Journal of the Marine Biological Association of the United Kingdom*, 39(2), 217-226.

Steele, J. H. and B. W. Frost (1977), The structure of plankton communities, *Philosophical Transactions of the Royal Society London*, 280, 485-534.

Steele, J. H. and M. M. Mullin (1977), Zooplankton dynamics, *The sea*, 6, 857-890.

Steele, J. H. and E. W. Henderson (1981), A simple plankton model, *The American Naturalist*, 117, 676-691.

Strickland, J. D. H. (1960), Measuring the production of marine phytoplankton, *Bulletin Fisheries Research Board of Canada*, 122: 1-172.

Sverdrup, H. U. (1953), On Conditions for the Vernal Blooming of Phytoplankton, *ICES Journal of Marine Science*, 18(3), 287–295.

Taylor, A. H. and J. A. Stephens (1993), Diurnal variations of convective mixing and the spring bloom of phytoplankton, *Deep Sea Research Part II: Topical Studies in Oceanography*, 40(1–2), 9-408, [https://doi.org/10.1016/0967-0645\(93\)90023-G](https://doi.org/10.1016/0967-0645(93)90023-G).

Tenore, K. R., et al. (1995), Fisheries and oceanography off Galicia, NW Spain: Mesoscale spatial and temporal changes in physical processes and resultant patterns of biological productivity, *Journal of Geophysical Research*, 100, 10943 - 10966.

Tett, P. B., Joint, I. R., Purdie, D. A., Baars, M., Oosterhuis, S., Daneri, G., Hannah, F., Mills, D. K., Plummer, D., Pomroy, A. J., Walne, A. W., Witte, H. J., Howarth, M. J., Lankester, R., Charnock, H., Dyer, K. R., Huthnance, J. M., Liss, P. S., and J. H. Simpson (1993), Biological consequences of tidal stirring gradients in the North Sea, *Philosophical Transactions of the Royal Society of London. Series A: Physical and Engineering Sciences*, 343, 493 - 508.

Thomas, H., Y. Bozec, K. Elkalay, and H. de Baar (2004), Enhanced open ocean storage of CO₂ from shelf sea pumping, *Science*, 304(5673), 1005-1008, <https://doi.org/10.1126/science.1095491>.

Thomas, A., Townsend, D., and R. Weatherbee (2003), Satellite-measured phytoplankton variability in the Gulf of Maine, *Continental Shelf Research*, 23, 971 - 989.

Tian, T., Su, J., Floser, G., Wiltshire, K., and K. Wirtz (2011), Factors controlling the onset of spring blooms in the German Bight 2002 - 2005: Light, wind and stratification, *Continental Shelf Research*, 31(10), 1140 - 1148, <https://doi.org/10.1016/j.csr.2011.04.008>.

Tilman, D. (1977), Resource competition between plankton algae: an experimental and theoretical approach, *Ecology*, 58(2), 338-348.

Tinker, J., Lowe, J., Pardaens, A., Holt, J., and R. Barciela (2016), Uncertainty in climate projections for the 21st century northwest European shelf seas, *Progress in Oceanography*, 148, 56 - 73, <https://doi.org/10.1016/j.pocean.2016.09.003>.

Townsend, D., M. Keller, M. Sieracki, and S. Ackleson (1992), Spring phytoplankton blooms in the absence of vertical water column stratification, *Nature*, 360(6399), 59-62.

Townsend, D., L. Cammen, P. Holligan, D. Campbell, and N. Pettigrew (1994), Causes and consequences of variability in the timing of spring phytoplankton blooms, *Deep-Sea Research Part I - Oceanographic Research Papers*, 41(5-6), 747-765.

Turner, J. S. (1973), *Buoyancy effects in fluids*, Cambridge: Cambridge University Press (2010). The melting of ice in the Arctic Ocean: the influence of double-diffusive transport of heat from below, *Journal of Physical Oceanography*, 40(1), 249-256.

Tusseau, M. H., Lancelot, C., Martin, J. M., and B. Tassin (1997), 1-D coupled physical-biological model of the northwestern Mediterranean Sea, *Deep Sea Research Part II: Topical Studies in Oceanography*, 44(3-4), 851 - 880, [https://doi.org/10.1016/S0967-0645\(96\)00087-2](https://doi.org/10.1016/S0967-0645(96)00087-2).

Tweddle, J. F., Sharples, J., Palmer, M. R., Davidson, K., and S. McNeill (2013), Enhanced nutrient fluxes at the shelf sea seasonal thermocline caused by stratified flow over a bank, *Progress in Oceanography*, 117, 37 - 47, <https://doi.org/10.1016/j.pocean.2013.06.018>.

Valiela, I. (1995), *Marine ecological processes*, New York: Springer-Verlag, 2, 686.

Valiela, I. (2010), *Marine Ecological Processes*, xviii, 702 p., Springer-Verlag New York.

van Leeuwen, S., J. van der Molen, P. Ruardij, L. Fernand, and T. Jickells (2013), *Modelling*

the contribution of deep chlorophyll maxima to annual primary production in the North Sea, *Biogeochemistry*, 113(1-3), 137-152, <https://doi.org/10.1007/s10533-012-9704-5>.

van Leussen, W., Radach, G., van Raaphorst, W., Colijn, F., and R. W. P. M. Laane (1996): The North-West European Shelf Programme (NOWESP): integrated analysis of shelf processes based on existing data sets and models, *ICES Journal of Marine Science*, 53(6), 926 - 932.

Vargas. C.A., R. Escribano, and S. Poulet (2006), Phytoplankton food quality determines time windows for successful zooplankton reproductive pulses, *Ecology*, 8, 2992-2999.

Vidal, J. (1980), Physioecology of zooplankton. I. Effects of phytoplankton concentration, temperature, and body size on the growth rate of *Calanus pacificus* and *Pseudocalanus* sp., *Marine Biology*, 56(2), 111-134.

Volterra V. (1926), Fluctuations in the abundance of a species considered mathematically, *Nature*, 118(2972), 558 - 560.

Wakelin, S., Holt, J., Blackford, J. C., Allen, J. I., Butenschon, M., and Y. Artioli (2012), Modeling the carbon fluxes of the northwest European continental shelf: Validation and budgets. *Journal of Geophysical Research*, 117 (C5). C05020, <https://doi.org/10.1029/2011JC007402>.

Wakelin, S., J. Holt, and R. Proctor (2009), The influence of initial conditions and open boundary conditions on shelf circulation in a 3D ocean-shelf model of the North East Atlantic, *Ocean Dynamics*, 59(1), 67-81, <https://doi.org/10.1007/s10236-008-0164-3>.

Waniek, J. J. (2003), The role of physical forcing in initiation of spring blooms in the northeast Atlantic, *Journal of Marine Systems*, 39, 57-82, [https://doi.org/10.1016/S0924-7963\(02\)00248-8](https://doi.org/10.1016/S0924-7963(02)00248-8).

Ward, B. A., Friedrichs M. A. M., Anderson T. R., and A. Oschlies (2010), Parameter optimisation techniques and the problem of underdetermination in marine biogeochemical

models, *Journal of Marine Systems*, 81(1-2), 34-43.

Ward, B. A., Schartau, M., Oschlies, A., Martin, A. P., Follows, M. J., and T. R. Anderson (2013), When is a biogeochemical model too complex? Objective model reduction and selection for North Atlantic time-series sites, *Progress in Oceanography*, 116, 49-65, <https://doi.org/10.1016/j.pocean.2013.06.002>.

Ware, D., and R. Thomson (2011), Link Between Long-Term Variability in Upwelling and Fish Production in the Northeast Pacific Ocean, *Canadian Journal of Fisheries and Aquatic Sciences*, 48, 2296 - 2306.

Werdell, P. J., Behrenfeld, M. J., Bontempi, P. S., Boss, E., Cairns, B., Davis, G. T., Franz, B. A., Gliese, U. B., Gorman, E. T., Hasekamp, O., Knobelspiesse, K. D., Manino, A., Martins, J. V., McClain, C. R., Meister, G., and L. A. Remer (2019), The Plankton, Aerosol, Cloud, Ocean Ecosystem Mission: Status, Science, Advances, *Bulletin of the American Meteorological Society*, 100, 1775 - 1794, <https://doi.org/10.1175/BAMS-D-18-0056.1>.

Williams, C., J. Sharples, C. Mahaffey, and T. Rippeth (2013), Wind-driven nutrient pulses to the subsurface chlorophyll maximum in seasonally stratified shelf seas, *Geophysical Research Letters*, 40(20), 5467-5472, <https://doi.org/10.1046/j.1365-2419.1997.00034.x>.

White, M. A. et al. (2009), Intercomparison, interpretation, and assessment of spring phenology in North America estimated from remote sensing for 1982 - 2006, *Global Change Biology*, 15, 2335 - 2359.

Wollast, R. (1998), Evaluation and comparison of the global carbon cycle in the coastal zone and in the open ocean, in *The Sea*, edited by K. H. Brink and A. R. Robinson, pp. 213-251.

Wroblewski, J. S., Sarmiento, J. L. and G. R. Flierl (1988), An ocean basin scale model of plankton dynamics in the North Atlantic. 1. Solutions for the climatological oceano-

- graphic conditions in May, *Global Biogeochemical Cycles*, 2, 199–218.
- Yin, K., Harrison, P. J., Pond, S., and R. J. Beamish (1995), Entrainment of Nitrate in the Fraser River Estuary and its Biological Implications. II. Effects of Spring vs. Neap Tides and River Discharge, *Estuarine, Coastal and Shelf Science*, 40(5), 529 - 544, <https://doi.org/10.1006/ecss.1995.0036>.
- Yoder, J. A. (1979), Effect of temperature on light-limited growth and chemical composition of *Skeletonema costatum* (Bacillariophyceae), *Journal of Phycology*, 15, 362-37.
- Yool, A., Popova, E. E., and T. R. Anderson (2011), Medusa-1.0: a new intermediate complexity plankton ecosystem model for the global domain, *Geoscientific Model Development*, 4, 381–417, <https://doi.org/10.5194/gmd-4-381-2011>.
- Young, E., Brown, J. Aldridge, J., Horsburgh, K. L. Fernand (2004), Development and application of a three-dimensional baroclinic model to the study of the seasonal circulation in the Celtic Sea, *Continental Shelf Research*, 24, 13 - 36.
- Zhao, H., Han, G., and D. Wang (2013), Timing and magnitude of spring bloom and effects of physical environments over the Grand Banks of Newfoundland, *Journal of Geophysical Research Biogeosciences*, 118, 1385 - 1396.